Nanoconfinement Design of MoS_2 Electrode Materials: Impact of Structural Modification and Electrochemical Ion Intercalation Properties

Zur Erlangung des akademischen Grades eines

DOKTORS DER NATURWISSENSCHAFTEN

(Dr. rer. nat.)

von der KIT-Fakultät für Chemie und Biowissenschaften

des Karlsruher Instituts für Technologie (KIT)

genehmigte

DISSERTATION

von

M.Sc. Jaehoon Choi

KIT-Dekan: Prof. Dr. Martin Bastmeyer

1. Referent: Dr. Simon Fleischmann

2. Referentin: Prof. Dr. Daria Mikhailova

Tag der mündlichen Prüfung: 02 Februar 2026

Abstract

The global transition toward a carbon-neutral energy landscape necessitates a fundamental paradigm shift in energy storage technologies. While intermittent renewable sources like wind and solar are rapidly expanding, their effective integration into the power grid and the widespread decarbonization of the transport sector are currently constrained by the performance limitations of two (EES) systems. Specifically, a critical performance gap exists between high-energy-density batteries, which typically suffer from slow charging/discharging kinetics, and high-power-density supercapacitors (SCs), which lack sufficient energy storage capacity. Bridging this gap requires the development of advanced electrode materials that can combine the high capacity of Faradaic redox reactions with the rapid kinetics of surface-controlled processes. This dissertation addresses this challenge by investigating nanoconfinement design in layered molybdenum disulfide (MoS_2) as a model system. By rationally tailoring the geometry and chemistry of the interlayer space, this work aims to overcome the sluggish solid-state diffusion inherent to bulk materials and unlock fast, pseudocapacitive ion storage mechanisms.

The first study establishes a versatile, one-pot hydrothermal synthesis strategy to simultaneously control the crystallite size and interlayer spacing of MoS_2. By adjusting the pH of the precursor solution and introducing 1,6-hexanediamine (HDA) as an organic pillar, the study effectively demonstrates the influence of particle size and lattice expansion on the charge storage properties. Electrochemical characterization reveals that reducing crystallite size and expanding the interlayer spacing act synergistically to promote capacitor-like kinetics. The optimized nanoconfinement-designed structure achieved a reversible lithium storage capacity of 199 mAh/g, significantly exceeding the theoretical intercalation limit of bulk MoS_2, while exhibiting a high *b*-value of 0.93, indicative of surface-dominant kinetics. This study demonstrates that nanoconfinement design can activate additional storage sites within the van der Waals (vdW) gaps, effectively transforming a battery-type material into a high-rate pseudocapacitive electrode material.

Building on the nanoconfinement design strategy, the second study investigates the critical role of host-pillar interactions and pillar density by introducing covalent functionalization with 1,6-hexanedithiol (HDT). This approach addresses the potential instability of non-covalent pillars by establishing robust chemical bonds between the organic pillar species and the MoS_2 host lattice. Through a comprehensive combination of experimental analysis and density functional theory (DFT) simulations, the study uncovers a fundamental trade-off between structural stability offered by pillars and the kinetic limitations to charge storage they impose. While an optimized pillar loading maintains high capacity (196 mAh/g), excessive pillar density is found to severely impede ion transport and block active storage sites, leading to a drastic

reduction in performance. This work provides direct evidence that organic pillars can act as kinetic barriers if overcrowded, establishing a vital design rule: high-performance nanoconfinement design requires a precise balance where pillars expand the layers sufficiently for ion access while sparse enough distribution to minimize diffusion pathway obstruction.

The third study elucidates the scalability of nanoconfinement design strategies by transitioning from the bottom-up, hydrothermal synthesis towards a top-down synthesis method based on commercially available, bulk MoS_2. Utilizing this scalable material platform to investigate the interplay between electrode structure and electrolyte solvent, the research reveals a divergence in storage mechanisms. While bulk MoS_2 undergoes a massive 132 % expansion of the c-lattice parameter in ether electrolytes due to solvent co-intercalation, the HDA pillared MoS_2 minimizes this expansion to approximately 8 %. This suggests that organic pillars prevent solvent co-intercalation while enabling desolvated Li^+ intercalation, which could offer distinct advantages for long-term cycling stability by mitigating the structural stress associated with excessive volume expansion.

In conclusion, this dissertation demonstrates that rational nanoconfinement design is a powerful tool to tailor the thermodynamics and kinetics of ion intercalation in layered materials. By providing a blueprint for designing electrodes that merge the high energy density of batteries with the high power density of SCs, this work contributes directly to the development of fast-charging, long-lasting energy storage systems essential for renewable energy applications, ultimately supporting the global societal goal of a sustainable, zero-emission future.

Kurzfassung

Die globale Wende zu einer kohlenstoffneutralen Energieversorgung erfordert einen grundlegenden Paradigmenwechsel bei den Energiespeichertechnologien. Während fluktuierende erneuerbare Energiequellen wie Wind und Sonne stärker genutzt werden, werden ihre effektive Integration in das Stromnetz und die weitgehende Dekarbonisierung des Verkehrssektors derzeit wegen der Leistungsbeschränkungen der beiden etablierten elektrochemischen Energiespeichersystemen (EES) eingeschränkt. Konkret besteht eine kritische Leistungslücke zwischen Batterien mit hoher Energiedichte, die typischerweise unter einer langsamen Lade-/Entladekinetik leiden, und Superkondensatoren (SCs) mit hoher Leistungsdichte, denen es an ausreichender Energiespeicherkapazität mangelt. Die Überbrückung dieser Lücke erfordert die Entwicklung fortschrittlicher Elektrodenmaterialien, die die hohe Kapazität faradaischer Redoxreaktionen mit der schnellen Kinetik oberflächengesteuerter Prozesse kombinieren können. Diese Dissertation adressiert diese Herausforderung durch die Untersuchung des Nanoconfinement-Designs in schichtstrukturiertem Molybdändisulfid (MoS_2) als Modellsystem. Durch die gezielte Maßschneiderung der Geometrie und Chemie des Zwischenschichtraums zielt diese Arbeit darauf ab, die träge Festkörperdiffusion, die Bulk-Materialien inhärent ist, zu überwinden und schnelle, pseudokapazitive Ionenspeichermechanismen zu erschließen.

Die erste Studie etabliert eine vielseitige Hydrothermalsynthese-Strategie zur gleichzeitigen Kontrolle der Kristallitgröße und des Zwischenschichtabstands von MoS_2. Durch Anpassung des pH-Werts der Vorstufenlösung und Einführung von 1,6-Hexandiamin (HDA) als organischem Molekül (fungiert als „Stützpfeiler“) demonstriert die Studie effektiv den Einfluss von Partikelgröße und Gitterexpansion auf die Ladungsspeichereigenschaften. Die elektrochemische Charakterisierung zeigt, dass die Reduzierung der Kristallitgröße und die Aufweitung des Zwischenschichtabstands synergistisch wirken, um kondensatorähnliche Kinetik zu fördern. Die optimierte, durch Nanoconfinement designte Struktur erreichte eine reversible Lithiumspeicherkapazität von 199 mAh/g, was das theoretische Interkalationslimit von Bulk MoS_2 deutlich übertrifft, während sie einen hohen b-Wert von 0,93 aufwies, der auf eine oberflächendominierte Kinetik hinweist. Diese Studie zeigt, dass das Nanoconfinement-Design zusätzliche Speicherplätze innerhalb der van-der-Waals-(vdW)-Lücken aktivieren kann und somit ein batterieartiges Material effektiv in ein hochratenfähiges pseudokapazitives Elektrodenmaterial transformiert.

Aufbauend auf der Nanoconfinement-Designstrategie untersucht die zweite Studie die kritische Rolle von Wirt-Molekül-Wechselwirkungen und Moleküldichte durch die Einführung einer kovalenten Funktionalisierung mit 1,6-Hexandithiol (HDT). Dieser Ansatz adressiert die potenzielle Instabilität nicht-kovalent gebundener Moleküle durch den Aufbau robuster

chemischer Bindungen zwischen den organischen Molekülen und dem MoS_2-Wirtsgitter. Durch eine umfassende Kombination aus experimenteller Analyse und DFT-Simulationen deckt die Studie eine fundamentale Ambivalenz zwischen der strukturellen Stabilität, die durch die Moleküle geboten wird, und den kinetischen Einschränkungen der Ladungsspeicherung, die sie verursachen, auf. Während eine optimierte Molekülbeladung eine hohe Kapazität (196 mAh/g) aufrechterhält, stellt sich heraus, dass eine übermäßige Säulendichte den Ionentransport stark behindert und aktive Speicherplätze blockiert, was zu einer drastischen Leistungsminderung führt. Diese Arbeit liefert den direkten Beweis, dass organische Moleküle als kinetische Barrieren wirken können, wenn sie den Zwischenschichtraum überfüllen, und etabliert eine wichtige Designregel: Hochleistungsfähiges Nanoconfinement-Design erfordert ein präzises Gleichgewicht, bei dem Moleküle die Schichten ausreichend für den Ionen-Zugang aufweiten, während sie spärlich genug verteilt sind, um die Blockierung der Diffusionswege zu minimieren.

Die dritte Studie beleuchtet die Skalierbarkeit von Nanoconfinement-Designstrategien durch den Übergang von der Bottom-up-Hydrothermalsynthese hin zu einer Top-down-Synthesemethode auf Basis von kommerziell erhältlichem Bulk-MoS_2. Unter Nutzung dieser skalierbaren Materialplattform zur Untersuchung des Zusammenspiels zwischen Elektrodenstruktur und Elektrolytlösungsmittel enthüllt die Forschung eine Divergenz in den Speichermechanismen. Während Bulk-MoS_2 in Ether-Elektrolyten aufgrund von Lösungsmittel-Co-Interkalation eine massive Expansion des c-Gitterparameters um 132 % erfährt, minimiert das HDA-gestützte MoS_2 diese Expansion auf etwa 8 %. Dies deutet darauf hin, dass organische Säulen die Lösungsmittel-Co-Interkalation verhindern, während sie die Interkalation desolvatisierter Li^+-Ionen ermöglichen, was durch die Milderung des mit übermäßiger Volumenexpansion verbundenen strukturellen Stresses deutliche Vorteile für die Langzeitzyklusstabilität bieten könnte.

Zusammenfassend demonstriert diese Dissertation, dass rationales Nanoconfinement-Design ein mächtiges Werkzeug ist, um die Thermodynamik und Kinetik der Ioneninterkalation in Schichtmaterialien maßzuschneidern. Indem sie einen Bauplan für das Design von Elektroden liefert, die die hohe Energiedichte von Batterien mit der hohen Leistungsdichte von SCs vereinen, trägt diese Arbeit direkt zur Entwicklung schnellladefähiger, langlebiger Energiespeichersysteme bei, die für Anwendungen im Bereich erneuerbarer Energien unerlässlich sind, und unterstützt letztlich das globale gesellschaftliche Ziel einer nachhaltigen, emissionsfreien Zukunft.

Table of Contents

Table of Contents

Table of Contents

Chapter 1: Introduction

1.1. Background and Motivation

The global energy transition toward energy and zero-carbon-emission polices is fundamentally reshaping the landscape of energy generation and consumption.[1,2] This massive shift is illustrated in **Fig. 1.1A**, which tracks the evolution of global electricity generation since 2000. While conventional sources like coal remain significant, the data highlights a rapid rise in intermittent renewable sources, particularly wind and solar photovoltaic (PV), in recent years. The consumption trends presented in **Fig. 1.1B** underscore the magnitude of the decarbonization challenge. The industry and transport sectors consistently dominate global energy demand, necessitating a comprehensive shift toward electrification. However, aligning the intermittent generation profile of renewables (**Fig. 1.1A**) with the high, growing demands of these sectors (**Fig. 1.1B**) creates a temporal mismatch. Consequently, this transformation has positioned electrochemical energy storage (EES) systems as essential infrastructure. EES is indispensable for stabilizing the power grid, preventing the waste of valuable generated energy, and enabling the widespread adoption of electric vehicles (EVs) and advanced portable electronics.[3,4]

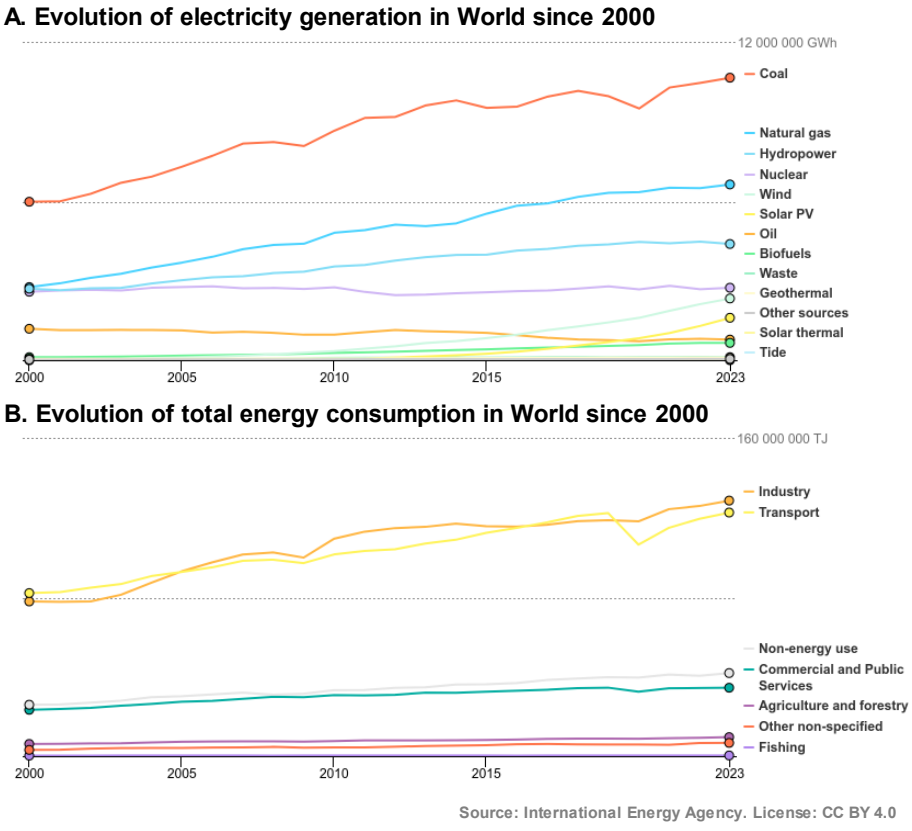

Figure 1.1: Trends in global energy production (A) and use (B) from 2000 to 2023. Panel A illustrates the evolution of electricity generation in the world since 2000, showing the rapid

growth of intermittent renewable sources. Panel B displays the evolution of total energy consumption, highlighting the sustained, dominant energy demand from the industry and transport sectors. Cited from the International Energy Agency (IEA), with a CC BY License.

The diverse demands across these sectors dictate two distinct, and often competing, performance requirements for EES systems. Applications demanding high power density, such as regenerative braking in vehicles or grid frequency regulation, require electrode materials capable of storing/releasing charge rapidly. Conversely, applications focused on high energy density, such as long-range EVs, long-duration grid load leveling, and portable electronics, require maximum capacity for extended operation time. This divergence highlights the central challenge: current commercial EES systems are typically constrained by an inherent power-energy density trade-off. Devices that deliver high energy often suffer from slow kinetics, while those with high power hold less energy. This limitation is among the central scientific motivations for next-generation battery materials research. To bridge this performance gap and realize the benefit of combining high energy and high power density, one of the current scientific approaches focuses on structural engineering of electrode materials. This imperative specifically drives the exploration of structural engineering strategies, such as manipulating the interlayer spacing of layered materials, to enhance ion transport and maximize the kinetics of charge storage. Ultimately, filling this knowledge gap requires a qualitative and quantitative understanding of the correlation between material structure and resulting electrochemistry, which will enable the rational tailoring of electrode structure for desired EES applications.

1.2. Electrochemical Energy Storage Technologies

The fundamental concepts of EES date back over 200 years, beginning with the landmark work of Alessandro Volta and his development of the Voltaic Pile in the late 1700s and early 1800s.[5] Over the subsequent centuries, the EES systems (batteries and supercapacitors) have been developed, and now they play an essential role across a vast range of technical applications. Future applications will also heavily rely on EES for decentralized peak power shaving, load levelling, and high-performance EVs. The success of these applications depends on continuous improvement in cycle life, specific power, specific energy, and cost considerations in their markets.

The fundamental performance characteristics of EES are determined by the charge storage mechanism that is defined by the electrode material interaction with charge-carrying ions in the electrolyte. This theoretical foundation is essential for understanding how the thermodynamics and kinetics of electrochemical processes change in response to structural

manipulation. As illustrated in the Ragone plot (**Fig. 1.2**), the field conventionally distinguishes two primary storage mechanisms: Faradaic redox reaction (battery-type) and electrical double-layer formation (capacitor-type).[6] The concept of pseudocapacitance, which effectively blurs this performance boundary, is addressed subsequently. These storage mechanisms are each governed by distinct electrochemical properties and equations.

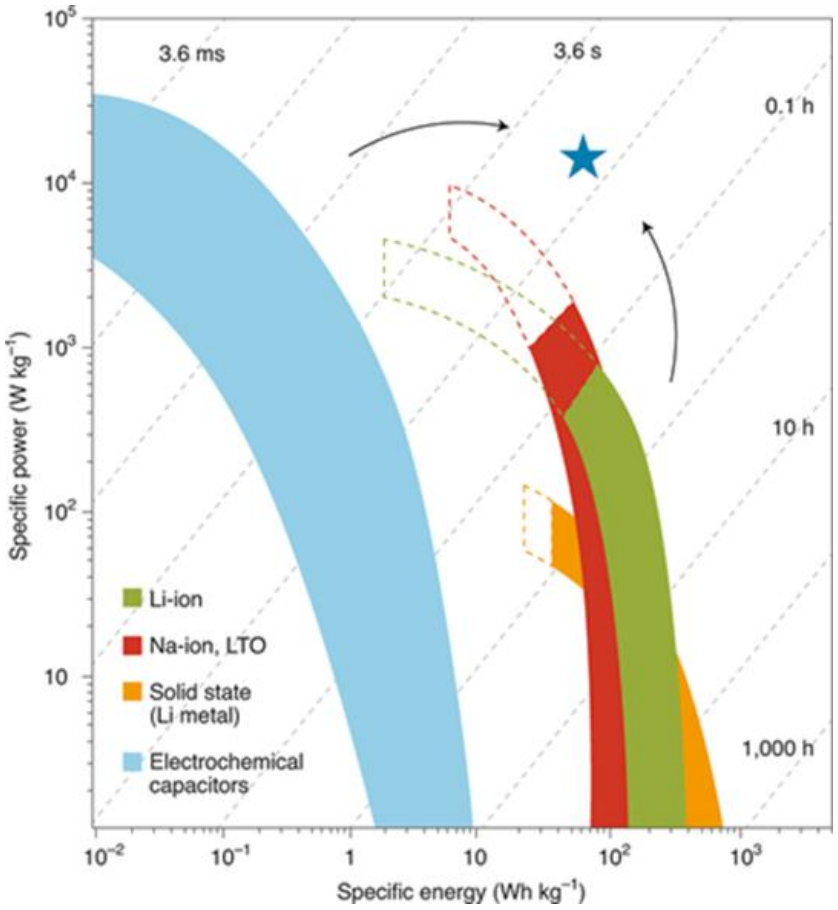

Figure 1.2: Ragone plot showing the characteristic specific power and specific energy of EES devices. The graph highlights the convergence of different types of batteries (green/red/yellow) and electrochemical capacitors (blue) toward a high performance ideal (indicated by star), which represents a device with both high specific energy and high specific power. Reproduced from Ref. [[6]], with permission from Springer Nature, © 2008.

1.2.1. Batteries

The foundation of modern battery technology was established over two centuries ago with the groundbreaking work of Alessandro Volta and the introduction of the world's first electric battery.[5] This historical progression continued with key inventions, including the development of the lead-acid battery by Gaston Planté, and the subsequent, pivotal contributions of J.B.

Goodenough, M.S. Whittingham, A. Yoshino and others to the lithium-ion battery (LIB).[7–12] These remarkable inventions, characterized by favorable energy and power densities alongside manufacturing advancements, fundamentally revolutionized portable electronics. Consequently, rechargeable LIBs remain the dominant battery technology compared to alternative systems (e.g., sodium ion, solid-state batteries, etc.), serving as one of the most popular energy devices across mobile electronics and EVs.

To understand the operational principles of LIB systems, several core concepts must be defined.[13] Fundamentally, battery-type materials store energy through Faradaic redox reactions ($Ox + ze^- \rightleftharpoons Red$), where Ox represents the oxidized species, Red the reduced species, and z is the number of electrons (e^-) transferred.

To ensure consistent terminology, the electrodes are defined according to the spontaneous discharge reactions: the anode (negative electrode) is the site where oxidation occurs, while the cathode (positive electrode) is the site where reduction occurs.[13] The thermodynamic potential difference between electrodes when no current flows is defined as the open circuit voltage (OCV). Furthermore, the total resistance to current flow within the cell, arising from ohmic resistance, charge transfer kinetics, and mass transport limitations, is collectively termed impedance, which directly influences power capability and efficiency.

These reactions generally involve three distinct ion storage mechanisms: intercalation, conversion, and alloying.[14,15] A standard LIB comprises two electrodes (anode and cathode) separated by an electrically insulating but ion-permeable separator. Upon charging, as illustrated in **Fig. 1.3A**, Li^+ ions are extracted from the cathode (oxidation), transferred across the electrolyte, and inserted into the anode. During discharge, the reverse process occurs: Li^+ ions are extracted from the anode and migrate back to the cathode. Simultaneously, electrons flow through the external circuit, driven by the electrochemical potential difference between the electrodes. The entire process allows the battery to store energy.[13,16]

The intercalation mechanism, in particular, proceeds through four primary stages:[17]

1. Ion diffusion from the bulk electrolyte to the electrode/electrolyte interface.
2. Ion migration across the surface and interphase to reach an intercalation site.
3. Charge transfer reactions at the interface.
4. Solid-state ion diffusion into the host material.

The Faradaic process in LIBs is often governed by bulk kinetics. Because ions must diffuse through the dense, two- or three-dimensional electrode material, the charging and discharging rate is typically limited by the rate of solid-state ion diffusion. While this Faradaic storage enables very high energy density, the slow bulk kinetics impose a significant practical limitation on power density (e.g., relevant for fast charging capability). Consequently, electrode

engineering aims to minimize the diffusion path length or increase the diffusion coefficient to enhance the overall rate performance of battery-type materials.

Beyond the primary mechanism, the applicability of any battery system is determined by several key performance metrics, including energy density, power density, capacity, cycle life, and coulombic efficiency. A Faradaic charge storage process, where the charge transfer originates from an electrochemical redox reaction, causes a Faradaic current (i_{farad}, in Ampere (A)) to flow over a time interval (t, in seconds (s)), yielding the total quantity of charge transferred (Q_{farad}, in Coulomb (C), **Equation 1**):[18,19]

$$Q_{farad} = \int i_{farad}\, dt \tag{1}$$

The maximum theoretical capacity of a host electrode material (**Equation 2**) is directly proportional to the maximum number of ions that can be reversibly stored, and thus, the number of electrons transferred in the electrode reaction, as defined by Faraday's law of electrolysis:

$$Q_{theoretical}[\frac{mAh}{g}] = \frac{n \times F\,[\frac{C}{mol}]}{M_w[\frac{g}{mol}] \times 3.6} \tag{2}$$

where n is the number of electrons transferred per formula unit of the host electrode (in intercalation reactions often ≤1 per transition metal), M_w is the molar mass of the host electrode (g/mol), and F (Faraday's constant) is the charge of one mole of electrons (96,485.3 C/mol). The commonly used unit of this theoretical capacity is mAh/g, utilizing the conversion factor 3.6 derived from converting C/g to mAh/g. The practical capacity (Q_{farad}) is typically lower than the theoretical maximum ($Q_{theoretical}$) due to kinetic limitations. Furthermore, in a full electrochemical cell, the total utilizable capacity is dictated by the electrode with the similar capacity, as each ion/electron that is released from one electrode needs to be taken up by the other electrode and vice versa.

The total energy (E, **Equation 3**) that can be gained from an electrochemical cell is calculated as the integral of the discharge voltage (V) multiplied by the discharge current (I_{farad}) over the discharge time:

$$E = \int V \cdot i_{farad} dt \tag{3}$$

This total accessible energy is the basis for determining the two key metrics of practical performance: gravimetric and volumetric energy densities. Gravimetric energy density (Wh/kg) normalizes the total energy by the mass of the electrode materials or entire cell (the former often used in academic papers, the latter relevant for applications), making it the critical metric for weight-sensitive applications, such as long-range EVs, drones, and portable electronics. In contrast, volumetric energy density (Wh/L) normalizes the total energy by volume, making it essential for space-constrained applications, including compact consumer electronics. Depending on the intended application, an electrode material is typically optimized to maximize either the gravimetric or volumetric metric, although this prioritization is often balanced against other critical factors such as cost, sustainability, and safety.

The instantaneous power (P) is calculated as the operating voltage (V) multiplied by the applied current (I), as described in **Equation 4**:

$$P = V \times I \tag{4}$$

To account for voltage during discharge, the power (P_{avg}, **Equation 5**) over the full discharge duration (t_{total}) is calculated by integrating the voltage and Faradaic current (i_{farad}) to find the total energy, then dividing by discharge time:

$$P_{avg} = \frac{E}{t_{discharge}} = \frac{\int V \cdot i_{farad} dt}{t_{discharge}} \tag{5}$$

Power density (W/kg or W/L) is then calculated by dividing this average power (P_{avg}) by its gravimetric (mass, kg) or volumetric (volume, L) value of the cell. Alternatively, it can be derived directly from the energy density ($E_{density}$) divided by the discharge time ($P_{density} = E_{density} / t_{discharge}$). Ultimately, while Faradaic storage enables high energy density,[20] the inherent challenges limit the current (I). This limitation on power density arises not only from slow solid-state ion diffusion within the active material but also from ohmic resistance, electrolyte concentration polarization, and saturation of the active material surface.[21,22] These kinetic bottlenecks underscore the critical need for structural and material improvements to enhance overall kinetics. It is notably observed that energy density is highly dependent on cell chemistry (e.g., the specific cathode and anode materials employed). The variations in energy density reported in 2019 are summarized in **Table 1**.[22]

Table 1: Various LIB cell chemistries for EVs. Adapted from Ref. [22], with permission from Springer Nature, © 2018.

Cell chemistry (cathode/anode)	Cells					
	Producer	Type	Capacity (Ah)	Voltage (V)	Energy density (Wh kg^{-1})	Energy density (Wh L^{-1})
LFP						
LFP/C	A123	Pouch	20	3.3	131	247
NCA						
NCA/C	Panasonic	Cylindrical	3.2	3.6	236	673
NCA/Si–C	Panasonic	Cylindrical	3.4	3.6	236	673
NMC						
NCA/Si–C	Panasonic	Cylindrical	4.75	3.6	260	683
NMC/C	Panasonic/Sanyo	Prismatic	25	3.7	130	215
NMC/LTO	Toshiba	Prismatic	20	2.3	89	200
NMC/C	LG Chem	Pouch	56	3.65	186	393
NMC/C	LG Chem	Pouch	59	3.7	241	466

C: graphite; LTO: $Li_4Ti_5O_{12}$; Si: silicon; LFP: $LiFePO_4$; NCA: $LiNi_{0.8}Co_{0.15}Al_{0.05}O_2$; NMC: $LiNi_{1/3}Mn_{1/3}Co_{1/3}O_2$.

1.2.2. Electrical Double-Layer Capacitors

The conceptual foundation of electrical double-layer capacitor devices (EDLCs) was established in 1957 with the first patent filed by Becker, which described using high specific surface area (SSA) porous carbon electrodes within a sulfuric acid electrolyte.[23] Commercial application began in 1971 when NEC (Japan), under license from SOHIO, developed aqueous electrolyte capacitors for power-saving units in electronics.[23] These devices marked the starting point for the commercial use of electrochemical capacitors, with subsequent research bolstered by new applications in diverse sectors, including mobile electronics, transportation, and so on.[24] Structurally, EDLCs are constructed similarly to a battery, utilizing two electrodes immersed in an electrolyte solution. An ion-permeable separator is located between the electrodes to prevent physical contact while facilitating ion conduction (**Fig. 1.3B**).

Ideal EDLCs operate purely via a non-Faradaic process. This charge storage mechanism occurs electrostatically through the reversible adsorption of electrolyte ions onto the surface of a polarized electrode.[25] The electrode materials for EDLCs are typically electrochemically inert towards redox reactions in the used voltage range, and often consist of high-surface-area carbon materials like activated carbon. It should be noted that the labels anode and cathode are not appropriate in EDLCs, since there are no redox reactions occurring at the electrodes. Rather, they should be labeled negative and positive electrodes, respectively. Charge separation is achieved upon polarization at the electrode/electrolyte interface, a phenomenon that produces the double-layer capacitance (*C*) as a consequence of a strong electric field gradient at the interface, first described by the (simplified) Helmholtz model in 1853.[26]

$$C = \frac{\varepsilon_0 \varepsilon_r A}{d} \quad (6)$$

where ε_r is the electrolyte dielectric constant, ε_0 is the dielectric constant of the vacuum, *d* is the effective thickness of the double layer, and *A* is the electrode surface area. The initial Helmholtz model (**equation 6**) was later refined by Gouy and Chapman, and subsequently by Stern and Geary, who introduced the critical concept of a diffuse layer in the electrolyte.[27–29] This diffuse layer forms as counter-ions accumulate near the charged electrode surface to balance the electric potential, creating a concentration gradient that extends into the bulk electrolyte. The double-layer capacitance typically ranges from 5 to 20 μF/cm^2 per unit interfacial area of planar electrodes, where organic electrolytes are favored over higher specific capacitance aqueous solutions due to their capacity to sustain a higher operation voltage, up to 2.7 V in symmetric systems.[30] The higher voltage is crucial because the energy is proportional to the square of the voltage, as depicted in **equation 7**.[31]

$$W = \left(\frac{1}{2}\right)\frac{CV^2}{3{,}600} \quad (7)$$

where *W* is the energy (watt hours), *C* is the total capacitance of the cell (in farads), and *V* is the cell voltage (volts) and the factor of 3600 translates joule into watt hours. It is important to note that the total cell capacitance is related to the individual electrode capacitance by the series relationship ($1/C_{cell} = 1/C_{pos.} + 1/C_{neg.}$), resulting in $C_{cell} \approx 0.5 \cdot C_{electrode}$ for symmetric cells.

The absence of any Faradaic contribution in the charge storage mechanism explains the specific electrochemical signature of these devices (at least in idealized EDLCs; realistic systems can include minor surface redox effects, e.g., on functional groups of porous carbon electrodes). As shown in **Fig. 1.3C**, this signature typically ranges from a rectangular box-shaped cyclic voltammogram to a linear, sloping profile during galvanostatic charge/discharge (GCD). While EDLCs are the main commercialized electrochemical capacitor devices, they suffer from limited energy density, meaning the primary challenge for SC research remains increasing the overall amount of energy stored.

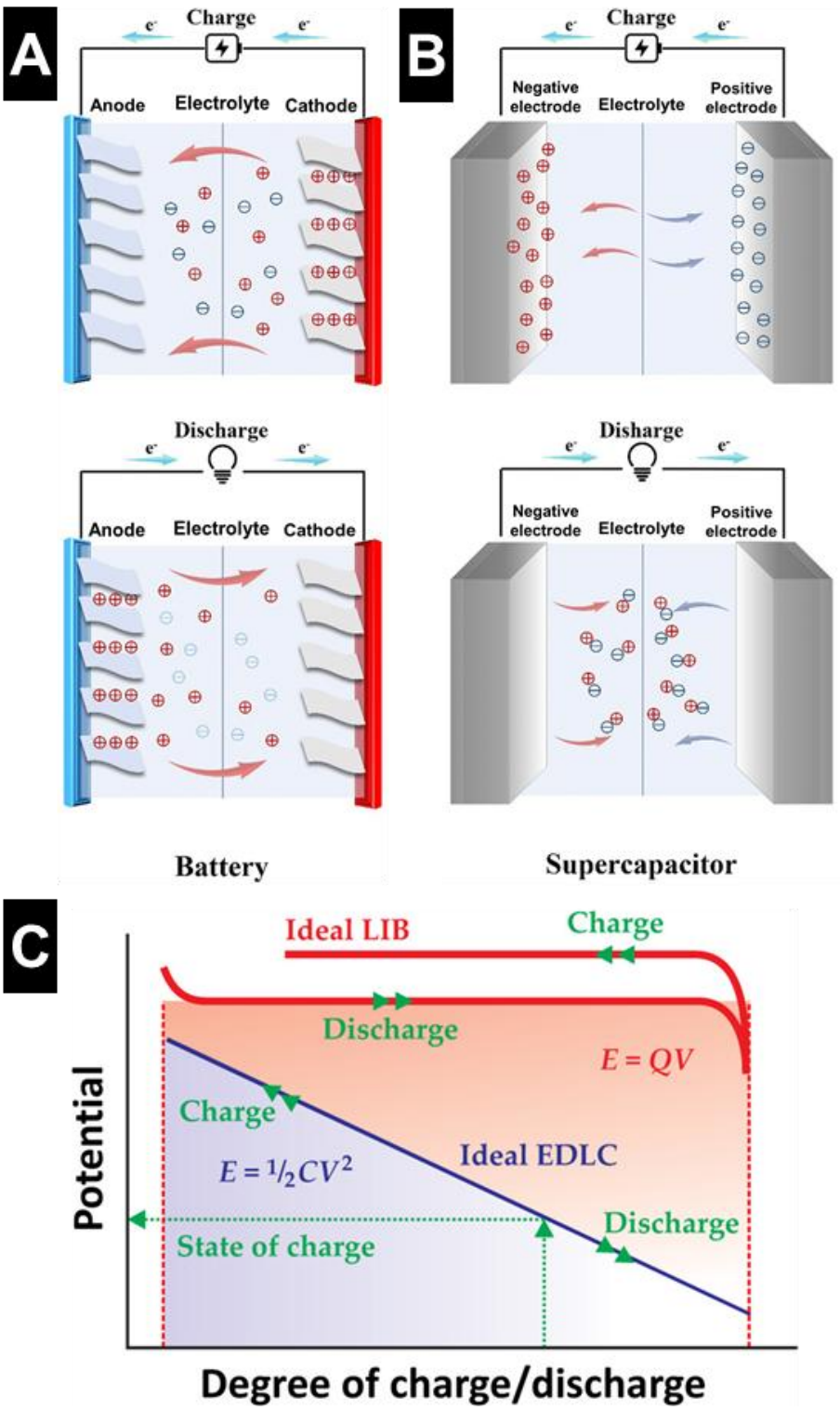

Figure 1.3: Schematic illustration of the cell setups of (A) batteries and (B) EDLCs. Adapted from Ref. [32], with permission from the Royal Society of Chemistry. (C) Characteristic electrochemical signature of the potential profile of an ideal battery (like the LIB), showing a long charge/discharge plateau at a constant voltage, versus the linear variation of voltage with the state of charge (SOC) found in an ideal EDLC. The figure highlights how the voltage provides a direct measure of the SOC for the EDLC, but not for the batteries. Reproduced from Ref. [33], with the permission of the American Institute of Physics.

While EDLCs offer superior power density and cyclability due to their fast, non-Faradaic mechanism, their performance is fundamentally constrained by limited energy density. Since charge storage is restricted entirely to the surface area, EDLCs cannot compete with the capacity offered by bulk battery-type electrode materials. This kinetic advantage, coupled with the energy limitation, motivated researchers to explore a hybrid approach that could combine the high capacity of Faradaic reactions with the fast kinetics of surface processes. This search led directly to the development and intensive study of pseudocapacitance, a mechanism suitable to bridge the gap between pure capacitive and battery behavior.

1.2.3. Pseudocapacitors

The origin of the term Pseudocapacitance stems from pseudo-capacity, which D.C. Grahame first described in 1941 in the context of electrochemically reversible interfacial charge not associated with classical double-layer formation.[34] The phenomenon was more prominently recognized by Conway and others in the 1970s, who observed that reversible redox reactions occurring at or near the surface of an electrode led to EDLC-like electrochemical features but resulted in much greater charge storage.[25]

A pseudocapacitor is a type of electrochemical capacitor (supercapacitor, SC) that often uses transition metal-based electrode materials. It stores charge via a fast faradaic charge transfer coupled with rapid ion transport, distinguishing it from EDLCs (another type of SCs).[35] As depicted in **Fig. 1.4**, the reversible charge storage of pseudocapacitance is classified into three types: underpotential deposition, surface redox pseudocapacitance, and intercalation pseudocapacitance.[36] These reactions occur on the surface, near-surface, or even via penetration into the electrode bulk.[35,37]

The underpotential deposition (**Fig. 1.4A**) process involves the chemisorption of cations from the electrolyte onto a different metal substrate, forming a monolayer at a potential positive to the Nernst potential for bulk deposition.[38] Distinct from this, surface redox pseudocapacitance (**Fig. 1.4B**) arises primarily from Faradaic electron transfer between ions in the liquid electrolyte and the surface atoms of the solid electrode, involving a change in oxidation state (e.g., RuO_x). Finally, intercalation pseudocapacitance (**Fig. 1.4C**) occurs when ions intercalate rapidly into the tunnels or layers of the electrode material via a solid-solution mechanism, accompanied by a fast Faradaic charge transfer that does not involve a change in crystallographic phase. This mechanism offers distinct kinetic advantages due to the structural stability maintained during the electrochemical reaction.[35]

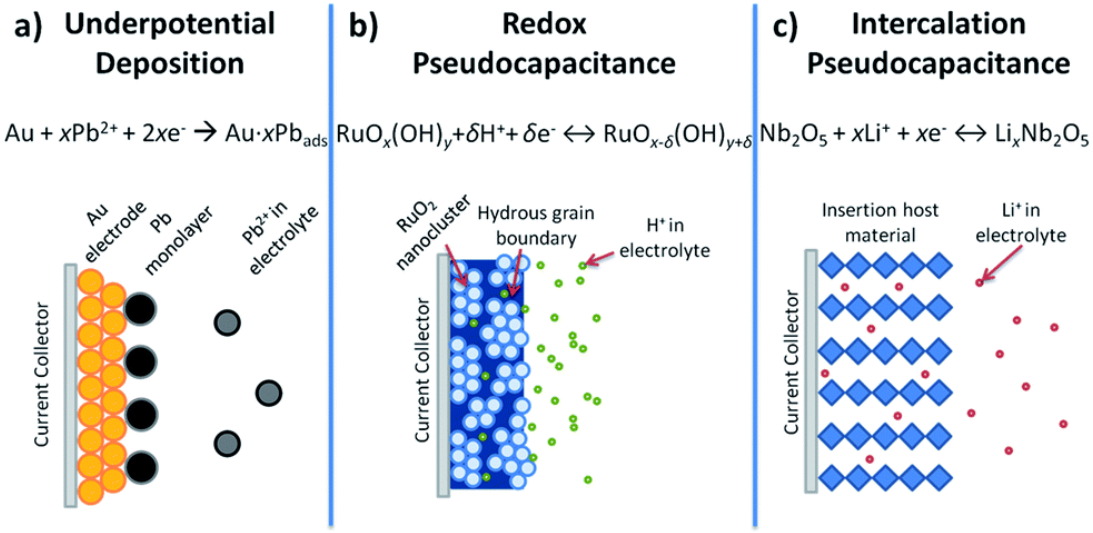

Figure 1.4: Three different mechanisms of pseudocapacitance: (A) underpotential deposition, (B) surface redox, and (C) intercalation pseudocapacitance. Reproduced from Ref. [39], with permission from the Royal Society of Chemistry.

The distinct charge storage mechanisms of EES applications are clearly reflected in their electrochemical signatures.[36,40] When subjected to potential scanning (cyclic voltammetry), EDLCs typically display a potential-independent current, resulting in a rectangular CV shape (**Fig. 1.5A** and **1.5B**). In contrast, batteries exhibit prominent, distinct redox peaks associated with the reduction and oxidation involved in Faradaic charge storage (**Fig. 1.5G** and **1.5H**). Similarly, during constant current discharge, the potential versus time plot for an EDLC is linear (**Fig. 1.5C**), while a potential versus time plot is profoundly non-linear for batteries (**Fig. 1.5I**), characterized by plateaus of nearly constant potential corresponding to the Faradaic redox reactions. Behavior intermediate between these two extremes signals the presence of pseudocapacitance (**Fig. 1.5D-F**). Therefore, the crucial first question must address when analyzing electrochemical data from a nanomaterial is whether the material exhibits battery-like or capacitor-like characteristics.[41]

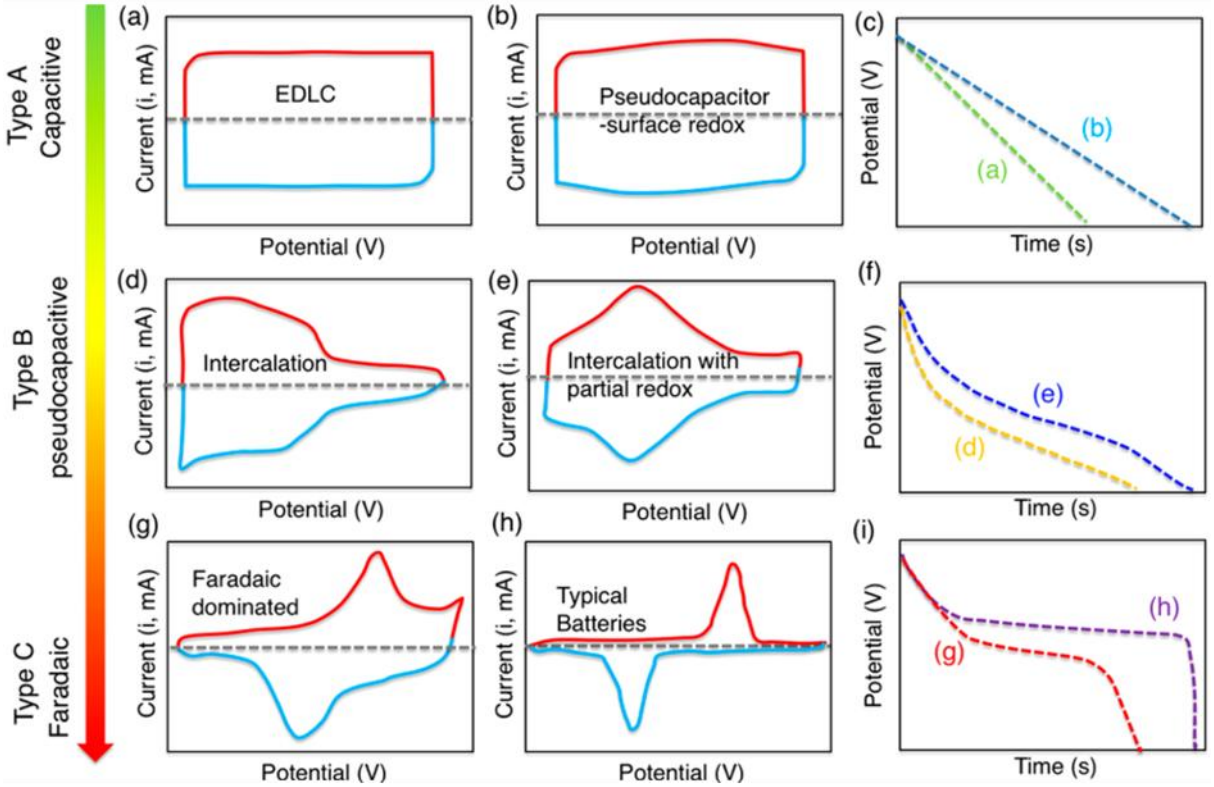

Figure 1.5: Examples of electrochemical signatures used to identify charge storage mechanisms. The figure presents cyclic voltammograms (a, b, d, e, g, h) and corresponding galvanostatic profiles (c, f, i), illustrating various storage types. The pseudocapacitive mechanisms shown include (b) surface redox pseudocapacitance (e.g., MnO_2 in neutral aqueous media) and intercalation pseudocapacitance (e.g., lithium insertion in Nb_2O_5 in organic electrolytes (d) and Ti_3C_2 in acidic aqueous electrolytes(e)). Panels g-i illustrate the typical electrochemical responses of battery-like materials. Reproduced from Ref. [41], with permission from American Chemical Society, © 2018.

The inherent challenge in kinetic analysis is distinguishing true surface-controlled storage from diffusion-limited processes by the power-law dependence of the current on the scan rate ($I = av^b$), where the *b*-value provides direct insight into the charge storage kinetics.[42,43] A *b*-value of 0.5 indicates semi-infinite linear diffusion-controlled kinetics, while a *b*-value equal to or close to 1 signifies surface-controlled kinetics.

1.3. State-of-the-Art: Layered MoS_2 and Nanoconfinement

1.3.1. Overview of Layered Materials in EES

The intercalation/deintercalation mechanism is the widely utilized one in modern rechargeable battery technologies like the LIB. This process involves a straightforward, reversible solid-state redox reaction within the host material. During ion storage or release, mobile guest ions from the electrolytes are reversibly inserted into and extracted from the interlayer space or the channels present in the host materials. Crucially, the ions maintain their ionic properties during intercalation, diffusing within the host materials driven by concentration gradients.[44] Meanwhile, the intercalation process inevitably causes the host materials to undergo certain volume changes, except for rare exceptions like spinel lithium titanate.[45]

The need to accommodate these structural changes directly highlights the importance of layered materials (e.g., graphite, transition metal oxides (TMOs), transition metal dichalcogenides (TMDs), and MXenes) in EES. Their characteristic structures, composed of two-dimensional (2D) atomic sheets held by weak van der Waals (vdW) forces, are inherently suited for the intercalation mechanism, offering the structural prerequisites and potential pathways to store a high number of ions.

Graphite is the most commonly utilized layered material as an anode for Li^+ ions in LIB systems, which comprises 2D carbon (graphene) layers, where the individual atoms are organized in a honeycomb structure.[44] Stacking of these individual layers forms a lamella structure of graphite, where the interlayer spacing is approximately 0.335 nm, held together via weak vdW forces originating from delocalized π-orbitals, allows guest ions (e.g., Li^+ ions) to have reversible intercalation/extraction between layers.[46] The mechanism of Li^+ ion intercalation is closely connected with this ideal 2D layered structure. Ions are easily inserted from the edge plane surface and undergo chemical reactions, leading to the formation of interlaminar compounds (graphite intercalation compound, GIC).[47] The Li^+ intercalation into graphite is described by the chemical reaction equation below.

$$C_6 + Li^+ + e^- \rightarrow LiC_6 \quad (8)$$

Highly crystalline graphite can host a maximum of one lithium atom per six carbon atoms, corresponding to the LiC_6 phase, and provides a theoretical lithium storage capacity of 372 mAh/g at a potential of ca. 0.15 vs. Li^+/Li.[48,49] Despite the intercalation capability of graphite on various ions (e.g., Li^+, K^+, and Cs^+), Na^+ ions are not intercalated efficiently, resulting in very low capacity (NaC_{186}).[50] It is due to the destabilization of GICs, caused by the strong interaction between Na^+ (or Mg^{2+}, Ca^{2+}) ions and graphene layers.[51] Later, it is observed that the co-intercalation phenomena, where Na^+ ions are intercalated along with solvents (solvated Na^+

ions) into ion host materials, enable graphite to store Na^+ ions in graphite layers via the formation of stable ternary GICs (graphite-Na^+-solvent).[49,52] This shows that electrochemical ion storage is also highly dependent on not only the materials of anodes or cathodes but also the electrolyte environments in the system.[53] This co-intercalation reaction does not require a full desolvation process, leading to excellent transfer kinetics and in some cases pseudocapacitive electrochemical properties.[54,55] However, irreversible co-intercalation and exfoliation due to repeated ion or solvated-ion intercalation/de-intercalation can affect the overall electrochemical performance, such as rate capability and long-term cycling stability.

In the LIB system, several structural engineering approaches, like expanding of interlayer and creating defects in the material design, are applied to overcome the technical bottlenecks to achieve fast-charging batteries.[46] As examples, expansion of layer spacing can reduce diffusion resistance of ion transport, and defect sites can provide short and multiple channels for ion insertion.[56,57]

Layered TMOs are also a common class of intercalation hosts. Their layered structures are generally built from transition metal-oxygen clusters, with the transition metal typically in octahedral (six-fold) coordination with oxygen ligands. These octahedra are assembled into extended sheets by sharing corners or edges. Layered lithium TMOs (often with the chemical formula $LiTMO_2$, where TM = Ni, Mn, Co, Al, etc.) are the most widely utilized, serving as the cathode materials in the current commercial LIB system due to their high specific capacity and high operating potentials, leading to high energy density in the cell (e.g., $LiNi_{1-x}M_xO_2$ and $Li_{1+x}M_{1-x}O_2$).[58,59] In these frameworks, the Li^+ ion is an essential structural component, which ionically bonds the negatively charged $[TMO_2]^-$ layers together. On the other hand, some layered TMOs, such as layered birnessite MnO_2, orthorhombic V_2O_5, and monoclinic $WO_3 \cdot 2H_2O$, are composed of charge-neutral MO_6 octahedra sheets held together by weak vdW forces.[60] This structural design, featuring wide interlayer spacing, allows for the intercalation of a large variety of guest ions and polymers. The intercalation mechanism ($MO + xA^+ + xe^- \rightleftharpoons A_xMO$, MO = layered TMO, A^+ = cation (e.g., H^+, Li^+, Na^+, etc.)) is considered the primary charge storage mechanism in metal oxides.[60] To enhance the kinetics of ion intercalation in bulk TMOs, a nanostructuring (or nanosizing) strategy is commonly used, which in some cases can lead to pseudocapacitive behavior.[39,58,61,62] Also, nanoconfinement design via an inorganic-organic hybrid structure of TMOs has been reported in recent years to demonstrate that the pillaring approach is a promising direction to tailor electrochemical properties.[63–66]

While graphite and TMOs represent established classes of layered materials for EES, the TMDs constitute another significant layered-type family. As the specific material system

selected for investigation in this thesis, the structural and electrochemical properties of TMDs will be discussed in detail, with a specific focus on Molybdenum disulfide.

1.3.2. Transition Metal Dichalcogenides

Since the first TMD compound was discovered in 1923, various TMD materials have been actively investigated due to their fascinating features similar to graphene or other layered families.[67,68] Various applications, such as energy storage[69,70], catalysis[71,72], and sensing[73,74], have shown interest in exfoliated 2D TMDs due to their large surface area, unique physical and electronic properties.[75]

Typically, TMDs (general formula MX_2, where M = transition metal, X = chalcogen) have various possible combinations, as shown in **Fig. 1.6A**. They are characterized by a sandwich structure, where a single layer of transition metal atoms is positioned between two layers of chalcogen atoms (X-M-X layers) connected by strong covalent bonds in the intralayer.[70] These individual sheets are stacked and held together by vdW forces, resulting in a 3D layered structure (**Fig. 1.6B-D**). This weak interlayer cohesion is a defining feature of TMDs, as it allows for the facile separation of the bulk crystal into single or few-layer sheets. Also, intercalants (ions or polymer species) can easily intercalate between these layers, resulting in structural modification of bulk TMDs.[76]

Furthermore, the specific arrangement and stacking order of these covalently bonded metal and chalcogen layers result in various structural polymorphs. The most common polymorphs are the hexagonal (2H), tetragonal (1T), and rhombohedral (3R) phases. Numbers (1, 2, 3) before the crystal symmetry (H, T, R) represent the number of layers in each repeating unit cell (**Fig. 1.6B-D**).[77] The most common polytype of TMDs is the 2H phase, which is thermodynamically stable and semiconducting. The unit cell consists of two layers, having an ABA BAB stacking pattern.[78] On the other hand, the 1T phase, which possesses octahedral MX_6 coordination, is metastable and metallic, and has an ABC stacking sequence. Due to the different electronic properties, the electrical conductivity of 1T-MoS_2 is 10^7 times higher than that of 2H-MoS_2.[79] The 2H-to-1T phase conversion can occur by interlayer atomic gliding, where one of the X layers goes through the transversal displacement.[80] Since the 1T phase is metastable, it leads to the formation of 1T' (distorted 1T) structure, which is a semi-metallic phase to reduce the formation energy under ambient conditions. The 3R phase (rhombohedral symmetry), which is thermodynamically stable and semiconducting, has a trigonal prismatic MX_6 coordination with ABA CAC BCB layer stacking in the unit cell.[78]

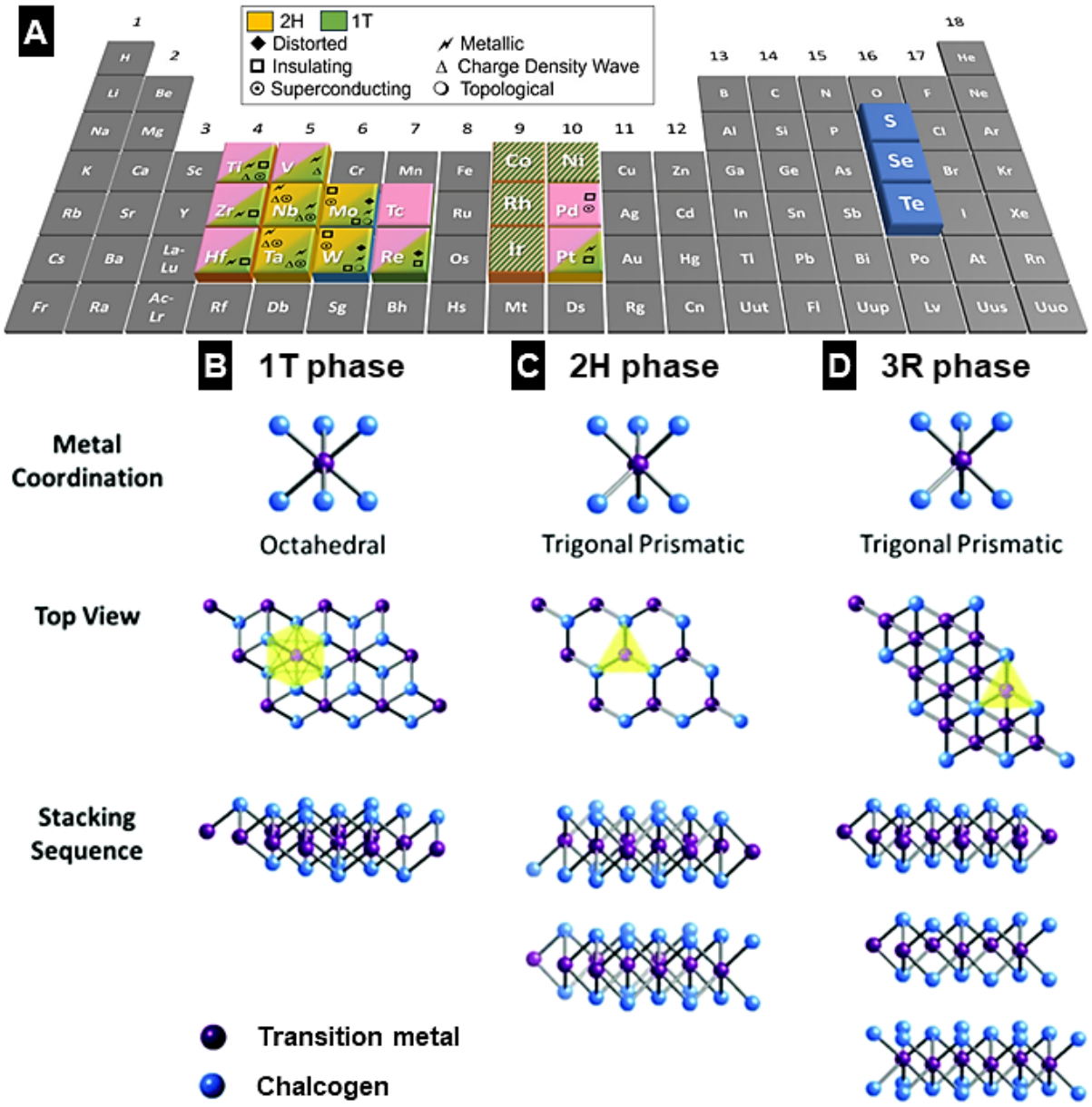

Figure 1.6: (a) Various combinations of TMDs (MX_2) in the periodic table. Adapted from Ref. [70], with permission from the American Chemical Society, © 2024. (b-d) Typical structures of TMDs. Adapted from Ref. [81], with permission from the Royal Society of Chemistry.

TMDs have been highlighted for EES, especially rechargeable batteries, due to their natural abundance, low cost, good mechanical strength, and high specific capacitance.[82,83] Although TiS_2 was used as the cathode material in the first rechargeable lithium battery, TMDs in modern approaches are predominantly investigated as anode-type materials due to their intermediate lithium intercalation potential (e.g., 1.1 - 2.0 V versus Li^+/Li for MoS_2).[9,84] While their structure, defined by strong intralayer covalent bonds and weak vdW interactions, provides an ideal space for ions (Li^+, Na^+, K^+, etc.) intercalation, major concerns regarding their application in

EES include slow ion diffusion kinetics, large strain resulting from volume change during electrochemical cycles, and the low electrical conductivity in bulk TMDs.[70,85]

To overcome these issues in electrochemical ion storage applications, modification of electrode materials, such as phase engineering,[86,87] nano-structuring,[62,88] and interlayer engineering[66,89] are widely studied. These approaches are commonly investigated across layered materials to control properties like electrical conductivity, ion diffusion, and structural stability, ultimately improving overall electrochemical performance. These structural modifications are further introduced with the specific case of MoS_2 intercalation host material in the subsequent section.

1.3.3. Molybdenum Disulfide

Molybdenum disulfide (MoS_2), a member of the TMD family, has attracted significant attention as a promising battery anode material since the 1980s.[90] This is primarily because its theoretical specific capacity (670 mAh/g), which involves combined intercalation and conversion mechanisms, is significantly higher than that of commercial graphite anodes (372 mA/g).[91] MoS_2 follows the general structural and electronic properties detailed in the previous section, including the existence of thermodynamically stable semiconducting phases (2H, 3R) and metastable metallic phases (1T) (**Fig. 1.6B-D**). Like other general types of TMD materials, MoS_2 features a 2D layered architecture where a plane of molybdenum atoms is sandwiched between two planes of sulfur atoms (**Fig. 1.7**).

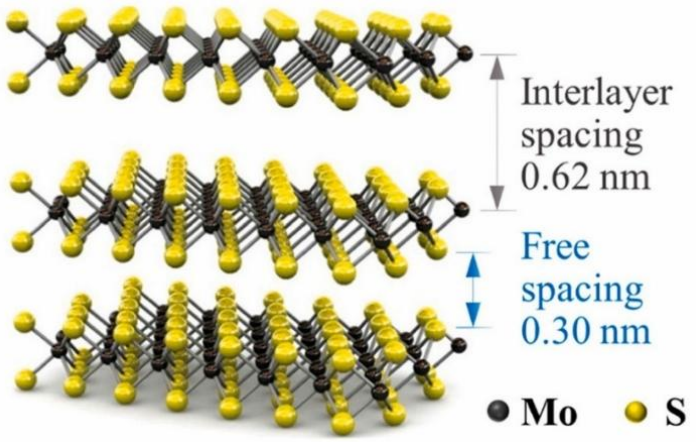

Figure 1.7: Schematic illustration of the layered trigonal prismatic 2H-MoS_2. Adapted from Ref. [92], with permission from American Chemical Society, © 2017.

These layers are internally stabilized by strong covalent Mo-S bonds, while the adjacent sheets are held together by weak vdW forces, resulting in an interlayer distance of approximately 0.62

nm. These weak vdW forces between layers create an advantageous pathway for cation diffusion. MoS_2 can accommodate charge storage via both intercalation and conversion reactions, depending on the operational voltages.[91,93] The storage process involves sequential mechanisms for lithium ion:

$$\text{Intercalation: } MoS_2 + xLi^+ + xe^- \rightarrow Li_xMoS_2\ (0 < x \leq 1) \quad (8)$$

$$\text{Conversion: } MoS_2 + 4Li^+ + 4e^- \rightarrow Mo + 2Li_2S \quad (9)$$

This lithium intercalation reaction in 2H-MoS_2 (**Equation 8**) occurs at a potential of ca. 1.1 V (vs. Li^+/Li), accompanying a phase transition from the semiconducting 2H phase to the metallic 1T phase (**Fig. 1.8**).[93,94] The resulting 1T-MoS_2 subsequently exhibits a reversible lithium intercalation process, typically within the potential range of 3.0 – 1.0 V.[95–99] The theoretical specific capacity for this intercalation reaction is 167 mAh/g, corresponding to the insertion of one Li^+ ion per MoS_2 formula unit.

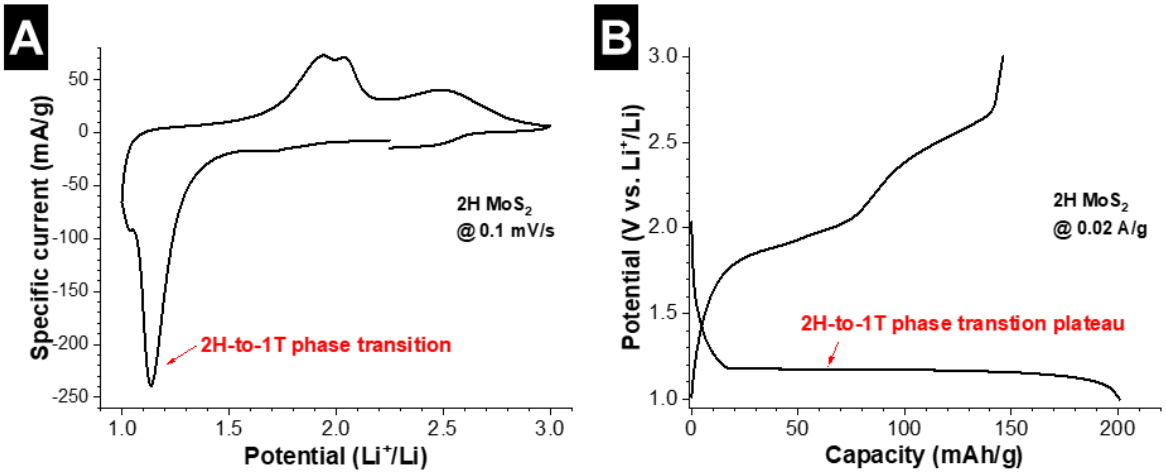

Figure 1.8: Electrochemical identification of the phase transition in 2H-MoS_2. (A) Cyclic voltammetry curve at 0.1 mV/s, showing a distinct reduction peak at ca. 1.1 V vs. Li^+/Li. (B) GCD profile at 0.02 A/g, showing the characteristic discharge plateau at ca. 1.1 V vs. Li^+/Li.

However, extending the discharge to 0.55 V triggers the conversion reaction of MoS_2 (**equation 9**).[100] This process leads to the formation of metallic Mo and lithium sulfide (Li_2S), initiating subsequent redox reactions of Li_2S in following cycles that resemble the lithium-sulfur battery mechanism ($Li_2S \leftrightarrow S + 2Li^+ + 2e^-$).[101] Therefore, defining the operating potential window is critical when isolating the intercalation properties of MoS_2-based materials. In this thesis, the study specifically focuses on the electrochemical lithium intercalation properties.

Consequently, the operating voltage is strictly maintained above 1.0 V (vs. Li^+/Li) to avoid conversion reactions and maintain the layered MoS_2 structural framework.

Natural MoS_2 (bulk MoS_2) exists as the thermodynamically favored 2H phase, with lattice parameters of a = 3.16 Å and c = 12.29 Å.[67] 2H-MoS_2 has been extensively studied for energy-storage-related systems, particularly SCs, owing to its thermodynamic stability and controllable structure via synthesis, which provides a large specific surface area (SSA).[102] However, it suffers from poor electronic conductivity and sluggish ion diffusion kinetics.[101] To address these kinetic, electronic, and structural issues, modification strategies such as phase engineering, nano-structuring, and interlayer engineering are widely studied along with various synthesis methods. These synthesis and modification methods are essential since the characteristics of MoS_2 are highly influenced by crystal phase, morphology, crystallite sizes, the number of layers, and so on.[94,99,101,103,104]

Various methods have been investigated for the synthesis of MoS_2 nanoparticles and MoS_2-based materials. The synthesis of MoS_2 can be classified into two major strategies, which are top-down and bottom-up methods. Both methods are highly desirable for the investigation of nanostructured (or nano-sizing) MoS_2 in the electrochemical storage field. Cook et al. demonstrated that the electrochemical ion intercalation properties in MoS_2 electrode materials are highly dependent on the MoS_2 crystallite size. The authors found that the phase transition during lithiation of bulk MoS_2 is suppressed in nanostructured MoS_2. This suppression leads to the emergence of solid-solution Li^+ intercalation with pseudocapacitive properties[97–99], characterized by kinetics that are not limited by solid-state diffusion.[36,40] Furthermore, Yao et al. further demonstrated that, in addition to decreased crystallite sizes, the introduction of lattice disorder can enable such pseudocapacitive intercalation properties of MoS_2.[105] The following subsections introduce the synthesis methods specifically employed for nanostructured MoS_2.

1.3.3.1. Top-Down Synthesis

The top-down approach is an exfoliation process of layered bulk materials. Mechanical and liquid-phase exfoliations are widely used to obtain mono- or few-layered MoS_2 sheets. Mechanical exfoliation, commonly known as the Scotch-tape method, was the first approach established to prepare 2D graphene nanosheets through mechanical fragmentation.[106] This technique involves detaching or peeling layers from a bulk crystal using adhesive tape or simply rubbing the bulk crystal against a solid surface.[107–109] This method does not require costly or specialized machinery and is a very easy and effective way to produce thin nanosheets. However, a significant drawback is that this technique cannot be utilized for large-scale processing, limiting its applications primarily to preparing samples for fundamental

research purposes.[110] On the other hand, liquid-phase exfoliation is suitable for the large-scale production of few-layered materials and is required for many applications.[83,111] Sonication-assisted liquid exfoliation is one of the widely utilized techniques that depends on ultrasonic energy to generate shock waves, thereby providing the necessary mechanical force to separate the bulk layered materials (**Fig. 1.9**).[112] An alternative approach, often used in conjunction with sonication, involves the chemical or electrochemical intercalation of alkali ions into the bulk MoS_2 lattice. This process is followed by exposure to water, which reacts with the intercalated alkali ions to generate hydrogen gas ($Li_xMoS_2 + xH_2O \rightarrow$ exfoliated $MoS_2 + x$LiOH $+ x/2 \cdot H_2 \uparrow$). The rapid evolution and expansion of this gas within the interlayer galleries exert a significant force, effectively overcoming the vdW interactions and delaminating the material into nanosheets.[79,113] In chemical lithiation of bulk MoS_2, *n*-butyllithium (*n*-BuLi) has been commonly used.[114,115] This method effectively produces 1T rich MoS_2 by inducing a 2H-to-1T phase transition, a structural rearrangement triggered by the donation of electrons from the alkali metals into the molybdenum atoms.[109,116] Some drawbacks of this liquid-phase exfoliation are the breakage of exfoliated sheets, long processing times, and poor uniformity.[112] However, it is still one of the commonly utilized techniques not only in laboratories but also in large-scale production.

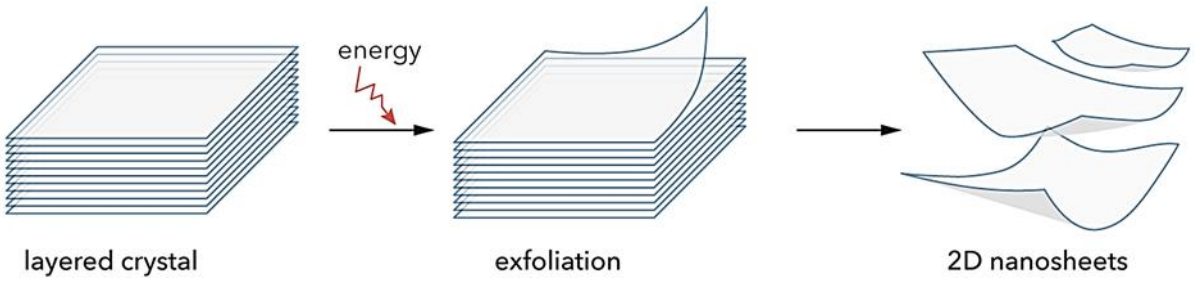

Figure 1.9: Illustration of the general exfoliation process for 2D materials. External energy is required to overcome the interlayer attraction to promote peeling. Adapted from Ref. [112], with permission from Elsevier, © 2022.

1.3.3.2. Bottom-Up Synthesis

MoS_2 can be synthesized via a bottom-up approach, including hydro/solvothermal synthesis, microwave synthesis, and chemical vapor deposition technique. This strategy is widely applied for synthesizing nanostructured MoS_2 by assembling atomic or molecular precursors through controlled chemical reactions. Among these, hydro/solvothermal synthesis represents a traditional wet chemical method that is extensively employed to obtain MoS_2 with diverse morphologies, offering precise control over crystallite size and ensuring homogeneous layer thickness.[117–119] Hydrothermal synthesis uses an aqueous solution environment, while solvothermal synthesis uses other solvents like ethanol.[120,121] The morphology of MoS_2

products synthesized via these methods highly depends on the chosen precursors, solvents, and synthesis conditions.[95,118,122]In the hydrothermal and solvothermal synthesis of MoS_2, the most frequently employed molybdenum precursors include ammonium heptamolybdate ($(NH_4)_6Mo_7O_{24}$), sodium molybdate (Na_2MoO_4), and molybdenum trioxide (MoO_3), and the sulfur component is commonly derived from organic sources such as thiourea (NH_2CSNH_2), thioacetamide (CH_3CSNH_2), or L-cysteine ($C_3H_7NO_2S$).[101,122] One example of hydrothermal synthesis of metallic 1T-MoS_2 is using molybdenum trioxide (MoO_3), thioacetamide (CH_3CSNH_2), and urea (NH_2CONH_2) precursors.[123] Hydrothermal or solvothermal synthesis does not require multistep procedures, such as chemical reduction and exfoliation, and is therefore often referred to as a one-pot synthesis. It would also be suitable to tailor emerging MoS_2 functional properties.[95,96] This method also enables the growth of MoS_2 nanoparticles on a conductive substrate, like reduced graphene oxide, or the formation of heterostructures comprising MoS_2 and other layered 2D materials.[124–126] One disadvantage of this method is that the synthesis requires a long processing time. The microwave-assisted hydrothermal strategy has attracted considerable attention due to its rapid synthetic rate compared to conventional heating methods. This method uses microwave irradiation to directly heat the solution in minutes.[127] MoS_2 growth on the substrates via the CVD method has been studied to obtain high crystalline MoS_2.[128] However, it is not suitable for the production of massive amounts of materials compared to hydrothermal or liquid exfoliation methods. In terms of scalability among bottom-up methods, calcination (e.g., the simple mixing of metal and sulfur precursors at high temperatures) represents a suitable and relatively facile process. However, this approach is less explored for the production of TMDs because the resulting product consists exclusively of semiconducting structures (composed of mixed 2H and 3R phases), lacking the metallic 1T-like phase.[129]

1.4. Nanoconfinement Design Strategies

As mentioned in section 1.3.1, layered materials represent some of the most successful electrodes due to their ability for reversible intercalation of ions. However, the slow diffusion and possible fracture during volume expansion at high rates remain issues for bulk layered materials (**Fig. 1.10A**).[130] Nanostructuring via exfoliation of bulk materials (top-down) or direct synthesis (bottom-up) has been developed, and improved kinetics and more facile volume expansion have been achieved using nanostructured 2D materials (**Fig. 1.10B**).[131,132] However, the large surface area often leads to detrimental effects, including high initial irreversible capacity and low Coulombic efficiency during the first cycle, largely driven by the promotion of parasitic side reactions at the large interface.[131,133] Moreover, the low bulk density of nanomaterials leads to an unfavorable volumetric energy density of the corresponding cells. A

new concept of nanoconfinement design has been demonstrated to adapt benefits from both a bulk layered structure and a nanostructured 2D structure, as shown in **Fig. 1.10C**. This structural design potentially combines the high energy storage capacity of bulk materials with the rapid solid-state diffusion of nanostructures, and could effectively mitigate volume changes during cycling.

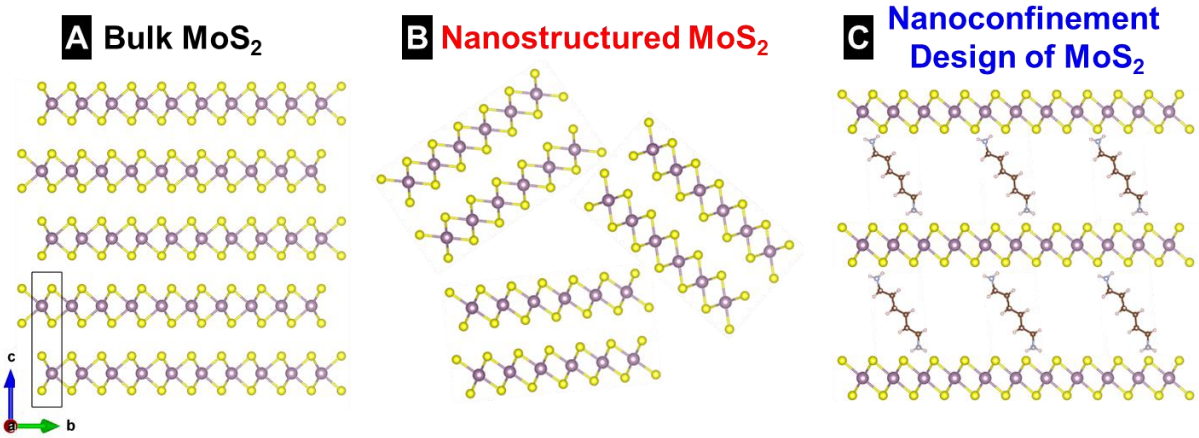

Figure 1.10: Schematic illustration of three types of material structures. (A) Bulk layered material, (B) nanostructured 2D structure derived from the bulk material, and (C) nanoconfinement design of 2D material with confined pillars. Inspired by Ref. [134], with permission from Elsevier, © 2017.

Structural modification via nanoconfinement design is achieved by functionalizing 2D materials with various organic and/or inorganic species.[60,134,135] In the context of layered materials, nanoconfinement refers specifically to the distinct physicochemical environment established within the nanometer-scale gap between adjacent atomic layers. This confined space imposes unique constraints on ion transport.[136–138] The strategy is intrinsically linked to interlayer engineering, as the insertion of organic pillars, ions, or solvent molecules directly dictates the interlayer spacing. By precisely manipulating this nanoconfinement-designed space, it could become possible to tailor diffusion kinetics and active site accessibility to optimize the EES performance of electrode materials.

Various layered materials, including TMOs, TMDs, and MXenes, have been selected as host materials for functionalization to control the nanoconfinement properties of the interlayer spacing, which plays a pivotal role in determining the overall ion intercalation performance.[136] For instance, increasing the interlayer spacing in TMOs has been shown to simultaneously influence ion intercalation kinetics, maximum storage capacity, and the charge storage mechanism itself.[64] MXenes represent another prominent class of 2D materials whose remarkable success in electrochemical applications can be largely attributed to their highly

tunable nanoconfinement chemistry and geometry.[139,140] This tunability allows for the precise engineering of ion transport pathways and charge storage mechanisms.[141] Similarly, manipulating the interlayer distance, specifically the geometry of the nanoconfined space between individual MoS_2 layers, has been described to promote electrochemical ion intercalation reactions by reducing diffusion barriers and increasing available ion storage sites.[142] For example, the use of hydroxy pillars in a 3D porous graphene aerogel decorated with oxygen-incorporated MoS_2 led to an expanded MoS_2 interlayer spacing from 6.15 to 10.15 Å, resulting in increased Li^+ intercalation kinetics and storage capacity.[143] Likewise, hollow nanospheres of hydroxy-containing MoS_2 nanosheet subunits showed an interlayer spacing between 9.5 and 10.0 Å, also leading to improved kinetics and capacity of Li^+ intercalation.[144]

Engineering of the MoS_2 interlayer environment can be achieved through both bottom-up and top-down synthesis strategies.[136] In the bottom-up synthesis, guest molecules are directly integrated into the host layers during the initial material formation. Hydrothermal synthesis is one of the most common methods for nanoconfinement design (**Fig. 1.11A**). The nanoconfinement designs of hydrothermally synthesized graphite intercalated 1T-MoS_2 (*d*-spacing of 0.99 nm)[145] and tetramethylammonium (TMA^+) cation-pillared MoS_2 (*d*-spacing of 1.06 nm)[146] are shown in **Fig. 1.11A** and **Fig. 1.11B**, respectively. Especially, MoS_2-TMA showed pseudocapacitive Zn^{2+} intercalation behavior (**Fig. 1.11C** and **1.11D**).

Conversely, in the top-down approach, intercalating guests can be inserted simultaneously with the exfoliation of the bulk MoS_2. Polyethylene oxide (PEO) molecule insertion into the MoS_2 lattice is one of the most studied nanoconfinement design strategies of MoS_2.[147–149] MoS_2-PEO electrode (*d*-spacing up to 1.45 nm) shows superior Na^+ intercalation properties with fast diffusion kinetics compared to the commercial MoS_2 electrode (**Fig. 1.11F**).[149] It is essential to note that organic molecules containing thiol groups have shown the capability of covalent functionalization of MoS_2 via the top-down method.[150–152] S. Ippolito et al. reported that the simple soaking method can interconnect MoS_2 sheets covalently, as thiol groups from organic pillars fill sulfur vacancies (**Fig. 1.11E**).[153,154]

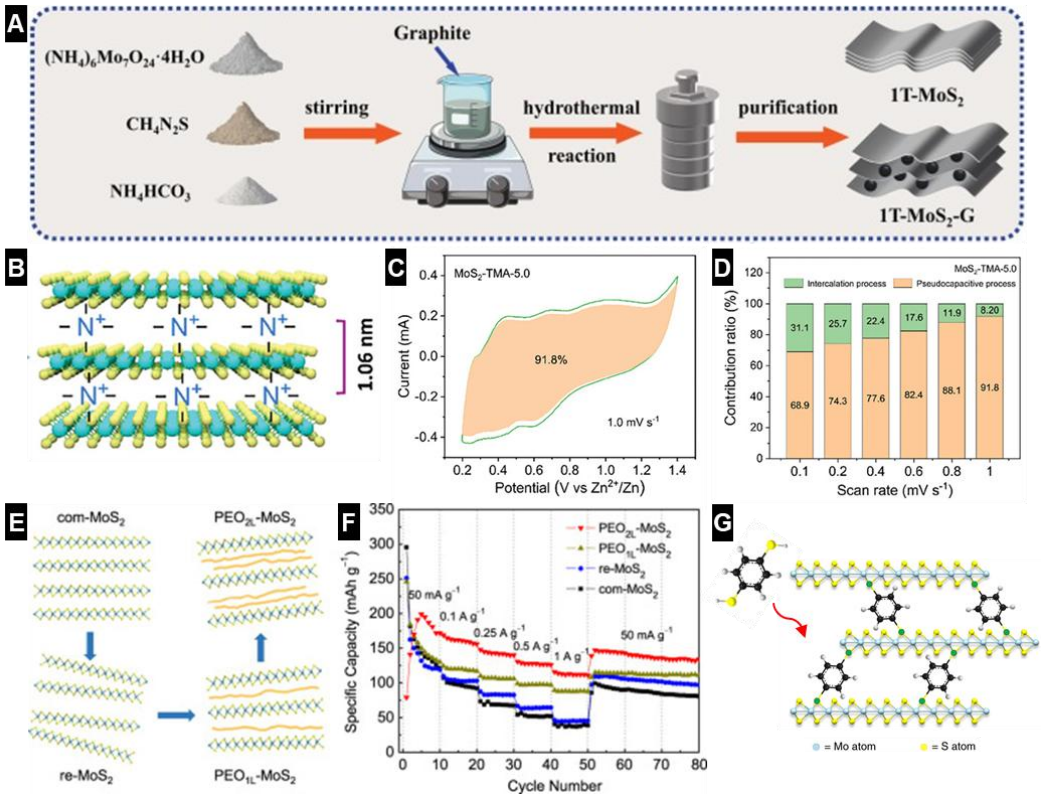

Figure 1.11: Schematic illustrations of nanoconfinement design approaches (A, E), nanoconfinement-designed MoS_2 structures (B, E, G), and electrochemical characterization results (C, D, F). (A) Hydrothermal synthesis pathway from precursors to the nanoconfinement-designed product. Adapted from Ref. [145], with permission from Elsevier, © 2025. (B) MoS_2-TMA nanoconfinement design, exhibiting an expanded *d*-spacing of 1.06 nm. (C) Pseudocapacitive CV profile at 1.0 mV/s and (D) pseudocapacitive contribution analysis at various scan rates in Zn^{2+} intercalation system. Adapted from Ref. [146], with permission from Wiley-VCH GmbH, © 2024. (E) Top-down chemical exfoliation-restacking process and (F) rate capability of PEO-MoS_2 electrodes in a Na^+ intercalation environment. Adapted from Ref. [149], with permission from Elsevier, © 2015. (G) Covalently interconnected MoS_2 networks formed via 1,4-bensenedithiol (BDT) pillaring. Adapted from Ref. [154], with permission from Springer Nature, © 2021.

Overall, the state-of-the-art literature on MoS_2 ion intercalation hosts clearly demonstrates that tuning of the interlayer spacing is a viable strategy to improve ion intercalation kinetics and storage capacity by reducing diffusion barriers and increasing storage sites. However, to date, no versatile synthesis approach to control crystallite size, interlayer spacing, and pillar concentration (or density) at once has been described. Also, the understanding of the MoS_2 host-pillar interaction in functionalized MoS_2 is insufficient, and it is unclear how pillars behave during electrochemical cycling. Although nanoconfinement design strategies utilizing organic

pillars show promise for enhanced pseudocapacitive behavior, these critical limitations must be addressed to successfully advance this method for next-generation EES.

Chapter 2: Principles of Techniques and Instruments

This chapter provides a detailed theoretical overview of the characterization techniques employed to investigate the physicochemical properties of MoS_2-based materials. The techniques are grouped into two main categories based on the type of information they provide: (1) physicochemical characterization, which encompasses structural, chemical, and morphological analysis, and (2) electrochemical characterization. For each technique, the fundamental principles are described, along with the type of information it delivers and its relevance to the study of functionalized MoS_2 materials.

2.1. Physicochemical Characterization

Physicochemical characterization encompasses a comprehensive suite of analytical techniques employed to elucidate the structural, chemical, and morphological properties of the synthesized MoS_2-based materials.

2.1.1. X-ray Diffraction

X-ray diffraction (XRD) stands as a fundamental, non-destructive technique for elucidating the atomic structure of crystalline matter. The technique relies on the characteristic interaction between X-rays (which possess a wavelength (λ) on the order of interatomic spacings (*d*)) and the ordered electron clouds of atoms within a crystal lattice. This periodic arrangement causes the scattered X-ray waves to undergo interference. An observable diffraction signal is only produced only when this interference is constructive. This critical condition is described by Bragg's Law (**Fig. 2.1**, **Equation 10**) [155]:

$$n\lambda = 2d \cdot sin\theta \quad (10)$$

Here, *n* is an integer representing the order of diffraction, *λ* is the wavelength of the X-rays, *d* is the interplanar spacing, and *θ* is the diffraction angle. Analysis of the diffraction peaks provides information about crystal structure, lattice parameters, interlayer spacing, and phase purity.

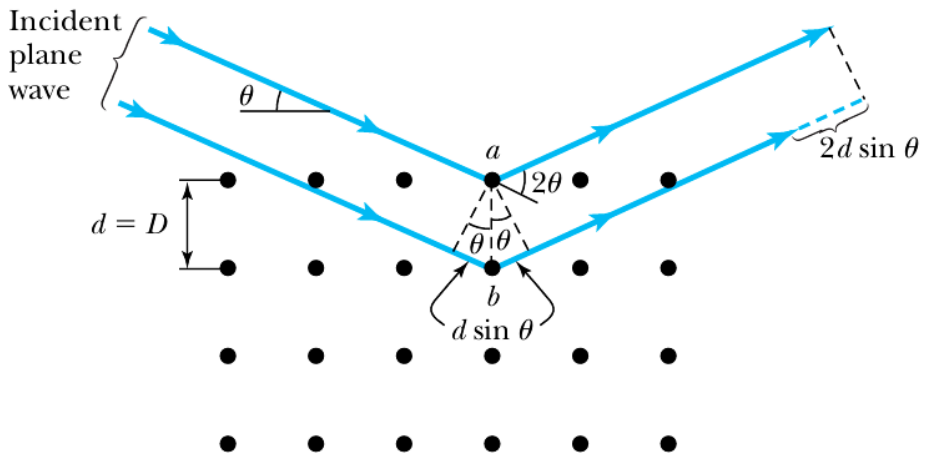

Figure 2.1: Schematic representation illustrating X-ray scattering from Bragg lattice planes. Reproduced from Ref. [156], © 2013 Cengage Learning, with permission.

While the fundamental principle of constructive interference described by Bragg's Law governs all XRD measurements, the practical method of data acquisition depends critically on the sample form and the instrument geometry. XRD patterns are typically measured in two distinct modes: reflection and transmission.[157] In the more common reflection configuration, such as the Bragg-Brentano setup, the X-ray beam impinges on the front surface of the sample, and the detector collects the scattered intensity from this same side. Conversely, the transmission configuration (e.g., Debye–Scherrer geometry) requires the X-ray beam to pass completely through a thin sample, with the detector placed behind it.

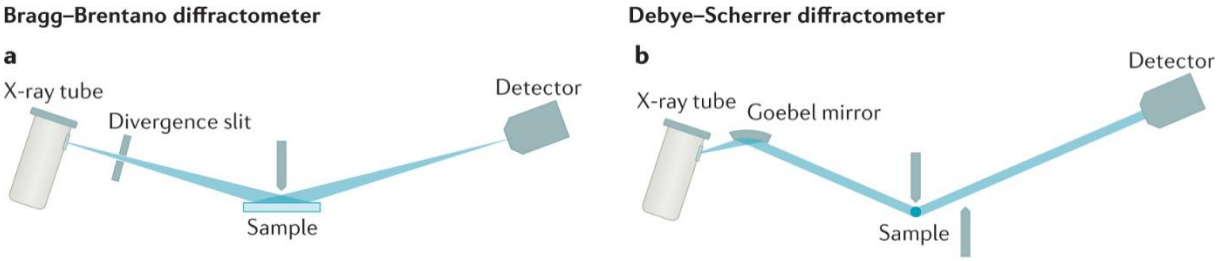

Figure 2.2: Schematic of (a) Bragg–Brentano diffractometer and (b) Debye–Scherrer diffractometer. Adapted from Ref. [157], with permission from Springer Nature, © 2021.

Critically, regardless of the specific instrumental configuration or the path of the X-rays through the material, the resulting diffraction pattern is a manifestation of the crystal structure. However, the exact angular position of the peaks, known as the 2θ value, is directly dependent on the X-ray source wavelength (λ). According to Bragg's Law, since the interplanar spacing (d) is a fixed property of the crystal, a change in λ will necessitate a corresponding change in the scattering angle θ. Consequently, the 2θ values for a given crystal will shift if the radiation

source is changed; for example, when switching from a Cu K_α source to an Ag K_α source, which possesses a significantly shorter wavelength. This dependence underscores the necessity of always specifying the wavelength used in the experiment.

In this thesis, powder diffraction patterns were collected using the reflection mode with a Cu K_α X-ray source (λ = 1.5406 Å for Cu $K_{\alpha1}$), and operando XRD experiments were conducted using the transmission mode with an Ag K_α source (λ = 0.5594 Å for Ag $K_{\alpha1}$).

2.1.2. Fourier Transform Infrared Spectroscopy

Fourier transform infrared spectroscopy (FTIR) is a widely used technique to identify the functional groups in materials (gas, liquid, and solid) by measuring the absorption of infrared (IR) radiation. The IR region of the electromagnetic spectrum lies between the visible and microwave regions. It is conventionally divided into three portions: near IR (14000 – 4000 cm-1), mid-IR (4000 – 400 cm-1), and far IR (400 – 40 cm-1).[158,159] The technique measures the intensity of radiation absorbed by a molecule. This absorption is only possible if the molecule is IR active, a condition met when the molecular motion induced by the IR radiation causes a temporary change in the net electric dipole moment. Consequently, homonuclear diatomic molecules such as H_2 or O_2 are IR inactive, while molecules without a permanent dipole moment (e.g., CO_2) may still exhibit IR-active vibrational modes.[158] This selectivity is crucial, as a particular IR frequency is absorbed at characteristic wavenumbers corresponding to specific vibrational mode. In FTIR spectroscopy, the entire IR range is collected simultaneously by an interferometer. This device outputs an interferogram, which is then computationally converted into the usable percent transmittance versus wavenumber (cm^{-1}) spectrum through the mathematical Fourier Transform. Prior to sample analysis, a background spectrum is recorded to computationally compensate for atmospheric artifacts, yielding the final absorption spectrum.

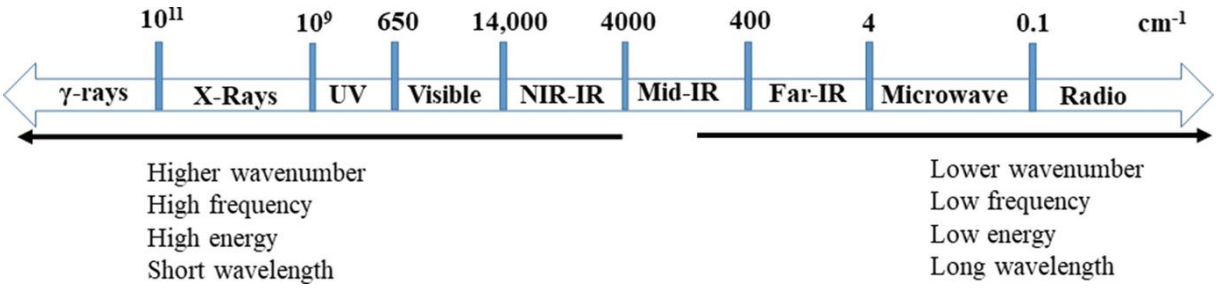

Figure 2.3: Schematic representation of the electromagnetic spectrum, showing the boundaries of major radiation regions. Reproduced from Ref. [159], with permission from Springer Nature, © 2022.

In this thesis, FTIR measurements were conducted exclusively using the Attenuated Total Reflectance (ATR) mode (Perkin-Elmer Spectrum Two), which is a highly effective, non-destructive technique for analyzing solid materials. The ATR configuration involves utilizing a high refractive index crystal (commonly diamond) pressed directly against the sample. The infrared beam reflects internally off the crystal interface, generating a short-lived evanescent wave that penetrates the sample surface by only a few micrometers (c.a. 0.5 to 2 µm, depending on wavelength and optical properties). This specialized configuration was used to investigate the successful incorporation and chemical state of the pillar molecules, specifically thiol- or amine-containing *n*-alkyl chains, within the MoS_2-based materials. The characteristic absorption bands of the C-H (alkyl chains), N-H (amine), and S-H (thiol) groups provide a definitive molecular fingerprint, confirming the presence, binding status, and structural integrity of these intercalation agents in the powder samples.

2.1.3. Raman Spectroscopy

Raman spectroscopy is an advanced, non-destructive analytical technique used to reveal the chemistry, structure, and molecular composition of materials by analyzing their vibrational modes. The technique was named with the name of the discoverer, C.V. Raman, who published the first paper on this technique.[160] Raman offers a specific structural fingerprint that allows for the identification of molecules. For 2D layered nanomaterials, this technique is particularly valuable for investigating critical characteristics like layer thickness, electronic structure-related properties, and interlayer coupling.[161]

The underlying physical process involves inelastic scattering of photons, referred to as Raman scattering.[162] When monochromatic light, usually from a laser source in the visible, near infrared, or near ultraviolet range, interacts with the sample, the energy of the scattered photon is shifted relative to the incident photon. The shift in energy, known as the Raman shift, represents the difference in wavenumber between the incident photon and the scattered photon. This energy exchange occurs due to interactions with vibrational excitations (phonons in crystalline solids). For a vibrational mode to be Raman active, the molecule must undergo a change in its polarizability during the vibration.

Raman and Infrared (IR) spectroscopy are distinct yet highly complementary techniques because they are sensitive to different molecular properties during vibration. Raman spectroscopy is fundamentally sensitive to vibrational modes that cause a change in the molecule's polarizability, while IR spectroscopy relies on a change in the molecule's dipole moment.[162,163] This difference in selection rules means that often, a mode active in one technique is inactive in the other, necessitating the use of both for comprehensive analysis.

The two techniques also differ fundamentally in their mechanism: Raman scattering is a two photon phenomenon, which involves an instantaneous virtual energy state, while IR absorption is a one photon process, as illustrated in these contrasting mechanisms in **Fig. 2.4**. When the scattered light possesses a lower frequency than the incident laser, it is termed Stokes scattering. Conversely, when the scattered frequency is higher, it is defined as anti-Stokes scattering (**Fig. 2.4**). Due to their significantly higher intensity, the Stokes bands are typically the only signals collected to form the Raman spectrum in general spectroscopy.

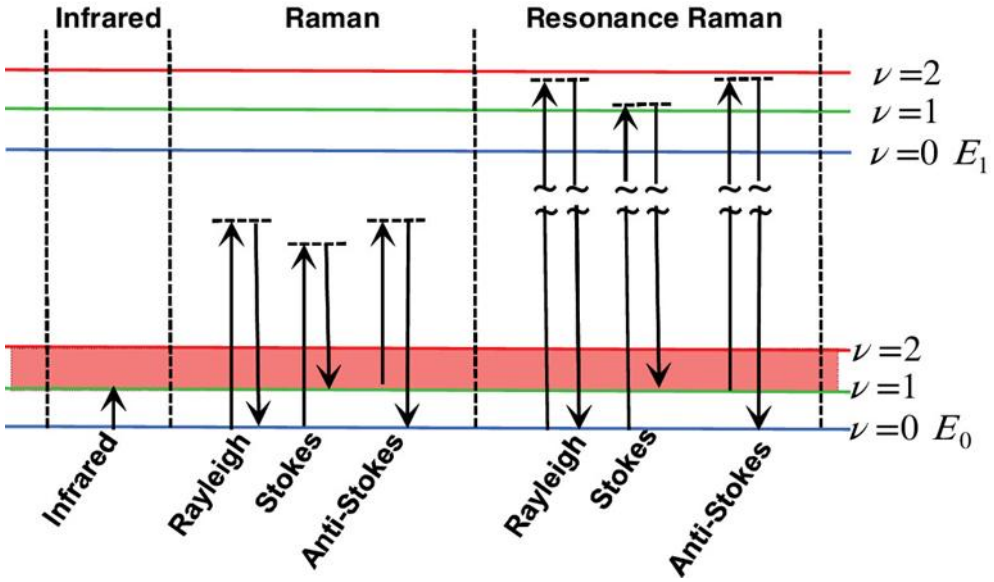

Figure 2.4: Energy level diagrams in IR and Raman. Reproduced from Ref. [163], with permission from Wiley, © 2009.

Confocal Raman spectroscopy combines the analytical power of Raman with microanalysis. This setup uses focusing optics to enhance the signal-to-noise ratio and reduce background interference by precisely isolating a small, focused area of the sample.[164] This reliable method is highly suited for obtaining local structural information from nanomaterials.

In this thesis, Raman spectroscopy was specifically utilized to determine the different crystalline phases of MoS_2, distinguishing between the metallic (1T) and semiconducting (2H) phases. Furthermore, the technique was critical for investigating layer thickness, band structures, and interlayer coupling within the 2D host material.

2.1.4. Thermogravimetric Analysis

Thermogravimetric analysis (TGA) is a thermal analysis technique that precisely tracks the change in mass of a material as it is subjected to a controlled thermal profile. The fundamental

principle relies on a highly sensitive microbalance situated inside a furnace, continuously recording the sample mass while the temperature increases. Mass change events signify the expulsion of volatile species, such as adsorbed moisture, solvent residues, or, critically, the thermal decomposition of organic or inorganic components. The resulting thermogram, lotted as mass percentage versus temperature, allows for determining the thermal stability profile, quantifying volatile content, and assigning temperature ranges associated with distinct thermal events or reactions. The derivative thermogravimetry (DTG) curve, which plots the rate of mass change, is often consulted to pinpoint the temperature of maximum mass-loss rate with high accuracy.

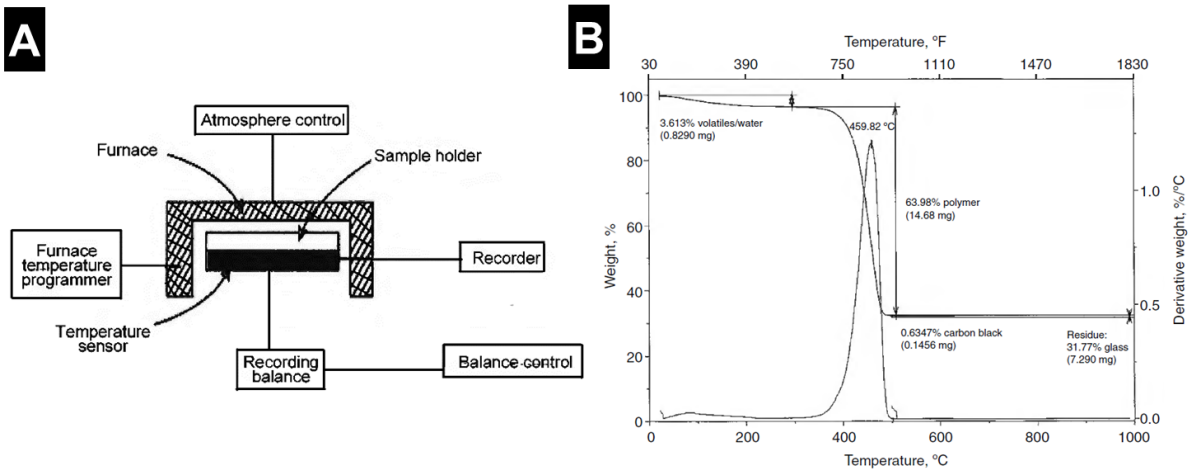

Figure 2.5: (A) Schematic illustration of a thermogravimetric instrument setup and (B) TGA curve showing the mass-loss profile with DTG curve for a 30% glass-fiber-reinforced material. Adapted from Ref. [165], © 2019 ASM International, with permission.

The practical application of TGA is entirely governed by controlled conditions, often requiring an inert atmosphere (e.g., nitrogen) to isolate decomposition from oxidation, although reactive atmospheres can be used to study oxidative stability. In this thesis, the TGA method was conducted under an oxidative atmosphere to analyze the MoS_2-based materials. The resulting thermogram clearly revealed three principal mass change events, including adsorbed water evaporation, oxidation of the MoS_2 host structure, and the thermal degradation and volatilization of the organic pillar molecules. By accurately calculating the mass fraction associated with the decomposition of the organic pillars and normalizing this value against the final stable residue, the TGA data enabled the estimation of the molar ratio of the organic pillars per MoS_2 unit. Crucially, this quantitative analysis of pillar density using TGA provided important quantitative support for the proposed nanoconfinement.

2.1.5. Gas Physisorption and Specific Surface Area Determination

Gas adsorption is the standard technique for characterizing the texture of porous solids and fine powders, specifically their surface area and pore size distribution. In this process, a probe gas (the adsorptive, typically N_2 or Ar) is brought into contact with the solid material (the adsorbent) at cryogenic temperatures (77 K). The interaction is driven by weak vdW forces, defined as physisorption, where gas molecules condense on the surface and within the pores without forming chemical bonds. By measuring the amount of gas adsorbed (n^a) as a function of the equilibrium relative pressure (p/p^0), an adsorption isotherm is generated, which serves as a fingerprint of the structural porosity or SSA of materials.

The reliability of physisorption data depends heavily on proper sample preparation and measurement protocols. Prior to analysis, the adsorbent must be outgassed under high vacuum and heat to remove physically adsorbed species from the surface. Then, the standard measurement employs a static manometric method. Successive doses of the adsorptive gas are introduced to the sample cell, and the pressure is allowed to equilibrate at each step. The amount adsorbed is calculated from the pressure drop, constructing the isotherm point-by-point from low to high relative pressures. The 2015 IUPAC classification identifies specific isotherm shapes that reveal the pore geometry of the host material.[166]

The specific surface area (unit: m^2/g) is evaluated using the Brunauer-Emmett-Teller (BET) method. The BET theory extends the Langmuir monolayer concept to multilayer adsorption.[167] It calculates the monolayer capacity, which is the amount of gas required to form a single molecular layer on the surface. The standard BET method is typically applied using a multi-point approach, where the SSA is calculated by fitting the BET equation to an adsorption isotherm over a linear range of relative pressures (usually $p/p^0 = 0.05 – 0.30$). This linear plot allows for the simultaneous determination of the monolayer capacity and the energetic constant, which indicates the strength of the adsorbent-adsorbate interaction. The monolayer capacity is indicative of the number of adsorbed molecules in a complete monolayer, which is then converted into the surface area by multiplying the number of molecules by the cross-sectional area effectively occupied by a single adsorbate molecule (e.g., 0.162 nm^2 for N_2 at 77K).

2.1.6. X-ray Photoelectron Spectroscopy

X-ray photoelectron spectroscopy (XPS) is a quantitative spectroscopic technique essential for determining the elemental composition, chemical state, and electronic state of elements within a material's surface. The foundational principles of XPS are primarily attributed to K. Siegbahn during the 1950s and 1960s.[168] The technique operates based on the photoelectric effect[169]:

when the sample surface is irradiated with a beam of soft X-rays (e.g., Al Kα), photons cause core-level electrons within the atoms to be ejected. The characteristic binding energy (BE) of the electron is then calculated, using the measured kinetic energy (KE) and the energy of the incident photon (hv), via the equation: BE = hv – KE – Ø, where Ø is the work function of the spectrometer.[170] Because the BE is highly sensitive to the local electronic environment (i.e., oxidation state and bonding partners), XPS provides a chemical fingerprint for the material, which is critical for EES analysis.

From a materials perspective, XPS is an inherently surface sensitive technique, sampling material from only the top 1 to 10 nanometers. This makes it indispensable in EES research for analyzing the electrode-electrolyte interface, where critical performance limiting phenomena occur. Although XPS analyzes only the near-surface region, it is highly applicable to powder materials because the majority of the active surface area of the individual powder particles is exposed to the X-ray beam. Practical analysis involves precise high-resolution scans and subsequent peak fitting to deconvolute signals and determine the various chemical states or oxidation states of single elements.

In this thesis, XPS analysis provided crucial insights into the chemical modification of the MoS_2-based materials. The technique was utilized for two primary purposes: phase-related chemical environments associated with metallic (1T-like) and semiconducting (2H) MoS_2 in the as-synthesized material, and functionalization confirmation. High-resolution scans were essential for determining the nature of the host-pillar interaction: for thiol-functionalized MoS_2, extra peaks corresponding to sulfur supported a covalent network, while for amine-functionalization, the -NH_3^+ species are consistent with ionic bonding between the organic pillar and the MoS_2 host layers.

2.1.7. Inductively Coupled Plasma Optical Emission Spectroscopy

Inductively coupled plasma optical emission spectroscopy (ICP-OES) is an elemental analysis technique used to quantitatively determine the concentration of metallic and non-metallic elements in a sample. Within an ICP (inductively coupled plasma spectroscopy), elements in the sample are broken down and excited into high energy states by the plasma's thermal energy. This occurs as electronic excitation of atoms and ions through collisions within the high-temperature plasma.[171] Subsequently, as the electron relaxes back to a lower energy state, it emits photons with a distinct wavelength corresponding to the precise energy difference between the two levels.[172] Since each element has unique energy levels, it emits photons at specific wavelengths that can be attributed to that element.[173] Crucially, the intensity

of this emitted light is directly correlated to the concentration of the element in the original sample (after calibration).[174]

The practical application of ICP-OES involves three main stages: sample introduction, plasma excitation, and spectroscopic detection (**Fig.2.6**).[173] First, solid samples must be prepared as a liquid solution (involving acid digestion). A solid powder sample is generally digested using appropriate acids or acid mixtures to dissolve the sample matrix. The prepared liquid sample is then drawn using a peristaltic pump, which controls its flow rate into a nebulizer. Argon converts the liquid into a fine mist (aerosol) within the spray chamber. The aerosol is subsequently delivered to the ICP torch. The high temperature (generally 8,000 – 10,000 K) argon plasma, sustained by an induction coil, breaks down the sample, atomizing and exciting the elemental species.[175] This process causes the atoms and ions to emit light (photons) characteristic of the elements present. Finally, the emitted light is transferred to the optical emission spectrometer. The separated light from a monochromator is directed onto a detector, which measures the intensity of light at each specific wavelength. Then, the data system calculates and outputs the final quantitative elemental concentrations.

In this thesis, ICP-OES was employed to analyze the stoichiometry of MoS_2-based materials, determine the elemental ratio (e.g., Mo:S), and evaluate the incorporation or retention of heteroatoms associated with (non-) covalent functionalization. It should be noted that ICP-OES alone cannot distinguish between lattice sulfur and organic pillar sulfur, requiring the combination of techniques to correctly quantify the sample composition.

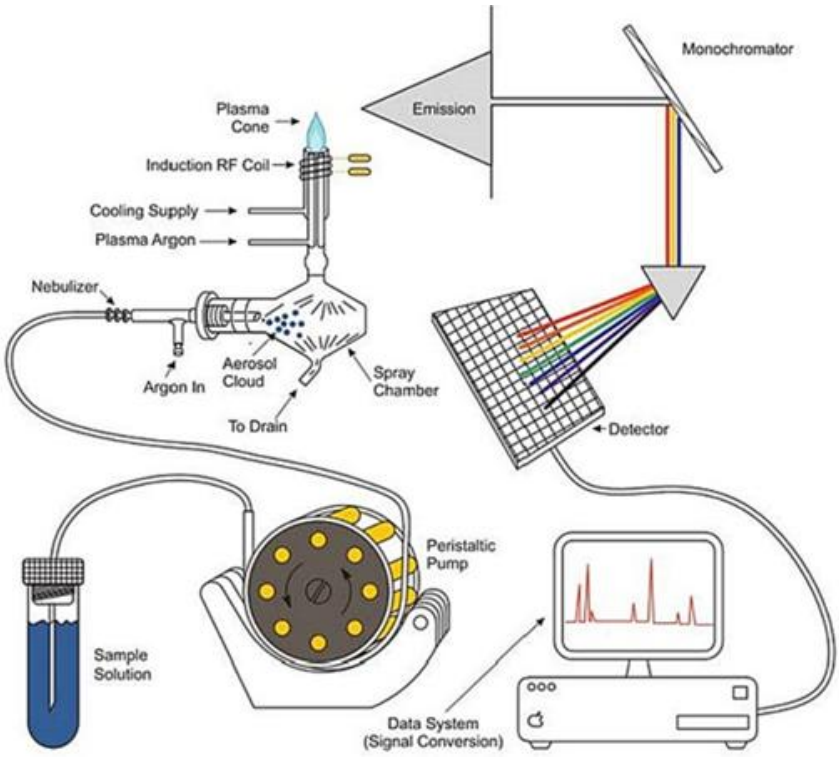

Figure 2.6: Schematic illustration of typical ICP-OES components. Reproduced from Ref. [173], with permission from Elsevier, © 2023.

2.1.8. Electron Microscopy

Electron microscopy is a powerful imaging technology that allows for the characterization of material at the nanoscale. It is primarily categorized into two main classes: scanning electron microscopy (SEM) and transmission electron microscopy (TEM).

SEM is a widely used imaging technique employed to obtain information about the morphology (size and shape), surface topography, and elemental composition.[176] The instrument generates a primary electron beam using an electron gun (e.g., tungsten or field-emission sources). This beam is accelerated by an anode and precisely focused onto the sample surface by a series of electromagnetic lenses and metal apertures.

The working principle relies on the electron-sample interaction. When the high-energy focused electron beam interacts with the specimen surface, a variety of signals are generated (**Fig. 2.7A**). These signals, including secondary electrons (SE), backscattered electrons, and X-rays, are recorded by electronic detectors.[177] The resulting images are formed by detecting emitted or scattered electrons as the beam scans across the sample.

TEM is the technique of choice for analysis of the microstructure, evaluation of nanostructures, imaging of atomic-scale high-resolution images, and determination of crystal structure and

phase identification.[178,179] This microscopy can be categorized into two modes: TEM and scanning transmission electron microscopy (STEM) modes. A parallel electron beam is used in TEM mode (**Fig. 2.7B**). The transmitted electrons form an electron diffraction pattern at the back focal plane and an image at the image plane of the objective lens. The TEM images acquired at low magnifications using TEM mode are useful for investigating the crystal morphologies and structural information by electron diffraction patterns. On the other hand, a converged electron beam (or electron probe) is used in STEM mode (**Fig. 2.7C**). Scanning the sample using the electron probe generates the scattered electrons detected by multiple detectors. High-angle annular dark-field (HAADF) STEM images are commonly used to study nanomaterials since HAADF-STEM images are often more straightforward to interpret.[179] STEM mode is powerful for high-resolution images to directly observe atomic geometry.

Energy-dispersive X-ray (EDX) analysis is usually combined with SEM and STEM imaging, which provides the simultaneous analysis results of the surface morphology and elemental composition of specimens. For this, an EDX spectrometer is typically integrated in microscopes since the operational principle of EDX depends on electron beam excitation (**Fig. 2.7D and 2.7E**).[178]

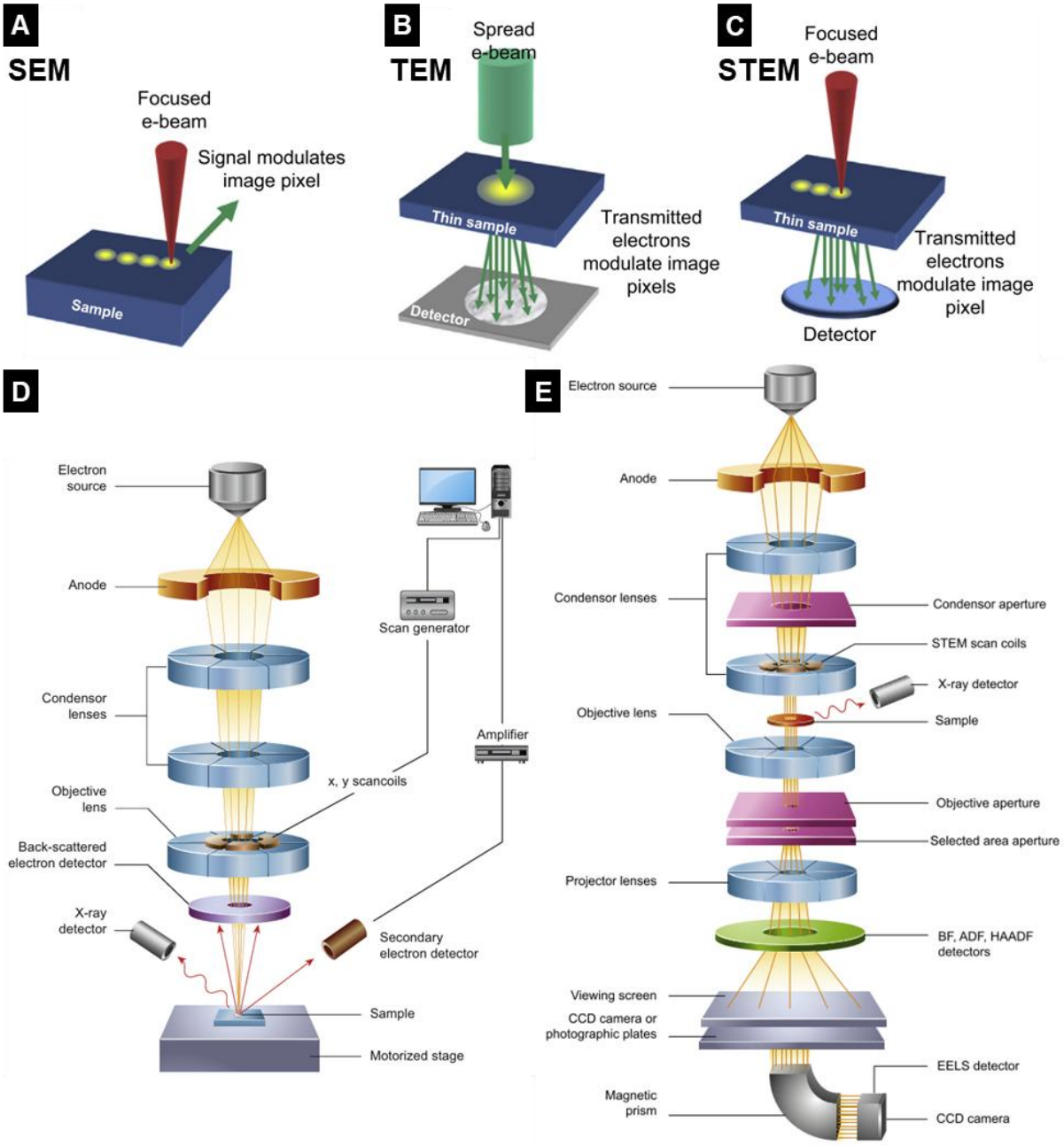

Figure 2.7: Schematic illustration of the imaging methodology of (A) SEM, (B) TEM, and (C) STEM, and the core components of (D) an SEM and (E) a TEM instrument. Adapted from Ref. [178], .

In this thesis, SEM images of as-synthesized MoS_2-based materials were captured to confirm the particle morphology in powder form. This visualization confirmed the overall size, shape, and aggregation of the materials prior to electrochemical testing. TEM was used to check the morphologies of the powder samples on the nanoscale. Electron diffraction patterns in TEM mode provided the structural information, and EDX mapping images in STEM mode confirmed

the homogenous distribution of elements with semi-quantitative atomic ratios between Mo and S elements.

2.1.9. Dynamic Light Scattering - Particle Size Analysis

Dynamic light scattering (DLS) is a well-established analytical technique for measuring particle size by leveraging the Brownian motion of particles in a liquid suspension or solution. When particles are dispersed in a liquid, they move randomly in all directions as they are constantly colliding with solvent molecules. This energy transfer has a greater effect on smaller particles, causing them to move at higher speeds than larger particles. The speed of the particles is given by the translational diffusion coefficient (*D*). The relationship between this diffusion coefficient and the particle size is formally described by the Stokes-Einstein equation (**Equation 11**):

$$D = \frac{k_B T}{3\pi\eta d_H} \tag{11}$$

where k_B is the Boltzmann constant, T is the absolute temperature, η is the solvent viscosity, and d_H is the hydrodynamic diameter of a spherical particle in the dilute limit. By measuring the particle speed, DLS can determine the hydrodynamic diameter, provided the temperature and viscosity are known. A basic requirement for this equation is that the particle movement must be solely based on Brownian motion. Therefore, the upper size limit for DLS is indicated by the onset of sedimentation, which prevents random movement, while the lower size limit is defined by the signal-to-noise ratio, as small particles do not scatter sufficient light.

When DLS is used for a non-spherical particle, such as the 2D nanosheets relevant to this thesis, the analysis is more complex. The measured hydrodynamic diameter (D_h) does not directly equal the lateral size (L) of the nanosheet. For disk-like objects (with thickness t and length L), there are theoretical models approximating the hydrodynamic volume (D_h^3) as proportional to $t \times L^2$. If the thickness is assumed to be relatively constant, as it is typical for exfoliated 2D materials, the hydrodynamic size has empirically been shown to be proportional to $L^{2/3}$.

$$L = (0.07 \pm 0.03) \times D_h^{(1.5 \pm 0.15)} \tag{12}$$

This theoretical relationship was experimentally verified for various liquid exfoliated 2D sheets (graphene, MoS_2, WS_2).[180] Although this method is not as precise as direct imaging via TEM

or AFM, DLS provides a fast, simple, and reasonable estimate of the lateral size of 2D nanosheets dispersed in a liquid.

In a DLS instrument (**Fig. 2.8**), the laser beam hits the dispersed sample in liquid, causing the particles inside to scatter the light as they undergo Brownian motion. The scattered light waves interfere due to the constant movement of particles. This causes the fluctuation of the collected signals in the detector over time. A digital signal processor analyzes the speed of these fluctuations by generating an autocorrelation function. Then, a computer applies the Stokes-Einstein equation to this function to calculate the final particle size distribution.

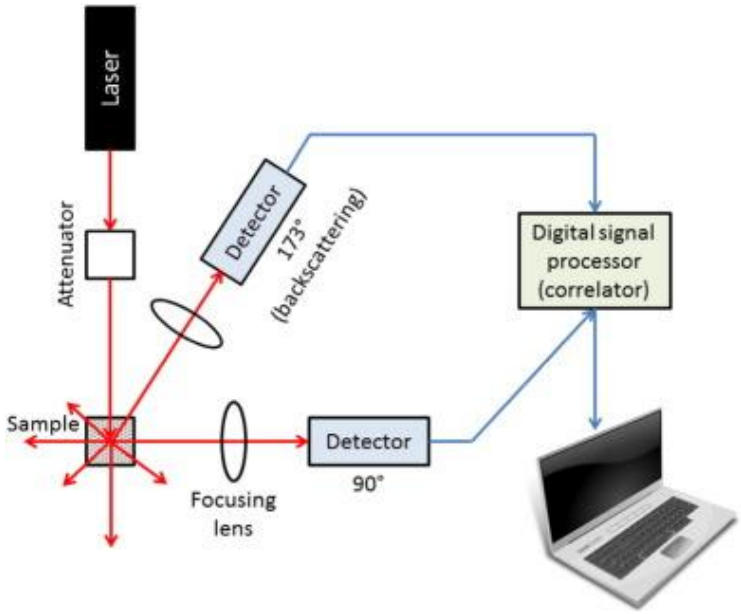

Figure 2.8: Schematic illustration of the DLS instrumentation. Reproduced from Ref. [181], with permission from Elsevier, © 2016.

2.1.10. Electrochemical Dilatometry

Electrochemical dilatometry (ECD) is a powerful operando technique utilized to precisely measure the thickness change of an electrode, often termed “electrode breathing”, during charging and discharging.[182] The technique has been employed in the electrochemical field since the 1970s.[183] This method is crucial for tracking volume changes in materials that undergo ion insertion or structural rearrangement (e.g., phase changes), as these dimensional changes are directly linked to mechanical stress and cycle life.[184]

The core mechanism involves the working electrode (WE) being sealed by a flexible metal membrane. When current (or potential) is applied to the cell (**Fig. 2.9**), causing the WE to expand or contract, this dimensional change is mechanically transferred through the flexible

membrane to an external load unit. The cell can be operated via a two- or three-electrode setup. Crucially, the counter electrode (CE) and the electrolyte-soaked glass frit separator are fixed. This rigid fixation ensures that the sensor detects the thickness change of the WE only, minimizing interference from any volume changes in the CE or other cell components.

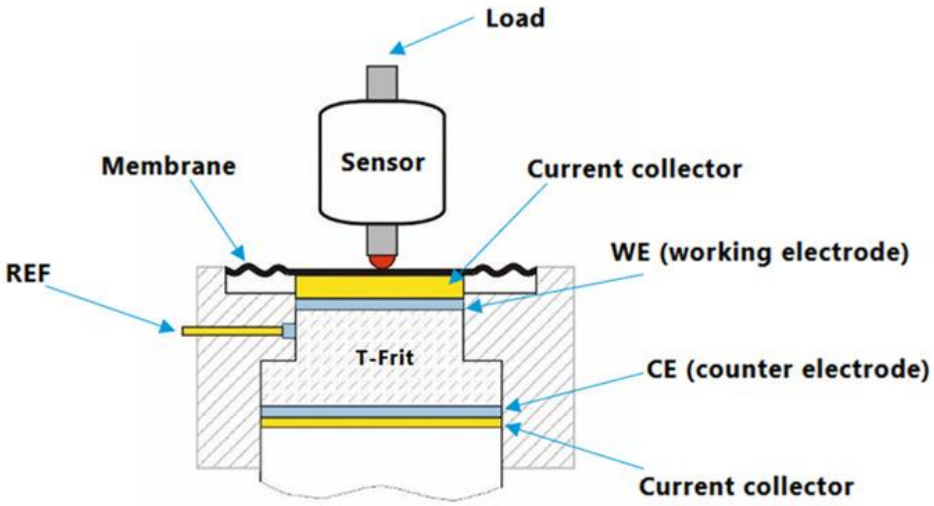

Figure 2.9: Schematic illustration of the ECD. Adapted from Ref. [184] under the terms of the Creative Commons Attribution 4.0 International License (CC BY 4.0), © 2022 The Authors, published by Wiley-VCH GmbH.

In this thesis, ECD was conducted as a crucial technique to understand the influence of solvents on the MoS_2-based electrodes. The ECD results directly revealed significant height changes in the electrode upon cycling, providing physical evidence consistent with the phenomenon of solvent co-intercalation (the insertion of the solvent, diglyme, alongside the Li^+ ions). This critical finding was not only observed in the dilatometry but was also independently confirmed by complementary operando XRD results, where the layer spacing expansion verified the co-intercalation mechanism. ECD provided essential, real-time monitoring of the dimensional strain imposed by the intercalation process.

2.2. Electrochemical Characterization

A comprehensive assessment of electrode materials is essential to evaluate their practical viability in energy storage applications. This evaluation focuses on determining critical performance metrics, including energy and power density, Coulombic and energy efficiency, and cycle life. These features are derived from fundamental parameters, specifically voltage, current, capacity, and testing duration, which are directly collected through various electrochemical measurements. While theoretical values can be calculated based on

thermodynamics (Gibbs free energy, $\Delta_r G$ can define the OCV) and Faraday's law, experimental results often deviate due to practical factors such as polarization and internal resistance. To capture these complex behaviors, electrochemical techniques are generally classified into three categories based on the control variable applied to the cell: potentiostatic or potentiodynamic techniques (controlled voltage), galvanostatic techniques (controlled current), and impedance techniques (small perturbation in a quasi-steady state). The following sections detail the specific methods employed in this thesis within these categories.

2.2.1. Cyclic Voltammetry

Cyclic voltammetry (CV) is an electrochemical technique in which the potential of a WE is linearly swept (scan rate, υ) between set limits (vertex potentials E_1 and E_2, **Fig. 2.10A**). At the same time, the resulting voltammogram reveals information about redox processes, capacitive behavior, and charge-transfer kinetics.[185] A typical current response of the single Faradaic reaction is shown in **Fig. 2.10B**, characterized by distinct peak voltages for anodic and cathodic reactions (E_{pa} and E_{pc}) and corresponding peak current (i_p) values.

The electrochemical reversibility of the system is evaluated by analyzing the relationship between the cathodic and anodic segments of these peaks. Specifically, the ratio of the peak currents (i_{pa}/i_{pc}) and the potential difference between the peaks (ΔE_p) serve as the primary diagnostic criteria for judging reversibility. The criteria for an ideally reversible Nernstian system at 25 °C are a value of ΔE_p=59/n mV (n is the number of electrons transferred), i_{pa}/i_{pc}=1 and $i_p \sim \upsilon^{1/2}$. However, it is important to note that while rechargeable batteries deliver reversible Faradaic capacity, they often exhibit quasi-reversible or irreversible behavior in a strict electrochemical sense due to kinetic limitations. Consequently, practical analysis focuses on the physical significance of the recorded parameters: the peak potential identifies the specific potential of the underlying electrode redox reactions, while integrated current associated with a redox peak is directly relevant to the magnitude of the Faradaic capacity (Q_F, **Equation 13**).

$$Q_F = \int i\,dt = \int i\frac{dE}{\upsilon} \tag{13}$$

It is noted that the total measured current ($i_{total} = i_{dl} + i_F$) is a composite of three primary response modes, each governed by different physical and chemical principles. First, the electric double-layer current (i_{dl}) behaves as a physical capacitor. This is a non-Faradaic process, meaning no chemical reactions occur. The current response is directly dependent on the double-layer capacitance (C_{dl}) and the scan rate (υ). Second, the Faradaic current (i_F) ($i_F = i_b + i_s$), which involves the chemical redox reactions, is further categorized based on reaction location: the

surface (i_S) or the bulk (i_b). This separation relies on the fundamental reality that charge carrier diffusion within a solid electrode is significantly slower than in a liquid electrolyte. The surface Faradaic processes (i_S) occur at the electrode surface. Their current response can be approximately proportional to the scan rate, and the potential is determined by the Gibbs free energy change of the surface redox reaction. On the other hand, the bulk Faradaic processes (i_B) occur deep within the material and are diffusion-controlled, characteristic of battery reactions.

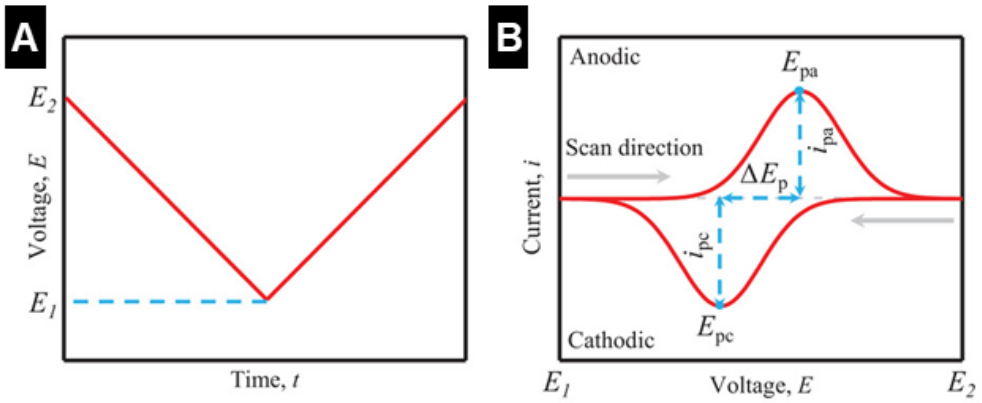

Figure 2.10: Principles of the CV technique. (a) Voltage profile applied in a CV experiment and (b) a current response versus voltage curve. Adapted from Ref. [185], with permission from Wiley-VCH GmbH, © 2019.

The total current response (i) at a specific potential (V) can thus be mathematically separated to distinguish these mechanisms, often using the power law relationship (**Equation 14**):

$$i = av^b \tag{14}$$

In this equation, i represents the peak current, v is the scan rate, and a and b are adjustable parameters. The b-value is determined by calculating the slope of the logarithm of the peak currents plotted against the logarithm of the scan rate (log i vs. log v). This parameter serves as a critical indicator of the dominant reaction kinetics. A b-value of 0.5 signifies a process governed by semi-infinite linear diffusion, which is typical for battery materials. Conversely, a b-value of 1.0 represents a purely surface-controlled response. For many advanced electrode materials, the b-value falls between these two limits ($0.5 \leq b \leq 1.0$). This can mean that mixed charge storage kinetics with both diffusion- and surface-limited kinetics are present, or finite length diffusion effects contribute to reduced diffusion-limitation, a case often seen in nanosized materials.[18,36] This analysis is particularly relevant for nanomaterials, which are frequently designed to minimize the diffusion limitation via their large surface area, thereby enhancing rate performance while maintaining high capacity. However, it is important to note

that a critical limitation of this approach is the underlying assumption that polarization-induced peak potential shifts with increasing scan rates are negligible, a condition that is frequently violated in experimental measurements.[185]

In this study, CV was employed to investigate the electrochemical redox behavior of MoS_2-based electrodes across varying structural configurations, including bulk, nanostructured, and nanoconfinement-designed materials.[95,96] Specifically, the kinetic mechanisms governing charge storage were elucidated through *b*-value analysis derived from the scan rate-dependent current response. This analytical approach enabled the quantitative distinction between diffusion-limited and surface-controlled processes, thereby revealing how structural engineering directly influences the fundamental reaction kinetics.

2.2.2. Galvanostatic Charge and Discharge

Galvanostatic charge/discharge (GCD), which is a form of chronopotentiometry, is the most practical electrochemical technique for assessing the capacity, cycle stability, and rate capability of electrode materials. The procedure involves applying a constant current (*i*) to the electrochemical cell until a certain cut-off voltage is reached.

A typical applied current profile is shown in **Fig. 2.11A**, where a constant positive and negative current is applied sequentially. The resulting voltage response, plotted against capacity (or time), provides critical insight into the electrochemical behavior (**Fig. 2.11B**). For battery-type materials, the voltage profile typically exhibits a distinct plateau corresponding to the thermodynamics of the electrode redox reactions, while capacitive materials show a more linear voltage slope, as depicted in **Fig. 1.5**. By repeating these charge/discharge cycles, it can be evaluated as the cycle life stability (**Fig. 2.11C**), defined as the number of cycles and electrode can sustain before its reversible capacity fades to a specific threshold (e.g., 80 % of its initial value).

Furthermore, GCD is essential for determining the rate capability of the material (**Fig. 2.11D**). This is evaluated by systematically adjusting the applied current density. As the current rate increases, the accessible capacity typically decreases due to aggravated polarization and kinetic limitations. This test reveals the ability to retain the capacity of the material under high-power demands, a key metric for practical applications.

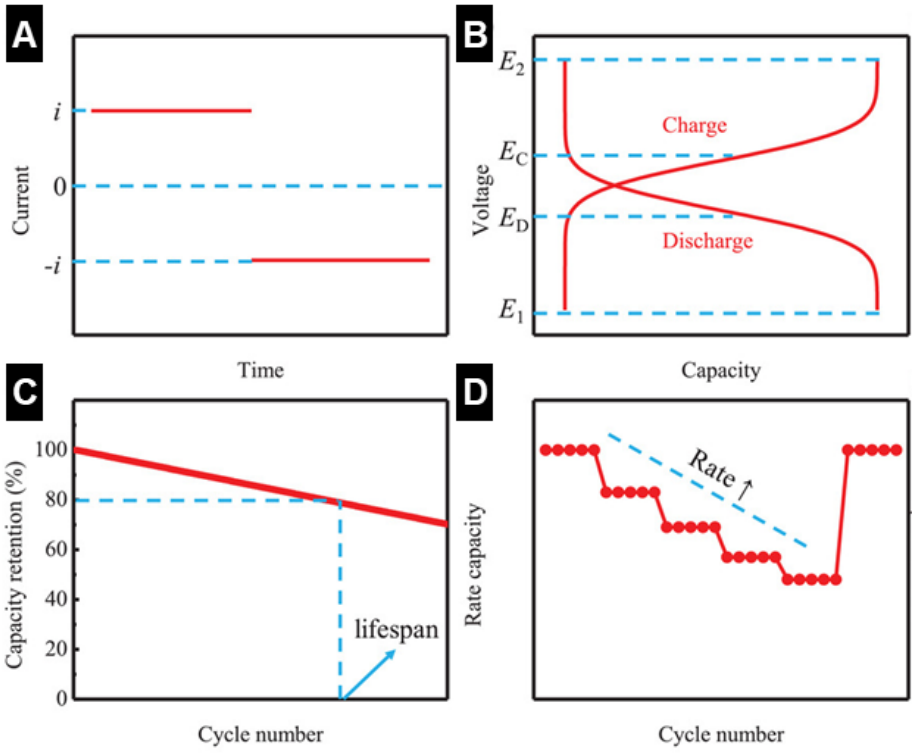

Figure 2.11: Schematic illustrations of (a) Applied current profile and (b) typical GCD (recorded voltage versus capacity) curves. Typical measurements for (c) long-term cycling stability and (d) rate capability performances. Adapted from Ref. [185] with permission from Wiley-VCH GmbH, © 2019.

In this thesis, GCD measurements were utilized to accurately determine the specific capacity of the MoS_2-based materials, particularly at low specific currents. Additionally, the technique was essential for evaluating the rate capability and monitoring capacity retention over cycling. Notably, the operando characterization techniques, including XRD and ECD, were also conducted under galvanostatic conditions to ensure a direct correlation between the electrochemical state and the observed structural changes.

2.2.3. Electrochemical Impedance Spectroscopy

Electrochemical impedance spectroscopy (EIS) is a powerful technique for resolving the various electrochemical processes occurring within a cell by their time constants. Unlike DC techniques, EIS measures the impedance (a complex AC response) of the system by applying a small sinusoidal voltage perturbation (typically a few mV) over a wide frequency range (e.g., 10^{-2} to 10^{5} Hz). This small amplitude is assumed to lead to a linear response, allowing the complex electrochemical system to be modeled as an equivalent circuit composed of resistors, capacitors, and inductors.

The resulting data is most commonly analyzed using a Nyquist plot, which displays the imaginary part of the impedance (-*Z*″) against the real part (*Z*′). As shown in **Fig. 2.12A**, a typical Nyquist plot for a battery system often exhibits a semicircle in the high-frequency region and a sloping line in the low-frequency region. This response is frequently modeled using a Randle circuit, which includes the internal resistance of the electrolyte and cell components (R_{int} or R_s), the charge transfer resistance (R_{ct}), the double-layer capacitance (C_{dl}), and Warburg impedance (Z_w). R_s is represented by the high-frequency intercept with the real axis (*Z*′), and R_{ct} corresponds to the kinetic barrier for the redox reactions at the electrode-electrolyte interface. Z_w is the impedance associated with the semi-infinite linear diffusion of active species into the bulk electrode. In the low-frequency region, this manifests as a straight line with a slope of approximately 45°. In practice, rough surfaces or non-uniform reactivity often cause the semicircle to be depressed. In such cases, the ideal capacitor (C_{dl}) is replaced by a constant phase element (CPE) to improve the model fit (**Fig. 2.12B**).

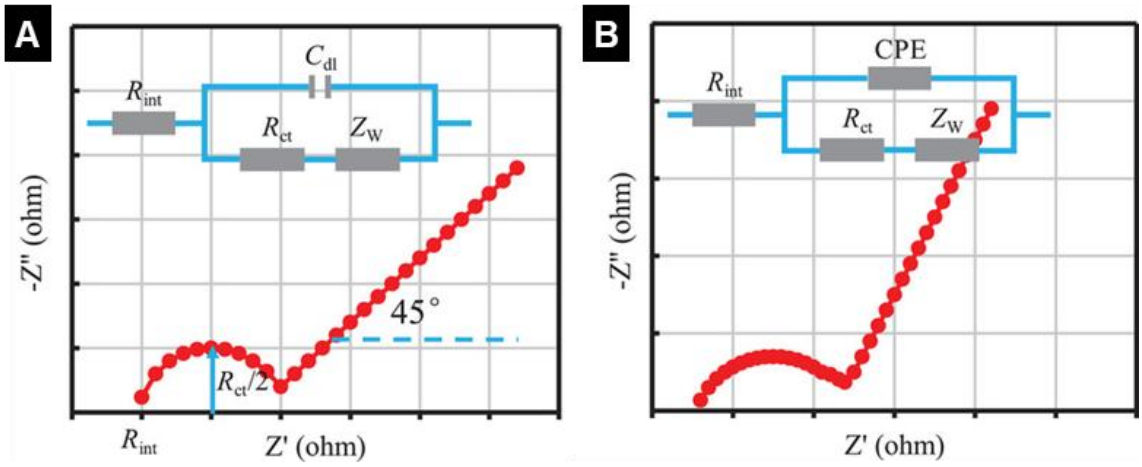

Figure 2.12: Schematic illustrations of (A) the Randles circuit model and the corresponding EIS. (B) Randles circuit model with CPE and the corresponding EIS. Adapted from Ref. [185], with permission from Wiley-VCH GmbH, © 2019.

However, in practical experiment scenarios, the Nyquist plot often exhibits a significantly more complex behavior than the ideal Randle model implies. Specifically at the electrode-electrolyte interface, the impedance response typically simplified as charge transfer resistance (R_{ct}) can aggregate multiple distinct physicochemical phenomena occurring in sequence. These steps include the desolvation of the charge carriers, interfacial ion adsorption on the active sites, and the subsequent electron transfer across the double layer.[138,186] Consequently, these overlapping processes may manifest as depressed or merged semicircles in the high-to-medium frequency region. Therefore, it is critically important to carefully analyze these events

using rigorous equivalent circuit modeling to identify and quantify the specific kinetic bottlenecks accurately within the system.

In this thesis, EIS was utilized to investigate the kinetic properties of MoS_2-based electrodes. The low-frequency region was specifically evaluated to discern surface-limited and diffusion-limited processes. Additionally, the impedance response in the high and middle frequency regions was investigated as a function of applied potential using staircase potentio-electrochemical impedance spectroscopy (SPEIS). This approach allowed for monitoring evolutions of internal and charge transfer resistances at various states of charge, providing evidence of how the introduction of organic pillars and the expansion of the interlayer spacing influenced the overall kinetics within the system.

Chapter 3: Aim of the Dissertation

The primary objective of this dissertation is to bridge the fundamental performance gap between high energy density batteries and high power density SCs by engineering the structure of layered electrode materials via nanoconfinement design. While MoS_2 possesses a high theoretical capacity based on conversion reactions, its reversible intercalation capacity is moderate (167 mAh/g). However, its unique value lies in its weak vdW forces and electronic tunability, which allow for precise structural modification and the stabilization of highly conductive metallic phases.

This thesis aims to leverage these intrinsic properties to overcome sluggish solid-state diffusion, establishing a quantitative correlation between the nanoconfinement environment, specifically the geometry and chemistry of the interlayer space, and the resulting electrochemical charge storage kinetics.

To achieve this goal, the research is divided into three specific aims, each addressing a critical knowledge gap in the understanding of pillared layered materials.

1. Simultaneous Structural Control for Pseudocapacitive Kinetics

While nanostructuring strategies for MoS_2 have been investigated, no versatile synthesis method to simultaneously control crystallite size and interlayer spacing at once has been described. Furthermore, the understanding of MoS_2 host-pillar interaction in interlayer-expanded MoS_2 is insufficient and it is unclear how pillars behave during electrochemical cycling. This study aims to establish a versatile one-pot hydrothermal approach that leverages pH adjustment and the introduction of organic pillars to tune these structural parameters concurrently. The primary research inquiry is to determine how the integration of *n*-alkyldiamine-based (HDA) pillars into nanostructured MoS_2 influences the electrochemical performance.

2. Elucidation of Covalent Host-Pillar Interactions and Density Limits

While pillaring expands the lattice, the stability and electronic effects of the pillars themselves remain poorly understood. Specifically, alkylamine-based pillars do not form strong covalent bonds with the MoS_2 lattice, which may compromise the long-term structural stability of the pillared architecture. To overcome this crucial bottleneck, the second aim of this study is to synthesize covalently connected MoS_2 by introducing 1,6-hexanedithiol (HDT) as an organic pillar capable of stronger interaction with the host. HDT is characterized by thiol (-SH) groups

that, based on prior investigations primarily on monolayers, can form robust covalent bonds with MoS_2.[152] For example, such studies have shown that thiol molecules react with defect sites and sulfur vacancies in MoS_2 to establish stable Utilizing a one-pot hydrothermal approach, this work establishes a covalent network between the organic pillars and the MoS_2 layers. A central objective is to demonstrate that controlling the density of these HDT pillars is crucial to fine-tune the diffusion pathways and storage sites available for electrochemically intercalating ions.

3. Transition of Nanoconfinement Design to Micron-Sized Architectures

To transition toward a more scalable manufacturing process compared to the hydrothermal methods used in previous chapters, this final study utilizes a top-down synthesis strategy to engineer micron-sized MoS_2 particles featuring an internal nanoconfinement design. By employing chemical exfoliation followed by pillaring with HDA, the benefits of expanded interlayer spacing are effectively translated from the nanoscale to bulk-like particle dimensions. This structural evolution is driven by the hypothesis that micron-sized architectures can retain the advantageous diffusion kinetics of nanostructures while offering processability. Consequently, this study aims to validate the electrochemical robustness of these engineered micron-sized architectures. We also investigate whether the nanoconfinement design can effectively regulate ion intercalation and structural stability, utilizing comparative studies in carbonate- versus ether-based electrolytes to monitor the architectural changes (e.g., lattice expansion) under different solvation environments.

By systematically addressing these objectives, this thesis intends to provide a mechanistic understanding of how nanoconfinement design can be utilized to rationally tailor the thermodynamics and kinetics of ion intercalation in layered TMDs.

Chapter 4: Experimental: Materials and Methods

This chapter details the specific experimental procedures employed in this thesis, building upon the theoretical principles outlined in **Chapter 2**. It provides a comprehensive description of the raw materials, synthesis protocols, electrode preparation methods, and the specific instrumental parameters utilized to generate the data presented in the subsequent **Chapter 5**: Results and Discussion.

4.1. Simultaneous Structural Control for Pseudocapacitive Kinetics

4.1.1. Material Synthesis

MoS_2 samples were synthesized using a one-pot hydrothermal method, following the procedure outlined by Geng et al.[123] 300 mg MoO_3 (Alfa Aesar), 450 mg thioacetamide (Thermo Fisher Scientific), and 3 g urea (Merck KGaA) were dissolved in 50 ml deionized (DI) water and stirred for 30 minutes in a glass beaker. To control the pH of the solution, 1 M hydrochloric acid (HCl, Merck) or 1 M lithium hydroxide (LiOH, Merck) were added as needed to reach either pH 1 (Nano-MoS_2) or pH 5.5 (Micro-MoS_2), respectively. The pH was measured using a pH meter (Blueline 14 pH/Xylem Analytics). The solution was transferred to a 100 ml Teflon vessel, which was used for hydrothermal synthesis in an autoclave (BRHS-100, Berghof). The synthesis temperature was set at 235 °C and maintained for two hours after reaching the target temperature. The pressure in the autoclave was maintained at ca. 13 – 18 bar. The reaction products were collected by centrifugation at 6000 rpm for 10 min, followed by vacuum filtration with washing in DI water and ethanol. The filtered powder was dried at 80 °C in an oven overnight.

Furthermore, interlayer-expanded MoS_2 samples were also synthesized by the one-pot hydrothermal approach. In this case, HDA, 1,8-octyldiamine (ODA) or 1,12-diaminododecane (DDDA) (all Thermo Fisher Scientific) were introduced to the precursor solution described in the previous section. The quantity of HDA/ODA/DDDA added was determined based on a molar ratio of 1:*x* between diamine and MoS_2, where x was either 1 or 0.5. Post addition of diamine, the pH of the hydrothermal solution was adjusted to pH 1. The synthesis conditions and methodology for the powder remained consistent with those employed for the pristine materials, with the exception of the synthesis temperature, which was set to 180 °C.

4.1.2. Material Characterization

Powder XRD patterns of the MoS_2-based materials were obtained in Bragg-Brentano geometry using a Bruker D8 Advance diffractometer operating with a Cu Kα radiation source (λ = 1.5406 Å) using a 0.02° step size and a dwell time of 1 s. Powder size distribution analysis was performed using a laser diffraction particle size analyzer (Mastersizer 3000, Malvern) to measure the size of non-spherical particles by the DLS method. A mixture of isopropanol and DI water (1:1 volumetric ratio) was used as a dispersant. Raman spectroscopy was performed on bulk powder samples using a Renishaw InVia confocal Raman microscope with a 532 nm excitation laser. The laser power was kept at 100 µW to prevent the decomposition of samples. At least three different spots were investigated to check the homogeneity of samples. FTIR was carried out using the FTIR spectrometer Spectrum Two (PerkinElmer). Powders were measured at a resolution of 1 cm^{-1} with 20 scans in the range of 400 – 4000 cm^{-1}.

Thermogravimetry analysis was performed using a TG 209 F1 Libra thermal analyzer (Netzsch) under oxygen flow (20 ml/min) at a heating rate of 2 K/min. SEM imaging was performed on a field emission scanning electron microscope (Crossbeam x340, Zeiss) under 5 kV operation voltage. TEM measurements were performed using a Talos F200i (Thermo Fisher Scientific, formerly FEI) operating at an accelerating voltage of 80 kV. For TEM sample preparation, powders were ground using a pestle and mortar. Then, the carbon-coated Formvar film of a copper TEM grid was carefully rubbed on the fine powders. The surface chemistry of the MoS_2-based materials was analyzed in powder form by XPS. The powder XPS was conducted in a SPECS UHV system (FOCUS 500 equipped with a monochromatic X-ray source, PHOIBOS 150 hemispherical energy analyzer with 2D DLD detector) using the Al Kα (*hv* = 1486.6 eV) radiation. The spectra were collected at 200 W with a pass energy of 10 eV and a step-size of 0.1 eV in a fixed analyzer transmission mode. The collected spectra were later calibrated to the signal of C-C/C-H sp3 at 284.8 eV as a reference on CasaXPS software.

4.1.3. Electrode Preparation and Electrochemical Characterization

The slurry consisted of 80 wt.% active material (pristine MoS_2 or interlayer-expanded MoS_2), 10 wt.% carbon black (CB), and 10 wt.% polyvinylidene difluoride (PVDF). Pristine and interlayer-expanded MoS_2 powders were ground with CB using a pestle and mortar and transferred into a small container together with 2 wt.% PVDF-containing N-Methyl-2-pyrrolidone (NMP) solution and then transferred into a speed mixer (ARE-250, Thinky), where it was mixed for 10 min at 1000 rpm. The wet mixture was coated on a carbon-coated aluminum foil with a wet film thickness of 60 µm using a doctor blade, and dried overnight in an oven at 80 °C to remove NMP solvent. Electrodes were punched using a handheld electrode cutter

with a diameter of 12 mm. Electrodes were stored in an 80 °C oven overnight before being transferred into an argon-filled glovebox. Metallic lithium discs (Honjo, 14 mm diameter) were used as negative electrodes. 2032-type coin cells were assembled with a 1 mm thick stainless steel spacer, a stainless steel spring, and glass microfiber filter (Whatman grade GF/A) as a separator in a glovebox (MBraun, O_2, H_2O <0.1 ppm). 120 µl of LP30 electrolyte (1 M $LiPF_6$ in ethylene carbonate (EC): dimethyl carbonate (DMC) (1:1 volumetric ratio), Solvionic) was used in each coin cell. CV and galvanostatic cycling tests were performed at different scan rates and currents between 1.0 and 3.0 V versus Li^+/Li in temperature-controlled chambers (Binder) at 20 °C using a potentiostat (Bio-Logic VMP3-e and VMP300). Long-term cycling tests were conducted at 0.5 A/g.

For the ex situ XRD analysis, the same electrodes as prepared for the electrochemical characterization are utilized. 2032-type coin cells are assembled following the procedures detailed above. Using GCPL with a specific current of 0.05 A/g, the electrode is reduced to 1.0 V vs. Li^+/Li. The coin cell is subsequently disassembled in an Ar-filled glovebox. The electrode is gently rinsed with diethyl carbonate (DEC), and then transferred to the glovebox prechamber, where a vacuum is applied for more than 10 minutes to ensure the complete removal of residual DEC from the electrode. After the electrode is transferred back into the glovebox, fixed onto an airtight XRD holder with Kapton tape and sealed with a domed-shaped lid. Then, XRD patterns of the lithiated electrode are collected between 4 and 25° (2 theta) using a Bruker D8 Advance diffractometer operating with a Cu Kα radiation source (λ = 1.5406 Å) using a 0.02° step size and a dwell time of 3 s.

4.2. Elucidation of Covalent Host-Pillar Interactions and Density Limits

4.2.1. Materials Synthesis

Synthesis of Pristine MoS_2: Metallic-phase MoS_2 was synthesized via a one-pot hydrothermal method. In a typical procedure, 150 mg of MoO_3 (Alfa Aesar), 175 mg of thioacetamide (Thermo Fisher Scientific), and 1.5 g of urea (Merck KGaA) were dissolved in 25 mL of DI water and stirred for 30 minutes in a glass beaker. The pH of the hydrothermal solution was adjusted to approximately 2 by adding diluted hydrochloric acid (HCl), as monitored with a Blueline 14 pH meter (Xylem Analytics). The resulting solution was transferred into a 100 mL Teflon vessel within an autoclave (BP-100 High-pressure Reactor, Berghof). The synthesis was conducted at 180 °C for 12 hours, with heating and cooling periods of 2 hours each. After synthesis, the reaction products were washed with DI water and ethanol via vacuum filtration. The material retained on a 0.22 µm hydrophilic PTFE membrane (Millipore) was collected by rinsing with 15–20 mL of DI water into a 50 mL centrifuge tube. The resulting MoS_2 slurry was dispersed by shaking and sonication for approximately 3 minutes. The well-dispersed solution was then frozen in liquid nitrogen, and the frozen sample was transferred directly to a freeze dryer (Alpha 3-4 LSCbasic, Martin Christ) for 72 hours. The resulting fine black MoS_2 powder was collected for further use.

Synthesis of HDT-Functionalized MoS_2: Functionalized MoS_2 with HDT (Thermo Fisher Scientific) was synthesized following the same procedure as for pristine MoS_2, with two additional steps. First, HDT was added to the 25 mL precursor solution in molar ratios of 0.2, 0.5, 1, 2, and 5 relative to molybdenum (Mo). Second, after the hydrothermal reaction, the products were washed with acetone during vacuum filtration to remove any unreacted HDT molecules. All collected powders were then dried in an 80 °C oven for 20–30 minutes prior to characterization.

4.2.2. Materials Characterization

Powder XRD: XRD patterns were recorded in Bragg–Brentano geometry using a Bruker D8 Advance diffractometer equipped with a Cu Kα radiation source (λ = 1.5406 Å), with a step size of 0.02° and a dwell time of 1 s.

TGA: TGA was conducted using a Discovery TGA 7 (TA Instruments) under a 1:1 oxygen/nitrogen gas flow (20 mL/min) at a heating rate of 2 K/min.

Nitrogen Sorption: Samples were degassed at 120 °C for 12 h prior to measurement. Nitrogen (N_2) adsorption−desorption isotherms were recorded using 34 data points for both adsorption and desorption branches. The BET surface area[167] of each sample was calculated

using the multipoint BET method based on five selected points in the linear region of the isotherm.

Raman Spectroscopy: Raman spectra were acquired using a Renishaw InVia confocal Raman microscope with a 532 nm excitation laser. The laser power was maintained at 0.5 mW, and at least three different spots were analyzed to assess sample homogeneity.

FTIR: FTIR measurements were performed using a Spectrum Two FTIR spectrometer (PerkinElmer) at resolutions of 8 and 16 cm^{-1} over 20 scans, covering the spectral range from 400 to 4000 cm^{-1}.

Microscopy: The morphology of the MoS_2-based materials was examined by SEM using a field emission SEM (Crossbeam x340, Zeiss) operated at 5 kV. TEM was performed on a Talos F200i (Thermo Fisher Scientific, formerly FEI) at an accelerating voltage of 80 kV. For TEM sample preparation, the powders were gently ground with a pestle and mortar, and a carbon-coated Formvar film on a copper TEM grid was carefully rubbed onto the fine powder. EDX spectroscopy was carried out using Bruker DualX windowless detectors in scanning TEM (STEM) mode with a HAADF detector to provide spatially resolved elemental composition.

Elemental Analysis: The sulfur (S) to molybdenum (Mo) ratio was determined using an inductively coupled plasma–optical emission spectrometer (ICP-OES, SPECTRO ARCOS, AMETEK). The instrument was initially calibrated using 1000 mg/L ICP standard solutions for S and Mo (Merck). Approximately 20–35 mg of MoS_2-based powder was digested in 4 mL of aqua regia using a Mars 6 microwave digestion system (CEM) with One-Touch technology.

XPS: XPS measurements were conducted in a SPECS UHV system (FOCUS 500) equipped with a monochromatic Al Kα source (hv = 1486.6 eV) and a PHOIBOS 150 hemispherical analyzer with a 2D DLD detector (Surface Concept). High-resolution spectra were collected at 200 W (12 kV) with a pass energy of 30 eV and a step size of 0.1 eV. Spectral fitting was performed using CasaXPS software (employing a Shirley background and GL(30) line shape), with calibration based on the C–C/C–H sp^3 signal at 284.8 eV.[187]

4.2.3. Electrode Preparation and Electrochemical Characterization

Electrode Fabrication: A slurry was prepared by mixing the active material (pristine MoS_2 or HDT-functionalized MoS_2), CB, and PVDF in a weight ratio of 8:1:1. Initially, the MoS_2-based powders and CB were ground together using a pestle and mortar. The mixture was then transferred to a small container, and a 2 wt.% PVDF solution in NMP was added. The slurry was homogenized using a speed mixer (ARE-250, Thinky) at 1000 rpm for 10 minutes. The resulting slurry was coated onto carbon-coated aluminum foil using a doctor blade (wet film

thickness of 90 µm) and dried overnight at 80 °C to remove the NMP solvent. Circular electrodes (12 mm diameter) were punched from the dried film and further dried overnight at 80 °C before transfer to an argon-filled glovebox. The mass loading of MoS_2 of electrodes is between 0.9 and 1.2 mg/cm^2. Mass normalizations refer to the 80 wt.% of active material within the electrodes, omitting the mass of inactive PVDF binder and CB.

Cell Assembly and Electrochemical Testing: Metallic lithium discs (14 mm, Honjo) served as the negative electrodes. 2032-type coin cells (Hohsen) were assembled inside a glovebox (MBraun; O_2, H_2O < 0.5 ppm), incorporating a 1 mm thick stainless steel spacer, a stainless steel spring, and a glass microfiber separator (Whatman grade GF/A). Each cell was filled with 120 µL of LP30 electrolyte (1 M $LiPF_6$ in a 1:1 volumetric mixture of EC and DMC (Solvionic)).

CV and GCD tests were performed using potentiostats (Bio-Logic VMP 3-e and VMP300) within a potential window of 1.0 to 3.0 V versus Li^+/Li at 20 °C (Binder temperature-controlled chambers). Long-term cycling tests were conducted at a current density of 0.1 A/g.

EIS: EIS and in situ EIS measurements were performed using a three-electrode setup. For the three-electrode cell (T-cell, Swagelok), the WE (MoS_2-based material on Al foil), the CE (Li), and a glass microfiber separator (Whatman grade GF/D, 12 mm diameter) were assembled. A lithium reference electrode was positioned centrally in the T-cell, separated from the other electrodes by an 8 mm GF/D membrane. Initially, 120 µL of LP30 electrolyte was added between the working and counter electrodes, followed by an additional 120 µL beneath the reference electrode. The SPEIS technique was used for in situ analysis at various states of charge. A total of 21 EIS spectra were collected during each cathodic and anodic cycle over a potential range of 3.0 to 1.0 V (vs. Li^+/Li), with a frequency range from 1 MHz to 10 mHz. Each frequency point was averaged three times, increasing logarithmically.

4.2.4. Computational Details

Density functional theory (DFT) calculations were performed using QUANTUM ESPRESSO with orthogonal norm-conserving Vanderbilt (ONCV) pseudopotentials, utilizing the Perdew-Burke-Ernzerhof (PBE) exchange-correlation functional from the PseudoDojo library.[188–190] For long-range dispersion corrections, the semiempirical vdW correction by Grimme with zero damping (PBE+D3) was applied consistently throughout all calculations.[191] The convergence criteria for total energy and forces were set at 10^{-6} Ry and 10^{-4} Ry bohr^{-1} or better, respectively. The Brillouin zone was integrated using a uniform reciprocal distance of 0.05 Å^{-1}, resulting in Γ-centered (4 × 4 × 2) k-point grids for the bulk MoS_2 (2 × 2 × 2) supercell. To simulate various d-spacings in MoS_2, each MoS_2 sheet was fixed with varied interlayer distances. For electronic structure calculations, self-consistent calculations were performed with twice denser k-point

grids in the irreducible Brillouin zone. The climbing image nudged elastic band (CI-NEB) combined with dynamic nudged elastic band (dyNEB) method was employed to investigate Li^+ mobility within the system.[192,193] A (2 × 2 × 2) supercell was used for all calculations throughout this study. For the Li^+ mobility study, simulations were converged better than f max < 0.08 eV/Å.

4.3. Transition of Nanoconfinement Design to Micron-Sized Architectures

4.3.1. Material Synthesis

For the preparation of chemically pre-lithiated, exfoliated and partially restacked, and HDA-functionalized MoS_2, 1g of commercial MoS_2 powder (Sigma-Aldrich, <2 µm, 98% purity) was chemically lithiated using n-butyllithium (*n*-BuLi, 1.6 M in hexane, Fisher Scientific). The MoS_2 powder was dispersed in 25 mL of hexane in a glass vial using magnetic stirring (500 rpm). Subsequently, 4.25 mL of *n*-BuLi solution (1.6 M in hexane, corresponding to ca. 1.1 Li per MoS_2) was added under the same stirring conditions. The suspension was maintained at 50 °C for 48 hours inside an Ar-filled glovebox (O_2, H_2O < 0.5 ppm).

A vial containing the suspension was then moved to a fume hood for washing and filtering. The resulting lithiated MoS_2 (Li_xMoS_2) was collected by vacuum filtration using a 0.22 µm hydrophilic polytetrafluoroethylene (PTFE) membrane (Millipore), washed thoroughly with hexane, and dried under vacuum to remove residual hexane.

For exfoliation, 200 mg of dried Li_xMoS_2 was dispersed in 100 mL of deionized (DI) water and stirred for 30 minutes, followed by 10 minutes of bath sonication. The resulting suspension was filtered, rinsed with DI water and ethanol, and then redispersed in 30 mL of DI water by hand-shaking and an additional 5 minutes of bath sonication. The suspension was frozen in liquid nitrogen and subsequently freeze-dried (Alpha 3-4 LSCbasic, Martin Christ) for 72 hours to yield exfoliated and partially restacked MoS_2 powder, labelled MoS_2-restack.

For the pillaring of 1,6-hexanediamine (HDA) molecules into MoS_2 layers, 25 µL of 60 wt.% aqueous HDA solution (Fisher Scientific) was added to 100 mL of deionized (DI) water. Subsequently, 200 mg of Li_xMoS_2 powder was dispersed in this solution, corresponding to a 1:0.1 molar ratio between MoS_2 and HDA, followed by 5 minutes of bath sonication and continuous stirring for 48 hours at ambient temperature.

After the reaction, the HDA-functionalized MoS_2 samples were vacuum-filtered and rinsed with DI water and ethanol to remove residual species. The resulting slurry was prepared using the same redispersion procedure as the exfoliated MoS_2 sample. The suspension was subsequently frozen and freeze-dried under the same conditions to obtain MoS_2-HDA powders.

4.3.2. Material Characterization

The crystalline structure of the synthesized powders was analyzed by X-ray diffraction (XRD) in Bragg-Brentano geometry using a Bruker D8 Advance diffractometer with Cu Kα radiation

source (λ = 1.5406 Å) and a LYNXEYE XE-T detector. Patterns were collected with a step size of 0.02° and a dwell time of 1 s.

Raman spectra were recorded to evaluate phase and structural changes using a Renishaw InVia confocal Raman microscope equipped with a 532 nm excitation laser. To prevent thermal degradation of the samples, the laser power was restricted to 0.5 mW, and spectra were averaged from at least three distinct sample locations.

Fourier transform infrared spectroscopy (FTIR) measurements were performed using a Spectrum Two FTIR spectrometer (PerkinElmer) at resolutions of 8 and 16 cm^{-1} over 20 scans, covering the spectral range from 400 to 4000 cm^{-1}.

Thermal stability and organic content were quantified via thermogravimetric analysis (TGA) using a Netzsch TG 209 F1 Libra analyzer. Samples were heated at a rate of 5 K min^{-1} under a flow of oxygen and nitrogen (1:1 ratio, 20 mL min^{-1}).

Nitrogen adsorption-desorption isotherms were measured at 77 K using a volumetric gas sorption analyzer (Quadrasorb, Quantachrome, Anton Paar). Prior to the measurement, samples were degassed for 24 h at 100 °C under vacuum (~0.02 mbar). The specific surface area was calculated using the Brunauer-Emmett-Teller (BET) method within a relative pressure range of $0.05 < p/p_0 < 0.2$ using ASiQwin software, Quantachrome.

Particle morphology was analyzed using a field emission scanning electron microscope (SEM, Zeiss Crossbeam x340) at an accelerating voltage of 5 kV.

Surface chemistry and oxidation states were probed by X-ray photoelectron spectroscopy (XPS) using a SPECS UHV system (FOCUS 500) with a monochromatic Al Kα source (*hv* = 1486.6 eV) and a PHOIBOS 150 hemispherical analyzer with a 2D DLD detector (Surface Concept). High-resolution spectra were recorded at a pass energy of 30 eV with a 0.1 eV step size. Surface charging was compensated during XPS acquisition using an electron flood gun operated at 5 eV and 2.5 µA. Data analysis was performed using CasaXPS software, applying a Shirley background and GL(30) line shape, with binding energies calibrated to the C–C/C–H sp^3 reference at 284.8 eV.

4.3.3. Electrode Preparation and Electrochemical Characterization

Standard Coin Cell Electrode Fabrication: A slurry was prepared by mixing the active material (bulk or HDA-functionalized MoS_2), carbon black (CB, Imerys, C-NERGY Super C65), and polyvinylidene difluoride (PVDF, Solvay, Solef 6020) in a weight ratio of 8:1:1. First, the MoS_2-based powders and CB were homogeneously ground together using a pestle and mortar.

This dry mixture was then transferred to a container, and a 2 wt.% PVDF solution in N-methyl-2-pyrrolidone (NMP, Sigma-Aldrich, 99.5 %) was added. The resulting slurry was homogenized using a speed mixer (ARE-250, Thinky) at 1000 rpm for 10 minutes.

The slurry was coated onto carbon-coated battery-grade aluminum foil (20 µm, Wellcos) using a doctor blade (wet film thickness: 90 µm) and dried overnight at 80 °C to remove the NMP solvent. Circular electrodes (12 mm diameter) were punched from the dried film and transferred to an argon-filled glovebox. The mass loading of the MoS_2 electrodes was maintained between 0.8 and 1.2 mg cm^{-2}. We purposefully employed electrodes with relatively low mass loadings to study intrinsic materials properties and minimize limitations imposed by the electrode architecture. Mass normalizations for electrochemical metrics refer to the active material, that is, MoS_2 and pillars combined, but omitting the mass of the inactive PVDF binder and CB additive.

Electrodes for Operando Experiments: A separate electrode formulation was prepared for operando XRD and electrochemical dilatometry (ECD) experiments, consisting of 60 wt.% active material, 30 wt.% CB, 10 wt.% PVDF dissolved in NMP. The mixture was stirred overnight on a stirring plate at room temperature to ensure homogeneous mixing. This prevented large polarization in (non-ideal) operando cells.

For operando XRD, the slurry was drop-casted onto a Ti mesh current collector and dried overnight in an oven at 80 °C. The dried electrodes were subsequently pressed under 1 ton using a hydraulic press (Spcac).

For ECD, the slurry was cast directly onto the stainless steel plunger of the dilatometer (which served as the current collector) and dried overnight at 80 °C. A final pressing step of 2 tons was applied to the dried electrode using the hydraulic press.

Cell Assembly and Electrochemical Testing: 2032-type coin cells (Hohsen) were assembled in an argon-filled glovebox (MBraun; O_2, H_2O < 0.5 ppm). Metallic lithium discs (14 mm diameter, Honjo) served as the negative electrodes. The cell components included a 1 mm thick stainless steel spacer, a stainless steel spring, and a glass microfiber separator (Whatman grade GF/A).

Two distinct electrolytes were prepared for this study. The carbonate-based electrolyte consisted of 1M Lithium bis(trifluoromethanesulfonyl)imide (LiTFSI, Sigma-Aldrich, 99.95 %) salt dissolved in a 1:1 volumetric ratio of ethylene carbonate (EC, Sigma-Aldrich, ≥99 %) and dimethyl carbonate (DMC, Thermo Scientific, 99+ %). The ether-based electrolyte was prepared by dissolving 1M LiTFSI in diethylene glycol dimethyl ether (2G, Sigma-Aldrich, 99.5 %). We used the TFSI-based salt because of its solubility across several solvents. All

electrolyte mixtures were prepared and stirred overnight in the glovebox (O_2, H_2O < 0.1 ppm). Each coin cell was filled with 120 µL of either the carbonate- or ether-based electrolyte.

Electrochemical tests were performed using potentiostats (Bio-Logic VMP3-e and VMP300). Cyclic voltammetry (CV) and galvanostatic charge/discharge (GCD) tests were conducted within a potential window of 1.0 to 3.0 V versus Li^+/Li at a controlled temperature chamber at 20 °C (Binder). Long-term cycling performance was evaluated at a constant specific current of 0.1 A g^{-1}.

For operando XRD experiments, a customized operando 2032-coin cell design with central windows was utilized. These cells featured 4 mm diameter central holes in both the negative and positive caps, which were sealed with Kapton tape, and a spacer with a 4mm diameter central hole. The overall procedure for the XRD cells matched that of the standard coin cells, but the electrolyte volume was increased to ca. 200 µL. The fabricated cells were mounted in a STADI-p diffractometer (STOE) equipped with a coin cell holder, utilizing a silver X-ray source (Ag K_α = 0.5594074 Å) for the experiment.

For ECD measurements, a high-resolution electrochemical dilatometer (ECD-4-nano, EL-CELL) was assembled in the Ar-filled glovebox. Li metal (8 mm diameter) served as the counter electrode, with a GF/A separator (10 mm diameter) positioned between the Li electrode and a glass T-Frit. Approximately 300–350 µL of electrolyte was injected onto the T-Frit, and the working electrode, coated directly onto the plunger, was placed on top of the T-Frit. The cell was sealed using the screw cap unit with a membrane to ensure airtightness and electrical contact. Following transfer from the glovebox, the sensor head was attached, and the cell was connected to a docking station (PAT-Stand-1, EL-CELL) housed in a temperature-controlled chamber at 22 °C and connected to a potentiostat (Bio-Logic VMP3).

Computational Details: For the isolated diglyme (2G) and Li^+-2G clusters, initial geometry optimization was performed using density functional theory (DFT) in ORCA[194] with the B3LYP functional.[195,196] The pre-optimized cluster structures were then used as input for Quantum Espresso simulations of 2G, Li^+-(2G), and Li^+-$(2G)_2$ intercalated 1T-MoS_2. All QE calculations employed orthogonal norm-conserving Vanderbilt (ONCV) pseudopotentials from the PseudoDojo library,[190] with the Perdew-Burke-Ernzerhof (PBE) exchange–correlation functional.[188] Long-range dispersion interactions were treated using Grimme D3 van der Waals correction with zero damping (PBE+D3),[191] applied throughout all QE calculations. Structure optimization was carried out in a (4×4×1) supercell, where Mo atoms were kept fixed within the layer plane, while interlayer distances and guest species were fully relaxed. The Brillouin zone was sampled using Γ-centered k-point grids generated from a uniform reciprocal-space spacing of 0.05 $Å^{-1}$ (equivalent to a 2×2×4 grid for the 4×4×1 MoS_2 supercell). Structural

relaxation convergence thresholds were set to 10^{-6} Ry for total energy and 10^{-4} Ry/bohr (or tighter) for forces. Then, the XRD spectra of the DFT-simulated MoS_2 variants were calculated via VESTA with Ag $K\alpha_1$ wavelength of 0.5594 Å.[197] Here, to examine the structural influence of trapped solvated Li species on the host interlayer spacing, a neutral Li-2G complex was employed as a simplified model in the periodic calculations, focusing on the steric and local coordination effects governing interlayer expansion.

Chapter 5: Results and Discussion

The results discussed in this chapter have been published or are in preparation for submission:

Chapter 5.1 (Study I): [95]

Jaehoon Choi, Hyein Moon, Simon Fleischmann:

Simultaneous Control of Crystallite Size and Interlayer Spacing of MoS_2 to Achieve Pseudocapacitive Lithium Intercalation, *Electrochimica Acta*, 2024, 476, 143774.

Contribution: J.C. conceptualized the study, performed synthesis and characterization (excluding XPS), analyzed data, and wrote the manuscript.

Chapter 5.2 (Study II): [96]

Jaehoon Choi, Kyeonghyeon Nam, Yoga T. Malik, Robert Leiter, Maider Zarrabeitia, Christoph Scheurer, Simon Fleischmann:

Interlayer Spacing Control of MoS_2 with Covalent Thiol Functionalization: Understanding Structure and Electrochemistry from Experiments and Simulation, *ACS Nano*, 2025, 19, 40, 35425-35437

Contribution: J.C. designed the study, conducted experiments (excluding XPS acquisition & DFT), analyzed data (excluding EIS fittings), and wrote the manuscript.

Chapter 5.3 (Study III):

Jaehoon Choi, Pakornrum Tulaphon, Franz Jacobi, Kyeonghyeon Nam, Jameela Karol, Mete B. Durukan, Christoph Scheurer, Desirée Leistenschneider, Simon Fleischmann:

Understanding Solvent-Dependent Electrochemistry in Interlayer Expanded MoS_2: Role of Nanoconfinement Tuned by Organic Pillars, *in preparation*.

Contribution: J.C. conceptualized the study, performed all synthesis and characterization (excluding operando XRD acquisition), analyzed data, and wrote the manuscript.

5.1. Simultaneous Control of Crystallite Size and Interlayer Spacing of MoS_2 to Achieve Pseudocapacitive Lithium Intercalation

A one-pot hydrothermal synthesis strategy for MoS_2 is developed that allows to simultaneously control both the crystallite size and geometric nanoconfinement environment (i.e., interlayer distance and guest species density) of the material. Pristine MoS_2 is obtained following a hydrothermal process outlined by Geng et al.,[123] and the particle size is controlled by adjusting the pH of the precursor solution, with more acidic conditions yielding smaller particle sizes. The obtained MoS_2 materials then allow us to study the influence of particle size on the electrochemical lithium intercalation properties. To analyze the impact of interlayer distance on lithium intercalation, MoS_2 materials with the same particle size, but varied interlayer distances are synthesized by facile adaptation of the one-pot route with added HDA molecular pillars to the precursor solution (**Fig. 5.1**). Finally, variation of the HDA concentration allows to determine the influence of pillar population in the MoS_2 interlayer space (nanoconfinement chemistry) on lithium intercalation properties, while particle size and interlayer distance are kept constant. Particular emphasis is put on obtaining and characterizing model materials with well-defined structural properties, allowing to individually study the impact of a single structural parameter on the lithium intercalation process.

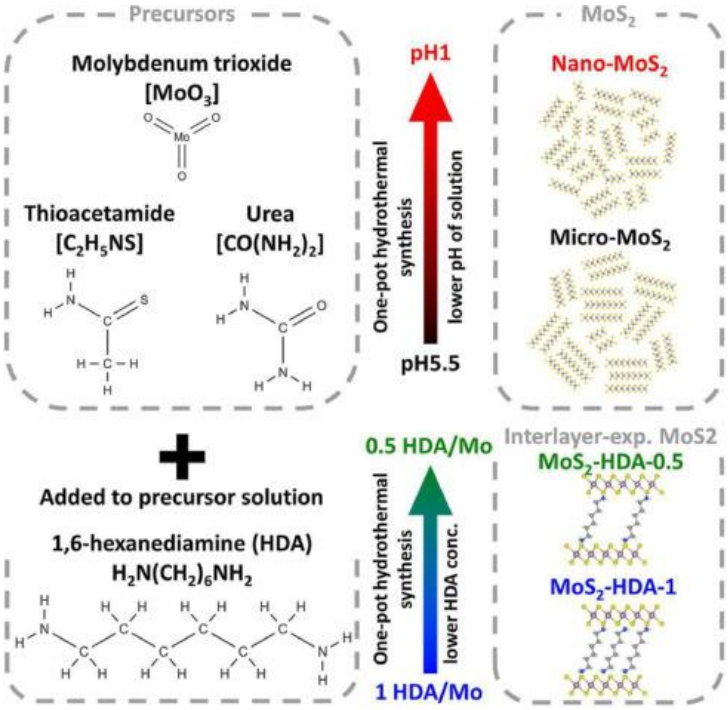

Figure 5.1: Schematic illustration of the one-pot hydrothermal synthesis of MoS_2-based materials.

5.1.1. Influence of Crystallite Size

5.1.1.1. Structural Characterization

Two MoS_2 samples are synthesized from precursor solutions with controlled pH value with the goal to achieve a variation in product crystallite size. Small and large particle/crystallite sizes of the MoS_2 products are obtained from hydrothermal processes with aqueous precursor solutions of pH 1 and pH 5.5, and labelled nano-MoS_2 and micro-MoS_2, respectively.

SEM images of the products show the formation of larger secondary particles consisting of agglomerates of flake-shaped primary particles, with several microns of secondary particle size for nano-MoS_2 (**Fig. 5.2A**) and tens of microns for micro-MoS_2 (**Fig. 5.2B**). The differences in primary particle sizes are revealed at higher magnification, with nano-MoS_2 exhibiting lateral dimensions of the 2D MoS_2 layers in the range of ca. 100 nm as well as a low thickness/number of layers well below 10 nm, as compared to micro-MoS_2 with lateral sizes around 500–1000 nm and a larger thickness (**Fig. 5.2A** and **5.2B**, insets). The observations from SEM are confirmed by DLS analysis, which can quantify the size of MoS_2 secondary particle agglomerates, revealing that the average size of the nano-MoS_2 agglomerates is around 8 µm and that of micro-MoS_2 is around 26 µm (**Fig. S1A**).

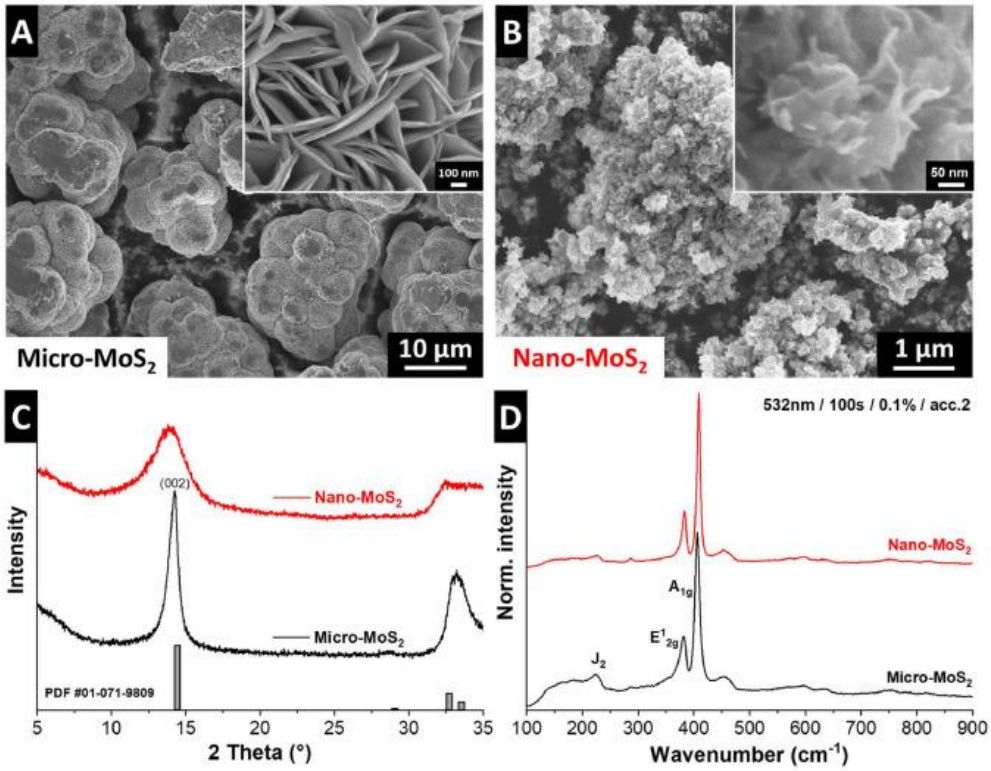

Figure 5.2: SEM images of MoS_2 synthesized (A) at pH 5.5 yielding micro-MoS_2, and (B) at pH 1 yielding nano-MoS_2. (C) XRD patterns including the ideal positions of hexagonal 2H-MoS_2 according to PDF card #01-071-9809 and (D) Raman spectra of both samples.

XRD is utilized to assign the crystal structure of the synthesized materials as hexagonal 2H-MoS_2 according to PDF card #01-071-9809 (**Fig. 5.2C**). The interlayer distance is identified according to the (002) signal at ca. 13.9° 2θ as 6.15 Å for both nano-MoS_2 and micro-MoS_2 samples. A significant peak broadening of the (002) peak at 13.9° for nano-MoS_2 is a further qualitative confirmation of the reduced crystalline domain size compared to micro-MoS_2.[198] Raman spectra of the two samples (**Fig. 5.2D**) show the two main characteristic peaks at 382 and 406 cm^{-1}, which correspond to E^1_{2g} and A_{1g} vibrational modes of the semi-conducting (2H) phase.[199] The results confirm that the employed hydrothermal synthesis route leads to the formation of 2H-MoS_2,[123] independent of crystallite size.

Overall, the structural investigation of nano-MoS_2 and micro-MoS_2 reveals that adjusting the pH of the precursor solution for the hydrothermal process to pH 1 or pH 5.5 is a suitable route to obtain 2H-MoS_2 materials with small or large crystallite sizes, respectively. The strategy thus allows to obtain model materials to study the influence of crystallite size on the lithium intercalation properties.

5.1.1.2. Electrochemical Characterization

To understand the influence of the crystallite size of hydrothermally synthesized MoS_2 materials on electrochemical lithium intercalation behavior, the samples are investigated in a standard, lithium-containing organic electrolyte (1 M $LiPF_6$ in EC/DMC, LP30) using CV. The potential range is selected from 1.0 to 3.0 V vs. Li^+/Li, allowing to study the Li^+ intercalation reaction according to

$$MoS_2 + xLi^+ + xe^- \leftrightarrow Li_xMoS_2,\ 0 \leq x \leq 1, \qquad (15)$$

with a theoretical capacity of 167 mAh/g (for $x = 1$), without occurrence of the conversion-type reaction below 1.0 V vs. Li^+/Li.[200] The CV profiles of micro-MoS_2 and nano-MoS_2 are presented in **Fig. 5.3A** and **5.3B**. At low sweep rates (up to ca. 1 mV/s), both samples reveal the presence of a redox signal centered around 1.7 V vs. Li^+/Li (cathodic sweep) and 1.9 V vs. Li^+/Li (anodic sweep), indicative of the Li^+ (de)intercalation reaction. For micro-MoS_2, it is visible that the signal is split into two separate peaks, while for nano-MoS_2, the signal is significantly broadened with the peaks apparently merging and a more significant rectangular current emerging. This behavior is indicative of an increasingly pseudocapacitive Li^+ intercalation behavior with decreasing crystallite size in nano-MoS_2, in line with previous reports.[97,98,201] Accordingly, at higher sweep rates above 10 mV/s, the CV signature of micro-MoS_2 rapidly becomes resistive, indicative of diffusion-limitations, while even at 100 mV/s, a capacitor-like

CV signal can be observed for nano-MoS_2 in line with kinetically favorable pseudocapacitive Li^+ intercalation.[36]

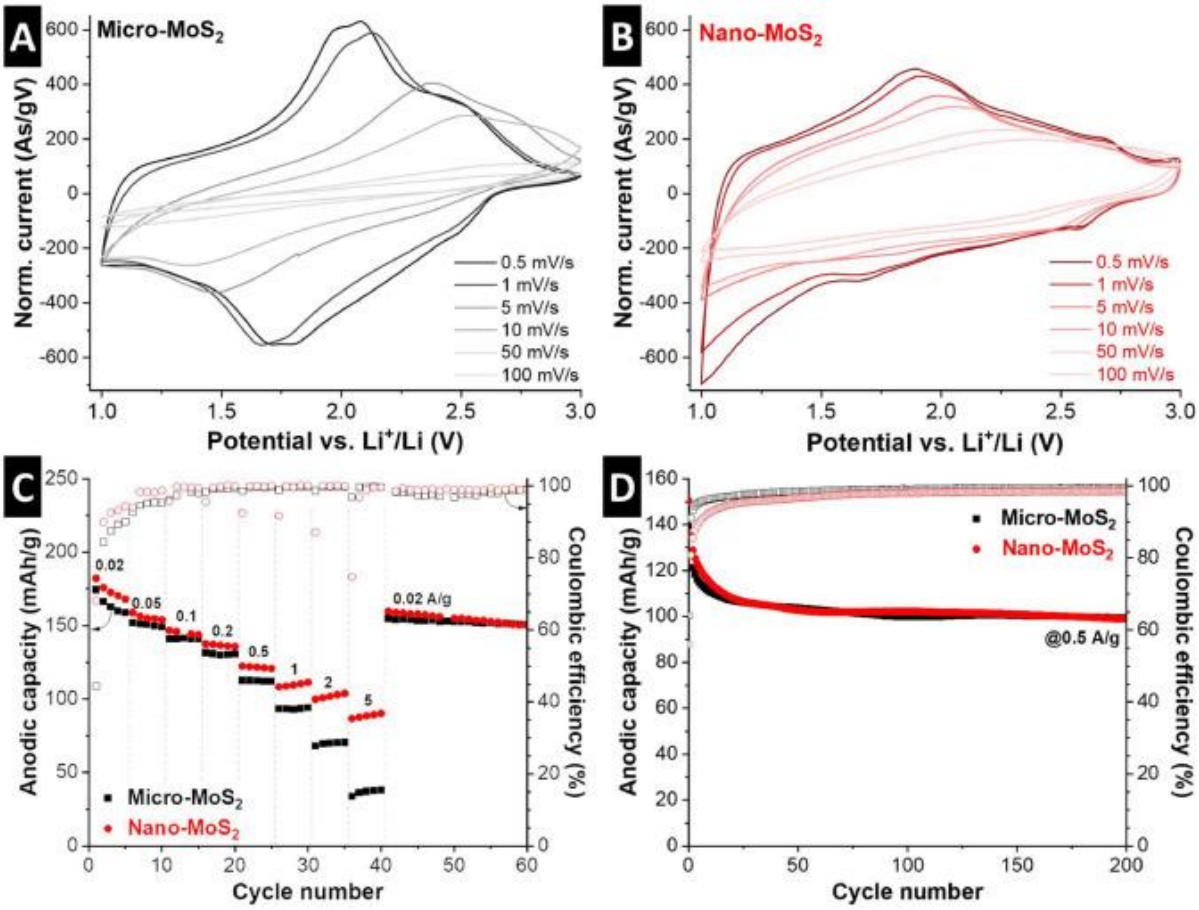

Figure 5.3: Cyclic voltammograms of (A) micro-MoS_2 and (B) nano-MoS_2 at sweep rates from 0.5 to 100 mV/s. (C) GCD experiments at constant specific currents from 0.02 to 5 A/g and (D) galvanostatic cycling stability at a constant specific current of 0.5 A/g of both MoS_2 samples. All experiments were carried out at 20 °C in coin cells against lithium metal in LP30 electrolyte.

GCD tests are performed at constant specific currents between 0.02 and 5 A/g (**Fig. 5.3C**). At the lowest rate of 20 mA/g, both MoS_2 samples show a comparable first cycle anodic (delithiation) capacity of 175 and 182 mAh/g for micro-MoS_2 and nano-MoS_2, respectively, slightly above the theoretical capacity of 167 mAh/g for Li_xMoS_2 with $x = 1$. At higher rates, specifically above 1 A/g, nano-MoS_2 delivers significantly higher capacities due to the reduced kinetic limitations by solid-state diffusion, confirming the CV results. Nano-MoS_2 still exhibits a capacity of 90 mAh/g at a high rate of 5 A/g, which corresponds to a charge/discharge time of ca. 1 min, while micro-MoS_2 only exhibits 38 mAh/g. These values are quantitatively comparable to a study of Cook et al., probing lithium intercalation in bulk versus nanostructured MoS_2, where the latter was prepared by thermal sulfurization of nanostructured MoO_2 in H_2S.[98]

Galvanostatic cycling stability is tested at an intermediate rate of 0.5 A/g (**Fig. 5.3D**). A capacity drop in the initial 15 cycles can be observed, before both samples stabilize at around 105 mAh/g. This capacity remains relatively stable, reaching around 100 mAh/g after 200 cycles. We hypothesize that the initial capacity drop can be related to the ongoing phase transformation from semiconducting 2H to metallically conducting 1T phase of MoS_2 during initial lithiation cycles that has been described before.[98] To complete the phase transformation, it was reported that 4–8 cycles may be necessary depending on the MoS_2 crystallite size,[98] which is reflected in the reduced Coulombic efficiency and capacity drop at low rates (**Fig. 5.3C**) as well as at higher rates (**Fig. 5.3D**) during the initial cycles. Hence a route to improve cycling stability could be utilizing fully 1T-transformed MoS_2.

It can be concluded that hydrothermally synthesized MoS_2 materials with facile crystallite size control *via* pH in this study show good agreement with the reported electrochemical performance of MoS_2 synthesized by other (more complex) approaches. In line with the initial goal of a multi-length scale control of MoS_2 structure, the next step is to further develop the best-performing nano-MoS_2 material on a microscopic, crystal structure level.

5.1.2. Influence of Interlayer Distance

5.1.2.1. Structural Characterization

Building on the one-pot hydrothermal synthesis route outlined in the previous section, the precursor solution of nano-MoS_2 is adapted to additionally achieve microscopic control over the MoS_2 crystal structure to further improve the electrochemical performance. This is done *via* the addition of pillar molecules, namely HDA, which we hypothesize will expand the interlayer space of MoS_2, modulating its geometric nanoconfinement environment. By using two different concentrations of HDA in the precursor solution (molar ratios of HDA/Mo of 1 and 0.5), the density of pillars is aimed to be controlled.

SEM characterization reveals comparable morphology with nano-MoS_2 samples, with few-micron sized secondary particles consisting of smaller flake-like primary particles with a lateral size in the range of 100 nm (**Fig. 5.4A** and **5.4B**). Both MoS_2-HDA-1 and MoS_2-HDA-0.5 appear comparable to nano-MoS_2, indicating that the addition of HDA does not significantly affect the resulting MoS_2 morphology when the pH of the precursor solution remained at 1. Quantitative analysis *via* DLS confirms a comparable secondary particle size distribution with MoS_2-HDA-0.5 showing slightly reduced sizes (**Fig. S1B**).

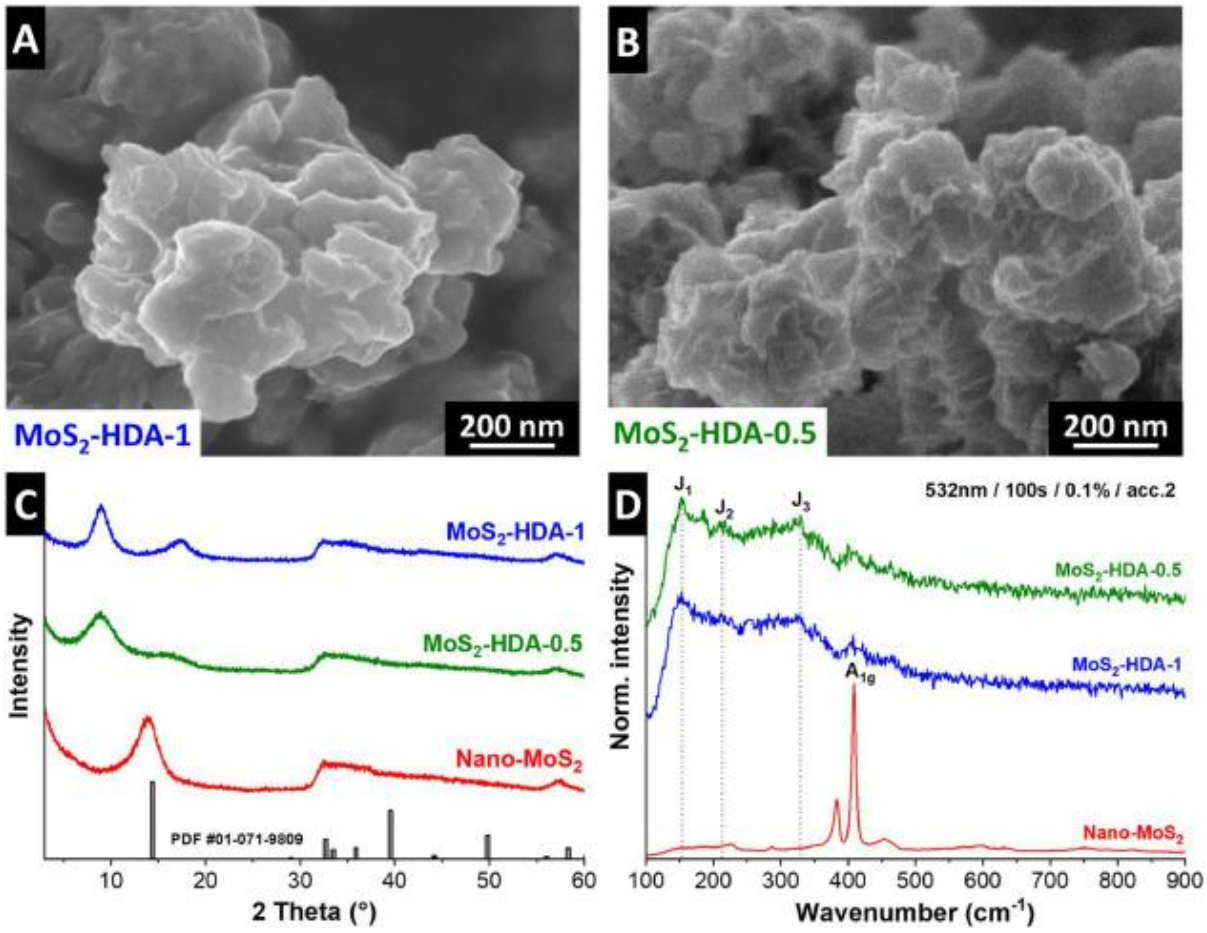

Figure 5.4: SEM images of interlayer-expanded MoS_2 using HDA pillars with precursor molar ratios of HDA/Mo of (A) 1:1 and (B) 0.5:1. (C) XRD patterns and (D) Raman spectra of a nano-MoS_2 (same as in Fig. 2C and D, for comparison), MoS_2-HDA-1, and MoS_2-HDA-0.5 samples.

XRD analysis shows the formation of MoS_2 with a shift of the (002) signal from 13.9° 2θ in nano-MoS_2 to 9.0° 2θ for both MoS_2-HDA-1 and MoS_2-HDA-0.5 samples (**Fig. 5.4C**). This confirms that the addition of HDA pillars to the precursor solution leads to the formation of interlayer-expanded MoS_2, with the (002) spacing expanding from 0.64 to 0.98 nm. The molecular conformation of HDA within the interlayer space has to be tilted with respect to the MoS_2 layers, considering an estimated length of HDA including its vdW radius of around 1.22 nm. While the Raman spectrum of nano-MoS_2 revealed the formation of the semiconducting 2H phase, the spectra recorded for MoS_2-HDA-1 and MoS_2-HDA-0.5 samples show a distinctly different signature (**Fig. 5.4D**). The spectra show the characteristic vibrational Raman modes J_1 at 153 cm^{-1}, J_2 at 213 cm^{-1}, J_3 at 329 cm^{-1}, and A_{1g} at 412 cm^{-1}.[199,202] The spectra indicate the formation of a distorted 1T phase of MoS_2 (1T' phase) upon the confinement of HDA pillars as guest species in the MoS_2 interlayer space. The distorted 1T phase (1T') can be distinguished from the ideal 1T phase *via* the presence of the A_{1g} mode at 412 cm^{-1} and the absence of the E_{2g} mode at 258 cm^{-1}.[199,203] We hypothesize that the 1T'

phase forms as a consequence of the confined interlayer guest species (i.e., HDA pillars), which has been described for hydrothermally synthesized MoS_2 materials with various organic guest species before.[204]

The HDA content of the samples is calculated from TGA under O_2-containing atmosphere that leads to a full burn-off of organic species (and concomitant MoS_2-to-MoO_3 transformation, **Fig. S2**). The calculated compositions for samples MoS_2-HDA-1 and MoS_2-HDA-0.5 are $(HDA)_{0.33}MoS_2$ and $(HDA)_{0.26}MoS_2$, respectively, confirming that the variation of HDA concentration in the precursor solution of the hydrothermal process can control the final composition of pillared MoS_2 to some extent. Furthermore, using FTIR, the presence of asymmetrical and symmetrical stretching vibrations of aliphatic C-H at 2915 and 2850 cm^{-1},[205] respectively, indicate that HDA does not decompose and remains intact under hydrothermal synthesis conditions (**Fig. S3A**). Additional verification is provided by the absence of D- and G-bands in their full Raman spectra, excluding the formation of amorphous carbon that would have resulted from HDA decomposition (**Fig. S3B**).

While the work mainly focuses on the interlayer-expansion of nano-MoS_2 because of its demonstrated superiority for electrochemical lithium intercalation, the generalizability of the one-pot hydrothermal synthesis approach is further demonstrated. By adjusting pH to 5.5, interlayer-expansion of micro-MoS_2 with HDA is successfully performed (**Fig. S4**). Furthermore, interlayer-expansion of nano-MoS_2 at pH 1 is also feasible with ODA and DDDA organic pillar molecules (**Fig. S5**).

TEM analysis of nano-MoS_2 and MoS_2-HDA-1 is carried out to obtain highly localized structural information of pristine versus interlayer-expanded MoS_2. The interlayer distances of both samples, as observed in the HRTEM images, closely align with the values obtained from XRD patterns, with 0.63 nm for nano-MoS_2 (**Fig. 5.5A**) and 1.00 nm for MoS_2-HDA-1 (**Fig. 5.5B**). The values can be confirmed by the diameter of first ring of the selected area electron diffraction (SAED) patterns. Furthermore, the second and third rings in the SAED patterns, corresponding to the (100) and (110) planes, are at identical positions for nano-MoS_2 and MoS_2-HDA-1. This indicates the absence of in-plane structural changes in the individual MoS_2 sheets upon addition of HDA pillaring molecules in the interlayer space. It suggests that the interlayer expansion, facilitated by HDA, does not affect the host structure beyond geometric expansion. Our findings are in contrast to previous studies that reported significant structural and chemical in-plane modification of MoS_2, such as nitrogen-doping *via* sulfur-substitution after the addition of pillaring molecules during hydrothermal synthesis.[204,206] Furthermore, the distribution of HDA pillars is analyzed via EDX in STEM, confirming a homogenous distribution of nitrogen throughout the sample (**Fig. S6**). It should be noted that

traces of nitrogen are also found in nano-MoS_2 (at much lower concentration, see **Table S1**), indicating small residues of thioacetamide and/or urea precursors.

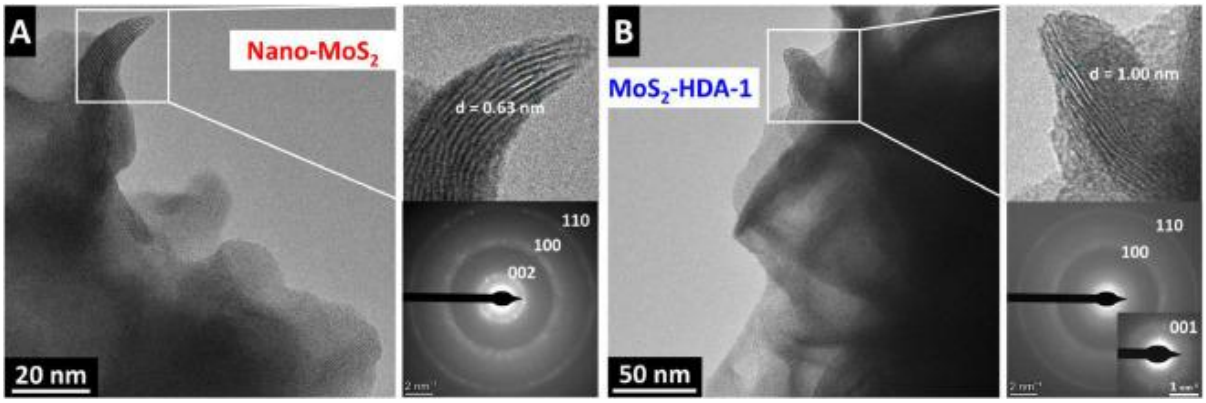

Figure 5.5: HRTEM images and selected area electron diffraction patterns (obtained at 80 kV to avoid electron beam damaging) of (A) nano-MoS_2 and (B) interlayer-expanded MoS_2-HDA-1 samples.

The interaction of HDA molecules with the MoS_2 host lattice is investigated via XPS. The Mo 3d and S 2p spectra of the MoS_2-based materials are displayed in **Fig. 5.6**. To analyze the possibility of covalent bonding between HDA molecules and interlayer-expanded MoS_2 host, the spectra of MoS_2-HDA-1 (as the sample with the highest HDA-content) are directly compared with those of pristine, nano-MoS_2. In **Fig. 5.6A**, the most intense signals of characteristic Mo^{4+} at around 229.0 eV and 232.4 eV are attributed to MoS_2.[207] Moreover, Mo^{4+} and Mo^{6+} from traces of precursor residue or/and oxidized MoS_2 at higher binding energies (i.e., MoO_3 and MoO_2)[208] are also present on the surface of the samples. However, the contributions are almost identical for both samples. The S 2p spectra in **Fig. 5.6B** include the MoS_2 related doublets at 162 eV and 163.1 eV, and the trace of organic sulfur (C=S) at 163.8 eV and 165 eV originating from the precursor (i.e., thioacetamide), suggesting precursor residues on the MoS_2 surface.[209] MoS_2-HDA-1 doublets in both regions show no apparent shifts in binding energy (BE) compared to the pristine nano-MoS_2 regardless of the interlayer-expansion found by XRD and TEM. Furthermore, the atomic concentration of each element acquired from survey data (**Fig. S7** and **Table S2**) also presents highly comparable to each other. The absence of any additional contribution to the XPS signals in MoS_2-HDA-1 compared to nano-MoS_2 is indicative of a purely physical interaction as opposed to covalent bonding of the amine group to the MoS_2 host lattice.[210] The results are in support of the electron diffraction results from TEM analysis that suggest no alteration of the in-plane MoS_2 structure in MoS_2-HDA-1 materials. Hence, the molecular pillaring approach *via* hydrothermal synthesis outlined in this work leads to MoS_2 with an expanded interlayer spacing with a purely physical host-pillar interaction in the absence of in-plane structural changes. This is significant for

the electrochemical analysis of the materials, because it allows for the electrochemical properties to be correlated with the expanded interlayer spacing, instead of being caused by a change in the MoS_2 in-plane structure.

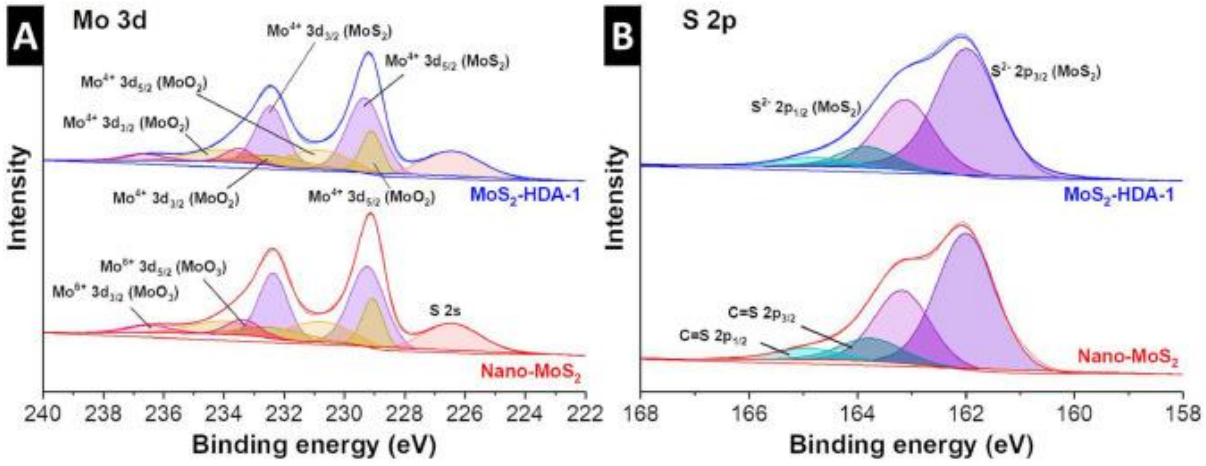

Figure 5.6: XPS of (A) Mo 3d region and (B) S 2p region of nano-MoS_2 and MoS_2-HDA-1 samples.

5.1.2.2. Electrochemical Characterization

The structural characterization of HDA-pillared MoS_2 materials demonstrates that the materials exhibit an expanded interlayer spacing compared to nano-MoS_2, while other structural properties like morphology, crystallite size and in-plane MoS_2 structure remained similar. Furthermore, the concentration of HDA pillars is increased in MoS_2-HDA-1 compared to MoS_2-HDA-0.5. Consequently, the materials can be used to study the influence of (1) interlayer spacing (i.e., nanoconfinement geometry) and (2) pillar concentration (i.e., nanoconfinement chemical composition) on the electrochemical lithium intercalation performance.

The potential profiles of the first five galvanostatic cycles of nano-MoS_2, MoS_2-HDA-1 and MoS_2-HDA-0.5 at a constant specific current of 20 mA/g are shown in **Fig. 5.7A–C**. For nano-MoS_2, a low initial Coulombic efficiency (ICE, 44 %) is observed, which is correlated to the above described 2H-to-1T phase transformation in the plateau region around 1.1 V vs. Li^+/Li during the first lithiation (**Fig. 5.7A**).[91] In comparison, both MoS_2-HDA-1 and MoS_2-HDA-0.5 exhibit higher ICEs of 65 % and 67 %, respectively, in the absence of the 2H-to-1T phase transformation plateau. Instead, they likely undergo a 1T'-to-1T transformation during the first lithiation (vide infra).[203]

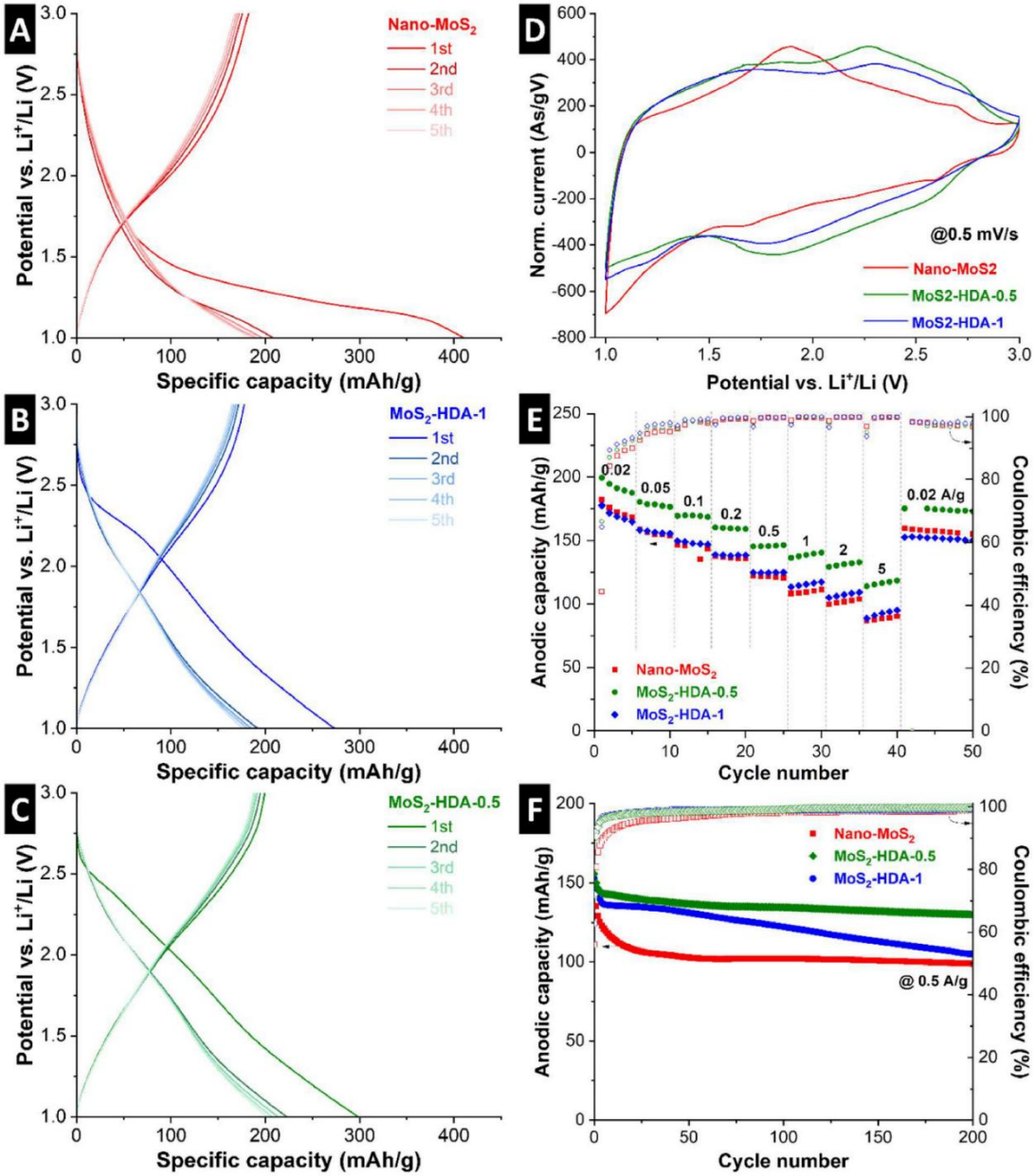

Figure 5.7: Galvanostatic profiles of the first five cycles of (A) nano-MoS_2, (B) MoS_2-HDA-1 and (C) MoS_2-HDA-0.5 at a constant specific current of 20 mA/g. (D) Cyclic voltammograms of the three samples at a sweep rate of 0.5 mV/s. (E) GCD experiments at specific currents from 0.02 to 5 A/g and (F) galvanostatic cycling stability at a constant specific current of 0.5 A/g of the three samples. All experiments carried out at 20 °C in coin cells against lithium metal in LP30 electrolyte.

The initial anodic (delithiation) capacities of nano-MoS_2 and MoS_2-HDA-1 are in the same range (182 and 178 mAh/g, respectively), while the delithiation capacity of MoS_2-HDA-0.5 is increased to 199 mAh/g. Given that these values are normalized to the full composite mass of MoS_2 and HDA, the capacities of HDA-pillared materials significantly exceed that of nano-

MoS_2 (1.09 Li^+) per transition metal, with 221 mAh/g_{MoS2} or 1.32 Li^+ per MoS_2-HDA-1 and 237 mAh/g_{MoS2} or 1.41 Li^+ per MoS_2-HDA-0.5. This is in line with previous reports of increased Li^+ storage in interlayer-expanded MoS_2 materials that potentially combines pseudocapacitive (Faradaic) Li^+ intercalation with an additional electric double-layer capacitance inside the widened interlayer galleries and/or at the solid/liquid interface.[137,144]

Cyclic voltammograms of interlayer-expanded MoS_2 electrodes show an increased capacitor-like, rectangular current profile and the absence of the broad redox peak around 1.7–1.9 V vs. Li^+/Li as compared to nano-MoS_2 (**Fig. 5.7D**). Given the lower content of electrochemically inactive HDA-pillars in MoS_2-HDA-0.5, its specific current signal has a slightly higher magnitude than MoS_2-HDA-1. The results indicate an increased pseudocapacitive Li^+ intercalation behavior of interlayer-expanded MoS_2 compared to nano-MoS_2. The lithiation process of MoS_2-HDA-1 results in a further expansion from 0.98 to 1.06 nm as indicated by *ex situ* XRD (**Fig. S8**), whereas lithiation of pristine MoS_2 is known not to lead to significant changes in d-spacing (changes < 0.01 nm for fully lithiated MoS_2 of various crystallite sizes and degrees of disorder).[105] This is indicative of a larger number or size of intercalating species into interlayer-expanded MoS_2, in line with the higher lithiation capacities measured for these samples ($Li_{1.32}$-MoS_2-HDA-1 and $Li_{1.41}$-MoS_2-HDA-0.5) compared to pristine MoS_2.

Quantitative GCD experiments (**Fig. 5.7E**) further underline the superior Li^+ intercalation performance of MoS_2-HDA-0.5 compared to the other samples. Its capacity retention of 118 mAh/g at a rate of 5 A/g corresponds to 63 % of the initial capacity (5th cycle at 20 mA/g) compared to 95 mAh/g for MoS_2-HDA-1 (58 %). The results underline that not only nanoconfinement geometry, i.e., an expanded interlayer spacing is beneficial for increased kinetics and storage capacity, but also the nanoconfinement chemical composition, i.e., the number of pillars determines electrochemical performance. The decreased number of pillars in MoS_2-HDA-0.5 not only reduces weight of (electrochemically) inactive component, but it is hypothesized that it is also beneficial for ion transport in the nanoconfined interlayer space.[211]

The Li^+ intercalation process is further analyzed via *b*-value analysis, where a *b*-value of 0.5 corresponds to diffusion-limited and a *b*-value of 1 to surface-limited intercalation kinetics (**Fig. S9**).[212] While decreasing of crystallite size shows an increase of the (cathodic) *b*-values from 0.85 for micro-MoS_2 to 0.93 for nano-MoS_2, the *b*-values for both MoS_2-HDA-0.5 and MoS_2-HDA-1 are also 0.93. Trends for the anodic *b*-values are similar. Overall, according to *b*-value analysis for sweep rates from 0.1 to 10 mV/s, there are no major differences in the kinetic limitations for all samples, with all of them exhibiting primarily surface-limited diffusion kinetics.[36]

Galvanostatic cycling stability over 200 cycles at 0.5 A/g is shown in **Fig. 5.7F**. While nano-MoS_2 shows a significant initial capacity decay described in the previous **Section 5.1.1.2**, this

initial decay is much smaller for both HDA-pillared samples. This can be explained by the absence of the 2H-to-1T transition for these samples, demonstrating the advantage of the 1T' phase formed for interlayer-expanded MoS_2. When comparing MoS_2-HDA-0.5 to MoS_2-HDA-1, the former shows significantly improved cycling stability. This is an indication that a reduced number of pillars confined in the interlayer space may be beneficial for cycling stability. The underlying mechanism and an investigation into the optimum number of pillars will be the topic of future investigation using operando techniques and post-mortem cryogenic TEM analysis.

5.1.3. Conclusions

This study introduces a versatile one-pot hydrothermal synthesis strategy that enables simultaneous control of MoS_2 structure over several length scales, ranging from macroscopic crystallite size to microscopic lattice parameter control. Lowering the pH of the precursor solution for hydrothermal synthesis leads to the formation of smaller crystallites. The addition of alkyldiamines like HDA to the same precursor solution will lead to their confinement between the forming MoS_2 layers, acting as structural pillars expanding MoS_2 interlayer spacing. By changing the HDA concentration, the content of structural pillars in interlayer-expanded MoS_2 can be varied to some extent. The interaction between HDA pillars and MoS_2 host is purely physical in the absence of covalent bonding, with no significant crystallographic changes in the MoS_2 in-plane structure after pillaring.

The influence of each structural parameter on the electrochemical lithium intercalation properties can be systematically studied. It is found that smaller crystallite sizes, as well as expanded interlayer spacing, both lead to increasingly pseudocapacitive Li^+ intercalation properties with a more and more capacitor-like CV shape. Among interlayer-expanded MoS_2 materials, reducing the number of confined HDA structural pillars leads to an improved specific capacity, rate capability and cycling stability. The number of lithium reversibly intercalated in per MoS_2 ranges from ca. 1 in micro-MoS_2 to up to almost 1.5 in MoS_2-HDA-0.5, emphasizing the importance of nanoconfinement properties of MoS_2 for electrochemical ion intercalation. Future work should also explore the influence of changes in pillar chemistry, for example, to trifunctional pillars which may further stabilize the expanded MoS_2 structure.

The materials described can also be of interest to field of multivalent ion intercalation, where expanded interlayer distances can enable reduced electrostatic interaction between ion and host. Furthermore, the materials can be of interest as hydrogen evolution electrocatalysts, where both an expanded interlayer distance and reduced crystallite size can increase the number of electrochemically active sites.

5.2. Interlayer Spacing Control of MoS_2 with Covalent Thiol Functionalization: Understanding Structure and Electrochemistry from Experiments and Simulation

This work explores covalent thiol functionalization for controlling MoS_2 interlayer spacing. Using a hydrothermal bottom-up synthesis, dithiolated molecules can be directly incorporated into the MoS_2 lattice to act as pillars. Using a comprehensive combination of experiments and simulation, we investigate the influence of dithiol pillar loading on the emerging structure, pillar–host interactions, and electrochemistry. Our results reveal clustering of pillars at low loading, leading to an inhomogeneous interlayer expansion. At high pillar loading, the formation of defective bonding configurations with excess sulfur is observed. Interlayer expansion leads to an increased electrochemical Li^+ storage capacity with a maximum of 1.43 Li^+ per MoS_2. However, dithiols occupy storage sites and impede Li^+ transport within the interlayer space, leading to unfavorable performance at high pillar loading. This underlines the importance of carefully adjusting the density of nanoconfined pillar molecules within the interlayer space. Overall, the work comprehensively analyzes covalent dithiol functionalization of TMD-based electrode materials, offering valuable insights for the design of advanced energy materials.

5.2.1. Structural Characterization of MoS_2-Based Materials

Fig. 5.8A schematically outlines our proposed materials design strategy, in which HDT are directly incorporated into the MoS_2 lattice where they act as organic pillar molecules that modify the nanoconfinement environment. The density of pillars is controlled by varying the molar ratio of pillar to Mo during hydrothermal synthesis between 0.2 and 5. The motivation behind this approach is to obtain a pillared MoS_2 structure with (1) covalent networks between host and pillar molecules and (2) a highly tunable pillar loading. This is a significant evolution from previous approaches that employed ionic pillars that weakly interact with the host lattice and exhibited limited variability in pillar loading.[64,95,213] The structural characterization is focused on determining how varying the HDT loading affects the resulting pillared architecture and analyzing the bonding character between HDT pillars and the MoS_2 lattice.

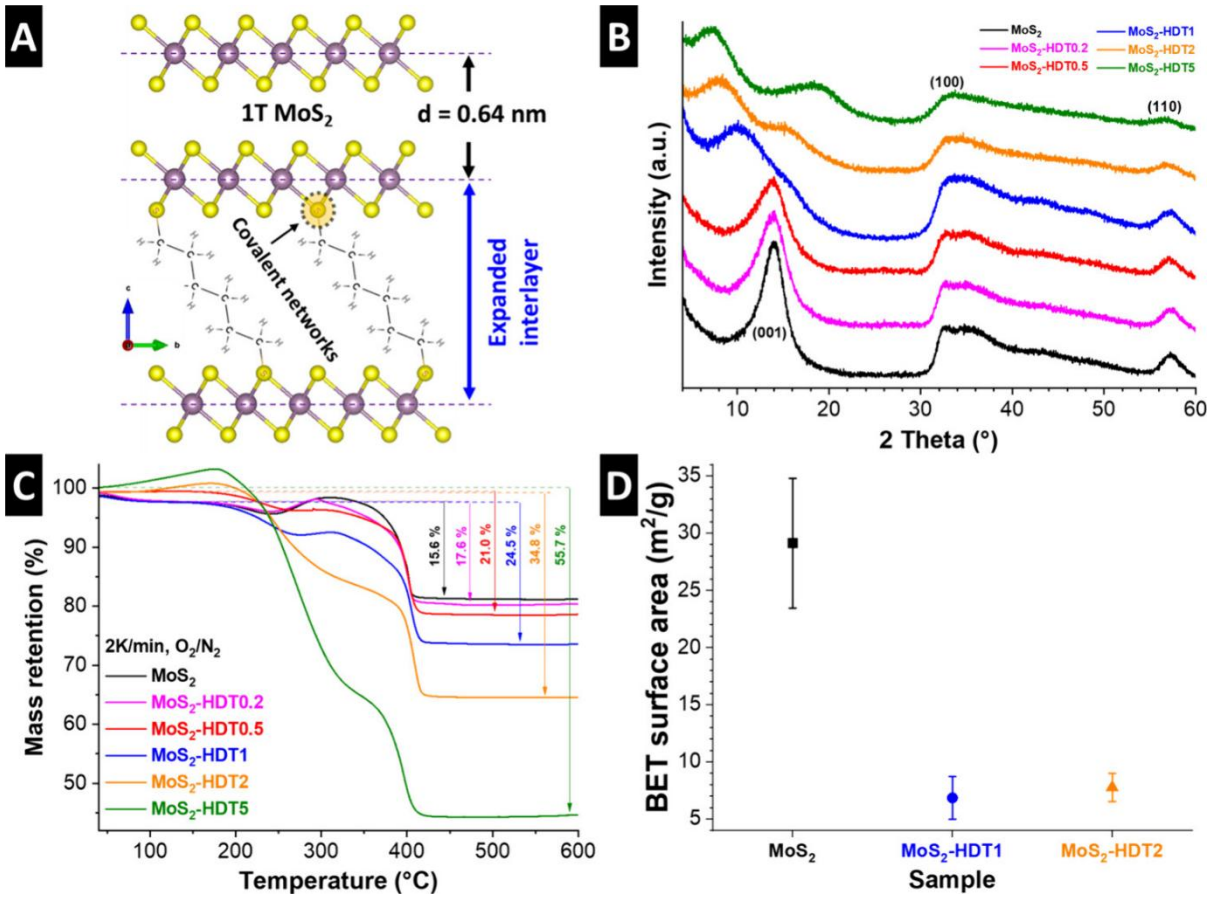

Figure 5.8: (A) Schematic illustration of the proposed formation of covalent networks between HDT pillars and MoS_2. (B) XRD patterns of the pristine and HDT-pillared MoS_2. (C) TGA curves and (D) BET specific surface area of MoS_2-based samples.

The structure of hydrothermally synthesized, MoS_2-based materials is initially investigated using XRD. The diffractograms of pristine and HDT-pillared MoS_2 materials with various HDT loadings are shown in **Fig. 5.8B**. The formation of pristine MoS_2 is verified by the broad reflexes centered at ca. 13.8° and 32.5° 2 Theta corresponding to the (001) and (100) planes of 1T-MoS_2, respectively, in line with previous work.[95] The addition of HDT in increasing quantities from 0.2 to 5 (molar ratio between pillar molecules to Mo during synthesis) causes changes in the diffractograms, predominantly related to the position and shape of the (001) signal representative of the interlayer spacing. With increasing HDT pillar loading, there is a progressive change of the (001) signal. Starting with the formation of a shoulder toward lower diffraction angles for samples with low HDT loading (MoS_2-HDT0.2 and MoS_2-HDT0.5), there is a significant shift toward lower diffraction angles for all samples with higher HDT loading. The shift and very broad shape of the (001) reflex is indicative of an uneven increase of the MoS_2 interlayer spacing in pillared materials with medium HDT loading. For high pillar loadings in MoS_2-HDT2 and MoS_2-HDT5, the (001) signal shifts further and sharpens again, indicative

of higher structural order and an evenly increased interlayer spacing of 1.1 and 1.3 nm, respectively. Moreover, we observe the formation of an additional broad diffraction signal at around 15° for MoS_2-HDT2 and 18° 2 Theta for MoS_2-HDT5 that can neither be related to the MoS_2 intralayer structure, nor to higher order interlayer spacing. Therefore, we hypothesize that the origin of the signals is related to the ordering of the organic chains of HDT pillars within the interlayer galleries, which decrease in characteristic distance at the highest HDT loading in MoS_2-HDT5.

The findings indicate that HDT-pillaring of MoS_2 is increasingly expanding the interlayer spacing with higher loading. The uneven expansion for low and medium pillar loadings indicates that pillars preferentially form domains, while some MoS_2 regions remain unpillared (the thermodynamic reasons are further elucidated in the simulation section). Only for high loadings, the entire MoS_2 structure becomes pillared by HDT.

The density of HDT in pillared MoS_2 samples is quantified using TGA. The mass loss under an oxidative atmosphere (O_2/N_2) is recorded up to 600 °C (**Fig. 5.8C**). At elevated temperatures, pristine MoS_2 converts to MoO_3 under the release of $SO_{2(g)}$, leading to a theoretical mass loss of 10%. Note that small mass gains at intermediate temperatures have been observed before and attributed to the formation of intermediates like MoO_2, which then further oxidize to MoO_3.[214] The presence of significant sulfur vacancies is unlikely though, given the elemental composition results, vide infra. The excess mass loss is therefore assigned to burned-off HDT pillar molecules, allowing to quantify the content in the materials as MoS_2-$(HDT)_{0.10}$, MoS_2-$(HDT)_{0.15}$, MoS_2-$(HDT)_{0.20}$, MoS_2-$(HDT)_{0.40}$, and MoS_2-$(HDT)_{1.10}$ for the samples MoS_2-HDT*x* with *x* = 0.2, 0.5, 1, 2, and 5, respectively. The results indicate that the pillar density is successfully varied from a sparsely pillared to a fully crowded interlayer space.

After covalent pillaring with HDT, the BET specific surface area decreases compared to the pristine MoS_2 sample (**Fig. 5.8D**).[167] The N_2 sorption isotherms of the MoS_2-based samples resemble Type IV (**Fig. S10**), indicative of mesoporous materials, with H3/H4-type hysteresis loops that have been described for aggregates of plate-like particles.[166] The findings indicate that covalent pillaring increases the interconnectivity of the MoS_2 sheets, aligning with microscopy observations, vide infra.

The structural properties of the materials are further elucidated using electron microscopy. Scanning electron micrographs of all samples show similar morphology across all samples, consisting of agglomerates of nanosized flakes (**Fig. S11**). This demonstrates that the hydrothermal process followed by freeze-drying ensures consistent particle morphology across samples, allowing for direct comparison of their electrochemical properties later. However, at the nanoscale, differences in the structure of the primary flakes are observed in each sample through TEM. In **Fig. 5.9A**, pristine MoS_2 exhibits a flake-like morphology with a lateral size of

approximately 50 nm. Lattice fringes show an interlayer spacing of about 0.67 nm. Three rings are observed in the selected area electron diffraction (SAED), corresponding to the (001), (100), and (110) planes. The *d*-spacing calculated from the first SAED ring is 0.64 nm, while the in-plane lattice spacings for the (100) and (110) planes are 0.25 and 0.15 nm, respectively, which is in agreement with XRD results. Pillared MoS_2 samples with low to medium HDT-loading (MoS_2-HDT0.2, MoS_2-HDT0.5, MoS_2-HDT1; **Fig. 5.9B–D**) show similar flake morphologies, but regions with expanded interlayer spacing observed in high-resolution images. It can be seen that the expansion is highly irregular. The (001) ring in the corresponding SAED patterns remains most prominent at the same position as in the pristine MoS_2, but SAED features with smaller radii can be seen particularly for MoS_2-HDT1, indicating regions of further interlayer expansion. The results confirm XRD results also on a nanoscale, demonstrating that the HDT pillars form domains and partially expand the MoS_2 layers, while non-expanded MoS_2 is retained in some regions. In contrast, HRTEM of densely pillared MoS_2-HDT2 and MoS_2-HDT5 (**Fig. 5.9E** and **5.9F**) shows larger interlayer spacings also in agreement with XRD. The related (001) rings are no longer visible in the SAED patterns due to the beam stopper. Meanwhile, the reflections corresponding to the in-plane structure remain largely unaffected by the insertion of pillars, as no significant changes are observed in (100) and (110) planes for all pillared samples. An elemental mapping using EDX in STEM mode (**Fig. S12**) depicts the homogeneous distribution of molybdenum, sulfur, and carbon in the as-synthesized samples.

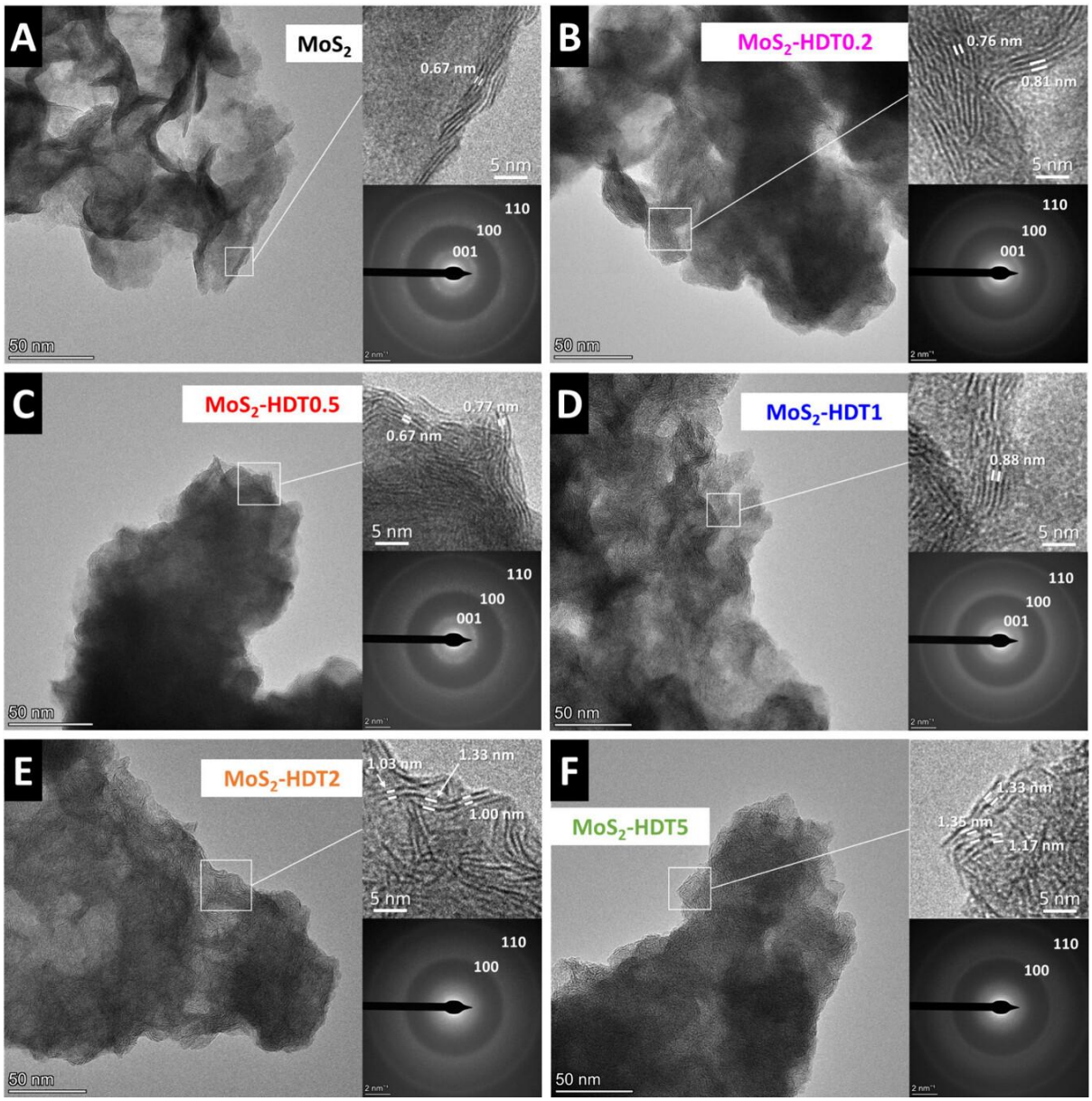

Figure 5.9: (HR)TEM images and SAED patterns of (A) the pristine MoS_2 and (B–F) HDT-pillared MoS_2 samples.

In the following, the bonding character between the MoS_2 host lattice and HDT pillars is examined with spectroscopic methods. Based on previous work on thiol-functionalized MoS_2 monolayers,[215,216] we hypothesize that HDT can form chemical bonds with the MoS_2 lattice yielding a covalent network. First, FTIR spectroscopy is employed to establish the spectroscopic signature of the HDT molecule and analyze how it changes upon functionalization in the MoS_2 lattice. Pure HDT molecules exhibit typical signatures of C–H stretching vibrations at around 2850–2960 cm^{-1} and a distinct peak corresponding to the S–H stretching vibration at 2554 cm^{-1} (**Fig. 5.10A**).[217] In HDT-pillared MoS_2 samples, the C–H stretching vibrations are still visible and increase in intensity for increased HDT loading.

However, the S–H stretching vibration can no longer be detected in any of the HDT-pillared MoS_2 samples, which indicates that the thiol functional groups undergo chemical changes, e.g., are involved in chemical bonding with the MoS_2 lattice. Raman spectra of pristine and HDT-functionalized MoS_2 samples show characteristic signatures at around 150 and 330 cm^{-1} (**Fig. 5.10B**), corresponding to the J_1 and J_3 modes of the metallic phase MoS_2. The absence of $E_2{}^1g$ (usually around 379 cm^{-1}) and A_{1g} (405 cm^{-1}) signals characteristic for the 2H-phase is supportive of the formation of 1T-MoS_2 in all our samples.[218] It should be noted that the Raman measurements are conducted with a low laser power to avoid the decomposition/carbonization of HDT molecules during the measurement.

The results of Raman and FTIR analysis indicate that all samples exhibit 1T-MoS_2 and that thiol molecules chemically bond to the MoS_2 lattice. We therefore hypothesize that thiol groups are directly incorporated into and participate in the formation of the MoS_2 layers. In other words, it can be assumed that thiols are acting as a sulfur source for MoS_2 formation during the bottom-up hydrothermal synthesis. If all thiol groups of HDT participated in the MoS_2 formation, the atomic ratio between S and Mo would remain constant at 2:1 across all samples. Therefore, we employed elemental analysis using both ICP-OES and STEM-EDX (**Fig. 5.10C**). While the S/Mo ratio is close to 2 for samples with low and medium HDT loadings (up to MoS_2-HDT1), both methods independently indicate that the sulfur ratio is increasing significantly for high HDT-pillar loadings (MoS_2-HDT2 and MoS_2-HDT5). We consider the ICP-OES measurements to be quantitatively more reliable than EDX due to two primary factors: (1) the Mo Lα (~2.3 keV) and S Kα (~2.3 keV) peaks are very close in energy, complicating the spectral deconvolution, and (2) X-ray absorption and scattering effects related to sample thickness can distort the EDX quantification. The results lead to the conclusion that several sulfur bonding configurations are simultaneously present in pillared MoS_2 samples, for which possible options are schematically depicted in **Fig. 5.10D**. Sulfur in MoS_2 not associated with an HDT molecule is labeled S1 (Mo-S) and sulfur in MoS_2 directly associated with an HDT molecule is labeled S2 (Mo-S-C-) ("ideal MoS_2"). Configurations responsible for S/Mo ratios greater than two ("non-ideal MoS_2") can be sulfur in MoS_2 (S1-type) which additionally bonds with a thiol group, which is then labeled S3 (Mo-S-S-C-) or a sulfur from a thiol group (S2-type) bonding with a sulfur in MoS_2 (S1-type), which is then labeled S3′ (Mo-S-S-Mo).

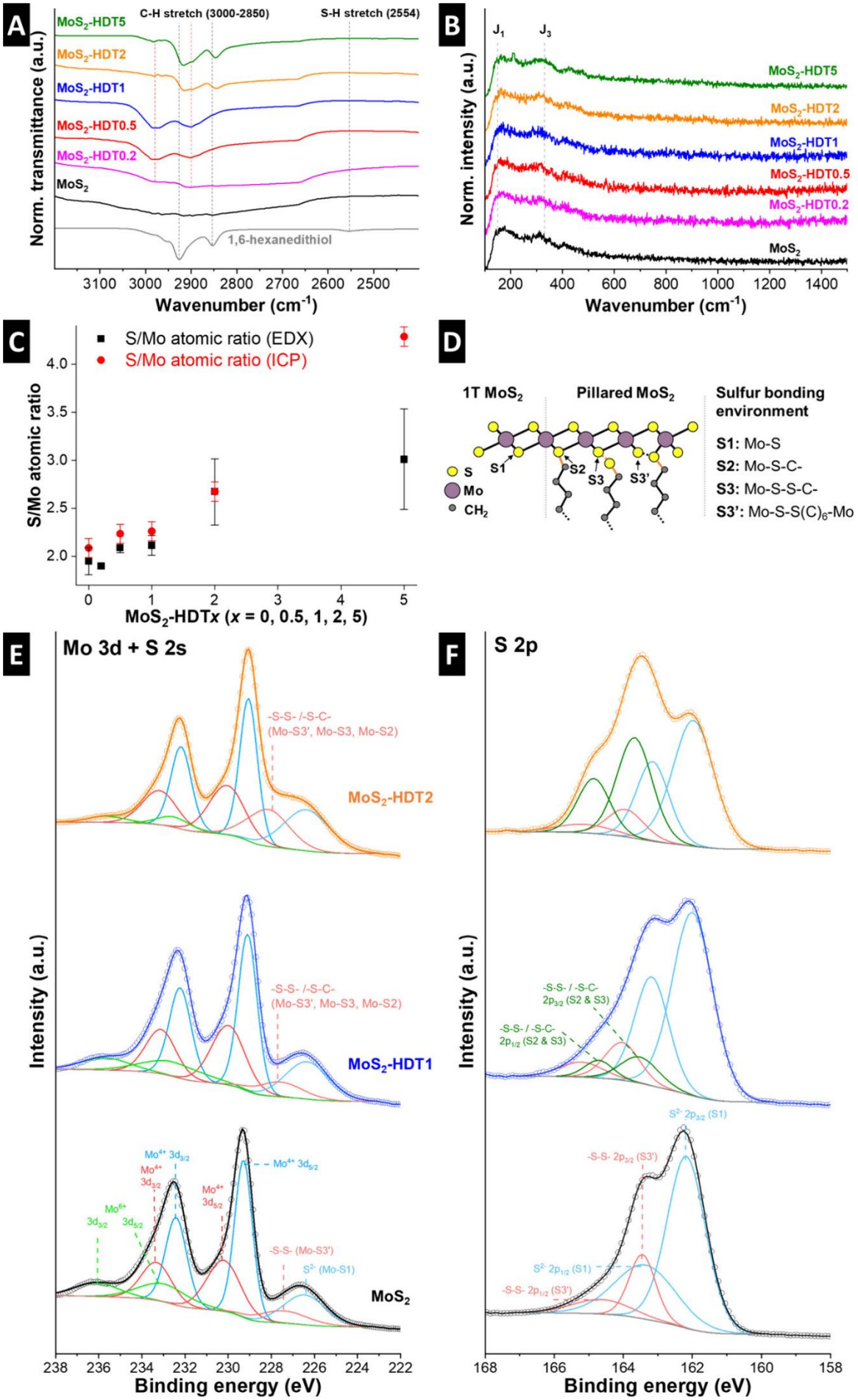
A
MoS2-HDT5
MoS2-HDT2
MoS2-HDT1
MoS2-HDT0.5
MoS2-HDT0.2
MoS2
1,6-hexanedithiol
C-H stretch (3000-2850)
S-H stretch (2554)
Norm. transmittance (a.u.)
Wavenumber (cm-1)
B
J1
J3
Norm. intensity (a.u.)
Wavenumber (cm-1)
C
S/Mo atomic ratio (EDX)
S/Mo atomic ratio (ICP)
S/Mo atomic ratio
MoS2-HDTx (x = 0, 0.5, 1, 2, 5)
D
1T MoS2
Pillared MoS2
Sulfur bonding environment
S1: Mo-S
S2: Mo-S-C-
S3: Mo-S-S-C-
S3': Mo-S-S(C)6-Mo
S
Mo
CH2
E
Mo 3d + S 2s
-S-S- /-S-C- (Mo-S3', Mo-S3, Mo-S2)
MoS2-HDT2
MoS2-HDT1
Mo4+ 3d3/2
Mo4+ 3d5/2
Mo6+ 3d3/2
Mo6+ 3d5/2
-S-S- (Mo-S3')
S2- (Mo-S1)
MoS2
Intensity (a.u.)
Binding energy (eV)
F
S 2p
-S-S- / -S-C- 2p3/2 (S2 & S3)
-S-S- / -S-C- 2p1/2 (S2 & S3)
S2- 2p3/2 (S1)
-S-S- 2p3/2 (S3')
S2- 2p1/2 (S1)
-S-S- 2p1/2 (S3')
Intensity (a.u.)
Binding energy (eV)

Figure 5.10: (A) FTIR and (B) Raman spectra of all samples. (C) Elemental composition of all MoS_2-based samples from ICP-OES and STEM-EDX. (D) Proposed structural configurations illustrating sulfur atoms from pristine MoS_2 (S1) and those corresponding to nonideal MoS_2, such as Mo-S-C- (S2), Mo-S-S-C- (S3), and Mo-S-S-Mo (S3′). XPS spectra of (E) Mo 3d and S 2s and (F) S 2p photoelectron regions of pristine (black), MoS_2-HDT1 (blue), and MoS_2-HDT2 (orange) samples.

XPS is employed to investigate the proposed sulfur bonding configurations in pristine MoS_2, as well as in pillared MoS_2 with medium (MoS_2-HDT1) and high (MoS_2-HDT2) HDT-loading. In **Fig. 5.10E**, the Mo 3d and S 2s spectra are presented. The Mo 3d region of pristine MoS_2 is fitted with three doublets and two single peaks corresponding to the S 2s region at low binding energies. The three doublet peaks at 229.3, 230.2, and 233.0 eV correspond to Mo^{4+} from the ideal and "non-ideal" MoS_2 (e.g., from the sulfur in the edges or poly sulfur species)[219] and Mo^{6+}, respectively. This result reveals the formation of 1T-MoS_2, in agreement with the Raman spectrum (**Fig. 5.10B**).[204] The display of the Mo^{6+} doublet peaks indicates the presence of some surface oxidation and/or traces of unreacted MoO_3 precursor. Meanwhile, the two doublets of Mo^{4+} suggested that the ideal stoichiometry of MoS_2 is synthesized (i.e., S1), as well as other poly sulfurs, such as the formation of disulfides bonded chemically to Mo atoms, as indicated in **Fig. 5.10D** (i.e., S3′). This assumption is in agreement with the S 2s and S 2p (**Fig. 5.10F**) regions. The sulfur signal shows a main peak corresponding to S^{2-} from MoS_2 (Mo-S1) and a less intense peak at higher binding energies attributed to the S–S bond (S3′, Mo-S-S-Mo).[219] It should be noted that the presence of the second doublet of Mo^{4+} could alternatively be correlated with 2H-MoS_2 instead of "non-ideal" MoS_2 with disulfide formation.[187] However, Raman results and the complete absence of any irreversible capacity during the initial electrochemical lithiation of the pristine MoS_2 sample (discussion in the electrochemistry section, vide infra) strongly point toward exclusive 1T-MoS_2 formation in our samples.

In both HDT-functionalized samples, the Mo^{4+} $3d_{5/3}$ peaks shift slightly to 229.1 eV (MoS_2-HDT1) and 229.0 eV (MoS_2-HDT2), indicating that molybdenum loses electrons to sulfur which can be explained by the formation of covalent bonds with the HDT pillars, in agreement with FTIR results. In addition, the intensity of the peak corresponding to disulfides is increasing, more significantly in the densely pillared MoS_2-HDT2, suggesting the formation of more "non-ideal" Mo-S-S-Mo bonds. In line with the peak increase in S 2s, a new doublet peak is displayed in the S 2p region (**Fig. 5.10F**). Considering that it appears at binding energies between Mo-S and Mo-S-S-Mo bonds, it could identify the new bond as Mo-S-C- (S2) or Mo-S-S-C- (S3) bonds. The ICP-OES and STEM-EDX analyses indicate the presence of a higher sulfur

concentration in the MoS_2-HDT2 sample, suggesting that S2-type bonds (Mo-S-C-) are more prevalent in less densely pillared MoS_2, whereas S3-type bonds (Mo-S-S-C-) become more dominant at higher pillar densities. Although S3-type bonds are less stable compared to S2-type bonds, their formation might be facilitated under the higher HDT concentrations during the bottom-up synthesis.

Overall, the correlation between the XPS results and elemental composition (S/Mo ratio) from ICP-OES and STEM-EDX confirms the presence of various sulfur configurations proposed in **Fig. 5.10D**. These configurations reflect different sulfur bonding environments influenced by the increasing loading of HDT in pillared MoS_2. The emergence of S3 and/or S3′ suggests distinct structural configurations, although their binding energies are likely very similar. These configurations also explain why the S/Mo atomic ratio increases with higher pillar loading in the samples. The underlying principles governing the formation of these specific structures require further investigation by simulation, which is carried out in the following.

5.2.2. Structure Optimization by DFT Simulation

Atomistic models of pristine and HDT-pillared MoS_2 are simulated via DFT calculations (**Fig. 5.11A** and **5.11B**). The optimized interlayer spacing for pristine MoS_2 is 0.601 nm, whereas HDT-inserted MoS_2 with 25% pillar site occupancy exhibits an expanded interlayer spacing of 1.088 nm. These results predicted by DFT simulations align closely with the XRD patterns for pristine MoS_2 and MoS_2-HDT2 shown in **Fig. 5.8B**, confirming the structural changes upon pillaring. Notably, the simulated HDT-pillared MoS_2 model reveals a covalent connection between the MoS_2 layers and HDT pillars, established by shared sulfur atoms. The lowest-energy configuration of alkyl chains between MoS_2 layers occurs when the pillars adopt a zigzag arrangement (**Fig. S13**). Additionally, DFT simulations of pristine MoS_2 show that the interlayer distance follows a Lennard-Jones-like potential (**Fig. S14**), suggesting that interlayer expansion results from the interplay between the energy cost of layer expansion and the stabilization energy gained from the adsorbed pillars.

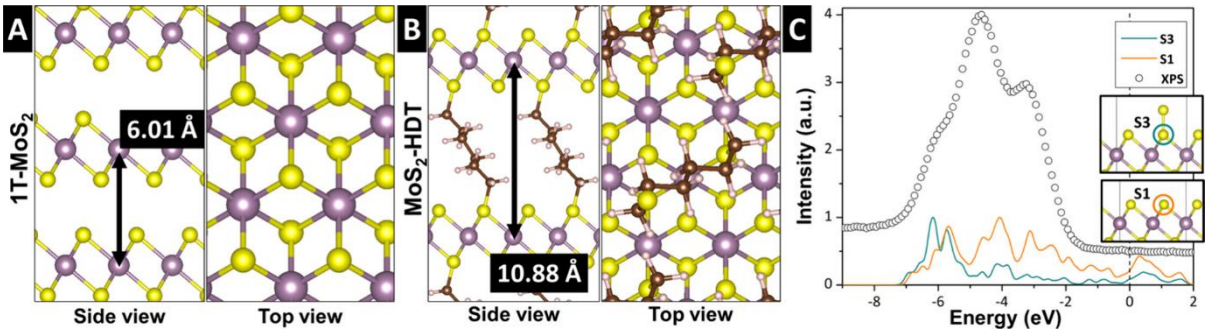

Figure 5.11: Simulated stable atomistic models of (A) pristine MoS_2 and (B) functionalized MoS_2-$HDT_{0.25}$, with optimized interlayer *d*-spacing indicated by a black arrow. (C) The DOS for the sulfur p orbital in pristine MoS_2 (orange) and the p orbital of a sulfur atom in MoS_2 with an extra bonded sulfur atom (blue), both found to be stable configurations, compared with the experimental XPS spectrum of MoS_2-HDT2 taken from **Fig. 5.10F** (circles). The dashed line represents the Fermi level of the simulated systems.

The insertion of HDT pillars promotes the formation of pillar domains, which minimizes energy loss associated with layer expansion at low pillar loading. This is in line with the broadening of XRD (001) signals due to the low periodicity of the expanded MoS_2 sheets. As these pillar domains grow and densify with higher pillar loading, the interlayer expansion becomes more homogeneous. This gradual domain growth explains the abrupt evolution of the (001) ring in SAED and the significant peak shift in XRD observed between MoS_2-HDT1 and MoS_2-HDT2. The clustering of HDT pillars causes the broad distribution of the interlayer spacings, as observed in XRD and TEM/SAED. However, for high HDT-pillar loadings, the MoS_2 layers show an increasingly homogeneous interlayer spacing. This dense arrangement may facilitate S–S bonding between the MoS_2 layers and HDT pillars, particularly at the disordered layer edges.

To further investigate the relationship between pillar density and the formation of S–S bonds, *ab initio* electronic structure analysis of sulfur atoms is performed. The calculated density of states (DOS) of a sulfur atom in pristine MoS_2 (S1) and a sulfur atom bonded to an additional sulfur atom (S3) have been compared with the experimental XPS spectrum (**Fig. 5.11C**). We calculate an energy shift of approximately 3 eV upon S–S bond formation, which corresponds to the emergence of S3-type sulfur peaks in the XPS spectrum (**Fig. 5.10F**). DOS analysis using a model that includes the HDT pillar reveals a similar energy shift in S3-type sulfur (**Fig. S15**). Given the hydrothermal synthesis conditions and the high concentration of HDT molecules serving as a sulfur precursor, the formation of S–S bonds is plausible. The bonding likely occurs not only within the bulk material but also at the surface, defects, and edges within disordered pillar domains.

5.2.3. Electrochemical Characterization

The electrochemical properties of pristine and HDT-pillared MoS_2 are evaluated as host electrode materials for Li^+ intercalation in standard organic electrolyte (LP30). Given the comparable morphology and 1T phase of all samples, we can unambiguously establish a connection between the electrochemistry and the specific nanoconfinement properties of interlayer-expanded, covalent networks of HDT-pillared MoS_2 and analyze the impact of pillar loading on ion transport and storage in detail. To exclude the influence of electrolyte wetting effects in electrodes with varying pillar loading, we have also monitored the OCV over 12 h before starting the measurements,[220] ensuring stabilization of the OCV prior to measurement (**Fig. S16**).

Cyclic voltammograms (CV) of the first (de)lithiation cycle are shown for all samples (**Fig. 5.12A**). While pristine MoS_2 exhibits a quasi-rectangular CV typical for pseudocapacitive lithium intercalation,[95,98,99,105] a reduction peak can be seen for all HDT-pillared samples that increases in intensity and shifts toward lower potentials for increasing HDT-loading from MoS_2-HDT0.2 to MoS_2-HDT2. In contrast, the subsequent oxidation peak is located at around 2.2 V for all these samples. The CV of MoS_2-HDT5 shows a drastic reduction in charge storage capacity. Interestingly, the magnitude of the redox peaks appears linked to the pillar loading, with increasing peak currents going from pristine MoS_2 to MoS_2-HDT1 (before rapidly decreasing for high pillar loadings). The findings indicate that covalent pillaring leads to stronger ion-host interaction manifested in an increased redox signature.[137] This is in contrast to noncovalent pillaring, for example, with hexanediamine pillars (HDA) that we have investigated previously.[95] While the addition of noncovalently interacting HDA to MoS_2 led to an increasingly rectangular/pseudocapacitive CV signature, covalently interacting HDT yields the opposite effect. This underlines the crucial importance of host-pillar interaction on the resulting electrochemical response.

In subsequent CV cycles (**Fig. S17** and **S18**), the reduction peak converges around 1.7–1.8 V for all pillared MoS_2 samples with different loadings (MoS_2-HDT0.2 to MoS_2-HDT2). We hypothesize that the initial reduction peak at varying potentials is due to an activation process involving the rearrangement of HDT pillars during the first lithiation cycle that is necessary to facilitate favorable Li^+ diffusion pathways. Impedance spectroscopy and DFT analysis will further support this hypothesis, vide infra.

GCD is employed to examine the maximum charge storage capacity of the samples during initial cycles at a low specific current of 20 mA/g (**Fig. 5.12B**, **Fig. S19**). The specific delithiation capacities of HDT-pillared MoS_2 with low to medium loading are in a comparable range with

196, 200, and 204 mAh/g for MoS_2-HDT1, MoS_2-HDT0.5, and MoS_2-HDT0.2, respectively, and it is 170 mAh/g for both pristine MoS_2 and MoS_2-HDT2. When taking into account the increasing mass contribution of HDT pillars, the capacity per MoS_2 increases up to medium pillar loading. The maximum reversible (de)lithiation capacities for the samples are $Li_{1.01}MoS_2$, $Li_{1.33}MoS_2$-HDT0.2, $Li_{1.36}MoS_2$-HDT0.5, $Li_{1.43}MoS_2$-HDT1, and $Li_{1.40}MoS_2$-HDT2. MoS_2-HDT5 with the highest pillar loading exhibits highly reduced capacity (21 mAh/g or $Li_{0.25}MoS_2$-HDT5), explainable by blocking of active sites by excessive pillar loading, as demonstrated by DFT vide infra.

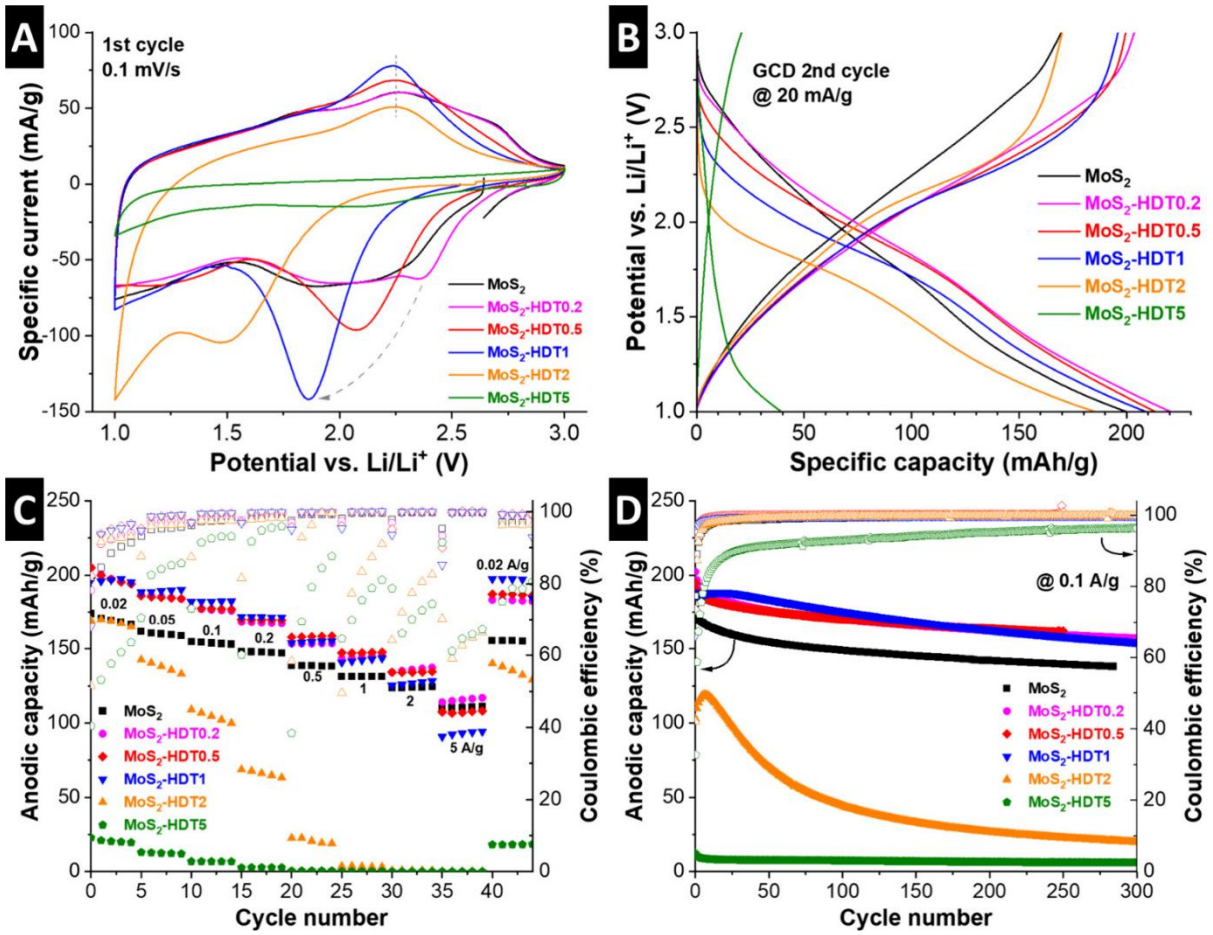

Figure 5.12: Electrochemical performance of MoS_2 and HDT-functionalized MoS_2. Comparison of (A) CVs at 0.1 mV/s (first cycle) and (B) GCD curves at 20 mA/g (second cycle). (C) Rate handling at specific currents of 0.02, 0.05, 0.1, 0.2, 0.5, 1, 2, and 5 A/g. (D) Galvanostatic cycling stability at a constant current of 0.1 A/g. All measurements are carried out in coin cells versus Li metal with LP30 electrolyte at a constant temperature of 20 °C.

The rate handling behavior of the samples is further quantified by GCD at various specific currents from 0.02–5 A/g (**Fig. 5.12C**). At increased rates, the samples with the lowest pillar loading showed superior capacity retention, which is similar to pristine MoS_2. The highest

performance is exhibited by the sample with the lowest pillar loading, MoS_2-HDT0.2, with a retention of ca. 120 mAh/g at 5 A/g. For MoS_2-HDT2 and MoS_2-HDT5, the capacity drastically dropped at higher rates, indicative of poor kinetics caused by the high HDT-pillar loading.

Overall, the basic electrochemical characterization reveals the ambivalent influence of HDT-pillaring on the capacity and rate performance of the lithium intercalation reaction in MoS_2. One the one hand, additional storage sites become activated in the interlayer galleries, even in the inhomogeneously expanded samples with low HDT loading. The capacity becomes maximized in samples with medium HDT loading, with homogeneously expanded interlayers, but before overcrowding with HDT takes place. The rate behavior benefits from low HDT loading, even if the interlayer expansion is inhomogeneous. This is due to the hindrance toward diffusion posed by HDT pillars, as is also shown by simulation, vide infra.

The cycling stability is tested by GCD at a medium rate of 0.1 A/g (**Fig. 5.12D**). For samples up to a medium pillar loading, the stability after 200 cycles is positively impacted by a higher HDT content. The MoS_2-HDT1 sample retains ca. 87% of its capacity after several hundreds of cycles, surpassing pristine MoS_2 (80%), MoS_2-HDT0.2 (80%), and MoS_2-HDT0.5 (84%). These results indicate improved stability of the electrochemical (de)lithiation process in covalently pillared MoS_2 materials. Samples with high pillar loading, however, rapidly fade in capacity.

The impact of HDT pillar content on the (de)lithiation kinetics is studied in detail using EIS at various states of charge over the full potential window of 3.0 – 1.0 V vs Li^+/Li during the first lithiation. We focus the analysis on understanding the reduction peak in the first cycle, which we explained by an “activation”/pillar rearrangement process during initial lithiation. Therefore, impedance spectra of individual electrodes are shown at 2.6 V vs Li^+/Li (roughly the OCV for each electrode), at the onset potential of the reduction process of each individual electrode and in the (almost) fully lithiated state at 1.2 V vs Li^+/Li (**Fig. 5.13A–C**). For pristine MoS_2, the Nyquist plots show comparable shape and magnitude at each of the probed potentials, with a pronounced charge transfer resistance in the midfrequency region and comparable open Warburg-type behavior in the low-frequency region indicative of finite-length diffusion (**Fig. 5.13A**).

For pillared MoS_2 electrodes with medium and high pillar density, a drastic change in the Nyquist plots is observed as a function of electrode potential. At OCV, both electrodes show blocking electrode behavior with large bending arcs in the low frequency region (**Fig. 5.13B** and **5.13C**). Moreover, both electrodes show a transition in the Nyquist plot shape around the potential region where their initial reduction peak occurs (**Fig. 5.12A**), which is around 2.0 V for MoS_2-HDT1 and around 1.6 V for MoS_2-HDT2. The results indicate that the interlayer spaces of pillared MoS_2 electrodes only become accessible for Li^+ intercalation after the initial,

irreversible reduction process. It is noteworthy that stronger reductive potentials are required with increasing HDT pillar densities. Finally, in their lithiated state (1.2 V), all three electrodes show comparable charge transfer resistance in the midfrequency region, while impedance in the Warburg-region associated with ion diffusion is most pronounced for MoS_2-HDT2 (**Fig. 5.13D**). This confirms the impeded ion transport in crowded interlayer space with high pillar loading. It should be noted that all electrodes exhibit an increased charge transfer resistance in the midfrequency range in their lithiated states, which can be explained by the formation of an interfacial layer at highly reductive potentials.[221] We also fitted the EIS data with an equivalent circuit model, as indicated in **Fig. S20**. The mid-frequency region consists of two semicircles, which indicate the presence of a surface film and a charge transfer resistance after initial reduction.[222]

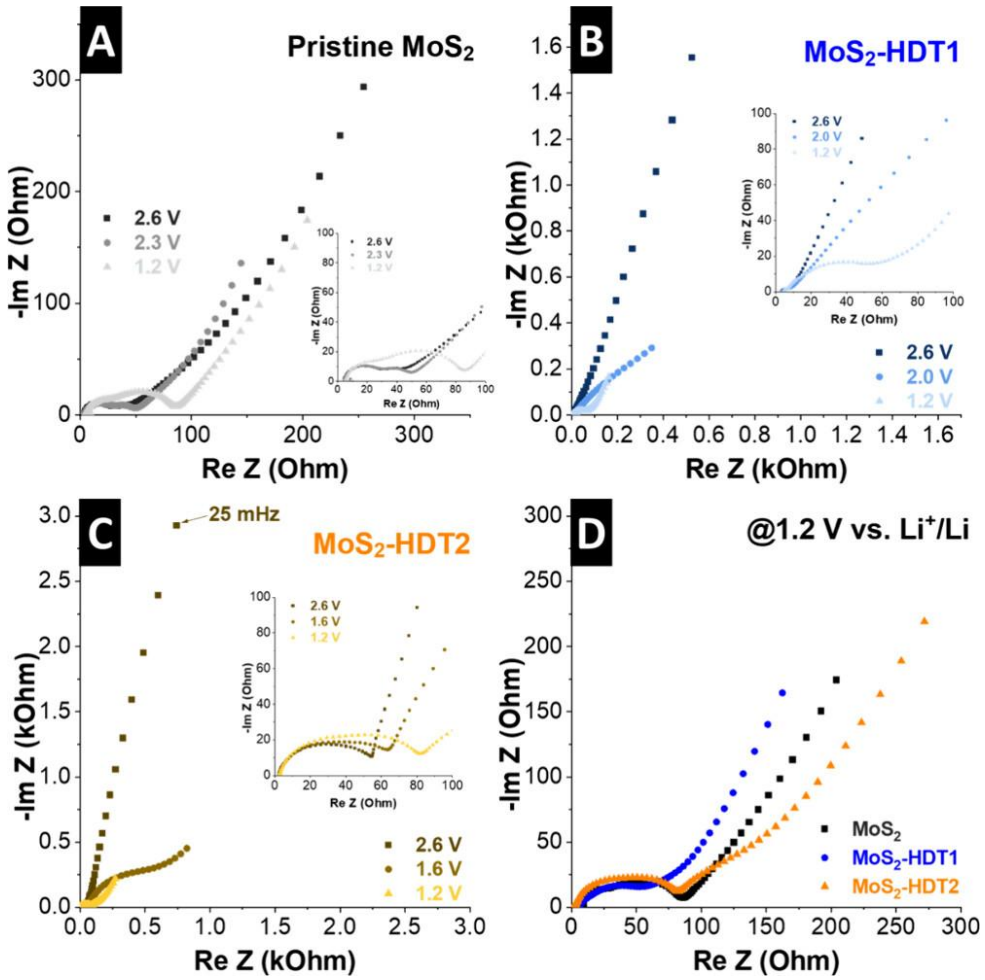

Figure 5.13: Nyquist plots at various electrode potentials versus Li^+/Li of (A) pristine MoS_2, (B) MoS_2-HDT1, and (C) MoS_2-HDT2. (D) Comparison of lithiated electrodes at 1.2 V vs Li^+/Li.

5.2.4. Atomistic Simulation of Electrochemical Lithiation Process

To elucidate the significant differences in maximum lithiation capacity and solid-state diffusion of Li^+ as a function of pillar density, lithiated structures of pristine and HDT-pillared MoS_2 are compared using DFT optimization (**Fig. 5.14**) and CI-NEB via DFT (**Fig. 5.15**). Simulations indicate that an increased interlayer distance can accommodate twice the number of Li^+ compared to the pristine material (**Fig. 5.14A**) by providing additional space at the Mo top sites above and below within the interlayer (**Fig. 5.14B**). However, while the pillars are essential for increasing the interlayer distance, they also hinder lithiation by blocking potential Li^+ sites, resulting in a charge capacity that is less than the anticipated doubled increase (**Fig. 5.12D** and **Fig. S19**). The increased lithiation sites contribute to the enhanced capacity observed in MoS_2-HDT samples with moderate pillar density. In contrast, in systems with high pillar density, such as MoS_2-HDT5, most lithiation sites are occupied by pillars, significantly reducing capacity. The high density of pillars occupying potential lithiation sites results in decreased charge storage capacity. The change in the optimized interlayer distance before and after full lithiation in pristine MoS_2 (+9%) is moderate but significantly higher than that of MoS_2-$HDT_{0.25}$ (+1%) (**Fig. 5.14**). This arises from the already extended interlayer distance in MoS_2-$HDT_{0.25}$ that is less susceptible to volumetric expansion upon lithiation compared to pristine MoS_2.

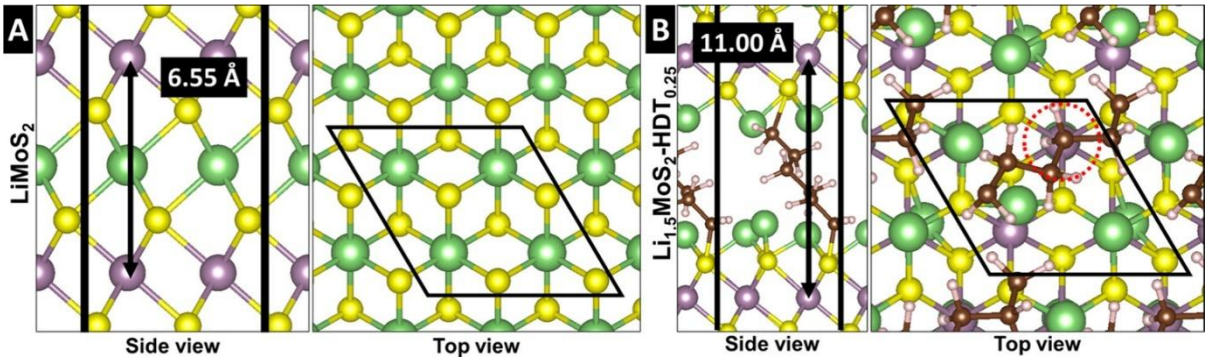

Figure 5.14: Simulated stable atomistic models of fully lithiated (A) $Li_{1.0}MoS_2$ and (B) $Li_{1.5}MoS_2$-$HDT_{0.25}$. Green spheres represent Li atoms. The optimized *d*-spacing with Li atoms is indicated with a black arrow. The black box outlines the simulated cell under the periodic boundary condition. Lithiation at the potential Li site (red circle) is inhibited by the pillar.

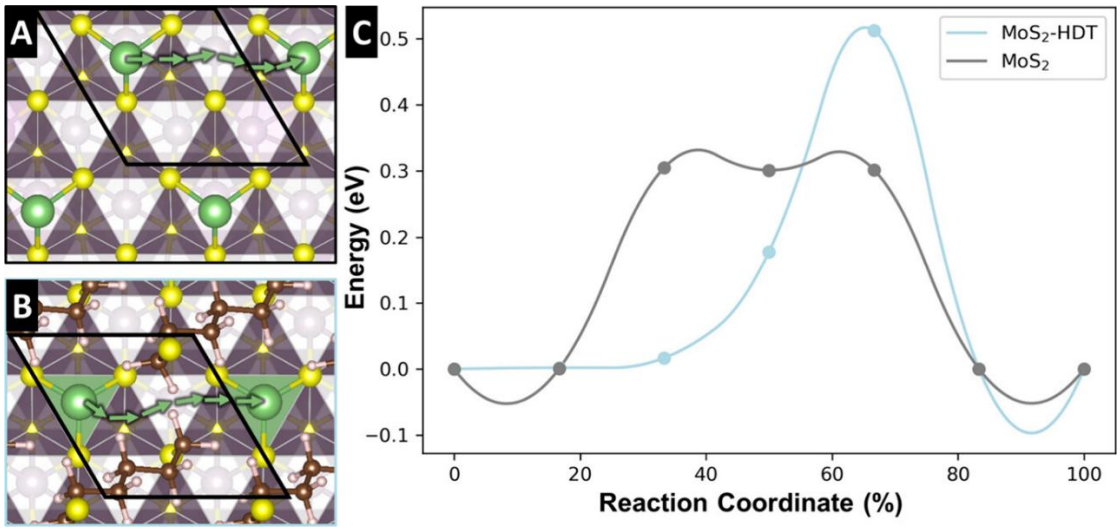

Figure 5.15: Top view of the Li^+ ion diffusion pathways in (A) MoS_2 and (B) MoS_2-HDT. (C) The energy profiles are plotted against the reaction coordinates. Green arrows in (A) and (B) represent the Li^+ diffusion pathway at each data point from (C). The interlayer distances are derived from **Fig. 5.11A** and **Fig. 5.11B**, respectively. The black box outlines the simulated cell under the periodic boundary condition. The complete images from pathways A and B are available in **Fig. S21**.

The energy barrier for Li^+ diffusion pathways is simulated for both pristine MoS_2 and MoS_2-$HDT_{0.25}$ (**Fig. 5.15**). The Li^+ diffusion barrier is 0.30 eV for MoS_2 and 0.51 eV for MoS_2-$HDT_{0.25}$. In pristine MoS_2, the Li^+ ion diffuses along sulfur atoms with a low energy barrier (**Fig. 5.15A**). However, in HDT-pillared MoS_2, the pillars impede Li^+ ion diffusion, increasing the energy barrier (**Fig. 5.15B**). The differences in energy barriers between the two systems suggest that Li^+ diffusion preferably occurs outside or around the perimeter of the pillar-inserted domains. The restructuring of the inserted pillars, driven by charge carrier diffusion affects the stability of the inserted pillar, also serves as an explanation for poor capacity retention of pillared MoS_2 with high pillar loadings. Hence our calculations emphasize the importance of balancing the pillar loading within covalently pillared MoS_2 host materials. While low HDT pillar loadings improve the lithiation capacity, increasing HDT loadings leads to active site occupation and, crucially, impeded Li^+ transport within the interlayer space.

5.2.5. Conclusion

In this work, we have demonstrated a strategy for tailoring the nanoconfinement environment in MoS_2 intercalation host materials via pillaring with HDT molecules. The materials consist of covalent networks between HDT pillars and the MoS_2 lattice, and we were able to demonstrate

a systematic variation in HDT pillar loading. Structural analyses by XRD, TEM, and SAED revealed that, at low to medium pillar loadings, the interlayer expansion is irregular because of the formation of thermodynamically preferential HDT domains, whereas high HDT loadings promote a more homogeneous expansion of MoS_2. A combination of XPS, elemental analysis and DFT calculations reveals the presence of several sulfur configurations depending on the HDT loading. While at low to medium loading, most pillars are directly incorporated in the lattice forming “ideal MoS_2” (Mo-S-C), high pillar loadings lead to increased formation of “non-ideal MoS_2” (Mo-S-S-C and Mo-S-S-Mo). Hence, we developed a comprehensive understanding of the structure of covalently pillared MoS_2 materials.

Electrochemical characterization reveals an increased storage capacity in pillared MoS_2. DFT simulation demonstrated that this is due to the availability of additional storage sites in the expanded interlayer, and a maximum reversible storage capacity of 1.43 Li^+ was measured experimentally in MoS_2-HDT1. However, it was shown that HDT pillars occupy Li^+ storage sites, hence at high pillar loadings, the capacity rapidly diminishes. Excessive pillar densities impede Li^+ diffusion by increasing the energy barrier along diffusion paths.

Overall, the study provides a comprehensive understanding of the structure and covalent interaction in HDT-pillared MoS_2 as a function of HDT loading and the resulting lithium intercalation capacity and kinetics. It presents covalent pillaring with thiols as a promising strategy for TMDs used as ion intercalation hosts materials. Crucially, the impact of pillar loading on the electrochemical performance is emphasized, underlining the importance of controlling materials structure to guide functional properties.

5.3. Interlayer Expansion of Bulk MoS_2 via Top-Down Organic Pillaring Enables Tunable Li^+ Intercalation and Controlled Solvent Co-Intercalation

5.3.1. Structural Characterization of MoS_2-Based Materials

The goal of this work is to extend the interlayer expansion strategy via molecular pillaring with hexanediammonium (HDA) from previously described bottom-up grown nanomaterials towards top-down pillaring of bulk MoS_2. We employ commercially available bulk MoS_2 as the starting material and use a chemical pre-reduction step with butyllithium to obtain Li_xMoS_2. Subsequent exposure to an aqueous solution of HDA leads to the formation of MoS_2-HDA. To disentangle the respective roles of chemical pre-reduction and interlayer expansion for the subsequent electrochemical tests, Li_xMoS_2 is also exposed to water without HDA molecules, to obtain exfoliated and partially restacked MoS_2 as a control sample. The synthesis procedure is outlined schematically in **Fig. 5.16**.

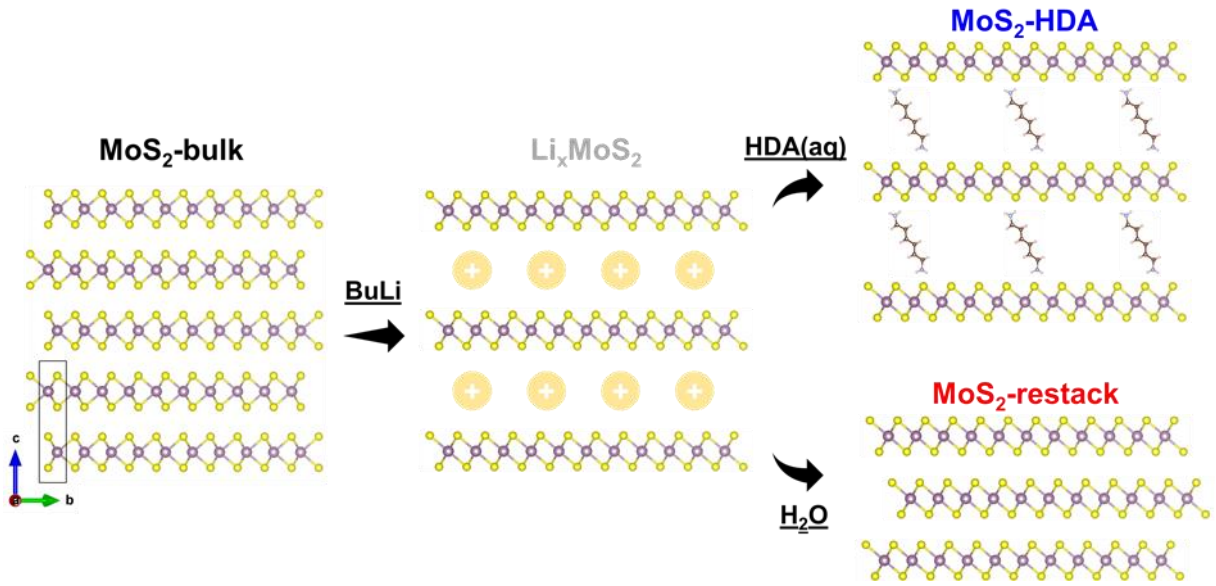

Figure 5.16: Schematic synthesis procedure of pillaring MoS_2-bulk via a top-down approach involving chemical pre-reduction using butyllithium to form Li_xMoS_2 and subsequent immersion in an aqueous solution of HDA pillars, resulting in MoS_2-HDA. Immersion of Li_xMoS_2 in H_2O and subsequent filtration yields a partially restacked MoS_2 control sample.

The morphological evolution of the materials was examined by scanning electron microscopy (SEM). Commercial, bulk MoS_2 consists of irregularly shaped, platelet-like particles with well-defined flat facets, consistent with layered crystal structure of MoS_2. The particles form micrometer-sized aggregates composed of stacked lamellae with clearly visible layered edges

(**Fig. 5.17A**). After chemical pre-reduction, exfoliation in water and partial restacking, the control sample MoS_2-restack exhibits compact platelet-like crystallites but displays a more disordered morphology composed of thinner sheets. The sample forms loosely packed aggregates with folded and partially delaminated layers, indicating a disruption of the original stacked lamellar structure after exfoliation and restacking (**Fig. 5.17B**). The pillared MoS_2-HDA sample shows a morphology similar to bulk MoS_2, however with a stacking that appears slightly looser and edges that indicate a partially separated lamellae structure (**Fig. 5.17C**).

The crystal structure of the materials was then characterized by X-ray diffraction (XRD, **Fig. 5.17D**). Commercial, bulk-MoS_2 exhibits the characteristic diffractogram of 2H-MoS_2, according to PDF card #01-071-9809, with an interlayer spacing of 0.62 nm, as visible from the diffraction peak at 14.4 °2θ corresponding to the 002 set of planes. After chemical lithiation with butyllithium, the interlayer spacing of Li_xMoS_2 increases to 1.13 nm, visible from a shift of the diffraction signal to 7.84 °2θ in agreement with previous reports.[223] This is indicative of Li^+ and hexane confined between the bulk MoS_2 layers, and the complete absence of the original 002 signal at 14.4° indicates extensive lithiation of the MoS_2 structure. The presence of a higher order diffraction peak indicates the high ordering of the lithiated MoS_2 material.

Upon immersion of Li_xMoS_2 in aqueous solution (both with and without HDA), the intercalated lithium reacts with water according to the well-known chemical exfoliation mechanism ($Li_xMoS_2 + xH_2O \rightarrow MoS_2\text{^}(\delta^-) + x\text{LiOH} + x/2\ H_2$)[114], generating MoS_2 sheets with negative partial charge that electrostatically repel each other and undergo exfoliation. Without the presence of HDA pillar molecules, the MoS_2 sheets (partially) restack and form again a crystalline MoS_2 structure with the characteristic interlayer spacing at 0.62 nm visible from the diffraction peak at 14.4°, however, the lower intensity and broadening of the 002 signal of MoS_2-restack compared to bulk MoS_2 indicates a decreased stacking order in agreement with SEM observations. When HDA is present in the aqueous solution, there is a distinct change in the diffraction pattern. The main diffraction signal is shifted to 9.04°, indicative of an interlayer spacing of 0.98 nm in MoS_2-HDA and the successful confinement of the cationic HDA molecules in the MoS_2 interlayer space. The same interlayer spacing was observed previously for HDA-pillared MoS_2 nanomaterials that were grown bottom-up during hydrothermal synthesis.[95] The higher order diffraction signal remains, indicating the high structural order of the expanded, pillared MoS_2-HDA structure.

Nitrogen sorption measurements were performed to evaluate the porosity and accessible surface area of the samples. The sorption isotherms of bulk MoS_2, MoS_2-restack and MoS_2-HDA all exhibit high similarity (**Fig. 5.17E**). They most-closely resemble a type III shape according to the IUPAC technical report,[166] indicative of their non-porous (or macroporous) structure. There are very small hysteresis loops noticeable for all samples that can best be

classified as type H3, indicative of non-rigid aggregates of plate-like particles.[166] The Brunauer-Emmett-Teller (BET) specific surface areas of bulk, restacked, and HDA-pillared MoS_2 are all around 9-10 $m^2\ g^{-1}$, quantitatively confirming that the top-down pillaring approach was able to maintain the bulk character of the MoS_2 sample, while primarily alters the internal interlayer structure.

Thermogravimetric analysis (TGA) was employed to quantify the number of confined guests within the pillared MoS_2 interlayer space (**Fig. 5.17F**). TGA profiles reveal two major mass-loss stages: (1) removal of adsorbed surface water up to ca. 130 °C, and (2) conversion of MoS_2 to MoO_3 under oxidative atmosphere (via $2MoS_2 + 5O_2 \rightarrow 2MoO_3 + 4SO_2$)[224] and evaporation and/or combustion of organic HDA molecules, above ca. 200 °C, where the latter two processes are partially overlapping. In stage 1, the mass loss of adsorbed surface water is 1.6 wt.% for bulk MoS_2, 2.4 wt.% for MoS_2-HDA and 3.9 wt.% for MoS_2-restack, which indicates the highest area for water adsorption on the latter sample despite its comparable BET surface area relative to MoS_2-bulk and MoS_2-HDA. In stage 2, further heating of MoS_2-bulk and MoS_2-restack leads to an additional mass loss of around 11 wt.% (relative to the weight after H_2O loss), which is consistent with the theoretical value (10.1 wt.%) expected for the conversion of MoS_2 to MoO_3. MoS_2-HDA shows an additional mass loss of 21.3 wt.%, leading to an estimated content of ca. 0.20 HDA molecules per formula unit of MoS_2.

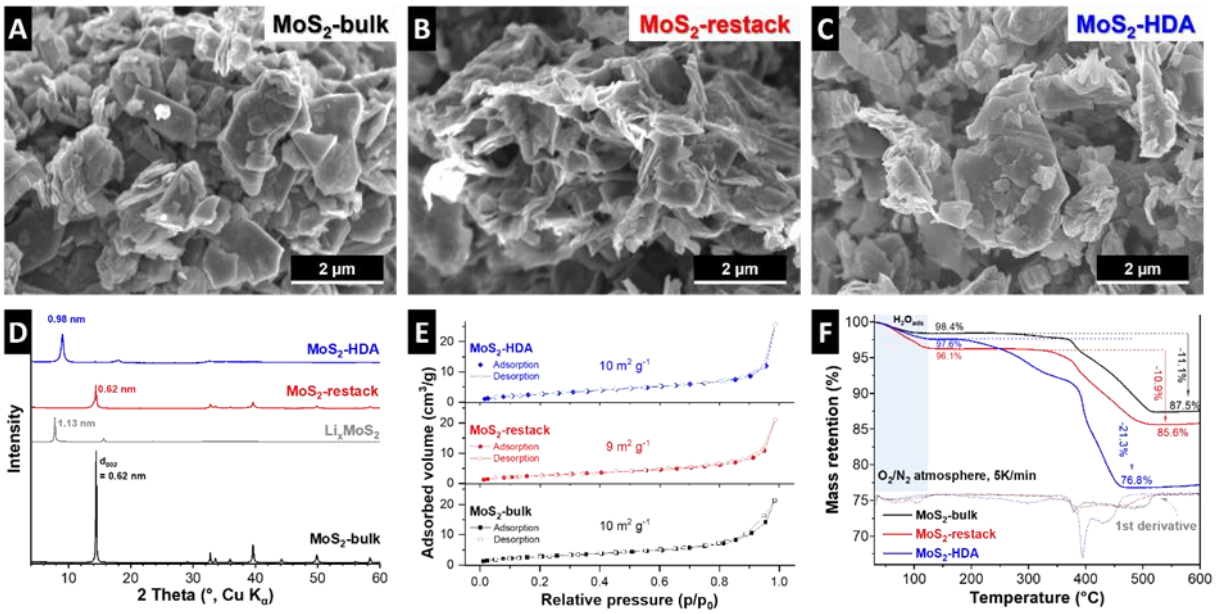

Figure 5.17: Scanning electron micrographs of (A) MoS_2-bulk, (B) MoS_2-restack, and (C) MoS_2-HDA. (D) X-ray diffractograms, (E) nitrogen sorption isotherms, and (F) thermogravimetric analysis in O_2/N_2 atmosphere at a heating rate of 5 K min^{-1} for the three materials.

Raman spectroscopy is carried out to assess the phase composition and layer coupling of the MoS_2 host material. The Raman spectra of bulk MoS_2 and MoS_2-restack exhibit characteristic E^1_{2g} (in-plane) and A_{1g} (out-of-plane) modes at 384 and 409 cm^{-1}, respectively (**Fig. 5.18A**).[101] In comparison, the MoS_2-HDA spectrum shows both modes shifted to lower wavenumbers (red shift) to 381 and 407 cm^{-1}, respectively. This red shift is attributed to the interlayer expansion induced by confined HDA pillars, which weakens the van der Waals coupling between adjacent layers, thereby releasing atomic vibrations and resulting in lower force constants.[225] Additionally, the emergence of J_1 (156 cm^{-1}) and J_2 (226 cm^{-1}) peaks in MoS_2-HDA (and to a lesser extent in MoS_2-restack) confirms the presence of the metallic 1T phase, resulting from the 2H-to-1T phase transformation induced during chemical pre-lithiation (**Fig. S22**).[226] These 1T-specific modes are absent in the MoS_2-bulk spectrum, which instead displays a strong E_g mode (287 cm^{-1}), indicating that MoS_2-bulk is in a purely semiconducting 2H-phase, while the modified samples coexist as mixed 2H/1T phases.[227] The Fourier transform infrared spectrum (FTIR, **Fig. 5.18B**) of functionalized MoS_2-HDA reveals two C–H stretching modes at 2912 and 2850 cm^{-1}, confirming the presence of *n*-alkyl chains that are originated from the HDA pillars and indicating successful incorporation between MoS_2 layers.[95] These peaks are absent in the spectrum of MoS_2-bulk.

X-ray photoelectron spectroscopy (XPS) reveals clear chemical changes in interlayer-expanded MoS_2 functionalized with HDA pillars. A distinct N 1s component at 401.9 eV (**Fig. 5.18C**) is consistent with protonated amine/ammonium species ($R\text{-}NH_3^+$). We thus hypothesize that cationic ammonium groups electrostatically interact with the partially negatively charged outer sulfide layers of the MoS_2 host material.[63,228] The Mo $3p_{3/2}$ peak shifts from 395.75 eV in bulk MoS_2 to 395.24 eV in MoS_2-HDA, and the Mo $3d_{5/2}$ peak from 229.86 eV to 229.41 eV (**Fig. S23**), suggesting modification of the electronic environment upon interlayer expansion and HDA confinement. In addition to the dominant 2H-MoS_2 features, lower binding energy components in the Mo 3d and S 2p regions corresponding to metallic 1T-MoS_2 are primarily observed in MoS_2-HDA (**Fig. 5.18D**), consistent with the Raman results and the 2H-to-1T phase transformation induced during chemical lithiation. Increased Mo^{6+} contributions in MoS_2-restack and MoS_2-HDA in the Mo 3p and Mo 3d regions, along with SO_x^{2-} (x = 3, 4) features at 168–170 eV in the S 2p region, indicating partial surface oxidation of MoS_2 during chemical processing.

These structural analyses confirm the successful preparation of three MoS_2-based materials with distinct interlayer architectures and phase compositions, providing a well-defined platform to investigate the influence of chemical activation and interlayer expansion on electrochemical lithium storage.

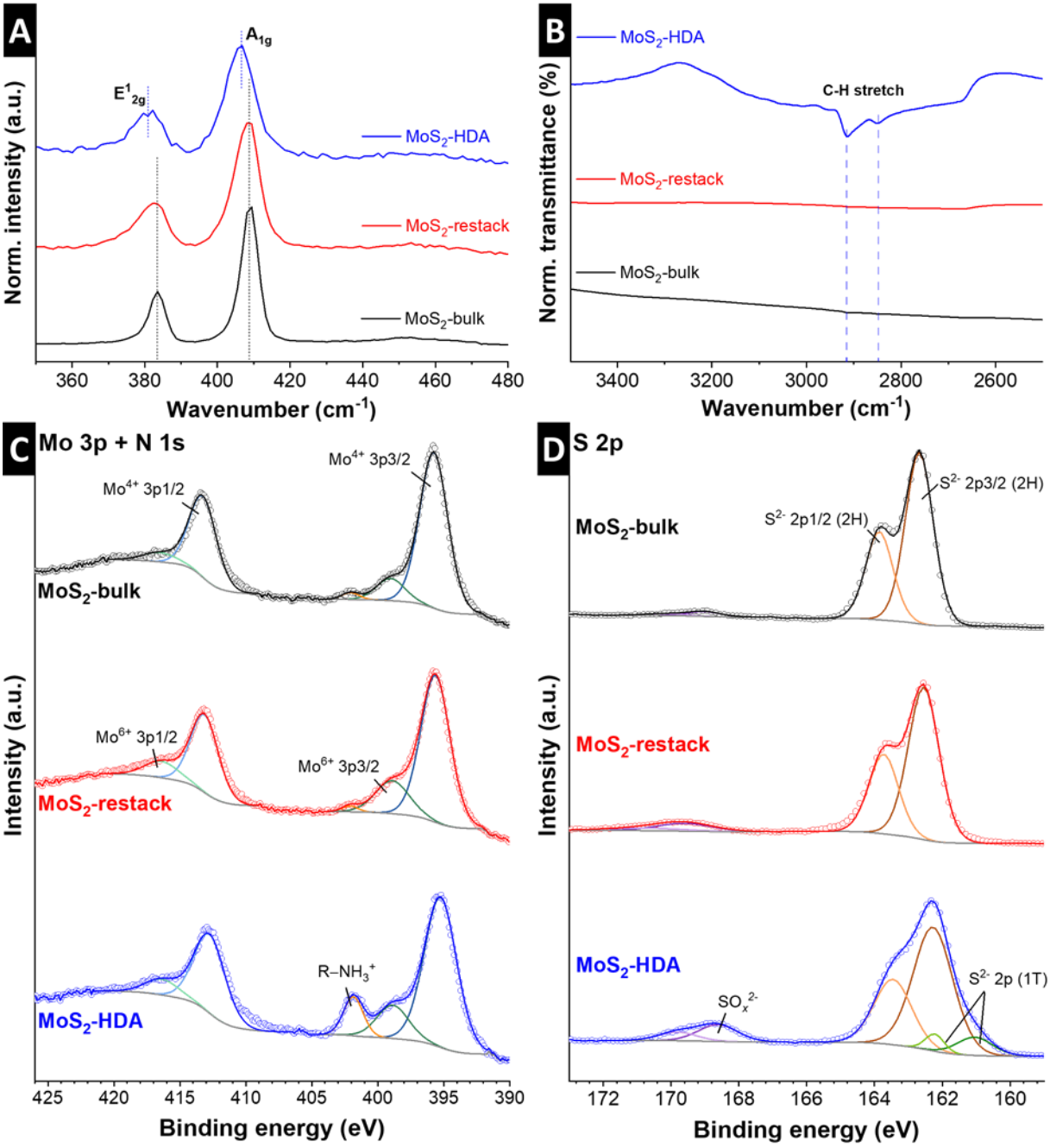

Figure 5.18: (A) Raman spectra of MoS_2-bulk, MoS_2-restack, and MoS_2-HDA. (B) FTIR spectra, and XPS of the (C) Mo 3p and N 1s and (D) S 2p regions of the MoS_2-bulk, MoS_2-restack, and MoS_2-HDA samples.

5.3.2. Electrochemical Characterization of MoS_2-Based Materials

The electrochemical investigation of the MoS_2-based samples focuses on three major scientific questions. First, we aim to elucidate how the chemical pre-lithiation via butyllithium, exfoliation and subsequent restacking alters the electrochemical behavior of MoS_2-bulk. Second, we analyze the role of interlayer expansion via HDA molecules. Third, we answer how the

electrolyte environment influences the intercalation mechanism by comparing a standard, carbonate-based electrolyte with diglyme, which is a solvent known for its propensity to co-intercalation.

The baseline of our investigation is MoS_2-bulk in the carbonate-based electrolyte (1M LiTFSI in ethylene carbonate and dimethyl carbonate, 1:1 by volume). The cyclic voltammogram (CV) shows a significant reduction peak around 1.2 V, which is typical for the 2H-to-1T phase transition in the first few cycles (**Fig. 5.19A**). Moreover, typical redox peaks around 1.7-2.0 V are indicative of reversible Li^+ (de)intercalation. The MoS_2-restacked sample shows high similarity to MoS_2-bulk, however, the reduction peak associated with 2H-to-1T transition is less pronounced, which can be explained by the partial 1T-MoS_2 formation during pre-reduction (CV and GCD of first cycles in **Fig. S24**). Moreover, a second redox peak couple centered around 2.5 V is more pronounced in this sample compared to pristine MoS_2-bulk. In the first galvanostatic charge-discharge (GCD) cycle, the reduction profile of MoS_2-bulk is dominated by the 2H-to-1T phase transition plateau, and the initial Coulombic efficiency (ICE) is 73% (**Fig. 5.19B**). The phase transition is less pronounced for MoS_2-restacked in agreement with CVs. Moreover, the MoS_2-restacked sample exhibits more sloping regions and a slightly increased ICE of 78%, suggesting that the chemical pre-treatment does not lead to increased parasitic reactions during electrochemical (de)lithiation. Both samples exhibit a comparable maximum anodic/delithiation capacity of 146 (MoS_2-bulk) and 140 mAh g^{-1} (MoS_2-restacked), corresponding to a reversible storage capacity of 0.84-0.87 Li^+ per formula unit of MoS_2. Interestingly, the rate capability of MoS_2-restacked is strongly improved over MoS_2-bulk (**Fig. 5.19C**). For example, at a high rate of 5 A g^{-1}, the electrode still delivers a reversible capacity of about 55 mAh g^{-1}, while MoS_2-bulk exhibits close to 0 capacity at this rate. This suggests that the chemical pre-reduction treatment and its associated partial exfoliation play a major role in enabling high rate electrochemical (de)lithiation of MoS_2. Even though both MoS_2-bulk and MoS_2-restacked exhibit the same BET-surface area, the reduced stacking order and/or partial 1T-phase transition in MoS_2-restack likely contribute to the enhanced charge storage kinetics. The presence of partially delaminated layers together with metallic 1T domains may enhance electronic conductivity and facilitate faster Li^+ intercalation. This interpretation is further supported by *b*-value analysis of CVs at varying rates, where MoS_2-bulk exhibits typical diffusion-limited kinetics and MoS_2-restack trends towards surface-limited kinetics (**Fig. S25**).

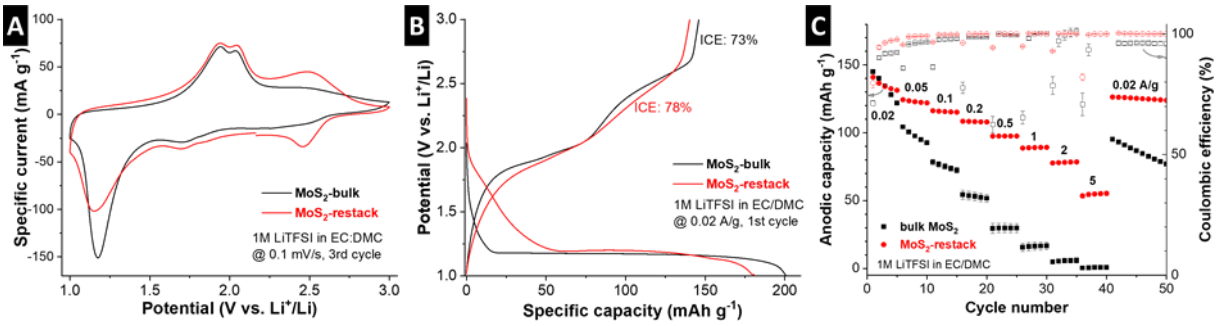

Figure 5.19: Investigating the influence of chemical pre-lithiation, comparing MoS_2-bulk and MoS_2-restack electrodes in EC/DMC electrolyte. (A) CV comparison at 0.1 mV s^{-1}, third cycle. (B) First GCD cycle at 0.02 A g^{-1}. (C) Anodic / delithiation capacity from GCD at varying rates from 0.02–5 A g^{-1}. All measurements are carried out in coin cells at 20 °C. Error bars indicate standard deviation from 3 measurements.

Having established the influence of the chemical pre-reduction, the influence of HDA pillaring can be isolated by a comparison of MoS_2-restack and MoS_2-HDA. The CV comparison shows several distinct differences between the two electrodes (**Fig. 5.20A**). First, MoS_2-HDA does not show the reduction peak of the 1T-phase transformation, further confirming that the material is mostly present as 1T already after synthesis. Second, in MoS_2-HDA, the redox peak features around 1.7–2.0 V and 2.5 V are smaller in magnitude, while in the low potential region, stronger rectangular features indicative of pseudocapacitance are visible. This is in agreement with previous observations of nanosized, HDA-pillared MoS_2.[95] The observations are confirmed in GCD, where also the first reduction of MoS_2-HDA does not show an obvious plateau for 1T formation (**Fig. 5.20B**). The ICE is reduced compared to MoS_2-restack with 66%. The maximum capacity of MoS_2-HDA is reduced to 112 mAh g^{-1}, but this includes the mass contribution of HDA pillars; the measured lithiation capacity translates to 0.78 Li^+ per MoS_2. The rate behavior of MoS_2-HDA is slightly reduced compared to MoS_2-restack (**Fig. 5.20C**), but still significantly improved compared to MoS_2-bulk. This trend is consistent with the corresponding *b*-value analysis (**Fig. S25A-C**). Importantly, these results confirm that chemical pre-reduction dominates the rate capability, while interlayer expansion via pillaring does not provide an additional enhancement under these conditions. Instead, the role of interlayer expansion becomes more evident in controlling the intercalation mechanism and structural stability, as discussed below.

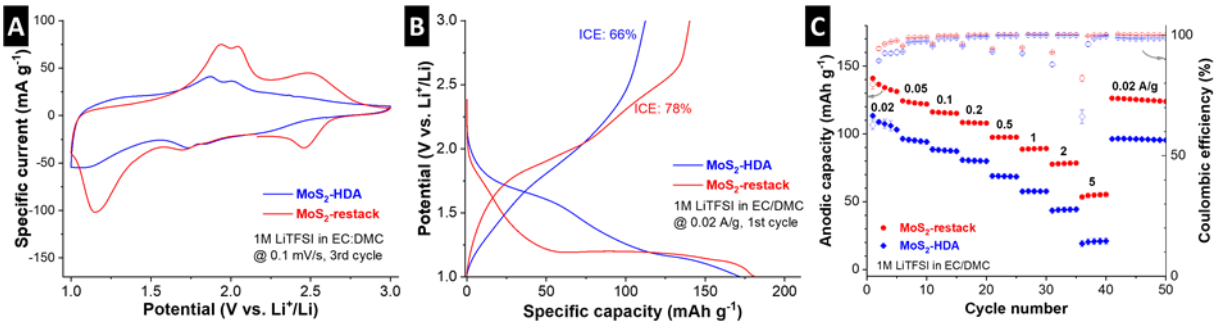

Figure 5.20: Investigating the influence of interlayer expansion by HDA-pillaring, comparing MoS_2-restack and MoS_2-HDA electrodes in EC/DMC electrolyte. (A) CV comparison at 0.1 mV s^{-1}, third cycle. (B) First GCD cycle at 0.02 A g^{-1}. (C) Anodic / delithiation capacity from GCD at varying rates from 0.02-5 A g^{-1}. All measurements are carried out in coin cells at 20 °C. Error bars indicate standard deviation from 3 measurements.

Finally, we probe the influence of the electrolyte solvent on the lithium intercalation properties of the MoS_2-based materials. Besides the standard, carbonate-based electrolyte system (EC/DMC), we probe the mechanism in an ether-based electrolyte, namely diglyme (2G), which is known for its strong solvating power and tendency to co-intercalate in sulfide-based electrode materials. A comparison of MoS_2-bulk in both electrolytes by CVs shows similar features, but the magnitude of the peaks around 2.5 V is slightly increased in 2G, while the reduction peak of the 1T-phase transformation is slightly suppressed (**Fig. 5.21A**). The first few cycles from CV and GCD in diglyme are further shown in **Fig. S26**. Strikingly, the rate capability of MoS_2-bulk is highly improved in 2G compared to EC/DMC. Even at a GCD rate of 5 A g^{-1}, there is still a reversible capacity of up to 33 mAh g^{-1} in 2G electrolyte, compared to practically zero in EC/DMC (**Fig. 5.21B**). The improved kinetics are also visible from *b*-value analysis (**Fig. S25D-F**). Given the tendency for solvent co-intercalation in 2G-based electrolytes, these results may indicate a solvent-dependent change of intercalation mechanism and kinetics.

When probing MoS_2-HDA in the two different electrolytes, there are almost no differences in the CV signatures, except a slight broadening of the redox peak features around 1.7–2.0 V in 2G electrolyte (**Fig. 5.21C**). Moreover, the rate capability in both electrolytes is also much closer than for the MoS_2-bulk electrodes, although a modest advantage of 2G electrolyte over EC/DMC remains (**Fig. 5.21D**), consistent with slightly higher *b*-values (**Fig. S25F**). However, the strongly overlapping CV curves and comparable rate capability do not necessarily suggest an electrolyte-dependent change of intercalation mechanism like in MoS_2-bulk. Overall, the baseline electrochemical characterization indicates a strong performance-dependence of the electrochemical Li^+ intercalation reaction from the electrolyte solvent (EC/DMC vs. 2G) in

MoS_2-bulk, but to a lesser extent in MoS_2-HDA, with significantly improved rate capability in 2G electrolyte for MoS_2-bulk electrodes. The underlying mechanisms will be investigated in the following section.

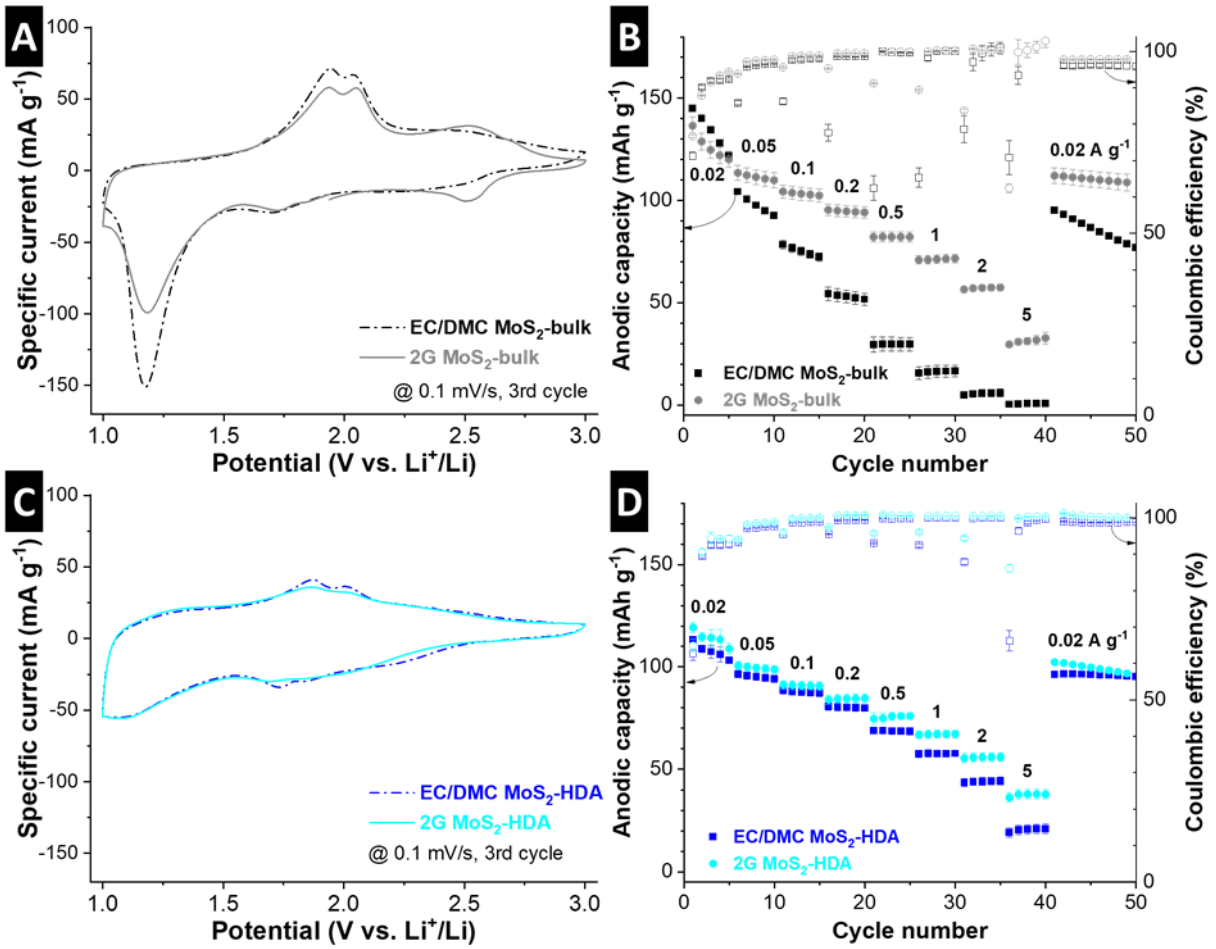

Figure 5.21: Investigating the influence of electrolyte solvent comparing MoS_2-bulk and MoS_2-HDA in EC/DMC and 2G electrolytes. (A) CV comparison of MoS_2-bulk at 0.1 mV s^{-1}, third cycle. (B) Anodic / delithiation capacity of MoS_2-bulk from GCD at varying rates from 0.02–5 A g^{-1}. (C) CV comparison of MoS_2-HDA at 0.1 mV s^{-1}, third cycle. (D) Anodic / delithiation capacity of MoS_2-HDA from GCD at varying rates from 0.02–5 A g^{-1}. All measurements are carried out in coin cells at 20 °C. Error bars indicate standard deviation from 3 measurements.

5.3.3. Analysis of Electrolyte-Dependent Lithium Intercalation Mechanisms

To correlate the distinct electrochemical behavior observed in carbonate- and diglyme-based electrolytes with specific storage mechanisms, both the crystallographic evolution and the macroscopic volume changes of MoS_2-based electrodes are monitored in real time using operando X-ray diffraction (XRD) and electrochemical dilatometry (ECD), respectively. These techniques are complementary and probe structural changes across multiple length scales,

providing insight into volume changes during (de)intercalation from the crystallographic level (XRD) to the electrode level (ECD).

MoS_2-bulk and MoS_2-HDA electrodes were investigated using operando XRD during GCD at a specific current of 0.02 A g^{-1} to monitor crystallographic evolution. For MoS_2-bulk (**Fig. 5.22A**), the initial (002) interlayer spacing of 6.15 Å expands to 6.29 Å during the first cathodic scan, coinciding with the 2H-to-1T phase conversion associated with Li^+ insertion into the MoS_2 layers. Upon subsequent delithiation and relithiation, the (002) reflection exhibits reversible expansion and contraction between approximately 6.30 and 6.37 Å. Excluding the irreversible expansion associated with the phase conversion (6.15 to 6.30 Å), the reversible breathing amplitude of the (002) plane is about 2.7%, indicating a solid-solution intercalation mechanism of desolvated Li^+ after the initial 2H-1T transformation when using the carbonate-based (EC/DMC) electrolyte.

In the ether-based electrolyte (1 M LiTFSI in diglyme, 2G), MoS_2-bulk displays a markedly different structural evolution (**Fig. 5.22B**). The initial interlayer spacing of 6.13 Å shifts to 6.30 Å during the 2H-to-1T phase conversion at 1.15 V (vs. Li^+/Li). In addition to this signal, a new reflection appears at 14.25 Å (2.25° 2θ using Ag Kα radiation) during the initial reduction plateau, corresponding to an expansion of more than 130% relative to the initial interlayer spacing. Such a drastic expansion is reminiscent of solvent co-intercalation reactions previously reported for TiS_2 electrodes in lithium- and sodium-based ether and propylene carbonate electrolytes.[229,230] The new reflection is therefore attributed to a fundamental $(001)_{co}$ set of planes corresponding to an expanded MoS_2 interlayer spacing hosting Li^+ together with diglyme solvent molecules. A second-order reflection indexed as $(002)_{co}$ is observed at 2θ = 4.5° (d = 7.12 Å), indicating the formation of an ordered expanded phase. Operando diffractograms with an extended 2θ-range are further shown in **Fig. S27**.

To further support this interpretation at the atomic scale, representative intercalation states were investigated using DFT-based geometry optimization. The optimized interlayer spacing for Li-$(2G)_2$ complex (model for solvated Li^+ species) intercalated MoS_2 was calculated to be 13.55 Å (**Fig. 5.22C**), in good agreement with the experimentally observed spacing of 14.25 Å. Upon partial delithiation while retaining trapped 2G molecules, the interlayer spacing contracts to approximately 10.3 Å (**Fig. 5.22D**), accompanied by structural flattening of the Li-$(2G)_2$ complex into a more two-dimensional configuration. Simulated XRD patterns derived from these optimized structures reproduce the emergence of a strong $(001)_{co}$ reflection near 13.55 Å and a corresponding $(002)_{co}$ peak near 6.78 Å (**Fig. 5.22E**), consistent with the operando diffraction features observed during lithiation. Simulated patterns for different coordination configurations (Li-$(2G)_x$, x=1, 2) are shown in **Fig. S28**.

After delithiation, the disappearance of the ordered expanded phase together with the persistence of a broad feature in XRD corresponding to a d-spacing of approximately 10-13 Å in XRD are consistent with residual solvent molecules remaining within the MoS_2 interlayer space (**Fig. 5.22B**). These results support the interpretation that ether-based electrolytes enable the formation of a solvation-induced expanded phase in MoS_2-bulk during lithiation, while a partially contracted but still expanded state reflects retained solvent molecules after Li^+ deintercalation.

To corroborate the findings from operando XRD, complementary operando ECD measurements were performed to monitor macroscopic electrode height changes. The MoS_2-bulk electrode cycled in EC/DMC exhibits a height increase of 7.2% during the initial cathodic cycle (**Fig. 5.22F**), coinciding with the 2H-to-1T phase transformation and Li^+ intercalation. Upon completion of the first lithiation/delithiation cycle, an irreversible height increase of 4.4% relative to the initial electrode thickness remains. In subsequent cycles, the dilatometric changes are limited to reversible variations of up to 2.8%. This moderate electrode breathing is consistent with a mechanism dominated by reversible intercalation of desolvated Li^+ ions and supports the structural evolution observed by operando XRD (**Fig. 5.22A**).

In contrast, the use of diglyme electrolyte induces a pronounced expansion of the MoS_2-bulk electrode. As shown in **Fig. 5.22G**, a substantial expansion of 11.9% occurs during the first cathodic scan, followed by a contraction of 5.9%, resulting in an irreversible height increase of approximately 6% after the first cycle, consistent with partial solvent trapping. In subsequent cycles, large reversible height changes of up to 6.8% are observed. These reversible variations significantly exceed the expansion expected for desolvated Li^+ intercalation and are consistent with the solvent co-intercalation mechanism identified by operando XRD (**Fig. 5.22B**). Notably, the electrode retains its expanded height up to approximately 1.7 V during the anodic scan before contracting sharply. The potential at which this contraction occurs correlates with the disappearance of the $(001)_{co}$ and $(002)_{co}$ reflections in operando XRD, linking the macroscopic electrode contraction to the loss of the crystallographic signature of the expanded co-intercalated phase. Together, the operando XRD and ECD results and DFT structure optimization indicate a transition in the lithium storage mechanism in MoS_2-bulk from conventional Li^+ intercalation to a solvated ion co-intercalation process.

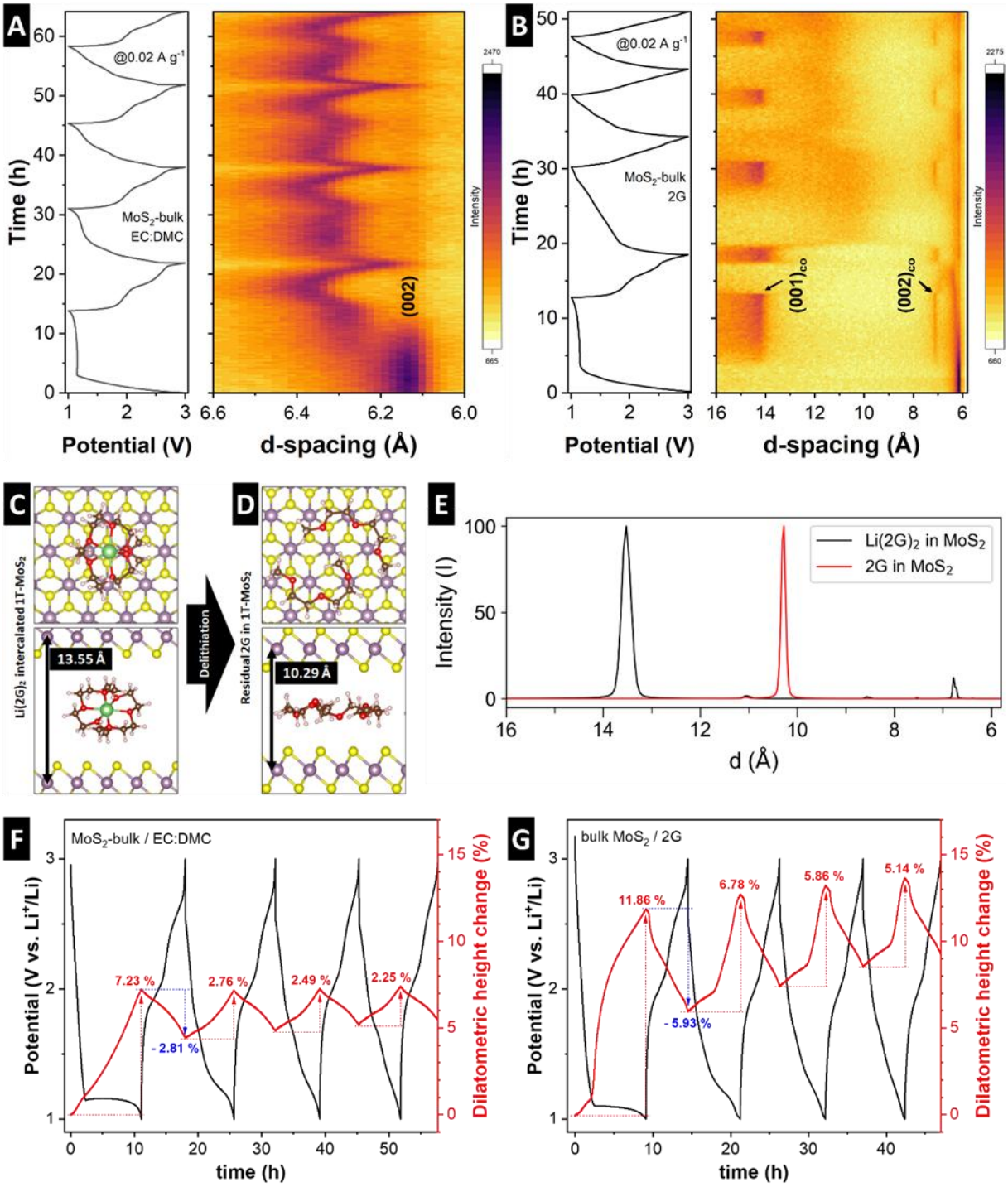

Figure 5.22: Analysis of the electrolyte-dependent intercalation mechanism in MoS_2-bulk. Operando XRD measurements of MoS_2-bulk in custom-made coin cells using a transmission geometry and Ag Kα X-ray source with (A) carbonate- and (B) diglyme-based electrolyte for four GCD cycles at 0.02 A g^{-1}. DFT-optimized structures of (C) Li-$(2G)_2$ complex intercalated in MoS_2, and (D) 2G molecules intercalated in MoS_2 without Li, and (E) corresponding simulated X-ray diffractograms. (F) Electrochemical dilatometry over four GCD cycles at 0.02 A g^{-1} in (F) carbonate- and (G) diglyme-based electrolyte.

To evaluate whether interlayer pillaring alters the solvent-dependent intercalation mechanism observed for bulk MoS_2, the structural evolution of MoS_2-HDA was investigated using operando XRD and ECD. MoS_2-HDA in carbonate electrolyte exhibits a moderate expansion of the (002) interlayer spacing from 9.9 Å to ca. 10.3 Å during the first lithiation (**Fig. 5.23A**). Upon further lithiation, the *d*-spacing increases to ca. 10.4 Å, corresponding to an overall expansion of approximately 5.1 % relative to the initial spacing. In subsequent cycles, the interlayer spacing gradually increases to about 10.6 Å, representing an additional expansion of ~1.9 % compared to the end of the first cycle. During lithiation, the intensity of the (002) reflection decreases, indicating decreased stacking order of the expanded layers, which partially recovers upon delithiation. Overall, the moderate lattice breathing and reversible structural evolution are consistent with a solid-solution intercalation mechanism involving Li^+ insertion into the expanded MoS_2 layers.

When cycled in diglyme electrolyte, MoS_2-HDA shows a gradual increase of the interlayer spacing from 9.9 Å to approximately 10.7 Å during the first lithiation/delithiation cycle (**Fig. 5.23B**). Importantly, no reflections corresponding to a highly ordered solvent co-intercalated phase, such as the 14.25 Å feature observed for bulk MoS_2, are detected (see also full range operando diffractograms in **Fig. S27**). Instead, the *d*-spacing evolution closely resembles that observed in the carbonate-based electrolyte. These observations indicate that the confined HDA pillars suppress the formation of a highly expanded solvent co-intercalated phase despite the larger initial interlayer spacing. This finding suggests that interlayer spacing alone is not the decisive factor enabling solvent co-intercalation in bulk-sized MoS_2 particles. Rather, we hypothesize that the confined organic pillars inhibit solvent incorporation through steric constraints and possible modifications of the local solvation environment within the interlayer space.

Due to the relatively low intensity of the XRD reflections, complementary operando ECD measurements provide additional insight into the structural evolution of MoS_2-HDA during lithium (de)intercalation. In carbonate electrolyte, the MoS_2-HDA electrode exhibits very small electrode breathing (**Fig. 5.23C**), with an initial thickness increase limited to 2.2 % and subsequent reversible variations of approximately 1.1 % during further cycles. These small height changes make solvent co-intercalation unlikely, in agreement with the operando XRD results. When cycled in diglyme electrolyte (**Fig. 5.23D**), the MoS_2-HDA electrode shows somewhat larger height variations, with an irreversible initial expansion of about 3.1 % followed by reversible thickness changes of up to ~2 %. Importantly, the large step-like expansion observed for MoS_2-bulk in 2G is absent. Together with the absence of a distinct co-intercalation XRD signature (**Fig. 5.23B**), the moderate electrode height changes indicate that solvent co-intercalation into MoS_2-HDA is strongly suppressed even in diglyme electrolyte. Overall, these results demonstrate that while ether electrolytes can induce solvated ion co-intercalation in

bulk MoS_2, the introduction of confined interlayer pillars could preserve a conventional, desolvated Li^+ intercalation mechanism and suppress excessive volumetric changes during cycling.

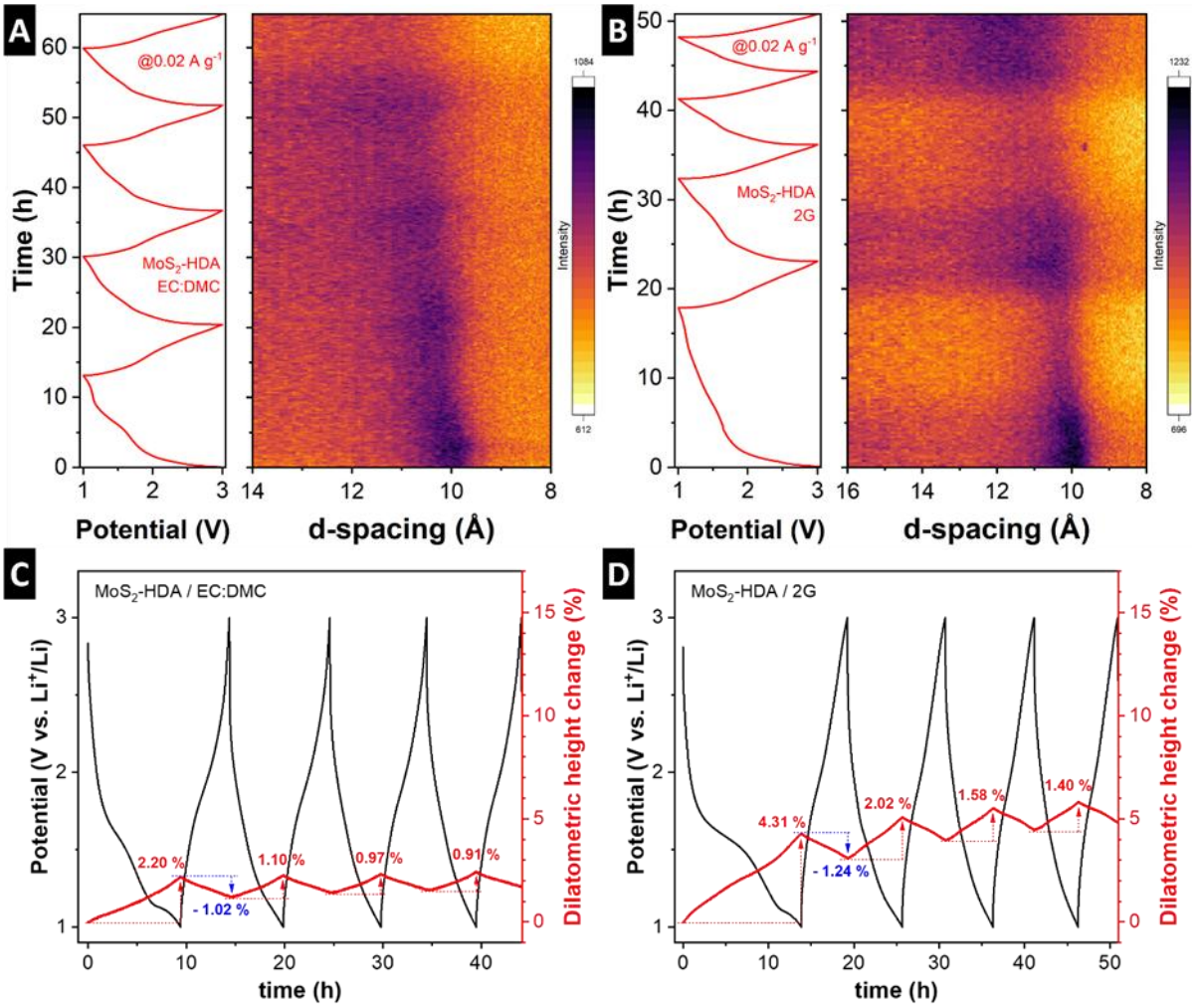

Figure 5.23: Analysis of the electrolyte-dependent intercalation mechanism in MoS_2-HDA. Operando XRD measurements of MoS_2-HDA in custom-made coin cells using a transmission geometry and Ag Kα X-ray source with (A) carbonate- and (B) diglyme-based electrolyte for four GCD cycles at 0.02 A g^{-1}. Electrochemical dilatometry over four GCD cycles at 0.02 A g^{-1} in (C) carbonate- and (D) diglyme-based electrolyte.

5.3.4. Conclusion

In this work, we demonstrate that interlayer engineering concepts previously developed for nanoscale MoS_2 materials can be translated to bulk-sized particles through a top-down pillaring strategy. Chemical pre-reduction of bulk MoS_2 using butyllithium enables exfoliation and subsequent insertion of hexanediammonium (HDA) pillars, resulting in an expanded interlayer spacing while preserving the macroscopic particle morphology and specific surface area of the

bulk material. Structural characterization confirms the formation of MoS_2-HDA with an increased interlayer spacing of 0.98 nm and a mixed 2H/1T phase composition arising from the chemical activation step.

Electrochemical analysis reveals that the improved rate capability of the modified MoS_2 materials is primarily associated with the chemical pre-reduction rather than with the interlayer expansion itself. In contrast, the electrolyte environment strongly influences the lithium storage mechanism. While MoS_2-bulk exhibits conventional Li^+ intercalation in carbonate electrolyte, the use of diglyme induces a transition to a solvent co-intercalation mechanism, as evidenced by large interlayer expansion in operando XRD and pronounced electrode swelling in electrochemical dilatometry.

Importantly, the pillared MoS_2-HDA structure suppresses this solvent co-intercalation behavior despite its larger interlayer spacing. Operando XRD and dilatometry show that MoS_2-HDA undergoes only moderate lattice breathing and electrode expansion in both carbonate and diglyme electrolytes, indicating that lithium storage proceeds via conventional Li^+ intercalation. These results demonstrate that solvent co-intercalation in layered MoS_2 is governed by the nanoconfined interlayer structure and steric constraints rather than by interlayer spacing alone.

Overall, this study provides mechanistic insight into how interlayer engineering and electrolyte solvation jointly determine the charge storage behavior of MoS_2 electrodes. The results highlight that top-down pillaring of bulk materials offers a viable strategy to control interlayer spacing and limit excessive volume expansion phenomena driven by solvent co-intercalation.

Chapter 6: Integrative Summary

6.1. Revisiting the Challenge: Bridging the Performance Gap

As outlined in the introduction, there is a fundamental trade-off in EES systems: the dichotomy between high-energy batteries and high-power SCs. While MoS_2 possesses the theoretical capacity to serve as a high-energy anode, its bulk form is severely limited by sluggish diffusion kinetics. This thesis was motivated by the hypothesis that nanoconfinement design, specifically the manipulation of the interlayer environment, could bridge this performance gap. By transforming the charge storage kinetics from diffusion-controlled to surface-limited intercalation, this work aimed to realize a material that delivers battery-like energy with capacitor-like power. The research presented herein successfully elucidates the critical correlation between the nanoconfinement-designed interlayer geometry, the chemical nature of the pillars including their interaction with the host, and the resulting electrochemical kinetics, providing a comprehensive pathway for designing next-generation layered electrodes.

6.2. Summary of Key Findings

Study I: Simultaneous Structural Control for Pseudocapacitive Lithium Intercalation

The first study established a versatile one-pot hydrothermal synthesis strategy to simultaneously tune the crystallite size and interlayer spacing of MoS_2 using pH control and 1,6-hexanediamine (HDA) pillars.

- Findings: The study demonstrated that reducing crystallite size via pH control and expanding the interlayer spacing via HDA pillars act synergistically to enhance kinetics. The optimized nanoconfinement-designed structure (MoS_2-HDA-0.5) exhibited a diffusion-independent, pseudocapacitive signature ($b \approx 0.93$) and achieved a reversible lithium capacity of 199 mAh/g. This quantitatively proved that physical nanoconfinement of HDA pillars can unlock capacity beyond the theoretical intercalation limit of bulk MoS_2 (1 Li^+ per formula unit) by activating additional storage sites.

Study II: The Critical Role of Pillar Density and Bonding

Building on the physical confinement approach of HDA pillars, the second study investigated the limits of this strategy by introducing covalent functionalization with 1,6-hexanedithiol (HDT) pillars. This directly addressed the knowledge gap regarding host-pillar interactions.

- Findings: While covalent bonding stabilized the structure, the study revealed a critical trade-off between stability and kinetic accessibility. Optimized loading (MoS_2-HDT1)

maintained high capacity (196 mAh/g), but excessive pillar density (MoS_2-HDT5) caused a drastic reduction of Li^+ storage (21 mAh/g). This provided evidence that pillars can act as barriers if overcrowded, fundamentally altering the diffusion pathways and competing for Li^+ storage sites. It established that high-performance nanoconfinement design requires a delicate balance: enough pillars to prop open the layers, but few enough to allow unobstructed ion transport.

Study III: Transition of Nanoconfinement Design to Bulk MoS_2: Impact on Ion Transport and Chemo-Mechanical Behavior

This study extends the nanoconfinement design strategy from nano-sized systems to electrode-relevant bulk MoS_2. By applying a top-down approach using commercially available MoS_2 and introducing HDA pillars, this study investigates how nanoconfinement influences ion transport and structural evolution in bulk materials, with particular emphasis on the role of electrolyte environments.

- Findings: The study demonstrated that nanoconfinement design in bulk MoS_2 enables a transition from diffusion-limited toward less diffusion-constrained electrochemical behavior, improving rate capability compared to pristine bulk materials. Importantly, this kinetic enhancement is not solely governed by interlayer expansion but is strongly influenced by the structural and chemical modifications introduced during the top-down process. The electrolyte environment plays a decisive role in determining the charge storage mechanism. In ether-based electrolytes, bulk MoS_2 exhibits pronounced structural expansion driven by solvent co-intercalation, while nanoconfinement-designed MoS_2 shows significantly suppressed volume expansion and no clear evidence of solvent co-intercalation. This indicates that organic pillars act as steric regulators of ion-solvent interactions, favoring desolvated Li^+ intercalation within the confined interlayer space. Consequently, nanoconfinement design not only modifies ion transport pathways but also governs the coupling between structure and solvation, leading to improved chemo-mechanical stability during cycling.

6.3. Conclusion and Outlook

The starting point of the thesis was sparse reports in the literature that an expanded interlayer spacing of layered electrode materials has been widely considered to improve ion intercalation capacity and/or kinetics, although this work demonstrates that interlayer expansion alone is not the sole determining factor. While under the right synthesis conditions, this initial assumption was confirmed, this thesis revealed much deeper mechanistic insights into the structural requirements and resulting electrochemistry of interlayer-expanded host materials.

Instead, it is demonstrated that the electrochemical performance is also largely driven by the complex interplay of pillar density, the nature of the pillar-host bonding, and the interaction with the electrolyte. Crucially, we have proven that nanoconfinement design can indeed bridge the power-energy trade-off. The nanoconfinement-designed MoS_2 architectures developed here exhibit the high capacity characteristic of batteries while accessing the rapid kinetics of pseudocapacitors.

By establishing a “gatekeeping function” of organic pillars towards electrolyte solvent, this work also opens new avenues for stabilizing layered electrodes against possible solvent-induced degradation. These findings provide significant new findings for rational design of future high-rate energy storage materials, suggesting that designing the “empty space” between layers is just as important as the layers themselves.

Appendix

Appendix 5.1: supporting information

Study I: Simultaneous control of crystallite size and interlayer spacing of MoS_2 to achieve pseudocapacitive lithium intercalation

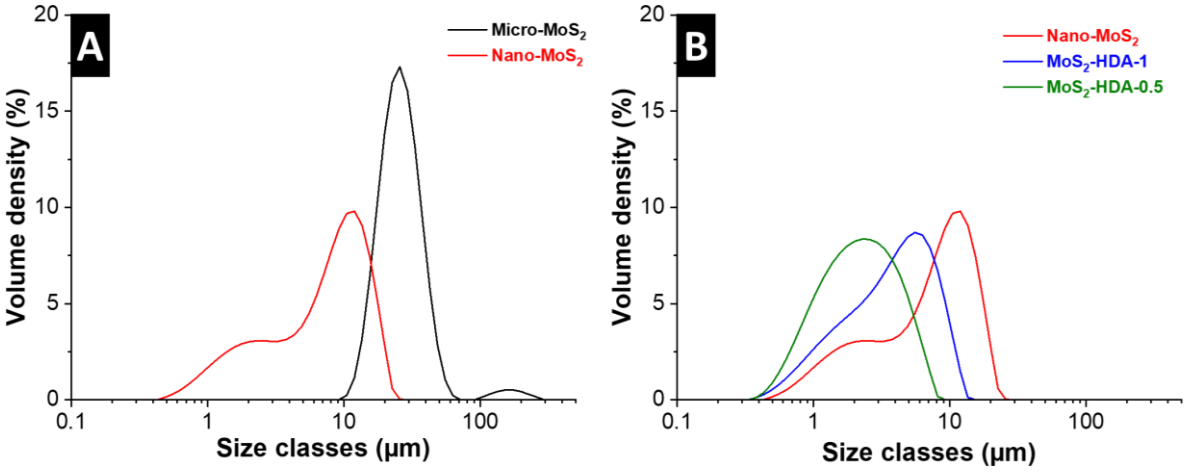

Figure S1: Secondary particle size distribution analyzed by DLS for (A) micro-MoS_2 and nano-MoS_2, and (B) interlayer-expanded MoS_2-HDA-1 and MoS_2-HDA-0.5, including reproduced data of nano-MoS_2 for better comparability.

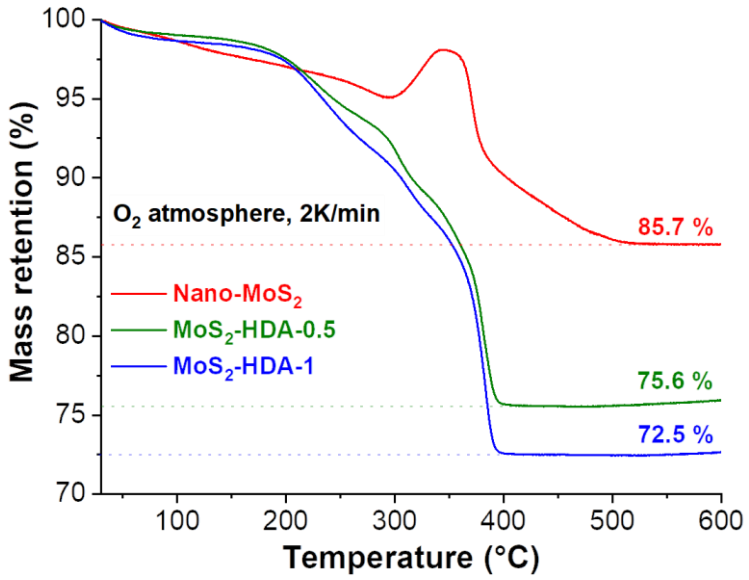

Figure S2: TGA curves of nano-MoS_2, MoS_2-HDA-0.5, and MoS_2-HDA-1 under flowing oxygen atmosphere at a heating rate of 2 K/min.

Assuming that interlayer-functionalized samples consist of MoS_2 and HDA at room temperature (100 % mass), and are fully converted to MoO_3 at 600 °C (75.6 % and 72.5 % mass, respectively), we calculate molar compositions of $(HDA)_{0.26}MoS_2$ for MoS_2-HDA-0.5 and $(HDA)_{0.33}MoS_2$ for MoS_2-HDA-1.

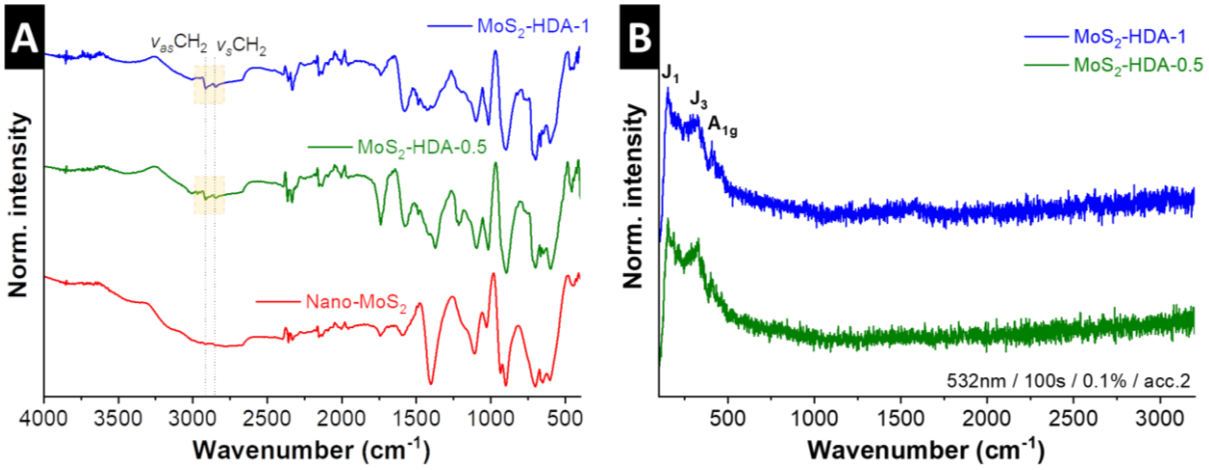

Figure S3: FTIR of MoS_2-HDA-1 and MoS_2-HDA-0.5 showing asymmetrical and symmetrical stretching vibrations of aliphatic C-H at 2915 and 2850 cm^{-1}, respectively, and nano-MoS_2 as comparison. (B) Raman spectra of MoS_2-HDA-1 and MoS_2-HDA-0.5 showing the absence of D- and G-signals, excluding the formation of amorphous carbon as a result of HDA decomposition.

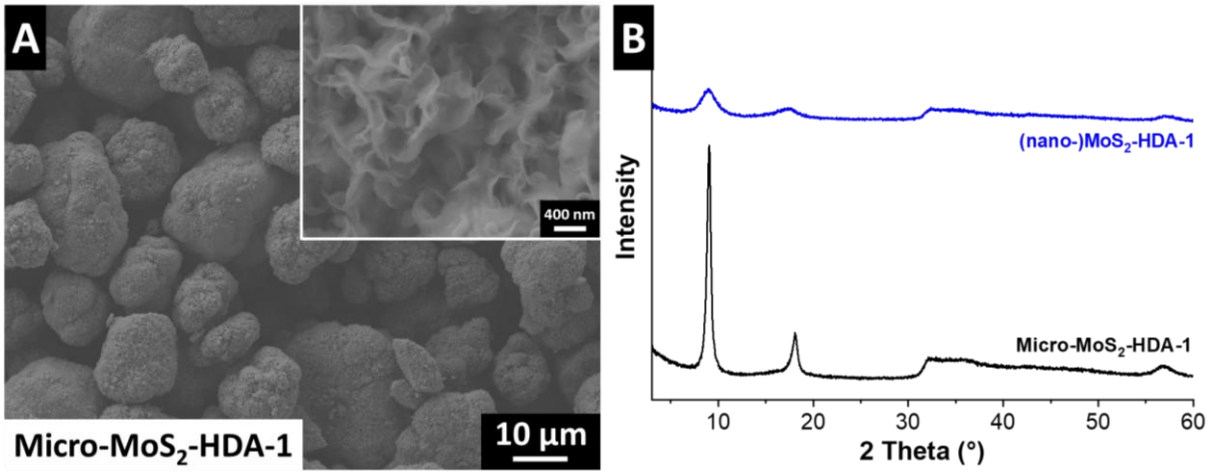

Figure S4: Characterization of "micro-MoS_2-HDA-1", which was synthesized at pH 5.5. (A) Scanning electron micrographs and (B) X-ray diffractograms, with reproduced diffractogram of (nano-)MoS_2-HDA-1 synthesized at pH 1 for direct comparison.

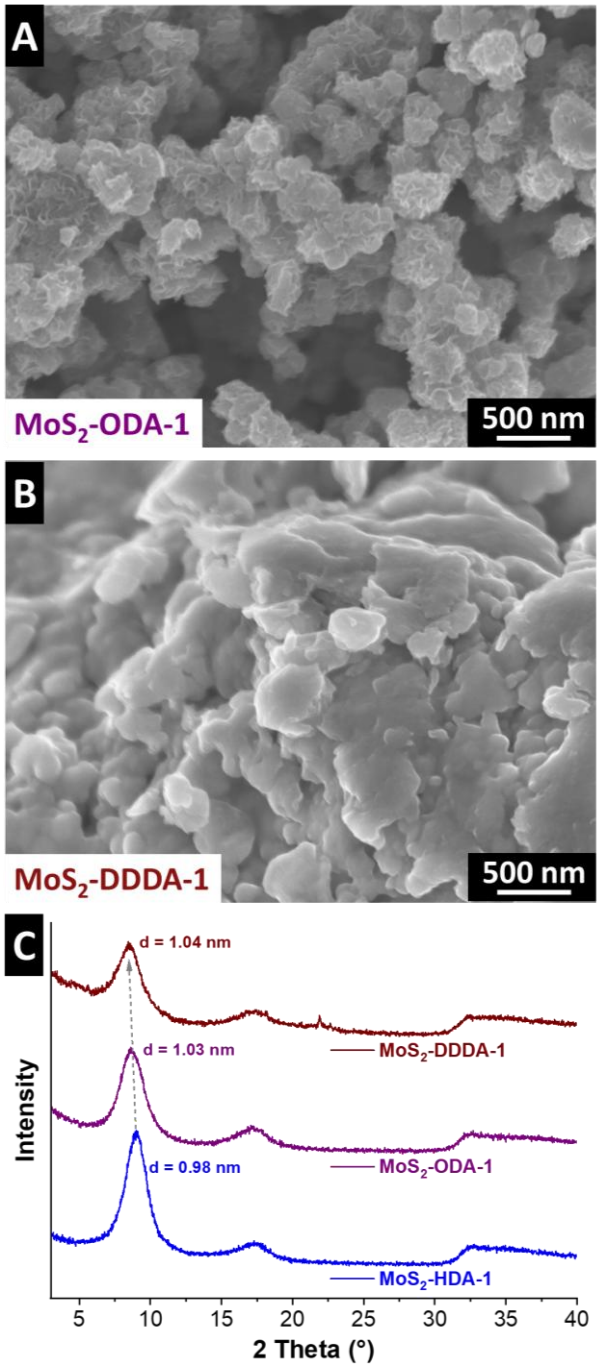

Figure S5: Characterization of interlayer-expanded MoS_2 materials synthesized at pH 1 using different organic pillar molecules, i.e., ODA and DDDA. Scanning electron micrographs of (A) MoS_2-ODA-1 and (B) MoS_2-DDDA-1, and (C) X-ray diffractograms with reproduced diffractogram of MoS_2-HDA-1 synthesized at pH 1 for direct comparison. The results demonstrate that larger sized molecules only lead to a minor further increase in d-spacing, indicating that the molecules' arrangement in the confined interlayer space is close to parallel to the MoS_2 sheets.

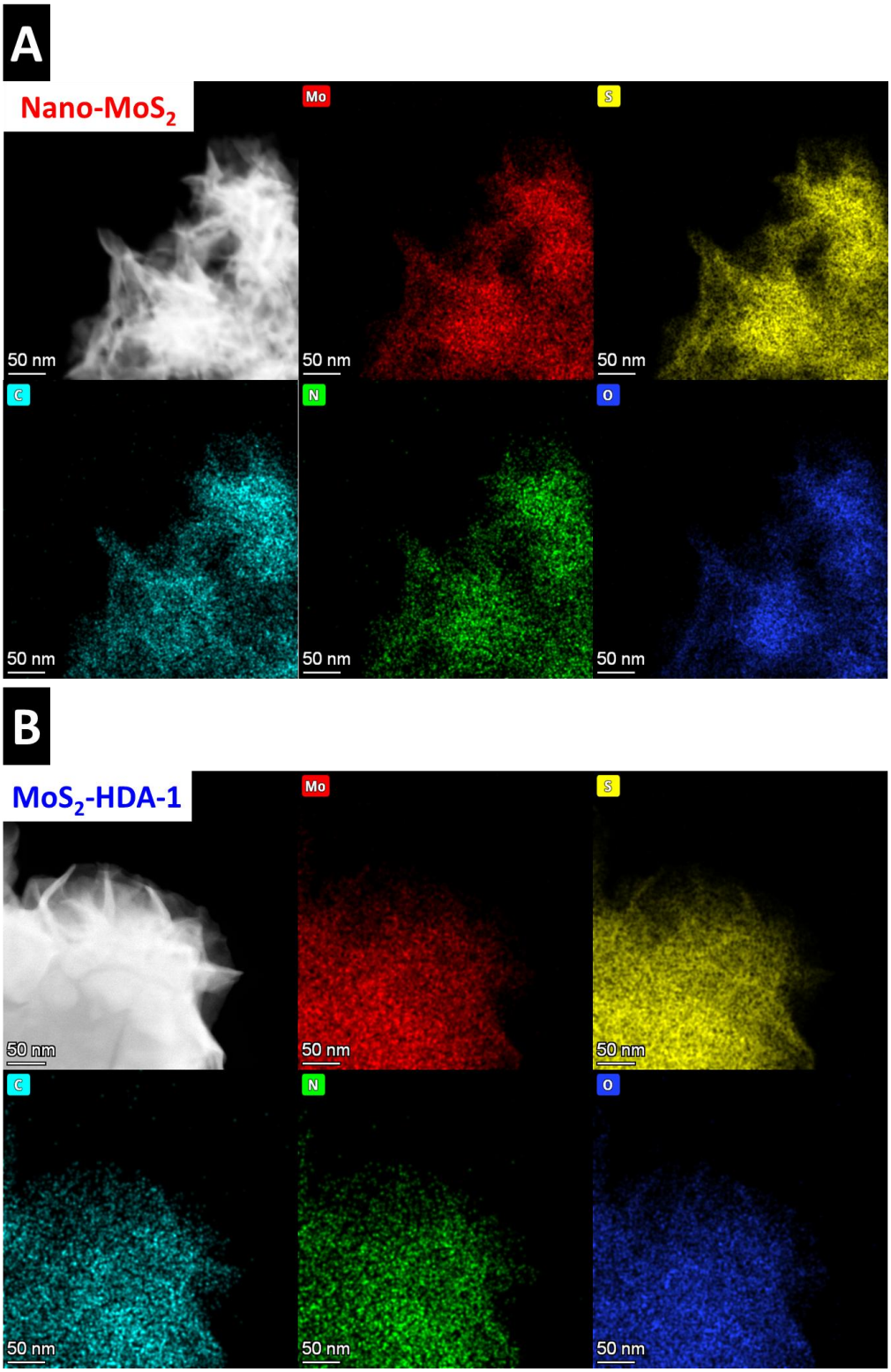

Figure S6: HAADF images from STEM technique including elemental mappings from energy dispersive X-ray spectroscopy (EDX) for Mo, S, C, N, and O of (A) nano-MoS_2 and (B) MoS_2-HDA-1, demonstrating even distribution of all elements throughout the samples.

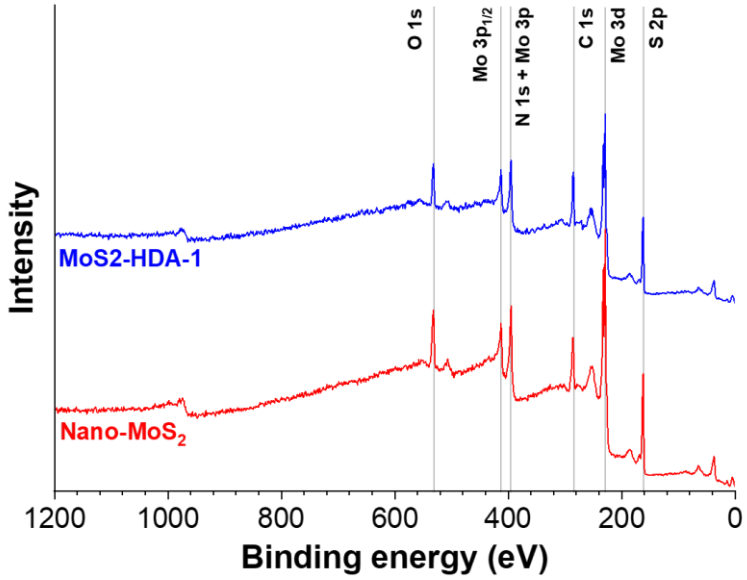

Figure S7: Full survey X-ray photoelectron spectra of nano-MoS_2 and MoS_2-HDA-1.

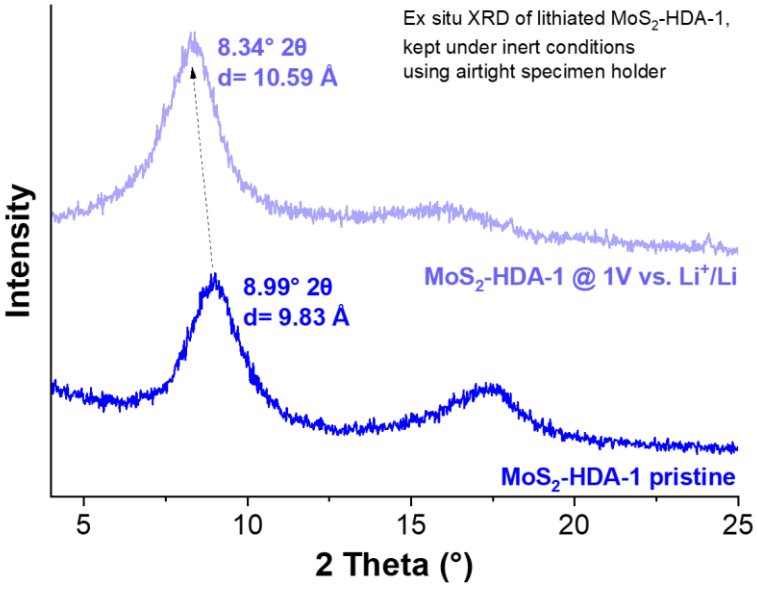

Figure S8: X-ray diffractograms of pristine MoS_2-HDA-1 and fully lithiated MoS_2-HDA-1 after the first electrochemical reduction to 1.0 V vs. Li^+/Li, indicating an increase in d-spacing from 9.83 to 10.59 Å after lithiation. The lithiated electrode was removed from the coin cell in a glovebox, rinsed with DEC solvent, placed in an airtight XRD specimen holder and immediately measured.

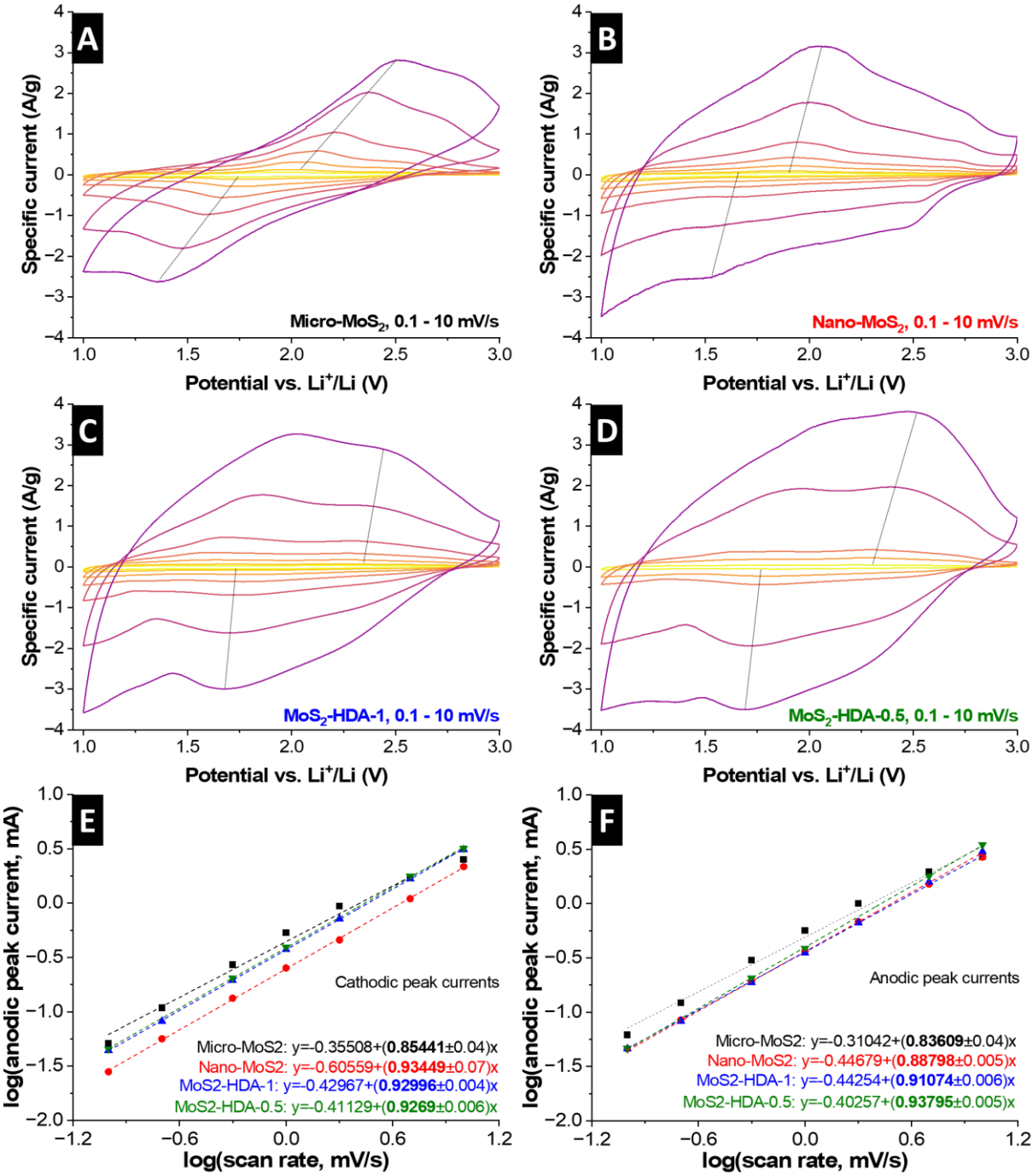

Figure S9: ***b*-value analysis**: Cyclic voltammograms with varying sweep rates from 0.1 – 10 mV/s for (a) micro-MoS_2, (B) nano-MoS_2, (C) MoS_2-HDA-1, and (D) MoS_2-HDA-0.5. Logarithmic plot of (E) cathodic peak current and (F) anodic peak current against logarithmic sweep rates, including linear fits of the data points. The slopes of the linear fits are indicated in the fit functions, corresponding to the cathodic or anodic *b*-value of the respective sample.

Table S1: Elemental composition calculated from STEM EDX analysis.

Element	**Nano-MoS_2 (at. %)**	**MoS_2-HDA-1 (at. %)**
C	6.48	16.70
S	61.25	50.56
Mo	22.54	16.85
O	8.49	10.67
N	1.24	5.22

Table S2: Elemental composition calculated from XPS surface analysis.

Signal	**Nano-MoS_2 (at. %)**	**MoS_2-HDA-1 (at. %)**
C 1s	34.71	39.27
S 2p	33.67	30.99
Mo 3d	18.59	18.66
O 1s	13.04	11.08

Appendix 5.2: supporting information

Study II: Interlayer Spacing Control of MoS_2 with Covalent Thiol Functionalization: Understanding Structure and Electrochemistry from Experiments and Simulation

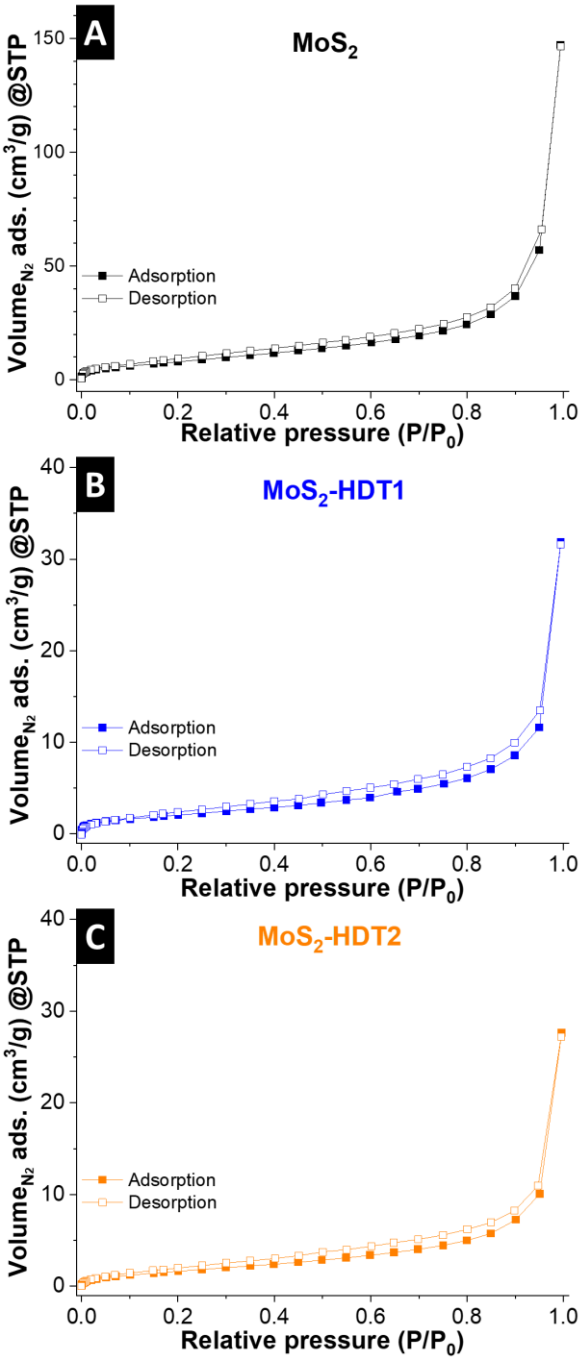

Figure S10: Nitrogen adsorption-desorption isotherms of (a) pristine MoS_2, (b) MoS_2-HDT1, and (c) MoS_2-HDT2 samples.

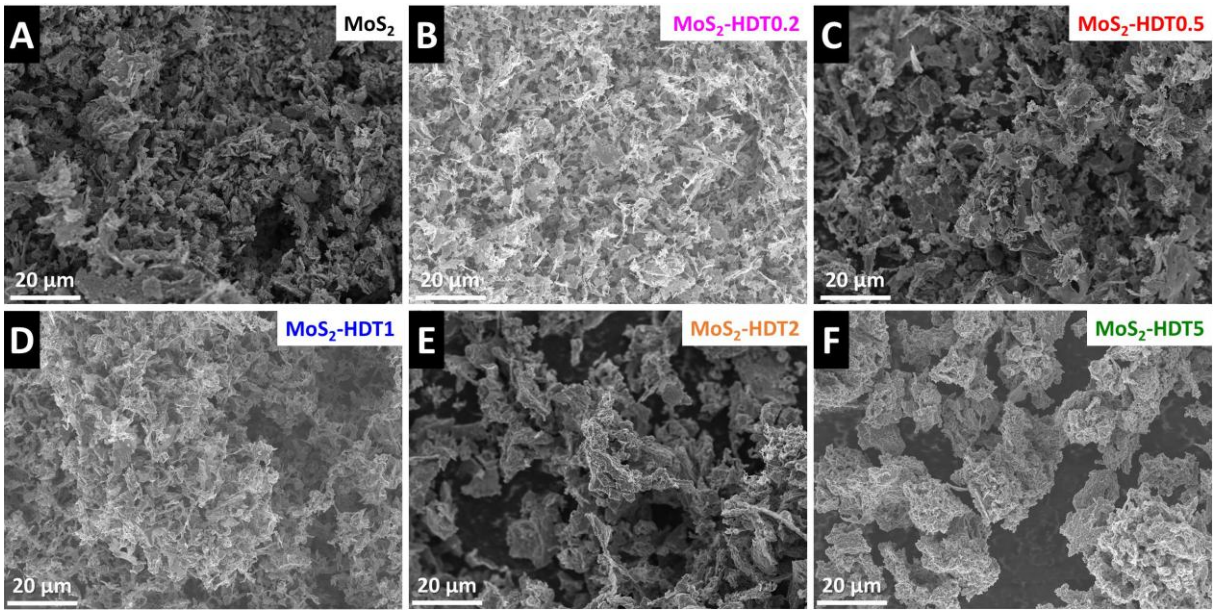

Figure S11: Scanning electron micrographs of (A) MoS_2, (B) MoS_2-HDT0.2, (C) MoS_2-HDT0.5, (D) MoS_2-HDT1, (E) MoS_2-HDT2, and (F) MoS_2-HDT5.

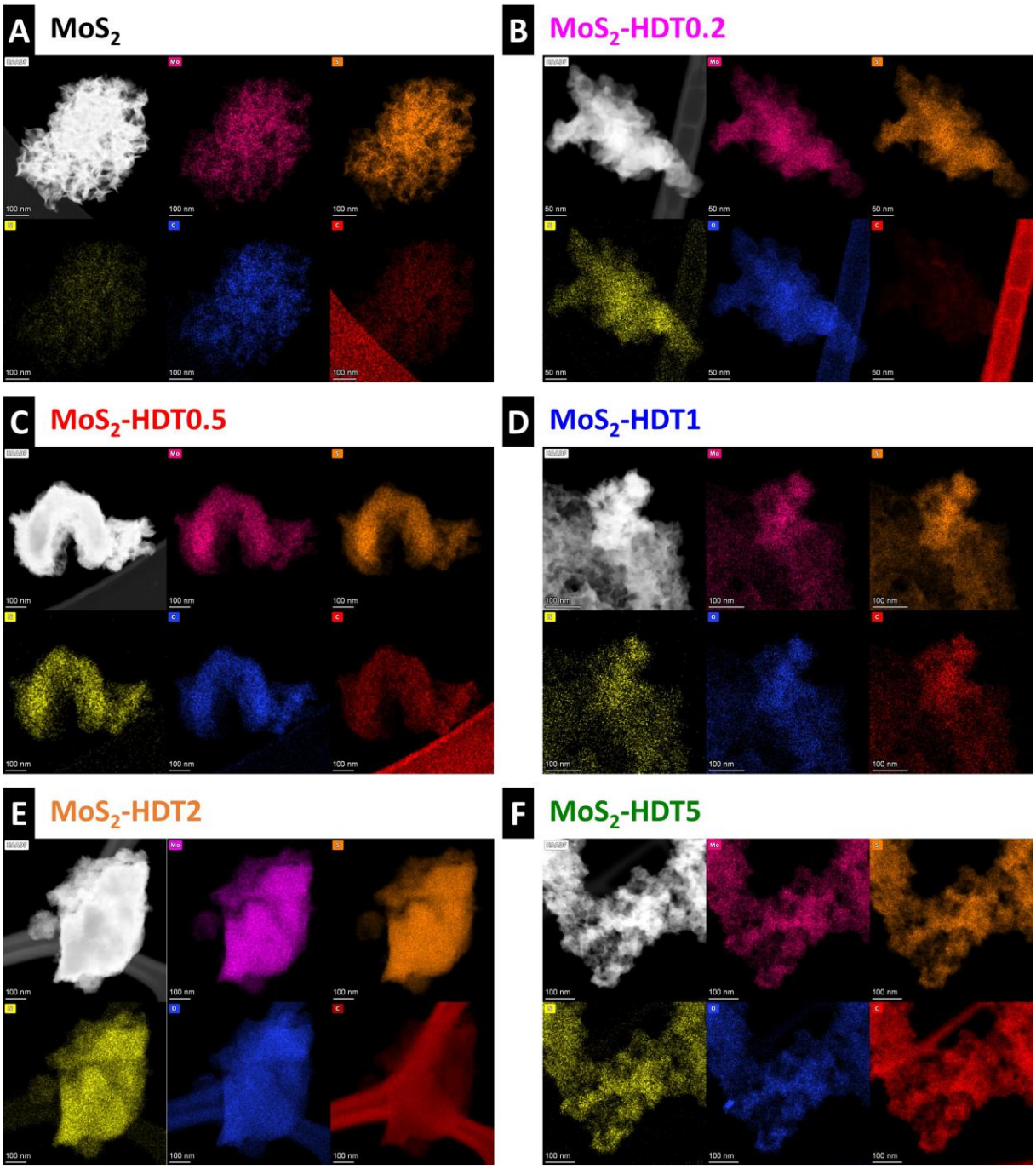

Figure S12: Elemental mapping of molybdenum (pink), sulfur (orange), nitrogen (yellow), oxygen (blue), and carbon (red) by EDX spectroscopy in STEM mode. Inset: High-angle annular dark field images.

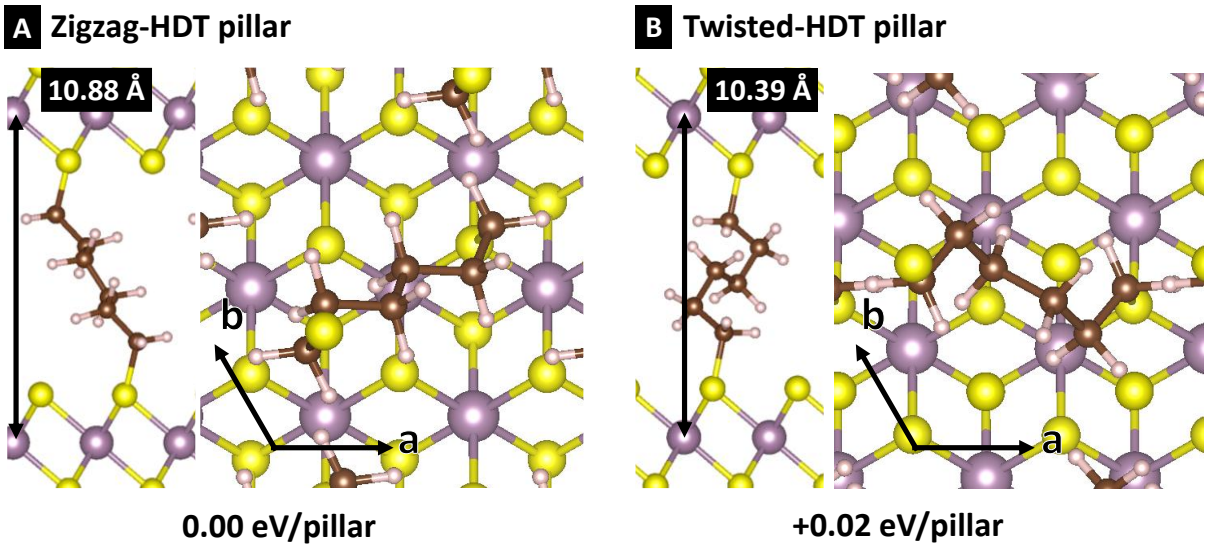

Figure S13: The two most stable geometries of the inserted HDT pillar in MoS_2 were simulated and compared for both the "zigzag" and "twisted" structures as shown in side views (left) and top view (right). The relative energy is provided in eV per number of inserted pillars, as shown below.

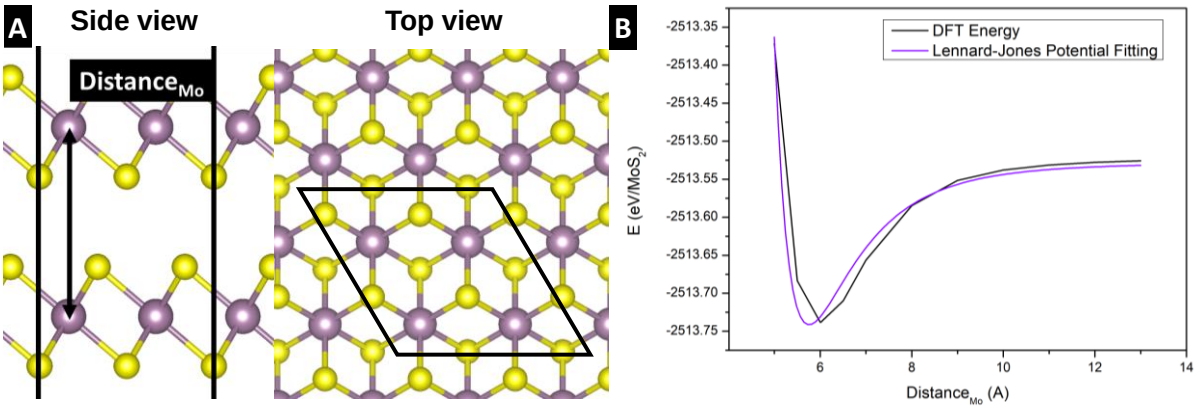

Figure S14: The increase in Mo-Mo distance in pristine MoS_2 and the corresponding energy calculated using DFT were compared. The results follow the Lennard-Jones potential.

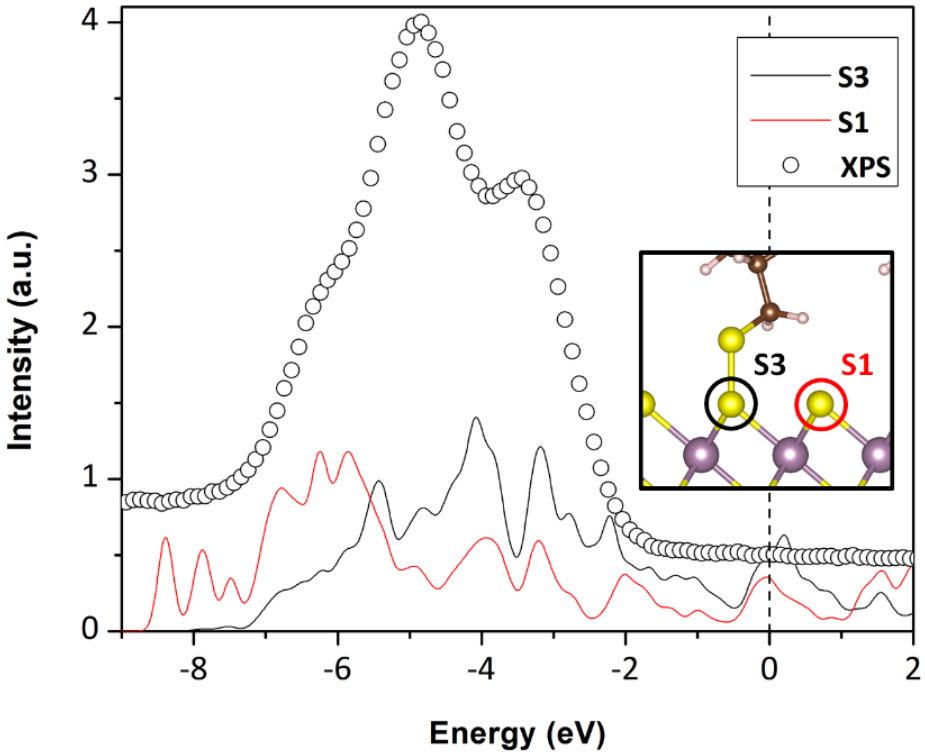

Figure S15: The DOS for the sulfur p orbital in pristine MoS_2 (red) and p orbital of a sulfur atom in MoS_2 with an extra bonded HDT molecule (black), both found to be stable configurations, compared with the experimental XPS spectrum of MoS_2-HDT2 taken from **Fig. 5.10F** (circles).

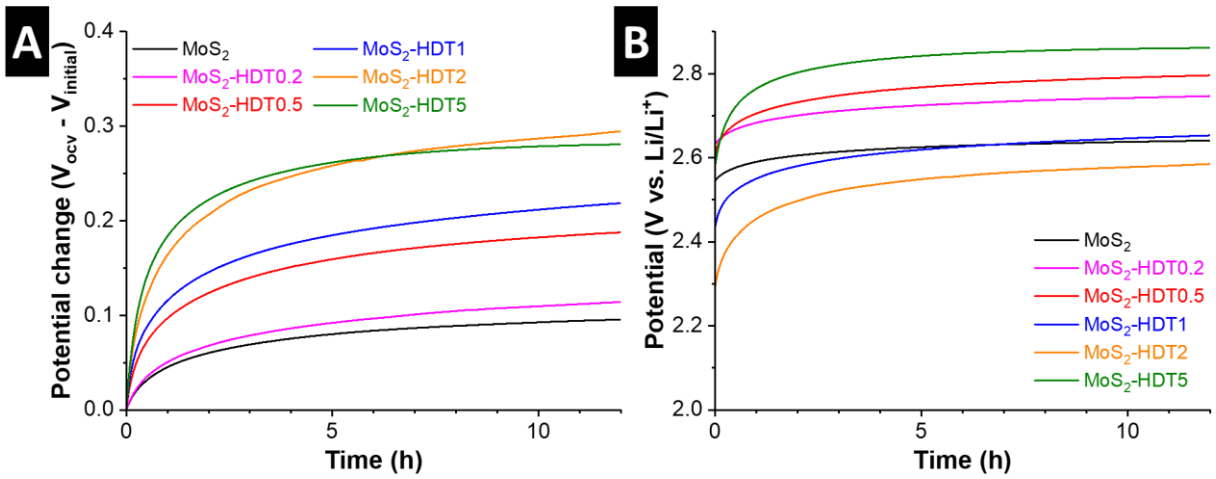

Figure S16: Development of the OCV of freshly assembled coin cells over 12 hours, prior to the start of the electrochemical measurements, (A) in terms of potential change over time, and (B) overall development of potential versus Li^+/Li, i.e., the cell voltage in the coin cell.

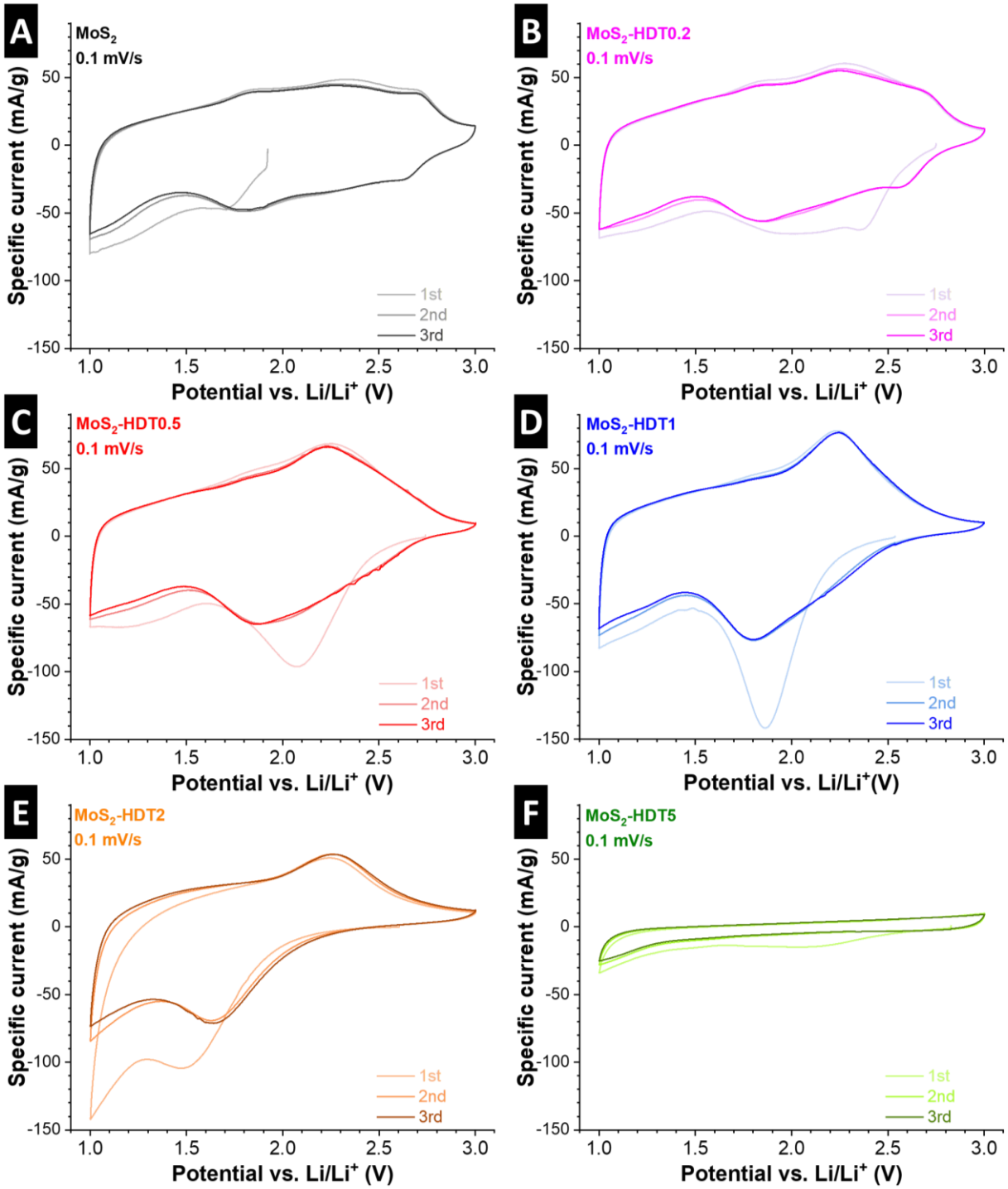

Figure S17: Cyclic voltammograms at 0.1 mV/s of the first three cycles of all MoS_2-based samples. Recorded in coin cells in LP30 electrolyte at a constant temperature of 20 °C.

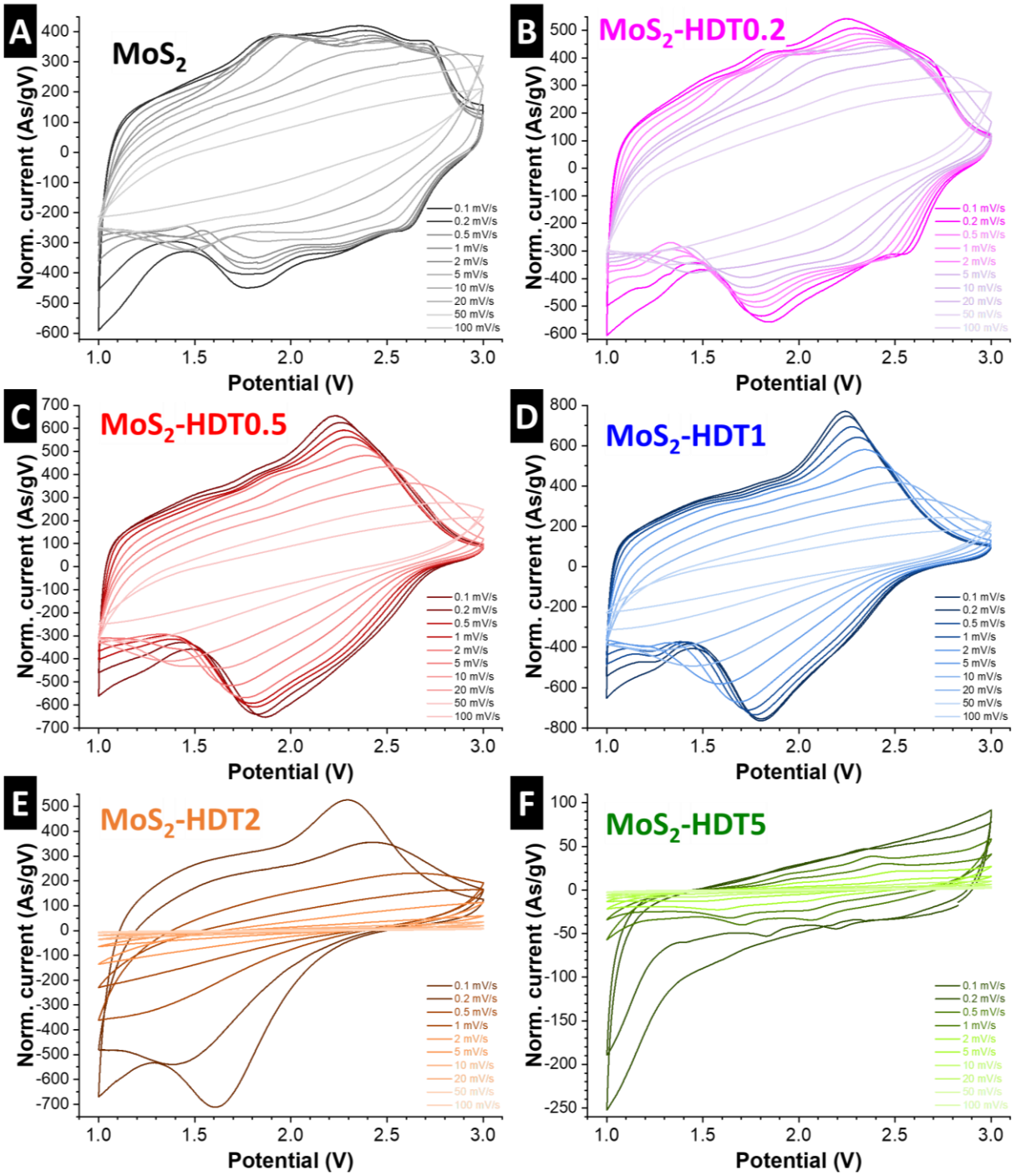

Figure S18: Cyclic voltammograms of all MoS_2-based samples at sweep rates of 0.1, 0.2, 0.5, 1, 2, 5, 10, 20, 50, and 100 mV/s. Current is normalized by scan rate for better visibility of low sweep rates. Recorded in coin cells in LP30 electrolyte at a constant temperature of 20 °C.

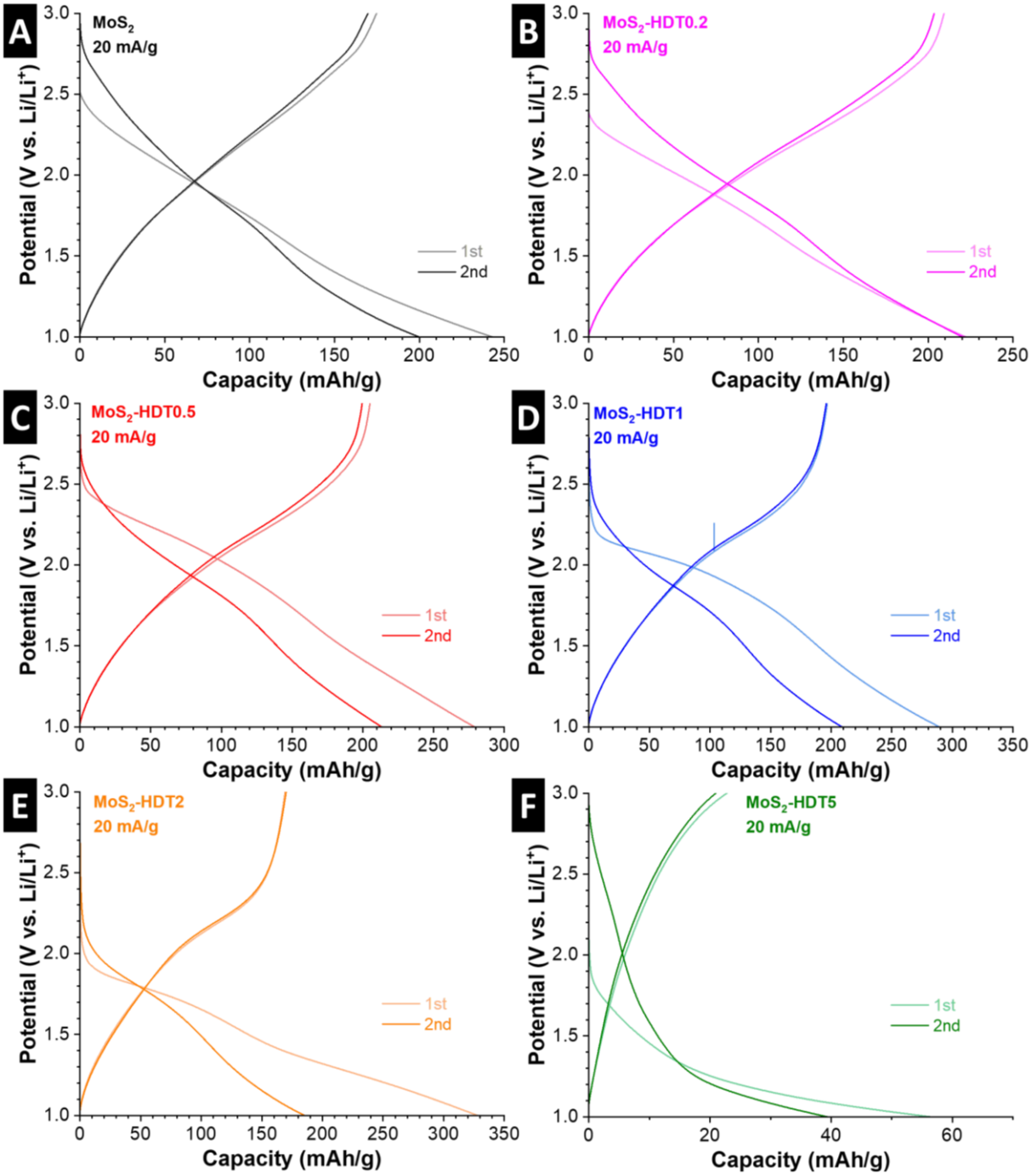

Figure S19: First two GCD curves of all MoS_2-based samples at a specific current of 20 mA/g. Recorded in coin cells in LP30 electrolyte at a constant temperature of 20 °C.

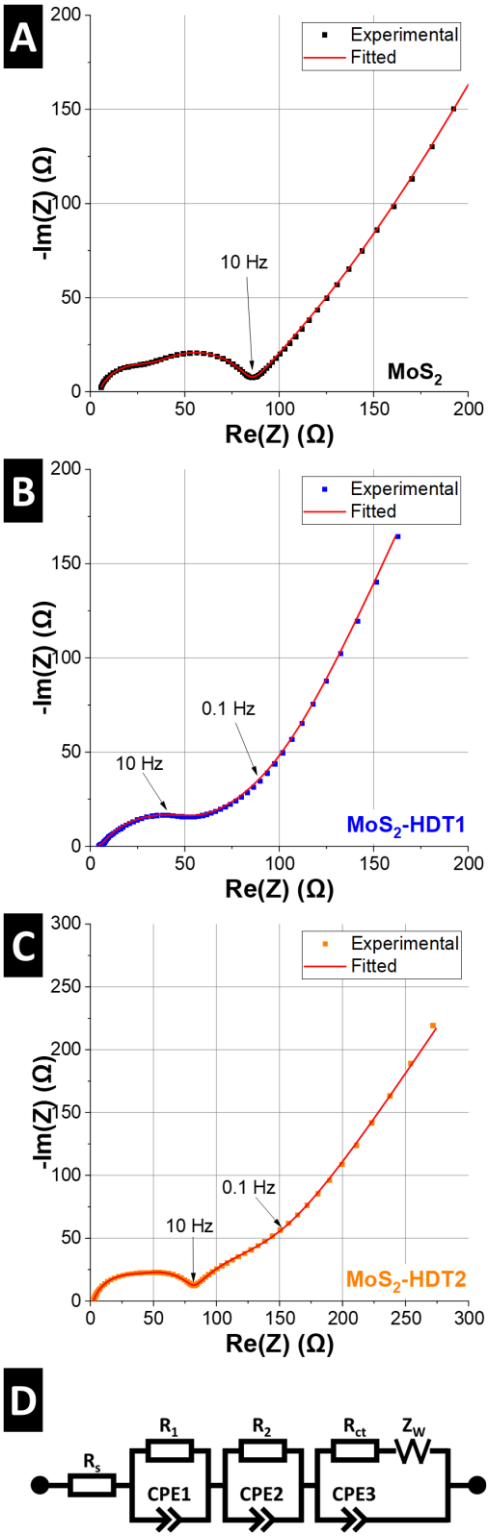

Figure S20: Electrochemical impedance spectra of (A) MoS_2, (B) MoS_2-HDT1, and (C) MoS_2-HDT2 at 1.2 V vs. Li^+/Li. The data is fitted using the equivalent circuit shown in (D). R_s corresponds to the ohmic resistance of the electrochemical cell, the first RQ-element is to correct for high-frequency artifacts from the CE, the second RQ-element corresponds to surface film impedance, R_{ct} is the charge transfer resistance and Z_w is an open Warburg element corresponding to finite-length diffusion.

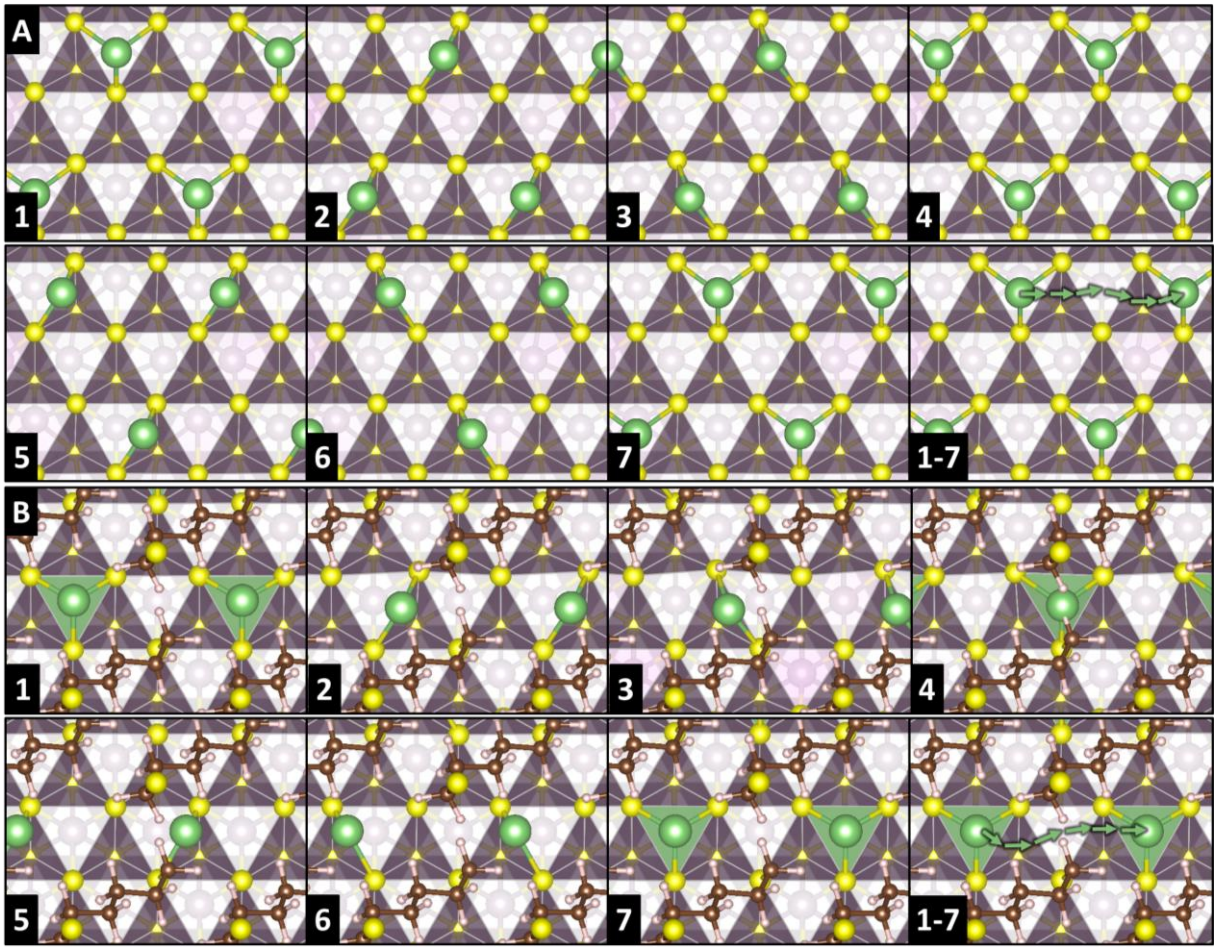

Figure S21: The top view of the complete trajectory for each CI-NEB simulation is presented for (A) pristine MoS_2 and (B) MoS_2-HDT. The pillar restructuring is observed in image **B3**.

Appendix 5.3: supporting information

Study III: Interlayer Expansion of Bulk MoS_2 via Top-Down Organic Pillaring Enables Tunable Li^+ Intercalation and Controlled Solvent Co-Intercalation

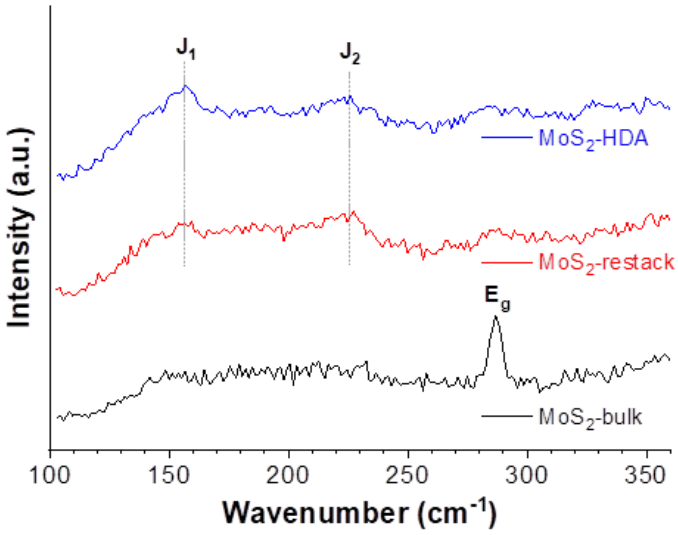

Figure S22: Supplementary Raman spectra of MoS_2-bulk, MoS_2-restack, and MoS_2-HDA.

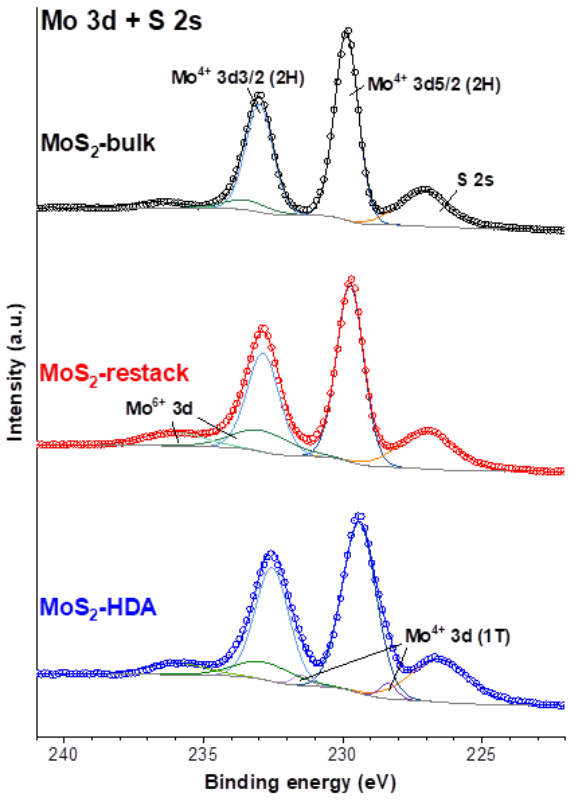

Figure S23: XPS spectra of the Mo 3d and S 2s regions of MoS_2-bulk (black), MoS_2-restack (red), and MoS_2-HDA (blue).

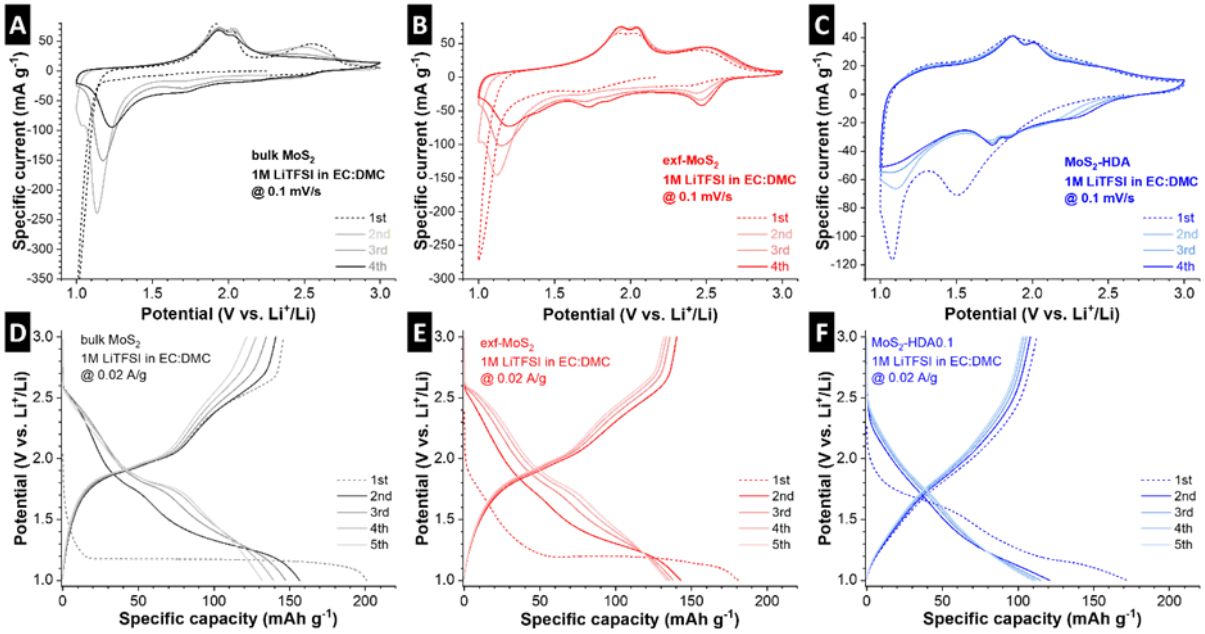

Figure S24: Initial CV and GCD cycles at 0.1 mV s^{-1} and 0.02 A g^{-1}, respectively, in carbonate electrolyte. (A, D) MoS_2-bulk, (B, E) MoS_2-restack, and (C, F) MoS_2-HDA.

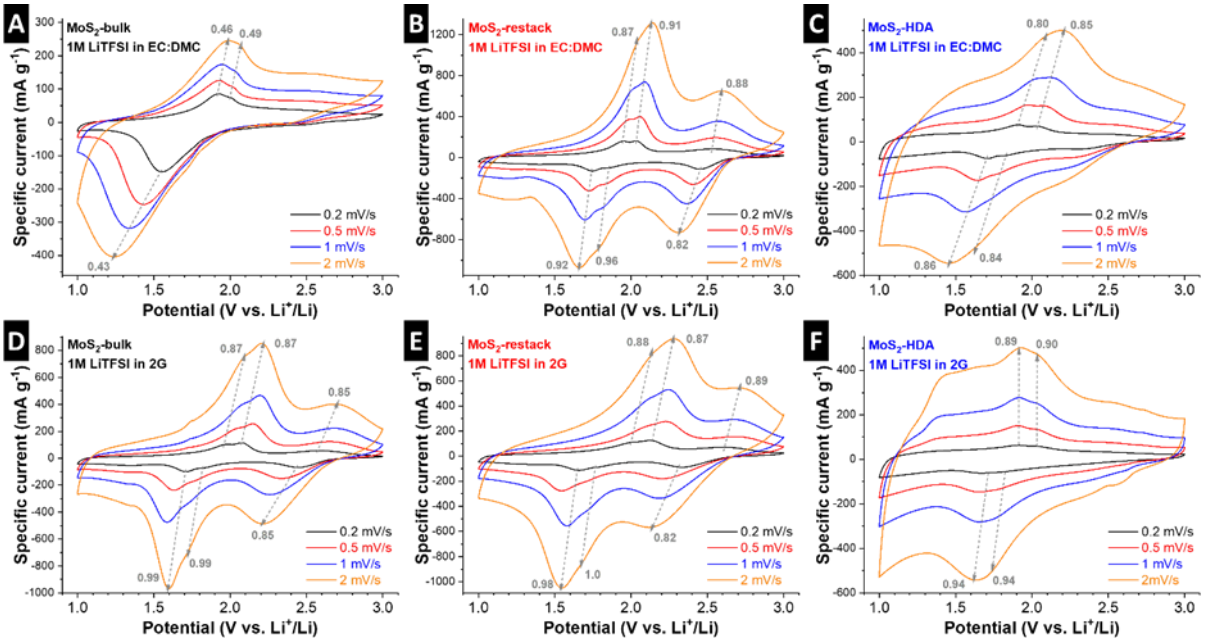

Figure S25: Cyclic voltammograms at different scan rates (0.2-2 mV s^{-1}) for (A) MoS_2-bulk, (B) MoS_2-restack, and (C) MoS_2-HDA electrodes in 1M LiTFSI in carbonate electrolyte, and for (D) MoS_2-bulk, (E) MoS_2-restack, and (F) MoS_2-HDA electrodes in diglyme electrolyte. The corresponding *b*-values, derived from the relationship $i = a \cdot v^b$, are indicated for the characteristic redox peaks and were used to evaluate the charge storage kinetics.

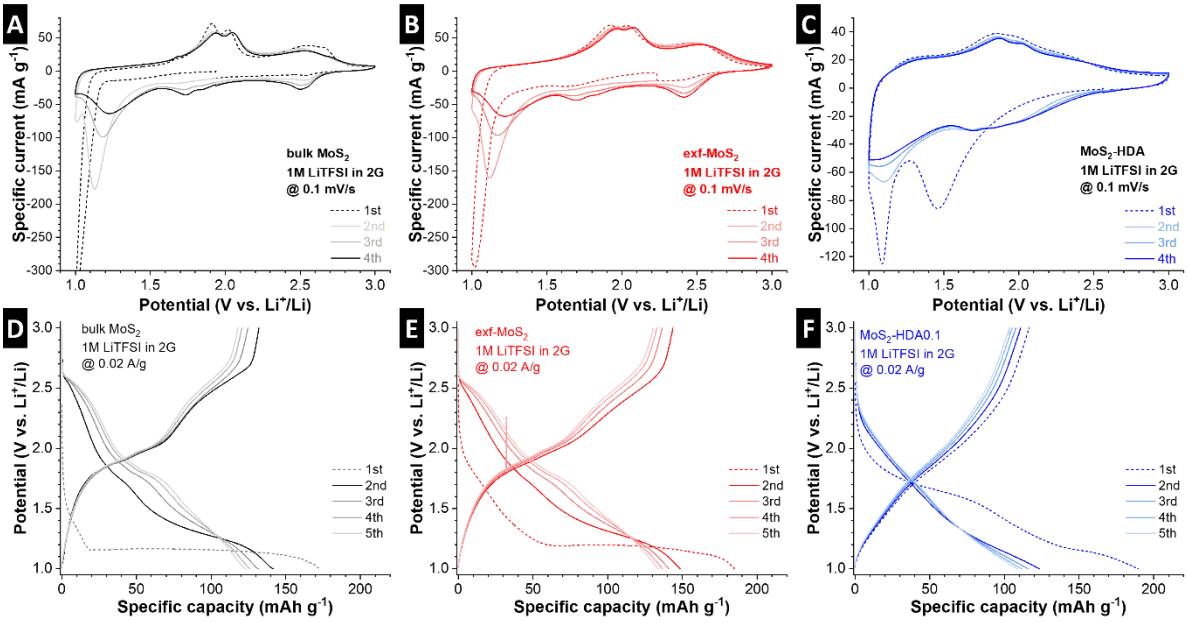

Figure S26: Initial CV and GCD cycles at 0.1 mV s^{-1} and 0.02 A g^{-1}, respectively, in diglyme electrolyte. (A, D) MoS_2-bulk, (B, E) MoS_2-restack, and (C, F) MoS_2-HDA.

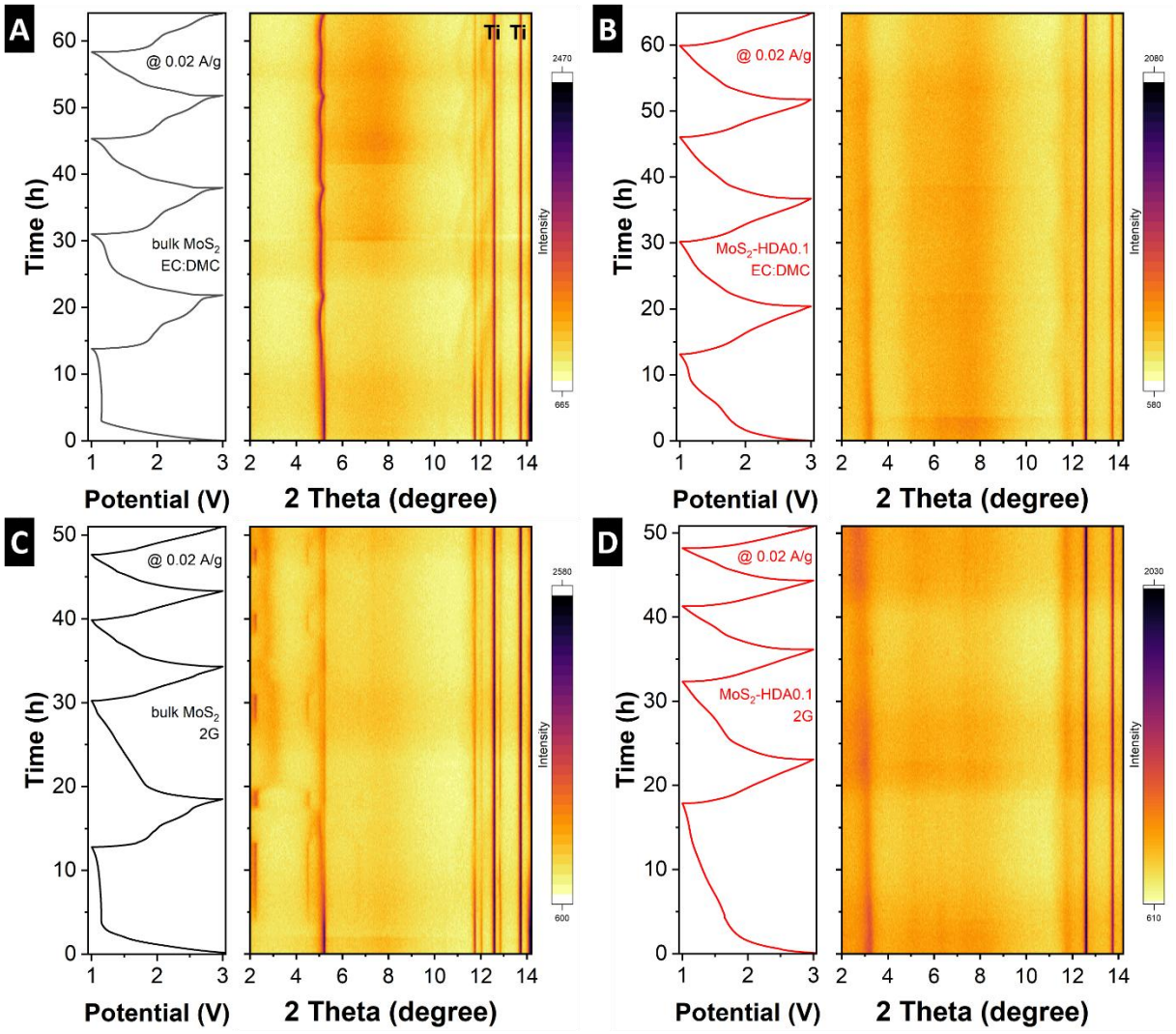

Figure S27: Full range operando X-ray diffraction measurements of (A) MoS_2-bulk and (B) MoS_2-HDA in carbonate electrolyte, and (C) MoS_2-bulk and (D) MoS_2-HDA in diglyme electrolyte. Each panel shows (left to right) the corresponding galvanostatic profile, the evolution of the low *d*-spacing (high-angle) region, and the full diffraction patterns collected using an Ag X-ray source.

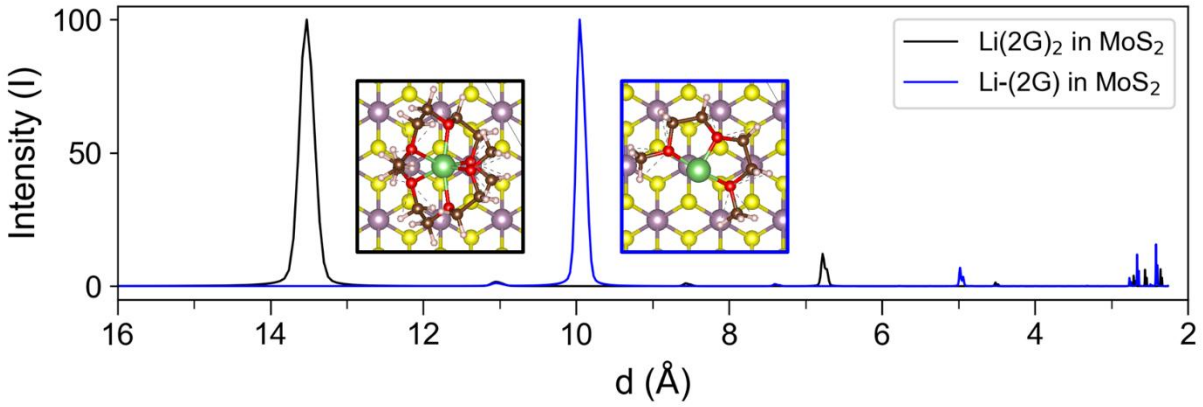

Figure S28: Simulated X-ray diffraction patterns of Li-$(2G)_2$ (black) and Li-(2G) (blue) complexes intercalated in MoS_2. The dominant reflections correspond to the $(001)_{co}$ planes, reflecting the interlayer spacing defined by the respective coordination structures (modeled using neutral Li-$(2G)_x$ complexes). Insets show the optimized geometries of the intercalated Li-$(2G)_2$ and Li-(2G) complexes within the MoS_2 interlayer space. The Li-$(2G)_2$ configuration yields an interlayer spacing of 13.55 Å, while the Li-(2G) complex shows ca. 9.9 Å.

List of Abbreviations

Abbreviation	Full Name
2D	Two-dimensional
2G	Diglyme
ATR	Attenuated Total Reflectance
BE	Binding energy
BET	Brunauer–Emmett–Teller
BuLi	Butyllithium
CB	Carbon black
CE	Counter electrode
CI-NEB	Climbing image nudged elastic band
CPE	Constant phase element
CV	Cyclic voltammetry
DDDA	1,12-diaminododecane
DEC	Diethyl carbonate
DFT	Density functional theory
DI	Deionized
DLS	Dynamic light scattering
DMC	Dimethyl carbonate
DTG	Derivative thermogravimetry
dyNEB	Dynamic nudged elastic band
EC	Ethylene carbonate
ECD	Electrochemical dilatometry
EDLC	Electrical double-layer capacitor
EDX	Energy-dispersive X-ray
EES	Electrochemical energy storage
EIS	Electrochemical impedance spectroscopy
EVs	Electric vehicles
FTIR	Fourier transform infrared spectroscopy
GCD	Galvanostatic charge/discharge
GIC	Graphite intercalation compound
HAADF	High-angle annular dark-field
HDA	1,6-hexanediamine
HDT	1,6-hexanedithiol
ICP	Inductively coupled plasma spectroscopy
ICP-OES	Inductively coupled plasma optical emission spectroscopy

List of Abbreviations

KE	Kinetic energy
LIB	Lithium-ion battery
MoS_2	Molybdenum disulfide
NMP	N-Methyl-2-pyrrolidone
OCV	Open circuit voltage
ODA	1,8-octyldiamine
ONCV	Orthogonal norm-conserving Vanderbilt
PBE	Perdew-Burke-Ernzerhof
PEO	Polyethylene oxide
PV	Potovoltaic
PVDP	Polyvinylidene difluoride
SC	Supercapacitor
SE	Secondary electron
SEM	Scanning electron microscopy
SOC	State of charge
SPEIS	Staircase potentio-electrochemical impedance spectroscopy
SSA	Specific surface area
STEM	Scanning transmission electron microscopy
TEM	Transmission electron microscopy
TGA	Thermogravimetric analysis
TMA	Tetramethylammonium
TMD	Transition metal dichalcogenide
TMO	Transition metal oxide
vdW	van der Waals
WE	Working electrode
XPS	X-ray photoelectron spectroscopy
XRD	X-ray diffraction

List of Tables

List of Figures

References

(1) Solyali, D.; Safaei, B.; Zargar, O.; Aytac, G. A Comprehensive State-of-the-Art Review of Electrochemical Battery Storage Systems for Power Grids. *Int. J. Energy Res.* **2022**, *46* (13), 17786–17812.

(2) Njema, G. G.; Ouma, R. B. O.; Kibet, J. K. A Review on the Recent Advances in Battery Development and Energy Storage Technologies. *J. Renewable Energy* **2024**, *1*, 2329261.

(3) Wang, L.; Zhang, Q.; Liu, J.; Wang, G. Science Mapping the Knowledge Domain of Electrochemical Energy Storage Technology: A Bibliometric Review. *J. Energy Storage* **2024**, *77*, 109819.

(4) Amer, M.; Masri, J.; Dababat, A.; Sajjad, U.; Hamid, K. Electric Vehicles: Battery Technologies, Charging Standards, AI Communications, Challenges, and Future Directions. *Energy Convers. Manage.: X* **2024**, *24*, 100751.

(5) De Santillana, G. Alessandro Volta. *Sci. Am.* **1965**, *212* (1), 82–91.

(6) Simon, P.; Gogotsi, Y. Perspectives for Electrochemical Capacitors and Related Devices. *Nat. Mater.* **2020**, *19* (11), 1151–1163.

(7) Xie, J.; Lu, Y. C. A Retrospective on Lithium-Ion Batteries. *Nat. Commun.* **2020**, *11* (1), 2499.

(8) Kurzweil, P. Gaston Planté and His Invention of the Lead-Acid Battery-The Genesis of the First Practical Rechargeable Battery. *J. Power Sources* **2010**, *195* (14), 4424–4434.

(9) Whittingham, M. S.; Gamble, F. R. The Lithium Intercalates of the Transition Metal Dichalcogenides. *Mat. Res. Bull.* **1975**, *10* (5), 363–371.

(10) Mizushima, K.; Jones, P. C.; Wiseman, P. J.; Goodenough, J. B. LixCoO2 (0< X<-1): A New Cathode Material for Batteries of High Energy Density. *Mat. Res. Bull.* **1980**, *15* (6), 783–789.

(11) Yoshino, A.; Sanechika, K.; Nakajima, T. USP4, 668,595. JP1989293, 1985.

(12) Yoshino, A. The Birth of the Lithium-Ion Battery. *Angew. Chem., Int. Ed.* **2012**, *51* (24), 5798–5800.

(13) Winter, M.; Brodd, R. J. What Are Batteries, Fuel Cells, and Supercapacitors? *Chem. Rev.* **2004**, *104* (10), 4245–4270.

(14) Lee, J.; Lee, J.; Lim, E. Recent Progress and Challenges in Potassium-Ion Battery Anodes: Towards High-Performance Electrodes. *Sci. Technol. Adv. Mater.* **2025**, *26* (1), 2518746.

(15) Nekahi, A.; Madikere Raghunatha Reddy, A. K.; Li, X.; Deng, S.; Zaghib, K. Rechargeable Batteries for the Electrification of Society: Past, Present, and Future. *Electrochem. Energy Rev.* **2025**, *8* (1), 1.

(16) Maniam, S. *Batteries: The Future of Energy Storage*; Maniam, S., Ed.; Jenny Stanford Publishing, 2024.

(17) Bruce, P. G.; Saidi, M. Y. The Mechanism of Electrointercalation. *J. Electroanal. Chem.* **1992**, *322* (1–2), 93–105.

(18) Schoetz, T.; Gordon, L. W.; Ivanov, S.; Bund, A.; Mandler, D.; Messinger, R. J. Disentangling Faradaic, Pseudocapacitive, and Capacitive Charge Storage: A Tutorial for the Characterization of Batteries, Supercapacitors, and Hybrid Systems. *Electrochim. Acta* **2022**, *412*, 140072.

(19) Bard, A. J.; Faulkner, L. R.; White, H. S. *Electrochemical Methods: Fundamentals and Applications*; John Wiley & Sons, 2022.

(20) Khan, F. M. N. U.; Rasul, M. G.; Sayem, A. S. M.; Mandal, N. Maximizing Energy Density of Lithium-Ion Batteries for Electric Vehicles: A Critical Review. *Energy Rep.* **2023**, *9*, 11–21.

(21) Lain, M. J.; Kendrick, E. Understanding the Limitations of Lithium Ion Batteries at High Rates. *J. Power Sources* **2021**, *493*, 229690.

(22) Ding, Y.; Cano, Z. P.; Yu, A.; Lu, J.; Chen, Z. Automotive Li-Ion Batteries: Current Status and Future Perspectives. *Electrochem. Energy Rev.* **2019**, *2* (1), 1–28.

(23) Kötz, R.; Carlen, M. Principles and Applications of Electrochemical Capacitors. *Electrochim. Acta* **2000**, *45* (15–16), 2483–2498.

(24) Miller, J. R.; Burke, A. Electrochemical Capacitors: Challenges and Opportunities for Real-World Applications. *Electrochem. Soc. Interface* **2008**, *17* (1), 53–57.

(25) Conway, B. E. *Electrochemical Supercapacitors: Scientific Fundamentals and Technological Applications*; Springer, 1999.

(26) Helmholtz, H. Ueber Einige Gesetze Der Vertheilung Elektrischer Ströme in Körperlichen Leitern, Mit Anwendung Auf Die Thierisch-Elektrischen Versuche (Schluss.). *Ann. Phys.* **1853**, *165* (7), 353–377.

(27) Chapman, D. L. LI. A Contribution to the Theory of Electrocapillarity. *The London, Edinburgh, and Dublin Philosophical Magazine and Journal of Science* **1913**, *25* (148), 475–481.

(28) Gouy, M. Sur La Constitution de La Charge Électrique à La Surface d'un Électrolyte. *J. Phys. Thor. Appl.* **1910**, *9* (1), 457–468.

(29) Stem, O. The Theory of the Electrolytic Double-Layer. *Z. Elektrochem.* **1924**, *30* (508), 1014–1020.

(30) Ikram, M.; Raza, A.; Ikram, M.; Mahmood, A. Carbon Nanocomposite-Based SCs as Wearable Energy Storage. In *Nanostructured Materials for Supercapacitors. Advances in Material Research and Technology*; Thomas, S., Gueye, A. B., Gupta, R. K., Eds.; Springer, Cham, 2022; pp 451–483.

(31) Conway, B. E. Transition from "Supercapacitor" to "Battery" Behavior in Electrochemical Energy Storage. *J. Electrochem. Soc.* **1991**, *138* (6), 153.

(32) Gao, X.; Wu, H.; Su, C.; Lu, C.; Dai, Y.; Zhao, S.; Hu, X.; Zhao, F.; Zhang, W.; Parkin, I. P.; Carmalt, C. J.; He, G. Recent Advances in Carbon-Based Nanomaterials for Multivalent-Ion Hybrid Capacitors: A Review. *Energy Environ. Sci.* **2023**, *16* (4), 1364–1383.

(33) Abruña, H. D.; Kiya, Y.; Henderson, J. C. Batteries and Electrochemical Capacitors. *Phys. Today* **2008**, *61* (12), 43–47.

(34) Grahame, D. C. Properties of the Electrical Double Layer at a Mercury Surface. I. Methods of Measurement and Interpretation of Results. *J. Am. Chem. Soc.* **1941**, *63* (5), 1207–1215.

(35) Liu, Y.; Jiang, S. P.; Shao, Z. Intercalation Pseudocapacitance in Electrochemical Energy Storage: Recent Advances in Fundamental Understanding and Materials Development. *Mater. Today Adv.* **2020**, *7*, 100072.

(36) Fleischmann, S.; Mitchell, J. B.; Wang, R.; Zhan, C.; Jiang, D. E.; Presser, V.; Augustyn, V. Pseudocapacitance: From Fundamental Understanding to High Power Energy Storage Materials. *Chem. Rev.* **2020**, *120* (14), 6738–6782.

(37) Simon, P.; Gogotsi, Y.; Dunn, B. Where Do Batteries End and Supercapacitors Begin? *Science.* **2014**, *343* (6176), 1210–1211.

(38) Herrero, E.; Buller, L. J.; Abruña, H. D. Underpotential Deposition at Single Crystal Surfaces of Au, Pt, Ag and Other Materials. *Chem. Rev.* **2001**, *101* (7), 1897–1930.

(39) Augustyn, V.; Simon, P.; Dunn, B. Pseudocapacitive Oxide Materials for High-Rate Electrochemical Energy Storage. *Energy Environ. Sci.* **2014**, *7* (5), 1597–1614.

(40) Choi, C.; Ashby, D. S.; Butts, D. M.; DeBlock, R. H.; Wei, Q.; Lau, J.; Dunn, B. Achieving High Energy Density and High Power Density with Pseudocapacitive Materials. *Nat. Rev. Mater.* **2020**, *5* (1), 5–19.

(41) Gogotsi, Y.; Penner, R. M. Energy Storage in Nanomaterials - Capacitive, Pseudocapacitive, or Battery-Like?, *ACS Nano*, **2018**, *12* (3), 2081–2083.

(42) Wang, Y.; Song, Y.; Xia, Y. Electrochemical Capacitors: Mechanism, Materials, Systems, Characterization and Applications, *Chem. Soc. Rev.*, **2016**, *45* (21), 5925–5950.

(43) Lindstrom, H.; Södergren, S.; Solbrand, A.; Rensmo, H.; Hjelm, J.; Hagfeldt, A.; Lindquist, S.-E. Li+ Ion Insertion in TiO_2 (Anatase). 2. Voltammetry on Nanoporous Films. *J. Phys. Chem. B* **1997**, *101*, 7717–7722.

(44) Wang, G.; Yu, M.; Feng, X. Carbon Materials for Ion-Intercalation Involved Rechargeable Battery Technologies. *Chem. Soc. Rev.* **2021**, *50* (4), 2388–2443.

(45) Mukai, K. A Series of Zero-Strain Lithium Insertion Materials That Undergo a Non-Topotactic Reaction, *Electrochim. Acta*, **2018**, *263*, 508–514.

(46) Liu, Y.; Shi, H.; Wu, Z. S. Recent Status, Key Strategies and Challenging Perspectives of Fast-Charging Graphite Anodes for Lithium-Ion Batteries. *Energy Environ. Sci.* **2023**, *16* (11), 4834–4871.

(47) Doh, C. H.; Han, B. C.; Jin, B. S.; Gu, H. B. Structures and Formation Energies of LixC6 (X=1-3) and Its Homologues for Lithium Rechargeable Batteries. *Bull. Korean Chem. Soc.* **2011**, *32* (6), 2045–2050.

(48) Tarascon, J.-M.; Armand, M. Issues and Challenges Facing Rechargeable Lithium Batteries, *Nature*, **2001**, *414*, 359–367.

(49) Park, J.; Xu, Z. L.; Kang, K. Solvated Ion Intercalation in Graphite: Sodium and Beyond. *Front. Chem.* **2020**, *8*, 432.

(50) Doeff, M. M.; Ma, Y.; Visco, S. J.; De Jonghe, L. C. Electrochemical Insertion of Sodium into Carbon. *J. Electrochem. Soc.* **1993**, *140* (12), L169.

(51) Liu, Y.; Merinov, B. V.; Goddard, W. A. Origin of Low Sodium Capacity in Graphite and Generally Weak Substrate Binding of Na and Mg among Alkali and Alkaline Earth Metals. *PNAS* **2016**, *113* (14), 3735–3739.

(52) Jache, B.; Adelhelm, P. Use of Graphite as a Highly Reversible Electrode with Superior Cycle Life for Sodium-Ion Batteries by Making Use of Co-Intercalation Phenomena. *Angew. Chem., Int. Ed.* **2014**, *53* (38), 10169–10173.

(53) Ming, J.; Cao, Z.; Li, Q.; Wahyudi, W.; Wang, W.; Cavallo, L.; Park, K. J.; Sun, Y. K.; Alshareef, H. N. Molecular-Scale Interfacial Model for Predicting Electrode Performance in Rechargeable Batteries. *ACS Energy Lett.* **2019**, *4* (7), 1584–1593.

(54) Goktas, M.; Bolli, C.; Berg, E. J.; Novák, P.; Pollok, K.; Langenhorst, F.; Roeder, M. v.; Lenchuk, O.; Mollenhauer, D.; Adelhelm, P. Graphite as Cointercalation Electrode for Sodium-Ion Batteries: Electrode Dynamics and the Missing Solid Electrolyte Interphase (SEI). *Adv. Energy Mater.* **2018**, *8* (16), 1702724.

(55) Kim, H.; Lim, K.; Yoon, G.; Park, J. H.; Ku, K.; Lim, H. D.; Sung, Y. E.; Kang, K. Exploiting Lithium–Ether Co-Intercalation in Graphite for High-Power Lithium-Ion Batteries. *Adv. Energy Mater.* **2017**, *7* (19), 1700418.

(56) Son, D. K.; Kim, J.; Raj, M. R.; Lee, G. Elucidating the Structural Redox Behaviors of Nanostructured Expanded Graphite Anodes toward Fast-Charging and High-Performance Lithium-Ion Batteries, *Carbon*, **2021**, *175*, 187–201.

(57) Cheng, Q.; Zhang, Y. Multi-Channel Graphite for High-Rate Lithium Ion Battery. *J. Electrochem. Soc.* **2018**, *165* (5), A1104–A1109.

(58) Yuan, M.; Liu, H.; Ran, F. Fast-Charging Cathode Materials for Lithium & Sodium Ion Batteries. *Mater. Today* **2023**, *63*, 360–379.

(59) Lee, W.; Muhammad, S.; Sergey, C.; Lee, H.; Yoon, J.; Kang, Y.; Yoon, W. Advances in the Cathode Materials for Lithium Rechargeable Batteries. *Angew. Chem., Int. Ed.* **2020**, *132* (7), 2578–2605.

(60) Augustyn, V. Tuning the Interlayer of Transition Metal Oxides for Electrochemical Energy Storage. *J. Mater. Res.* **2017**, *32* (1), 2–15.

(61) Okubo, M.; Hosono, E.; Kim, J.; Enomoto, M.; Kojima, N.; Kudo, T.; Zhou, H.; Honma, I. Nanosize Effect on High-Rate Li-Ion Intercalation in $LiCoO_2$ Electrode. *J. Am. Chem. Soc.* **2007**, *129* (23), 7444–7452.

(62) Gan, Z.; Yin, J.; Xu, X.; Cheng, Y.; Yu, T. Nanostructure and Advanced Energy Storage: Elaborate Material Designs Lead to High-Rate Pseudocapacitive Ion Storage. *ACS Nano* **2022**, *16* (4), 5131–5152.

(63) Karol, J.; Ogolla, C. O.; Sotoudeh, M.; Dillenz, M.; Tobis, M.; Vollmer, E.; Malik, Y. T.; Zarrabeitia, M.; Groß, A.; Butz, B.; Fleischmann, S. Nanoconfinement Geometry of

Pillared V_2O_5 Determines Electrochemical Ion Intercalation Mechanisms, Storage Sites, and Diffusion Pathways. *ACS Nano* **2025**, *19* (29), 26904–26919.

(64) Elmanzalawy, M.; Song, H.; Tobis, M.; Leiter, R.; Choi, J.; Moon, H.; Tsai, W. Y.; Jiang, D. en; Fleischmann, S. Nanoconfinement-Induced Electrochemical Ion-Solvent Cointercalation in Pillared Titanate Host Materials. *Angew. Chem., Int. Ed.* **2025**, *137* (20), e202423593.

(65) Zhang, X.; Andris, R.; Averianov, T.; Zachman, M. J.; Pomerantseva, E. Hybrid Bilayered Vanadium Oxide Electrodes with Large and Tunable Interlayer Distances in Lithium-Ion Batteries. *J. Colloid Interface Sci.* **2024**, *674*, 612–623.

(66) Yao, X.; Zhao, Y.; Castro, F. A.; Mai, L. Rational Design of Preintercalated Electrodes for Rechargeable Batteries. *ACS Energy Lett.* **2019**, *4* (3), 771–778.

(67) Dickinson, R. G.; Pauling, L. The Crystal Structure of Molybdenite. *J. Am. Chem. Soc.* **1923**, *45* (6), 1466–1471.

(68) Wilson, J. A.; Yoffe, A. D. The Transition Metal Dichalcogenides Discussion and Interpretation of the Observed Optical, Electrical and Structural Properties. *Adv. Phys.* **1969**, *18* (73), 193–335.

(69) Yun, Q.; Li, L.; Hu, Z.; Lu, Q.; Chen, B.; Zhang, H. Layered Transition Metal Dichalcogenide-Based Nanomaterials for Electrochemical Energy Storage. *Adv. Mater.* **2020**, *32* (1), 1903826.

(70) Roy, S.; Joseph, A.; Zhang, X.; Bhattacharyya, S.; Puthirath, A. B.; Biswas, A.; Tiwary, C. S.; Vajtai, R.; Ajayan, P. M. Engineered Two-Dimensional Transition Metal Dichalcogenides for Energy Conversion and Storage. *Chem. Rev.* **2024**, *124* (16), 9376–9456.

(71) Yang, R.; Fan, Y.; Zhang, Y.; Mei, L.; Zhu, R.; Qin, J.; Hu, J.; Chen, Z.; Hau Ng, Y.; Voiry, D.; Li, S.; Lu, Q.; Wang, Q.; Yu, J. C.; Zeng, Z. 2D Transition Metal Dichalcogenides for Photocatalysis. *Angew. Chem.* **2023**, *135* (13), e202218016.

(72) Fu, Q.; Han, J.; Wang, X.; Xu, P.; Yao, T.; Zhong, J.; Zhong, W.; Liu, S.; Gao, T.; Zhang, Z.; Xu, L.; Song, B. 2D Transition Metal Dichalcogenides: Design, Modulation, and Challenges in Electrocatalysis. *Adv. Mater.* **2021**, *33* (6), 1907818.

(73) Ping, J.; Fan, Z.; Sindoro, M.; Ying, Y.; Zhang, H. Recent Advances in Sensing Applications of Two-Dimensional Transition Metal Dichalcogenide Nanosheets and Their Composites. *Adv. Funct. Mater.* **2017**, *27* (19), 1605817.

(74) Goswami, P.; Gupta, G. Recent Progress of Flexible NO_2 and NH_3 Gas Sensors Based on Transition Metal Dichalcogenides for Room Temperature Sensing. *Mater. Today Chem.* **2022**, *23*, 100726.

(75) Zhao, B.; Shen, D.; Zhang, Z.; Lu, P.; Hossain, M.; Li, J.; Li, B.; Duan, X. 2D Metallic Transition-Metal Dichalcogenides: Structures, Synthesis, Properties, and Applications. *Adv. Funct. Mater.* **2021**, *31* (48), 2105132.

(76) Stark, M. S.; Kuntz, K. L.; Martens, S. J.; Warren, S. C. Intercalation of Layered Materials from Bulk to 2D. *Adv. Mater.* **2019**, *31* (27), 1808213.

(77) Chhowalla, M.; Shin, H. S.; Eda, G.; Li, L. J.; Loh, K. P.; Zhang, H. The Chemistry of Two-Dimensional Layered Transition Metal Dichalcogenide Nanosheets. *Nat. Chem.* **2013**, *5* (4), 263–275.

(78) Voiry, D.; Mohite, A.; Chhowalla, M. Phase Engineering of Transition Metal Dichalcogenides. *Chem. Soc. Rev.* **2015**, *44* (9), 2702–2712.

(79) Acerce, M.; Voiry, D.; Chhowalla, M. Metallic 1T Phase MoS_2 Nanosheets as Supercapacitor Electrode Materials. *Nat. Nanotechnol.* **2015**, *10* (4), 313–318.

(80) Lin, Y. C.; Dumcenco, D. O.; Huang, Y. S.; Suenaga, K. Atomic Mechanism of the Semiconducting-to-Metallic Phase Transition in Single-Layered MoS_2. *Nat. Nanotechnol.* **2014**, *9* (5), 391–396.

(81) Toh, R. J.; Sofer, Z.; Luxa, J.; Sedmidubský, D.; Pumera, M. 3R Phase of MoS_2 and WS_2 Outperforms the Corresponding 2H Phase for Hydrogen Evolution. *Chem. Comm.* **2017**, *53* (21), 3054–3057.

(82) Ali, S.; Ahmad Shah, S. S.; Sufyan Javed, M.; Najam, T.; Parkash, A.; Khan, S.; Bajaber, M. A.; Eldin, S. M. M.; Tayeb, R. A.; Rahman, M. M.; Qi, J. Recent Advances of Transition Metal Dichalcogenides-Based Materials for Energy Storage Devices, in View of Monovalent to Divalent Ions. *Chem. Rec.* **2024**, *24* (1), e202300145.

(83) Coleman, J. N.; Lotya, M.; O'neill, A.; Bergin, S. D.; King, P. J.; Khan, U.; Young, K.; Gaucher, A.; De, S.; Smith, R. J.; Shvets, I. V; Arora, S. K.; Stanton, G.; Kim, H.-Y.; Lee, K.; Kim, G. T.; Duesberg, G. S.; Hallam, T.; Boland, J. J.; Wang, J. J.; Donegan, J. F.; Grunlan, J. C.; Moriarty, G.; Shmeliov, A.; Nicholls, R. J.; Perkins, J. M.; Grieveson, E. M.; Theuwissen, K.; Mccomb, D. W.; Nellist, P. D.; Nicolosi, V. Two-Dimensional Nanosheets Produced by Liquid Exfoliation of Layered Materials, *Science*, **2011**, *331*, 568–571.

(84) Sahoo, R.; Singh, M.; Rao, T. N. A Review on the Current Progress and Challenges of 2D Layered Transition Metal Dichalcogenides as Li/Na-Ion Battery Anodes. *ChemElectroChem* **2021**, *8* (13), 2358–2396.

(85) Zhang, X.; Lai, Z.; Ma, Q.; Zhang, H. Novel Structured Transition Metal Dichalcogenide Nanosheets. *Chem. Soc. Rev.* **2018**, *47* (9), 3301–3338.

(86) Voiry, D.; Goswami, A.; Kappera, R.; Silva, C. D. C. C. E.; Kaplan, D.; Fujita, T.; Chen, M.; Asefa, T.; Chhowalla, M. Covalent Functionalization of Monolayered Transition Metal Dichalcogenides by Phase Engineering. *Nat. Chem.* **2015**, *7* (1), 45–49.

(87) Chen, Y.; Lai, Z.; Zhang, X.; Fan, Z.; He, Q.; Tan, C.; Zhang, H. Phase Engineering of Nanomaterials. *Nat. Rev. Chem.* **2020**, *4* (5), 243–256.

(88) Hu, X.; Zhang, W.; Liu, X.; Mei, Y.; Huang, Y. Nanostructured Mo-Based Electrode Materials for Electrochemical Energy Storage. *Chem. Soc. Rev.* **2015**, *44* (8), 2376–2404.

(89) Yang, J.; Zhang, Y.; Ge, Y.; Tang, S.; Li, J.; Zhang, H.; Shi, X.; Wang, Z.; Tian, X. Interlayer Engineering of Layered Materials for Efficient Ion Separation and Storage. *Adv. Mater.* **2024**, *36* (18), 2311141.

(90) Selwyn, L. S.; Mckinnon, W. R.; Von Sacken, U.; Jones, C. A. Lithium Electrochemical Cells at Low Voltage: Decomposition of Mo and W Dichalcogenides. *Solid State Ion.* **1987**, *22* (4), 337–344.

(91) Fang, X.; Hua, C.; Guo, X.; Hu, Y.; Wang, Z.; Gao, X.; Wu, F.; Wang, J.; Chen, L. Lithium Storage in Commercial MoS_2 in Different Potential Ranges. *Electrochim. Acta* **2012**, *81*, 155–160.

(92) Wang, Z.; Mi, B. Environmental Applications of 2D Molybdenum Disulfide (MoS_2) Nanosheets. *Environ. Sci. Technol.* **2017**, *51* (15), 8229–8244.

(93) Py, M. A.; Haering, R. R. Structural Destabilization Induced by Lithium Intercalation in MoS_2 and Related Compounds. *Can. J. Phys.* **1983**, *61* (1), 76–84.

(94) Abdel Maksoud, M. I. A.; Bedir, A. G.; Bekhit, M.; Abouelela, M. M.; Fahim, R. A.; Awed, A. S.; Attia, S. Y.; Kassem, S. M.; Elkodous, M. A.; El-Sayyad, G. S.; Mohamed, S. G.; Osman, A. I.; Al-Muhtaseb, A. H.; Rooney, D. W. MoS_2-Based Nanocomposites: Synthesis, Structure, and Applications in Water Remediation and Energy Storage: A Review. *Envrion. Chem. Lett.* **2021**, *19* (5), 3645–3681.

(95) Choi, J.; Moon, H.; Fleischmann, S. Simultaneous Control of Crystallite Size and Interlayer Spacing of MoS_2 to Achieve Pseudocapacitive Lithium Intercalation. *Electrochim. Acta* **2024**, *476*, 143774.

(96) Choi, J.; Nam, K.; Malik, Y. T.; Leiter, R.; Zarrabeitia, M.; Scheurer, C.; Fleischmann, S. Interlayer Spacing Control of MoS_2 with Covalent Thiol Functionalization: Understanding Structure and Electrochemistry from Experiments and Simulation. *ACS Nano* **2025**, *19* (40), 35425–35437.

(97) Cook, J. B.; Kim, H. S.; Yan, Y.; Ko, J. S.; Robbennolt, S.; Dunn, B.; Tolbert, S. H. Mesoporous MoS_2 as a Transition Metal Dichalcogenide Exhibiting Pseudocapacitive Li and Na-Ion Charge Storage. *Adv. Energy Mater.* **2016**, *6* (9).

(98) Cook, J. B.; Lin, T. C.; Kim, H. S.; Siordia, A.; Dunn, B. S.; Tolbert, S. H. Suppression of Electrochemically Driven Phase Transitions in Nanostructured MoS_2 Pseudocapacitors Probed Using Operando X-Ray Diffraction. *ACS Nano* **2019**, *13* (2), 1223–1231.

(99) Cook, J. B.; Kim, H. S.; Lin, T. C.; Lai, C. H.; Dunn, B.; Tolbert, S. H. Pseudocapacitive Charge Storage in Thick Composite MoS_2 Nanocrystal-Based Electrodes. *Adv. Energy Mater.* **2017**, *7* (2), 1601283.

(100) Zhu, X.; Su, Z.; Wu, C.; Cong, H.; Ai, X.; Yang, H.; Qian, J. Exfoliation of MoS_2 Nanosheets Enabled by a Redox-Potential-Matched Chemical Lithiation Reaction. *Nano Lett.* **2022**, *22* (7), 2956–2963.

(101) Rahmatinejad, J.; Ye, Z. Advanced MoS_2 Nanocomposites for Post-Lithium-Ion Batteries. *Chem. Eng. J.* **2024**, *500*, 156872.

(102) Ding, S.; He, P.; Feng, W.; Li, L.; Zhang, G.; Chen, J.; Dong, F.; He, H. Novel Molybdenum Disulfide Nanosheets–Decorated Polyaniline: Preparation, Characterization and Enhanced Electrocatalytic Activity for Hydrogen Evolution Reaction. *J. Phys. Chem. Solids* **2016**, *91*, 41–47.

(103) Rasamani, K. D.; Alimohammadi, F.; Sun, Y. Interlayer-Expanded MoS_2. *Mater. Today* **2017**, *20* (2), 83–91.

(104) Guo, C.; Pan, J.; Li, H.; Lin, T.; Liu, P.; Song, C.; Wang, D.; Mu, G.; Lai, X.; Zhang, H.; Zhou, W.; Chen, M.; Huang, F. Observation of Superconductivity in 1T′-MoS_2 Nanosheets. *J. Mater. Chem. C* **2017**, *5* (41), 10855–10860.

(105) Yao, Y.; Cumberbatch, H.; Robertson, D. D.; Chin, M. A.; Lamkin, R.; Tolbert, S. H. On the Interplay between Size and Disorder in Suppressing Intercalation-Induced Phase

Transitions in Pseudocapacitive Nanostructured MoS_2, *Adv. Funct. Mater.*, **2024**, *34* (50), 2304896.

(106) Novoselov, K. S.; Geim, A. K.; Morozov, S. V; Jiang, D.; Zhang, Y.; Dubonos, S. V; Grigorieva, I. V; Firsov, A. A. Electric Field Effect in Atomically Thin Carbon Films, *Science*, **2004**, *306* (5696), 666–669.

(107) Novoselov, K. S. Nobel Lecture: Graphene: Materials in the Flatland. *Rev. Mod. Phys.* **2011**, *83* (3), 837–849.

(108) Pollmann, E.; Sleziona, S.; Foller, T.; Hagemann, U.; Gorynski, C.; Petri, O.; Madauß, L.; Breuer, L.; Schleberger, M. Large-Area, Two-Dimensional MoS_2 Exfoliated on Gold: Direct Experimental Access to the Metal–Semiconductor Interface. *ACS Omega* **2021**, *6* (24), 15929–15939.

(109) Yang, Z. J.; Li, Z.; Lampronti, G. I.; Lee, J. I.; Wang, Y.; Day, J.; Chhowalla, M. Environmental and Thermal Stability of Chemically Exfoliated Li_xMoS_2 for Lithium-Sulfur Batteries. *Chem. Mater.* **2024**, *36* (9), 4829–4837.

(110) Ottaviano, L.; Palleschi, S.; Perrozzi, F.; D'Olimpio, G.; Priante, F.; Donarelli, M.; Benassi, P.; Nardone, M.; Gonchigsuren, M.; Gombosuren, M.; Lucia, A.; Moccia, G.; Cacioppo, O. A. Mechanical Exfoliation and Layer Number Identification of MoS_2 Revisited. *2D Mater.* **2017**, *4* (4), 045013.

(111) Ruoff, R. Calling All Chemists. *Nat. Nanotechnol.* **2008**, *3* (1), 10–11.

(112) Zheng, W.; Lee, L. Y. S. Beyond Sonication: Advanced Exfoliation Methods for Scalable Production of 2D Materials. *Matter* **2022**, *5* (2), 515–545.

(113) Zheng, J.; Zhang, H.; Dong, S.; Liu, Y.; Tai Nai, C.; Suk Shin, H.; Young Jeong, H.; Liu, B.; Ping Loh, K. High Yield Exfoliation of Two-Dimensional Chalcogenides Using Sodium Naphthalenide. *Nat. Comm.* **2014**, *5* (1), 2995.

(114) Joensen, P.; Frindt, R. F.; Morrison, S. R. Single-Layer MoS_2. *Mat. Res. Bull.* **1986**, *21* (4), 457–461.

(115) Ramakrishna Matte, H. SS.; Gomathi, A.; Manna, A. K.; Late, D. J.; Datta, R.; Pati, S. K.; Rao, C. N. R. MoS_2 and WS_2 Analogues of Graphene. *Angew. Chem., Int. Ed.* **2010**, *49* (24), 4059–4062.

(116) Chang, K.; Hai, X.; Pang, H.; Zhang, H.; Shi, L.; Liu, G.; Liu, H.; Zhao, G.; Li, M.; Ye, J. Targeted Synthesis of 2H- and 1T-Phase MoS_2 Monolayers for Catalytic Hydrogen Evolution. *Adv. Mater.* **2016**, *28* (45), 10033–10041.

(117) Zhao, L.; Wang, Y.; Wei, C.; Huang, X.; Zhang, X.; Wen, G. MoS_2-Based Anode Materials for Lithium-Ion Batteries: Developments and Perspectives. *Particuology* **2024**, *87*, 240–270.

(118) Hu, W. H.; Han, G. Q.; Dai, F. N.; Liu, Y. R.; Shang, X.; Dong, B.; Chai, Y. M.; Liu, Y. Q.; Liu, C. G. Effect of PH on the Growth of MoS_2 (002) Plane and Electrocatalytic Activity for HER. *Int. J. Hydrogen Energy* **2016**, *41* (1), 294–299.

(119) Strachan, J.; Masters, A. F.; Maschmeyer, T. Critical Review: Hydrothermal Synthesis of 1T-MoS_2 – an Important Route to a Promising Material. *J Mater. Chem. A* **2021**, *9* (15), 9451–9461.

(120) Wang, S.; Li, Y.; Hu, Y.; Zhou, X.; Zhang, M.; Jia, X.; Yang, Y.; Lin, B. L.; Chen, G. One-Step Synthesis of 1T MoS_2 Hierarchical Nanospheres for Electrocatalytic Hydrogen Evolution. *ACS Appl. Energy Mater.* **2022**, *5* (9), 11705–11712.

(121) Li, J.; Listwan, A.; Liang, J.; Shi, F.; Li, K.; Jia, J. High Proportion of 1 T Phase MoS_2 Prepared by a Simple Solvothermal Method for High-Efficiency Electrocatalytic Hydrogen Evolution. *Chem. Eng. J.* **2021**, *422*, 130100.

(122) Tobis, M.; Elmanzalawy, M.; Choi, J.; Frąckowiak, E.; Fleischmann, S. Controlling Structure and Morphology of MoS_2 via Sulfur Precursor for Optimized Pseudocapacitive Lithium Intercalation Hosts. *Batter. Supercaps* **2024**, *7* (11), e202400277.

(123) Geng, X.; Sun, W.; Wu, W.; Chen, B.; Al-Hilo, A.; Benamara, M.; Zhu, H.; Watanabe, F.; Cui, J.; Chen, T. P. Pure and Stable Metallic Phase Molybdenum Disulfide Nanosheets for Hydrogen Evolution Reaction. *Nat. Comm.* **2016**, *7* (1), 10672.

(124) Wang, G.; Zhang, J.; Yang, S.; Wang, F.; Zhuang, X.; Müllen, K.; Feng, X. Vertically Aligned MoS_2 Nanosheets Patterned on Electrochemically Exfoliated Graphene for High-Performance Lithium and Sodium Storage. *Adv. Energy Mater.* **2018**, *8* (8), 1702254.

(125) Long, L. N.; Bich, T. T. N. Hydrothermal Phase Engineering of 1T/2H MoS_2/Graphene Nanocomposites for Enhanced Electronic, Catalytic, and Electrochemical Performance. *Adv. Mater. Technol.* **2025**, *10* (21), e00454.

(126) Wang, X.; Li, H.; Li, H.; Lin, S.; Ding, W.; Zhu, X.; Sheng, Z.; Wang, H.; Zhu, X.; Sun, Y. 2D/2D 1T-MoS_2/Ti_3C_2 MXene Heterostructure with Excellent Supercapacitor Performance. *Adv. Funct. Mater.* **2020**, *30* (15), 0190302.

(127) Kour, P.; Deeksha; Yadav, K. Electrochemical Performance of Mixed-Phase 1T/2H MoS_2 Synthesized by Conventional Hydrothermal v/s Microwave-Assisted

Hydrothermal Method for Supercapacitor Applications. *J. Alloys Compd.* **2022**, *922*, 166194.

(128) Wang, X.; Feng, H.; Wu, Y.; Jiao, L. Controlled Synthesis of Highly Crystalline MoS_2 Flakes by Chemical Vapor Deposition. *J. Am. Chem. Soc.* **2013**, *135* (14), 5304–5307.

(129) Coogan, Á.; Gun'Ko, Y. K. Solution-Based "Bottom-up" Synthesis of Group VI Transition Metal Dichalcogenides and Their Applications. *Mater. Adv.* **2021**, *2* (1), 146–164.

(130) Parida, S.; Dobley, A.; Carter, C. B.; Dongare, A. M. Phase Engineering of Layered Anode Materials during Ion-Intercalation in Van Der Waal Heterostructures. *Sci. Rep.* **2023**, *13* (1), 5408.

(131) Peng, L.; Zhu, Y.; Chen, D.; Ruoff, R. S.; Yu, G. Two-Dimensional Materials for Beyond-Lithium-Ion Batteries. *Adv. Energy Mater.* **2016**, *6* (11), 1600025.

(132) Bruce, P. G.; Scrosati, B.; Tarascon, J. M. Nanomaterials for Rechargeable Lithium Batteries. *Angew. Chem., Int. Ed.* **2008**, *47* (16), 2930–2946.

(133) Rosa Palacín, M.; Simon, P.; Tarascon, J.; Rosa, M.; Marie Tarascon, J. Nanomaterials for Electrochemical Energy Storage: The Good and the Bad. *Acta Chim. Solv.* **2016**, *63*, 417–423.

(134) Augustyn, V.; Gogotsi, Y. 2D Materials with Nanoconfined Fluids for Electrochemical Energy Storage. *Joule* **2017**, *1* (3), 443–452.

(135) Xu, J.; Zhang, J.; Zhang, W.; Lee, C. S. Interlayer Nanoarchitectonics of Two-Dimensional Transition-Metal Dichalcogenides Nanosheets for Energy Storage and Conversion Applications. *Adv. Energy Mater.* **2017**, *7* (23), 1700571.

(136) Zhang, Y.; Ang, E. H.; Yang, Y.; Ye, M.; Du, W.; Li, C. C. Interlayer Chemistry of Layered Electrode Materials in Energy Storage Devices. *Adv. Funct. Mater.* **2021**, *31* (4), 2007358.

(137) Fleischmann, S.; Zhang, Y.; Wang, X.; Cummings, P. T.; Wu, J.; Simon, P.; Gogotsi, Y.; Presser, V.; Augustyn, V. Continuous Transition from Double-Layer to Faradaic Charge Storage in Confined Electrolytes. *Nat. Energy* **2022**, *7* (3), 222–228.

(138) Guo, H.; Elmanzalawy, M.; Sivakumar, P.; Fleischmann, S. Unifying Electrolyte Formulation and Electrode Nanoconfinement Design to Enable New Ion-Solvent Cointercalation Chemistries. *Energy Envrion. Sci.* **2024**, *17* (6), 2100–2116.

(139) Anasori, B.; Lukatskaya, M. R.; Gogotsi, Y. 2D Metal Carbides and Nitrides (MXenes) for Energy Storage. *Nat. Rev. Mater.* **2017**, *2* (2), 16098.

(140) Li, Y.; Shao, H.; Lin, Z.; Lu, J.; Liu, L.; Duployer, B.; Persson, P. O. Å.; Eklund, P.; Hultman, L.; Li, M.; Chen, K.; Zha, X. H.; Du, S.; Rozier, P.; Chai, Z.; Raymundo-Piñero, E.; Taberna, P. L.; Simon, P.; Huang, Q. A General Lewis Acidic Etching Route for Preparing MXenes with Enhanced Electrochemical Performance in Non-Aqueous Electrolyte. *Nat. Mater.* **2020**, *19* (8), 894–899.

(141) Liang, K.; Matsumoto, R. A.; Zhao, W.; Osti, N. C.; Popov, I.; Thapaliya, B. P.; Fleischmann, S.; Misra, S.; Prenger, K.; Tyagi, M.; Mamontov, E.; Augustyn, V.; Unocic, R. R.; Sokolov, A. P.; Dai, S.; Cummings, P. T.; Naguib, M. Engineering the Interlayer Spacing by Pre-Intercalation for High Performance Supercapacitor MXene Electrodes in Room Temperature Ionic Liquid. *Adv. Funct. Mater.* **2021**, *31* (33), 2104007.

(142) Chen, B.; Chao, D.; Liu, E.; Jaroniec, M.; Zhao, N.; Qiao, S. Z. Transition Metal Dichalcogenides for Alkali Metal Ion Batteries: Engineering Strategies at the Atomic Level. *Energy Environ. Sci.* **2020**, *13* (4), 1096–1131.

(143) Gong, S.; Zhao, G.; Lyu, P.; Sun, K. A Pseudolayered MoS_2 as Li-Ion Intercalation Host with Enhanced Rate Capability and Durability. *Small* **2018**, *14* (48), 1803344.

(144) Gong, S.; Zhao, G.; Lyu, P.; Sun, K. Insights into the Intrinsic Capacity of Interlayer-Expanded MoS_2 as a Li-Ion Intercalation Host, *J. Mater. Chem. A*, **2019**, *7* (3), 1187–1195.

(145) Zhang, F.; Li, C.; Liu, Y.; Yao, M.; Chen, Z.; Zhang, A. Interlayer Spacing Engineering of 1T-MoS_2 for Enhanced Capacitive Deionization Performance in Water Desalination. *Desalination* **2025**, *616*, 119339.

(146) Xin, D.; Zhang, X.; Zhang, Z.; Sun, J.; Li, Q.; He, X.; Jiang, R.; Liu, Z.; Lei, Z. Pre-Intercalation of TMA Cations in MoS_2 Interlayers for Fast and Stable Zinc Ion Storage. *Small* **2024**, *20* (44), 2403050.

(147) Lmmon, J. P.; Wu, J.; Oriakhi, C.; Lerner, M. M. Preparation of Nanocomposites Containing Poly(Ethylene Oxide) and Layered Solids. *Electrochim. Acta* **1995**, *40*, 2245–2249.

(148) Lemmon, J. P.; Lerner, M. M. Preparation and Characterization of Nanocomposites of Polyethers and Molybdenum Disulfide. *Chem. Mater.* **1994**, *6*, 207–210.

(149) Li, Y.; Liang, Y.; Robles Hernandez, F. C.; Deog Yoo, H.; An, Q.; Yao, Y. Enhancing Sodium-Ion Battery Performance with Interlayer-Expanded MoS_2-PEO Nanocomposites. *Nano Energy* **2015**, *15*, 453–461.

(150) Chen, X.; McDonald, A. R. Functionalization of Two-Dimensional Transition-Metal Dichalcogenides. *Adv. Mater.* **2016**, *28* (27), 5738–5746.

(151) Chen, X.; Berner, N. C.; Backes, C.; Duesberg, G. S.; McDonald, A. R. Functionalization of Two-Dimensional MoS_2: On the Reaction between MoS_2 and Organic Thiols. *Angew. Chem.* **2016**, *55* (19), 5803–5808.

(152) Presolski, S.; Pumera, M. Covalent Functionalization of MoS_2. *Mater. Today* **2016**, *19* (3), 140–145.

(153) Ippolito, S.; Urban, F.; Zheng, W.; Mazzarisi, O.; Valentini, C.; Kelly, A. G.; Gali, S. M.; Bonn, M.; Beljonne, D.; Corberi, F.; Coleman, J. N.; Wang, H. I.; Samorì, P. Unveiling Charge-Transport Mechanisms in Electronic Devices Based on Defect-Engineered MoS_2 Covalent Networks. *Adv. Mater.* **2023**, *35* (15), 2211157.

(154) Ippolito, S.; Kelly, A. G.; Furlan de Oliveira, R.; Stoeckel, M. A.; Iglesias, D.; Roy, A.; Downing, C.; Bian, Z.; Lombardi, L.; Samad, Y. A.; Nicolosi, V.; Ferrari, A. C.; Coleman, J. N.; Samorì, P. Covalently Interconnected Transition Metal Dichalcogenide Networks via Defect Engineering for High-Performance Electronic Devices. *Nat. Nanotechnol.* **2021**, *16* (5), 592–598.

(155) Bragg, W. H.; Bragg, W. L. The Reflection of X-Rays by Crystals. *Proc. A* **1913**, *88* (605), 428–438.

(156) Thornton, S.; Rex, A. F. *Modern Physics for Scientists and Engineers*, 4th ed.; Cengage Learning, 2013.

(157) Kaduk, J. A.; Billinge, S. J. L.; Dinnebier, R. E.; Henderson, N.; Madsen, I.; Černý, R.; Leoni, M.; Lutterotti, L.; Thakral, S.; Chateigner, D. Powder Diffraction. *Nat. Rev. Methods Primers* **2021**, *1*, 77.

(158) *Handbook of Materials Characterization*; Sharma, S. K., Verma, D. S., Khan, L. U., Kumar, S., Khan, S. B., Eds.; Springer, 2018.

(159) Abidi, N. *FTIR Microspectroscopy: Selected Emerging Applications*; Springer, 2023.

(160) Raman, C. V.; Krishnan, K. S. A New Type of Secondary Radiation. *Nature* **1928**, *121*, 501–502.

(161) Zhang, X.; Tan, Q. H.; Wu, J. Bin; Shi, W.; Tan, P. H. Review on the Raman Spectroscopy of Different Types of Layered Materials. *Nanoscale* **2016**, *8* (12), 6435–6450.

(162) Long, D. A. *The Raman Effect: A Unified Treatment of the Theory of Raman Scattering by Molecules*; John Wiley & Sons, 2002.

(163) Guerrero-Pérez, M. O.; Patience, G. S.; Bañares, M. A. Experimental Methods in Chemical Engineering: Raman Spectroscopy. *Can. J. Chem. Eng.* **2021**, *99* (1), 97–107.

(164) Allakhverdiev, K. R.; Lovera, D.; Altstädt, V.; Schreier, P.; Kador, L. Confocal Raman Microscopy: Non-Destructive Materials Analysis with Micrometer Resolution. *Rev. Adv. Mater. Sci.* **2009**, *20* (1), 77–84.

(165) *ASM Handbook, Volume 10: Materials Characterization*; Bruno, T. J., Deacon, R., Jansen, J. A., Magdefrau, N., Mueller, E., Vander Voort, G. F., Yang, D., Eds.; ASM International: Materials Park, OH, USA, 2019.

(166) Thommes, M.; Kaneko, K.; Neimark, A. V.; Olivier, J. P.; Rodriguez-Reinoso, F.; Rouquerol, J.; Sing, K. S. W. Physisorption of Gases, with Special Reference to the Evaluation of Surface Area and Pore Size Distribution (IUPAC Technical Report). *Pure Appl. Chem.* **2015**, *87* (9–10), 1051–1069.

(167) Brunauer, S.; Emmett, P. H.; Teller, E. Adsorption of Gases in Multimolecular Layers. *J. Am. Chem. Soc.* **1938**, *60*, 309–319.

(168) Siegbahn, K.; Nordling, C.; Fahlman, A.; Nordberg, R.; Hamrin, K.; Hedman, J.; Johansson, G.; Bergmark, T.; Karlsson, S. E.; Lindgren, I.; Lindberg, B. *ESCA: Atomic, Molecular and Solid State Structure Studied by Means of Electron Spectroscopy*; Almqvist & Wiksells: Uppsala, Sweden, 1967.

(169) Hertz, H. Ueber Einen Einfluss Des Ultravioletten Lichtes Auf Die Electricshe Entladung. *Ann. Phys.* **1887**, *267* (8), 983–1000.

(170) Greczynski, G.; Haasch, R. T.; Hellgren, N.; Lewin, E.; Hultman, L. X-Ray Photoelectron Spectroscopy of Thin Films. *Nat. Rev. Methods Primers* **2023**, *3*, 40.

(171) Boffard, J. B.; Piech, G. A.; Gehrke, M. F.; Anderson, L. W.; Lin, C. C. Measurement of Electron-Impact Excitation Cross Sections out of Metastable Levels of Argon and Comparison with Ground-State Excitation. *Phys. Rev. A* **1999**, *59* (4), 2749–2763.

(172) Lajunen, L. H.; Perämäki, P. *Spectrochemical Analysis by Atomic Absorption and Emission*, 2nd ed.; Royal Society of Chemistry, 2004.

(173) Douvris, C.; Vaughan, T.; Bussan, D.; Bartzas, G.; Thomas, R. How ICP-OES Changed the Face of Trace Element Analysis: Review of the Global Application Landscape. *Sci. Total Environ.* **2023**, *905*, 167242.

(174) Wright, R. J.; Stuczynski, T. I. Atomic Absorption and Flame Emission Spectrometry. In *Methods of Soil Analysis: Part 3 Chemical Methods*; Sparks, D. L., Ed.; Soil Science Society of America, American Society of Agronomy: Madison, WI, USA, 1996; Vol. 5, pp 65–90.

(175) Khan, S. R.; Sharma, B.; Chawla, P. A.; Bhatia, R. Inductively Coupled Plasma Optical Emission Spectrometry (ICP-OES): A Powerful Analytical Technique for Elemental Analysis. *Food Anal. Methods* **2022**, *15* (3), 666–688.

(176) Ural, N. The Significance of Scanning Electron Microscopy (SEM) Analysis on the Microstructure of Improved Clay: An Overview. *Open Geosci.* **2021**, *13* (1), 197–218.

(177) Seiler, H. Secondary Electron Emission in the Scanning Electron Microscope. *J. Appl. Phys.* **1983**, *54* (11), R1–R18.

(178) Inkson, B. J. Scanning Electron Microscopy (SEM) and Transmission Electron Microscopy (TEM) for Materials Characterization. In *Materials Characterization Using Nondestructive Evaluation (NDE) Methods*; Hübschen, G., Altpeter, I., Tschuncky, R., Herrmann, H.-G., Eds.; Woodhead Publishing: Oxford, UK, 2016; pp 17–43.

(179) Li, G.; Zhang, H.; Han, Y. Applications of Transmission Electron Microscopy in Phase Engineering of Nanomaterials. *Chem. Rev.* **2023**, *123* (17), 10728–10749.

(180) Lotya, M.; Rakovich, A.; Donegan, J. F.; Coleman, J. N. Measuring the Lateral Size of Liquid-Exfoliated Nanosheets with Dynamic Light Scattering. *Nanotechnology* **2013**, *24* (26), 265703.

(181) Bhattacharjee, S. DLS and Zeta Potential - What They Are and What They Are Not? *J. Controlled Release* **2016**, *235*, 337–351.

(182) Ferrero, G. A.; Åvall, G.; Janßen, K.; Son, Y.; Kravets, Y.; Sun, Y.; Adelhelm, P. Solvent Co-Intercalation Reactions for Batteries and Beyond. *Chem. Rev.* **2025**, *125* (6), 3401–3439.

(183) Metrot, A.; Willmann, P.; Herold, A. Insertion Electrochimique Du Complexe BF3,(C2H5)2O Dans Un Pyrographite. *Mater. Sci. Eng.* **1977**, *31*, 83–86.

(184) Escher, I.; Hahn, M.; A. Ferrero, G.; Adelhelm, P. A Practical Guide for Using Electrochemical Dilatometry as Operando Tool in Battery and Supercapacitor Research. *Energy Technol.* **2022**, *10* (5), 2101120.

(185) Yang, X.; Rogach, A. L. Electrochemical Techniques in Battery Research: A Tutorial for Nonelectrochemists. *Adv. Energy Mater.* **2019**, *9* (25), 1900747.

(186) Malik, Y. T.; Braig, M.; Simon, P.; Zeis, R.; Fleischmann, S. Analysis of Battery-like and Pseudocapacitive Ion Intercalation Kinetics via Distribution of Relaxation Times. *J. Electrochem. Soc.* **2024**, *171* (11), 110515.

(187) Eda, G.; Yamaguchi, H.; Voiry, D.; Fujita, T.; Chen, M.; Chhowalla, M. Photoluminescence from Chemically Exfoliated MoS_2. *Nano Lett.* **2011**, *11* (12), 5111–5116.

(188) Perdew, J. P.; Burke, K.; Ernzerhof, M. Generalized Gradient Approximation Made Simple. *Phys. Rev. Lett.* **1996**, *77* (18), 3865.

(189) Giannozzi, P.; Baroni, S.; Bonini, N.; Calandra, M.; Car, R.; Cavazzoni, C.; Ceresoli, D.; Chiarotti, G. L.; Cococcioni, M.; Dabo, I.; Dal Corso, A.; De Gironcoli, S.; Fabris, S.; Fratesi, G.; Gebauer, R.; Gerstmann, U.; Gougoussis, C.; Kokalj, A.; Lazzeri, M.; Martin-Samos, L.; Marzari, N.; Mauri, F.; Mazzarello, R.; Paolini, S.; Pasquarello, A.; Paulatto, L.; Sbraccia, C.; Scandolo, S.; Sclauzero, G.; Seitsonen, A. P.; Smogunov, A.; Umari, P.; Wentzcovitch, R. M. QUANTUM ESPRESSO: A Modular and Open-Source Software Project for Quantum Simulations of Materials. *J. Phys.: Condens. Matter* **2009**, *21* (39), 395502.

(190) van Setten, M. J.; Giantomassi, M.; Bousquet, E.; Verstraete, M. J.; Hamann, D. R.; Gonze, X.; Rignanese, G. M. The PSEUDODOJO: Training and Grading a 85 Element Optimized Norm-Conserving Pseudopotential Table. *Comput. Phys. Commun.* **2018**, *226*, 39–54.

(191) Grimme, S.; Antony, J.; Ehrlich, S.; Krieg, H. A Consistent and Accurate Ab Initio Parametrization of Density Functional Dispersion Correction (DFT-D) for the 94 Elements H-Pu. *J. Chem. Phys.* **2010**, *132* (15), 154104.

(192) Lindgren, P.; Kastlunger, G.; Peterson, A. A. Scaled and Dynamic Optimizations of Nudged Elastic Bands. *J. Chem. Theory Comput.* **2019**, *15* (11), 5787–5793.

(193) Henkelman, G.; Uberuaga, B. P.; Jónsson, H. Climbing Image Nudged Elastic Band Method for Finding Saddle Points and Minimum Energy Paths. *J. Chem. Phys.* **2000**, *113* (22), 9901–9904.

(194) Neese, F. The ORCA Program System. *WIREs Comput. Mol. Sci.* **2012**, *2* (1), 73–78.

(195) Becke, A. D. Density-Functional Thermochemistry. III. The Role of Exact Exchange. *J. Chem. Phys.* **1993**, *98* (7), 5648–5652.

(196) Stephens, P. J.; Devlin, F. J.; Chabalowski, C. F.; Frisch, M. J. Ab Initio Calculation of Vibrational Absorption and Circular Dichroism Spectra Using Density Functional Force Fields. *J. Phys. Chem.* **1994**, *98* (45), 11623–11627.

(197) Momma, K.; Izumi, F. VESTA 3 for Three-Dimensional Visualization of Crystal, Volumetric and Morphology Data. *J. Appl. Cryst.* **2011**, *44* (6), 1272–1276.

(198) Kumar, N.; Siroha, P.; Shankar, H.; Singh, D.; Sharma, Y.; Kumar, R.; Ramovatar; Yadav, N.; Dey, K. K.; Borkar, H.; Gangwar, J. Probing into Crystallography and Morphology Properties of MoS_2 Nanoflowers Synthesized via Temperature Dependent Hydrothermal Method. *Nano Ex.* **2022**, *3* (3), 035001.

(199) Yu, Y.; Nam, G. H.; He, Q.; Wu, X. J.; Zhang, K.; Yang, Z.; Chen, J.; Ma, Q.; Zhao, M.; Liu, Z.; Ran, F. R.; Wang, X.; Li, H.; Huang, X.; Li, B.; Xiong, Q.; Zhang, Q.; Liu, Z.; Gu, L.; Du, Y.; Huang, W.; Zhang, H. High Phase-Purity 1T′-MoS_2- and 1T′-$MoSe_2$-Layered Crystals. *Nat. Chem.* **2018**, *10* (6), 638–643.

(200) Stephenson, T.; Li, Z.; Olsen, B.; Mitlin, D. Lithium Ion Battery Applications of Molybdenum Disulfide (MoS_2) Nanocomposites. *Energy Environ. Sci.* **2014**, *7* (1), 209–231.

(201) Wu, B.; Lochala, J.; Taverne, T.; Xiao, J. The Interplay between Solid Electrolyte Interface (SEI) and Dendritic Lithium Growth. *Nano Energy* **2017**, *40*, 34–41.

(202) Nam, G. H.; He, Q.; Wang, X.; Yu, Y.; Chen, J.; Zhang, K.; Yang, Z.; Hu, D.; Lai, Z.; Li, B.; Xiong, Q.; Zhang, Q.; Gu, L.; Zhang, H. In-Plane Anisotropic Properties of 1T′-MoS_2 Layers. *Adv. Mater.* **2019**, *31* (21), 1807764.

(203) Hou, X.; Zhang, W.; Peng, J.; Zhou, L.; Wu, J.; Xie, K.; Fang, Z. Phase Transformation of 1T′-MoS_2 Induced by Electrochemical Prelithiation for Lithium-Ion Storage. *ACS Appl. Energy Mater.* **2022**, *5* (9), 11292–11303.

(204) Kwak, I. H.; Kwon, I. S.; Abbas, H. G.; Jung, G.; Lee, Y.; Debela, T. T.; Yoo, S. J.; Kim, J. G.; Park, J.; Kang, H. S. Nitrogen-Rich 1T′-MoS_2 Layered Nanostructures Using Alkyl Amines for High Catalytic Performance toward Hydrogen Evolution. *Nanoscale* **2018**, *10* (30), 14726–14735.

(205) Marshall, C. P.; Javaux, E. J.; Knoll, A. H.; Walter, M. R. Combined Micro-Fourier Transform Infrared (FTIR) Spectroscopy and Micro-Raman Spectroscopy of Proterozoic Acritarchs: A New Approach to Palaeobiology. *Precambrian Res.* **2005**, *138* (3–4), 208–224.

(206) Kwak, I. H.; Kwon, I. S.; Abbas, H. G.; Seo, J.; Jung, G.; Lee, Y.; Kim, D.; Ahn, J. P.; Park, J.; Kang, H. S. Intercalated Complexes of 1T′-MoS_2 Nanosheets with Alkylated Phenylenediamines as Excellent Catalysts for Electrochemical Hydrogen Evolution. *J. Mater. Chem. A* **2019**, *7* (5), 2334–2343.

(207) Major, G. H.; Fairley, N.; Sherwood, P. M. A.; Linford, M. R.; Terry, J.; Fernandez, V.; Artyushkova, K. Practical Guide for Curve Fitting in X-Ray Photoelectron Spectroscopy. *J. Vac. Sci. Technol. A* **2020**, *38* (6), 061203.

(208) Scanlon, D. O.; Watson, G. W.; Payne, D. J.; Atkinson, G. R.; Egdell, R. G.; Law, D. S. L. Theoretical and Experimental Study of the Electronic Structures of MoO_3 and MoO_2. *J. Phys. Chem. C* **2010**, *114* (10), 4636–4645.

(209) Counsell, J. D. P.; Coultas, S. J.; Gerrard, N. MoS_2 by XPS Using Monochromatic Ag Lα x Rays. *Surf. Sci. Spectra* **2021**, *28* (2), 024007.

(210) Park, K. T.; Kong, J. Chemistry and Physics of Alkali Metals on MoS_2 Surfaces. *Top. Catal.* **2002**, *18*, 175–181.

(211) Banda, H.; Périé, S.; Daffos, B.; Taberna, P. L.; Dubois, L.; Crosnier, O.; Simon, P.; Lee, D.; De Paëpe, G.; Duclairoir, F. Sparsely Pillared Graphene Materials for High-Performance Supercapacitors: Improving Ion Transport and Storage Capacity. *ACS Nano* **2019**, *13* (2), 1443–1453.

(212) Wang, J.; Polleux, J.; Lim, J.; Dunn, B. Pseudocapacitive Contributions to Electrochemical Energy Storage in TiO_2 (Anatase) Nanoparticles. *J. Phys. Chem. C* **2007**, *111* (40), 14925–14931.

(213) Hu, W.; Liu, H.; Dong, W.; Akif Munir, H.; Fan, X.; Tian, X.; Pang, L. Ammonium Ions Intercalated 1T/2H-MoS_2 with Increased Interlayer Spacing for High-Efficient Electrocatalytic Hydrogen Evolution Reaction. *J. Electroanal. Chem.* **2023**, *949*, 117882.

(214) Utigard, T. Oxidation Mechanism of Molybdenite Concentrate. *Metall. Mater. Trans. B* **2009**, *40* (4), 490–496.

(215) Li, Q.; Zhao, Y.; Ling, C.; Yuan, S.; Chen, Q.; Wang, J. Towards a Comprehensive Understanding of the Reaction Mechanisms Between Defective MoS_2 and Thiol Molecules. *Angew. Chem., Int. Ed.* **2017**, *56* (35), 10501–10505.

(216) Chou, S. S.; De, M.; Kim, J.; Byun, S.; Dykstra, C.; Yu, J.; Huang, J.; Dravid, V. P. Ligand Conjugation of Chemically Exfoliated MoS_2. *J. Am. Chem. Soc.* **2013**, *135* (12), 4584–4587.

(217) Oztürk, N.; Aˇ Grı C ¸ Irak, C. ¸; Bahçeli, S. FT-IR Spectroscopic Study of 1,5-Pentanedithiol and 1,6-Hexanedithiol Adsorbed on NaA, CaA and NaY Zeolites. *Z. Naturforsch. A* **2005**, *60*, 633–636.

(218) Marinov, A. D.; Bravo Priegue, L.; Shah, A. R.; Miller, T. S.; Howard, C. A.; Hinds, G.; Shearing, P. R.; Cullen, P. L.; Brett, D. J. L. Ex Situ Characterization of 1T/2H MoS_2 and Their Carbon Composites for Energy Applications, a Review. *ACS Nano* **2023**, *17* (6), 5163–5186.

(219) Shirota, G.; Nasu, A.; Deguchi, M.; Sakuda, A.; Tatsumisago, M.; Hayashi, A. Mechanochemical Synthesis of Amorphous MoS_x (x = 3, 4, 5, 6, and 7) Electrode for All-Solid-State Sodium Battery. *J. Ceram. Soc. Jpn.* **2022**, *130* (4), 308–312.

(220) Cui, H.; Song, Y.; Ren, D.; Wang, L.; He, X. Electrocapillary Boosting Electrode Wetting for High-Energy Lithium-Ion Batteries. *Joule* **2024**, *8* (1), 29–44.

(221) Choi, W.; Shin, H. C.; Kim, J. M.; Choi, J. Y.; Yoon, W. S. Modeling and Applications of Electrochemical Impedance (EIS) for Lithium-Ion Batteries. *J. Electrochem. Sci. Technol.* **2020**, *11* (1), 1–13.

(222) Deng, C.; Wang, H.; Wang, S. Clarifying the Lithium Storage Behavior of MoS_2 with in Situ Electrochemical Impedance Spectroscopy. *J. Mater. Chem. A* **2021**, *9* (28), 15734–15743.

(223) Li, Z.; Sami, I.; Yang, J.; Li, J.; Kumar, R. V.; Chhowalla, M. Lithiated Metallic Molybdenum Disulfide Nanosheets for High-Performance Lithium–Sulfur Batteries. *Nat. Energy* **2023**, *8* (1), 84–93.

(224) Zhu, W.; Kamali, A. R. Thermal Oxidation of MoS_2 into Defective Crystalline MoO3 with Enhanced Li-Ion Storage Kinetics. *J. Alloys Compd.* **2023**, *968*, 171823.

(225) Li, H.; Zhang, Q.; Yap, C. C. R.; Tay, B. K.; Edwin, T. H. T.; Olivier, A.; Baillargeat, D. From Bulk to Monolayer MoS_2: Evolution of Raman Scattering. *Adv. Funct. Mater.* **2012**, *22* (7), 1385–1390.

(226) Jimenez Sandoval, S.; Yang, D.; Frindt, R. F.; Irwin, J. C. Raman Study and Lattice Dynamics of Single Molecular Layers of MoS_2. *Phys. Rev. B* **1991**, *44* (8), 3955.

(227) Molina-Sánchez, A.; Hummer, K.; Wirtz, L. Vibrational and Optical Properties of MoS_2: From Monolayer to Bulk. *Surface Science Reports*. Elsevier December 1, 2015, pp 554–586.

(228) Moore, T. S.; Winmill, T. F. CLXXVII.—The State of Amines in Aqueous Solution. *J. Chem. Soc., Transactions* **1912**, *101*, 1635–1676.

(229) Houdeville, R. G.; Black, A. P.; Ponrouch, A.; Palacín, M. R.; Fauth, F. Operando Synchrotron X-Ray Diffraction Studies on TiS_2: The Effect of Propylene Carbonate on Reduction Mechanism. *J. Electrochem. Soc.* **2021**, *168* (3), 030514.

(230) Alvarez Ferrero, G.; Åvall, G.; Mazzio, K. A.; Son, Y.; Janßen, K.; Risse, S.; Adelhelm, P. Co-Intercalation Batteries (CoIBs): Role of TiS_2 as Electrode for Storing Solvated Na Ions. *Adv. Energy Mater.* **2022**, *12* (47), 2202377.

Acknowledgement

My PhD research was funded by the German Federal Ministry of Education and Research (BMBF) within the “NanoMatFutur” program (grant No. 03XP0324) and received basic funding from the Helmholtz Association.

I would like to express my deepest gratitude to my supervisor, Dr. Simon Fleischmann, for the opportunity to pursue my PhD under his exceptional mentorship. This work would not have been possible without his unwavering support. Under his guidance, I mastered numerous research techniques, including TEM, SEM-FIB, Raman spectroscopy, operando/in-situ EIS, XRD, and ECD, and had the privilege of attending many international conferences and workshops. Most importantly, I learned how to manage research projects, develop logical and critical scientific thinking, and effectively communicate scientific results. His mentorship has inspired me to pursue a future career in academia.

I also extend my thanks to all co-authors and collaborators for their assistance with experiments and valuable scientific discussions. Your contributions were instrumental in achieving our shared outcomes and bringing this PhD work to completion.

A special thank you goes to Yoga Malik, a fellow PhD student in my group, for the countless meaningful discussions and for being my "running mate" throughout my time at HIU. It was a pleasure to share ideas and grow together as researchers. I also thank all members of the NGF group for their supports in the office and the lab.

I am also grateful to the SEM team, Dr. Dominik Stepien (K2), Dr. Mintao Wan, Priya Ganesan, Ping Liu, Alexander Rampf, and Enrique, for their dedication to maintaining the SEM/FIB instruments and for their collaborative efforts in troubleshooting device issues.

Beyond my professional circle, I would like to thank my friends. Mahdi, Mehrdad, and Luigi generously shared their time, providing fun and relaxation outside of the institute. I am especially grateful to Hyunjung (Lim), Uzair, and Priya (the "Patient 1419 team") for taking such good care of me during my recovery from a broken collarbone.

My sincere thanks go to the entire HIU community. I will never forget the hospitality and kindness shown to me from my very first day.

Finally, I would like to thank my family in South Korea for their enduring love and support. Although I am not always good at expressing my feelings, I want to take this opportunity to say that I love you all.